High Performance Impurity and Carbon Tolerant and Microstructurally Durable Fuel Electrodes for Solid Oxide Electrolysis Cells

Clausen, Anders Kring

Publication date:
2023

Document Version
Publisher's PDF, also known as Version of record

Citation (APA):
Clausen, A. K. (2023). *High Performance Impurity and Carbon Tolerant and Microstructurally Durable Fuel Electrodes for Solid Oxide Electrolysis Cells*. Technical University of Denmark.

High Performance Impurity and Carbon Tolerant and Microstructurally Durable Fuel Electrodes for Solid Oxide Electrolysis Cells

Anders Kring Clausen

PhD Thesis

Supervisors:
Prof. Peter Vang Hendriksen
Anne Hauch
Xiufu Sun

Department of Energy Conversion and Storage
Technical University of Denmark
March 2023

DTU Energy
Department of Energy Conversion and Storage
Technical University of Denmark

Anders Kring Clausen
Fysikvej 310
2800 Kongens Lyngby, Denmark
www.energy.dtu.dk
Submission date: 27th March 2023

Preface

This thesis is submitted to DTU as a part of the fulfilments to obtain the Ph.D degree. The work was carried out from November 2019 to March 2023 at DTU Energy - Department of Energy Conversion and Storage, under the supervision of Anne Hauch, Prof. Peter Vang Hendriksen and, Development Engineer Xiufu Sun. This work has been by internal funding from DTU Energy.

The project included a three and a half month external stay at the Robert Walker group at Montana State University, thanks to Kaj and Hermilla Ostenfelds Fond for additional funding during the external stay.

Anders Kring Clausen
Kgs. Lyngby - 27/03/2023

Acknowledgements

They say that it takes a village, not about the PhD, but it could as well be the case. I would therefore like to extend my gratitude to all of you whom has played a part in getting me to where I am.
Thank you Anne Hauch for introducing me to SOECs and giving me the chance to pursue a career in research, and the support to do so. I would like to thank Prof. Peter Vang Hendriksen to pick up the mantle as main-supervisor in the last year of the project and your valuable feedback throughout the project. I would also like to thank you Xiufu Sun for teaching me about testing of electrochemical cells, your feedback, and your moral support when the project got hard.

I would also like to acknowledge Lone Christmas for her foresight, you saw this outcome before I did.

Thank you to all whom have taught me the methods used throughout the project. Karl T. S. Thyden, for your help and expertise at the microscope, you light up the world or at least the percolating Ni, also thanks for all the fruitful discussions. Marie L. Traulsen, whom taught me about Raman spectroscopy, an exciting method for material characterisation. Henrik Henriksen, thank you for teaching and assisting me at the cell test rig, your help has been invaluable. Annelise Mikkelsen, Lene Knudsen, and Ebtisam Abdellahi, for help in the laboratories with screen printing and preparation of microstructural samples. Anne and Elisabeth, for help with all of the administrative work.
Thank you Mogens Mogensen for our fruitful conversations, they were very inspiring.

I would like to extend a thanks to Robert Walker and his research group at Montana State University, thank you for giving me the opportunity to visit your group and for your hospitality during my stay. Thank you to Tanner Henning for our collaboration during the stay, and Rhys Trousdale for including me in social activities such as cookouts, and hikes in the Rockies.

A special mention to Aiswarya and Victor, for countless good times during the extent

of my PhD studies, you were there when I needed someone to talk with, whether it was relevant or not to the project. I would also like to thank my other PhD/PostDoc colleagues who has in some shape or form made my project what it is today, so thank you: Francesco, Jens, Anders, Carlos, Jixi, Morten, Achilles, Albert, Miao, Vasileios, and Team Lorentz.

Thank you to all the teachers who have brought me to where I am, specially you Lisa Freeman and Terence Warner, people like you are not acknowledged enough for your great work.

Nearing the end, I would like to thank my friends outside of the PhD world: Ajo, Karen, and Jesper, thank you for being there for me and having my back, I am looking forward to continuing the adventures with you.
My gratitude goes to my parents whom have been there for me throughout my life. Thank you for making me who I am, and supported my choices. You are the reason for where and who I am.
Also thank you to Mette, my sister for being a great sister and being able to keep our secrets.

Finally, thank you Rosa my love. Thank you for being there through the years, both the good, the bad, and the isolated. This would have been much harder without you. You are definitely the best.

Abstract

The Solid Oxide Electrolysis Cell (SOEC) technology provides a method of energy storage, that is required in the transition to relying on renewable energy sources. Energy storage is needed because electricity production when using solar-panels and wind-turbine is dependent on weather-phenomena, which can not be adjusted to match the energy consumption. The energy transition is motivated by the need to reduce the anthropogenic CO_2 emissions from combustion of fossil fuels to reduce global warming. SOECs have the ability to play a double role in the reduction of CO_2 emissions since they, in addition to storing energy, can use CO_2 as the feedstock, where after the splitting the energy is stored in the CO. The CO can then be combined with H_2 to create create hydrocarbons, alcohols or other useful molecules thtn can be used as feed stocks in chemical industry or as "synthetic" fuel. These molecules can replace compounds normally sourced from the petrochemical industry thus reducing the use of fossil resources.

A major issue impeding widespread implementation of SOECs for CO production insufficient lifetime. In this project, the fuel electrode degradation of state-of-the-art anode supported (ASC) Ni/YSZ SOECs has been studied. The degradation mechanisms addressed include: Inhibition of the reaction sites through carbon deposition or poisoning by impurities in the gas feed, and microstructural damage through coarsening or migration of Ni.

The degradation of ASC Ni/YSZ SOECs was studied through a series of long-term (≈1000 h) durability test under CO_2 electrolysis operations, during which their performance were monitored by electrochemical impedance spectroscopy (EIS). The microstructural changes of the SOECs were characterised post-operation using scanning electron microscopy, and Raman spectroscopy for detection of carbon in the fuel electrodes. In all tests in this project the cells were operated at a temperature of 750 °C with a fuel inlet composition of 10/90 CO/CO_2 and with O_2 supplied to the oxygen electrode.

The impact of the current density in the cell and tje fuel utilisation was studied by testing SOECs at various combinations of these parameters (0.375-0.75 A cm^{-2} and 29/58 % CO_2 utilisation). The study has revealed that carbon deposition occurs when the TPB-related overpotential of the fuel electrode η_{TPB} reaches 190-200 mV.

η_{TPB} is the total fuel electrode overpotential minus voltage losses due to conversion and diffusion. It furthermore found that the best durability and performance is observed when current density is 0.375 A cm^{-2}, where the low production rate is compendated by a strongly extended lifetime, such that overall lifetime yield is maximised. One of the tested cells had it gas cleaned upstream by passing it through crushed Ni/YSZ fuel electrode. This was expected to remove gas phase impurities e.g. sulphur containing species that would otherwise be reduced at the TPBs in the active fuel electrode leading to degradation. This test displayed improved performance in comparison to the tests without, indicating the presence and negative effect of gas phase impurities in the used CO_2.

The impact of infiltration of CGO in the fuel electrode for performance and lifetime was investigated. Two SOECs where the fuel electrodes had been infiltrated with different loadings of $Ce_{0.9}Gd_{0.1}O_{1.9}$ (CGO) were tested at 0.625 A cm^{-2} with 29% CO_2 utilisation. The tests revealed that, while the addition of CGO improves electrochemical performance and durability, it did not affect the threshold for carbon formation. However, the infiltration by CGO clearly mitigates Ni migration.

Attempts were made to detect carbon deposition *in-operando* coupling EIS and Raman spectroscopy. While carbon was successfully observed through the electrolyte, its presence was determined to stem from another source than operation.

Based on the findings in this project optimal operation of SOECs for CO_2 electrolysis should be carried out with CGO infiltrated fuel electrodes, cells should be operated at low current density ($i \approx 0.375$ A cm^{-2} at 750 °C), effectively a current density that keeps η_{TPB} below 200 mV, and the supplied CO_2 should be cleaned upstream to reduce the level of sulphur species below 5 ppb.

Dansk Resumé

Omstillingen til elektricitetsproduktion baseret på vedvarende energikilder er udfordret af den ustadige natur af vejrfænomener som solceller og vindmøller er underlagt. Vejrets ustadighed betyder at produktionen af elektricitet ikke på samme måde som afbrænding af fossile brændstoffer kan justeres for at tilpasse sig forbruget. Derfor skal vi som forbrugere enten tilpasse vores forbrug så det stemmer overens med produktionen, eller energien skal lagres til den skal bruges.

Fast oxid elektrolysecelle (SOEC) teknologien er en af de mulige metoder, der kan anvendes i forbindelse med lagring af energi. Den producerede CO kan efter produktion kombineres med H_2 hvormed at der kan skabes mere komplicerede kulstofsholdige kemikalier der ellers skulle have været udvundet fra den petrokemiske industri.

Til trods for SOEC teknologiens potentiale er den stadig ikke udbredt implementeret. Dette skyldes at levetiden af cellerne er udfordret af forskellige degraderings processer. Dette projekts fokus har været de degraderings processer, der foregår i brændselselektroden på state-of-the-art anode supporterede (ASC) Ni/YSZ SOECer. Disse processer inkluderer: inhibering af de aktive sites i elektroden via deponering af kulstof eller adsorption af urenheder fra den benyttede gas, samt mikrostrukturelle ændringer via agglomerering og migrering af Ni.

Degradering af brænselselektroden under CO_2 elektrolyse er i dette projekt studeret vha. langtidstest ($\approx$ 1000 t) af ASC Ni/YSZ SOECer hvorunder ydeevnen er fulgt ved brug af elektrokemisk impedans spektroskopi. Efter testene er cellernes mikrostruktur karakteriseret vha. elektron mikroskopi (SEM), Raman spektroskopi er endvidere anvendt til bestemmelse af hvorvidt kulstof havde deponeret i cellerne under brug. Alle test i dette projekt er udført ved 750 °C med 10/90 CO/CO_2 føde til brændselselektroden, og med O_2 tilført til iltelektroden.

Indvirkningen af strømtætheden i cellen og omsætningsgraden af CO_2 blev studeret ved at afprøve forskellige kombinationer af de nævnte parametre (0.375-0.75 A cm^{-2} og 29/58 % CO_2 omsætning). Dette studie viste at kulstof deponerer når en bestemt grænseværdi for det dominerende elektrokemiske trin i elektrode processen overstiges. Denne grænseværdi er fundet til at være 190-200 mV. Studiet viste også at holdbarheden og ydeevnen var bedst for cellen anvendt med en strømtæthed på 0.375 A cm^{-2}, samt at den lave omsætningshastighed blev mere end kompenseret af en længere levetid, hvorved produktion af CO over cellens levetid maksimeres. I en af de undersøgte celler blev CO_2 og CO renset for gas urenheder, så som svovlholdige forbindelser, ved at føre gassen igennem knuste Ni/YSZ brændselselektroder hvorpå urenhederne kunne adsorbere. Dette affødte en forbedring i ydeevne og levetid i cellen, da urenhederne ikke kom i kontakt med den aktive celle. Endvidere er betydningen af at infiltrere brændselselektroderne med $Ce_{0.9}Gd_{0.1}O_{1.9}$ (CGO) afprøvet ved 0.625 A cm^{-2} og 29% CO_2 udnyttelsesgrad. Dette studie viste en forbedret ydeevne og holdbarhed i de celler som indeholdte CGO. Tilføjelse af CGO til cellerne påvirkede ikke grænseværdien for kulstof deponering, men reducerede omlejringen af Ni og forringelsen af Ni-perkolationen.

Forsøg på at detektere kulstof deponering under drift (*in-operando*) ved at kombinere EIS og Raman spektroskopi lykkedes ikke. Det lykkedes at detektere kulstof igennem YSZ elektrolytten, dog kunne dette kulstof ikke tilskrives driften af cellen, men snarere urenheder fra opsætningen.

Baseret på fundene i dette projekt anbefales det for optimal operation af SOECer til CO_2 elektrolyse at der opereres på celler med CGO infiltrerede brændselselektroder ved lav strøm (i $\approx$ 0.375 A cm^{-2} ved 750 °C), samt ved brug af gasrens således at overpotentialet ved TPB holdes under grænseværdien 200 mV.

List of Publications

Manuscripts included in this thesis:

1. **Proceeding I:** CGO-Infiltrated Ni/YSZ SOEC Fuel Electrodes for Increased Carbon Tolerance During CO2 Electrolysis
   Clausen, A. K., Traulsen, M. L., Hendriksen, P. V., Sun, X., & Hauch, A.
   In: ECS Transactions. 2021; Vol 103, No. 1, pp. 1945-1954 [Appendix A]

Manuscripts not included in this thesis:

1. **Proceeding II:** Effect of Anode Side Purge Gas on the Degradation of Solid Oxide Electrolysis Cells
   Sun, X., Hendriksen, P. V., Hauch, A., **Clausen, A. K.**, Lehtinen, T., & Noponen, M.
   In: ECS Transactions. 2021; Vol 103, No. 1, pp. 1083-1091

Nomenclature

C	Carbon
CH_4	Methane
CO	Carbon Monoxide
CO_2	Carbon Dioxide
e^-	Electron
H^+	Proton
H_2	Hydrogen
NH_3	Ammonia
O^{2-}	Super Oxide anion
O_2	Oxygen
ABO3	General Formula for Perovskites
LSCF	$(La/Sr)(Co/Fe)O_3$ - Lanthanum Strontium Cobalt Ferrate
LSF	$(La/Sr)(Fe)O_3$ - Lanthanum Strontium Ferrate
LSM	$(La/Sr)(Mn)O_3$ - Lanthanum Strontium Manganate
LST	$(La/Sr)(Ti)O_3$ - Lanthanum Strontium Titanate
SFM	$(Sr)(Fe/Mo)O_3$ - Strontium Iron Molybdate
3YSZ	Zirconia stabilized with 3 mole% Yttria
8YSZ	Zirconia stabilized with 8 mole% Yttria
CGO	Gadolinia Doped Ceria
TiO_2	Titanium Oxide

YSZ	General term for Yttria Stabilised Zirconia, covers both 3YSZ and 8YSZ.
ZrO_2	Zirconia
η_{TPB}	The overpotential for the electron transfer process at the Ni-YSZ triple phase boundary.
(FE-)SEM	(Field Emission) Scanning Electron Microscopy
ASR	Area Specific Resistance
CNLS	Complex-Nonlinear-Square
CPE	Constant Phase Element
DRT	Distribution of Relaxation Times
ECM	Equivalent Circuit Model
EDS	Energy-Dispersive X-ray Spectroscopy
EIS	Electrochemical Impedance Spectroscopy
EMF	Electromotive Force
G	Gerisher element
OCV	Open Circuit Voltage
PSU	Power Supply Unit
R_Ω	Serial or Ohmic Resistance
R_p	Polarisation Resistance
RQ	Resistor and CPE in parallel
SE	Secondary Electrons
Z_i	Imaginary part of Impedace
Z_R	Real part of Impedace
DTU	Technical University of Denmark
SDG	Sustainable Development Goal
SoA	State of the Art

UN	United Nations
ASC	Anode (fuel electrode) Supported Cell
Cermet	Ceramic metallic material
CNT	Carbon Nano Tube
ESC	Electrolyte Supported Cell
LTD	Low Temperature Degradation of YSZ
PEM	Proton Exchange Membrane - Alternate fuel cell technology
pO_2	Partial pressure of Oxygen
PtX/P2X	Power-to-X
SOC	Solid Oxide Cell
SOEC	Solid Oxide Electrolysis Cell
SOFC	Solid Oxide Fuel Cell
TPB	Triple Phase Boundary

Contents

List of Figures

List of Tables

Chapter 1

Introduction

The increase in the average global temperature and the concentration of anthropogenic CO_2 in the atmosphere was first linked by Callendar in 1938 [1], with the positive remark *"the combustion of fossil fuel [...] is likely to prove beneficial in several ways"*. Since then the perception on the increase to global average surface temperature has changed, and it has been coined under the term global warming, where reports such as "Our Common Future" by the UN, also known as the Brundtland report describes it as a major threat to humanity [2]. A challenge that requires a global approach to be solved as both industries and policy makers are expected to make the needed changes [3, 4]. Since then organisations such as the UN have made efforts to deal with the challenges by getting them into the public domain, with efforts such as the Sustainable Development Goals (SDGs) [5]. While it has taken a while gaining traction among the public [6], climate change is now widely acknowledged for being a major threat to human existence as we know it [7, 8], and more efforts than ever are being put into mitigating climate change [5, 9].

One of the major causes of the global warming is anthropogenic emission of greenhouse gasses, where the worst contributor is CO_2 due to the sheer amount that is emitted [10]. With the exception of a few years, the anthropogenic CO_2 emissions have increased almost exponentially every year since the industrial revolution in 1760 (10 Mt), to a staggering 37 Gt in 2021 [11]. The CO_2 emission mainly comes from the use and combustion of fossil fuels (93.6%), and also industries such as cement production (4.5%) [11]. To this end, the move away from using fossil fuels as energy source would drastically decrease CO_2 emissions [11]. Since the middle of the 1970s there has been a five-fold increase in energy production from renewable sources such as solar panels and wind turbines [12]. This has, so far, mainly lead to an increase in the total energy production rather than replacement of the energy produced by power plants fuel by non-renewable resources on a global scale [12]. Although the clean energy increase the consumption for some countries, it have had the intended effect in others, i.e. Denmark has during the last 20 years (1991-2021) went from renewable energy making up 3% of the total electricity production to 75%, for the same approximate amount of electricity [13].

The large renewable energy sources such as wind and solar power, does however, come with a major challenge, they are intermittent due to their reliance on the weather [14]. This means that whereas the production of energy from combusting fossil fuels can be adjusted to match consumption, the wind might not be sufficiently strong during peak consumption hours. On the other hand it also means that there are periods where the energy production surpasses the consumption, and the excess energy needs to be dealt with, either by limiting production or exporting it to other countries. Both of these solutions are suboptimal, in the case of limiting production it will mean losing out on a lot of potential energy. On the other hand, export of energy is mainly possible when neighbouring countries are at a deficit, which becomes less likely when both produce energy based on, and experience the same weather phenomena [15].

Two of the major challenges that exists today are hence, dealing with the increasing CO_2 emissions, and providing a stable source of electricity that do not lead to net emission of CO_2 to the atmosphere [5].

It so happens that a technology exists to deal with both challenges: The Solid Oxide Cell.

1.1 The Solid Oxide Cell - Fundamentals

Solid Oxide Cells (SOC) are electrochemical devices for energy conversion that converts electrical to chemical energy and vice versa [16]. Figure 1.1 shows an SOC during its two modes of operation a) fuel cell operation and b) electrolysis cell operation. A SOC largely consists of three parts, a fuel electrode, an oxygen electrode, and an electrolyte [16]. The fuel electrode should be electrocatalytically active towards splitting the fuel, electronically conductive, and allow gas flow to the reaction site near the electrode, and should furthermore be ionically conductive to allow flow of O^{2-} towards the electrolyte [17]. The most widely available and proven fuel electrode is a porous Ni and yttria stabilised zirconia (YSZ) cermet [18–22], where the Ni provides electrocatalytic activity and electronic conduction, while YSZ acts an ionic conductor [17]. The oxygen electrode has similar requirements to the fuel electrode, though the catalytic activity should be towards the oxygen splitting reaction [17]. The oxygen electrode of most SOCs consist of a mixed ionic and electronic conducting (MIEC) material, usually with the perovskite structure such e.g. lanthanum strontium cobalt ferrite (LSCF) [23], lanthanum strontium cobaltite

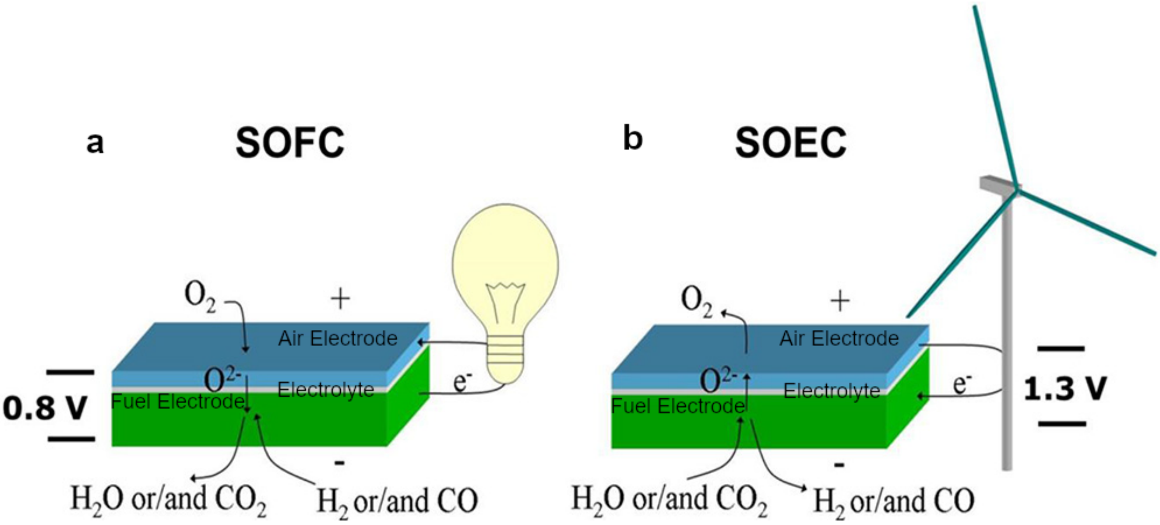

Figure 1.1: Operation principle of SOC. Picture taken from [16], fig. 1.3

(LSC) [24], or lanthanum strontium manganite (LSM) [25]. The electrolyte acts as a separator between the two electrodes and should hence be gas tight, and it should be an ionic conductor while being electronically insulating [17]. Most SOCs use YSZ for the electrolyte [26–28].

During fuel cell operation of the SOC, two electrochemical reactions occur. At the oxygen electrode O_2 is supplied with electrons and splits into O^{2-}-ions [29].

$$O_2 + 4e^- \rightleftharpoons 2O^{2-} \tag{1.1}$$

At the fuel electrode the fuel e.g. H_2 loses its electrons at becomes H^+ [29].

$$H_2 \rightleftharpoons 2H^+ + 2e^- \tag{1.2}$$

The O^{2-} will, due to the chemical potential of the reaction and the YSZ being ionically conductive towards O^{2-}, travel from the oxygen electrode through the electrolyte to the fuel electrode where it will combine with the hydrogen. The total reaction is then the combination of reaction 1.1 and 1.2 [29]

$$H_2 + \frac{1}{2}O_2 \rightleftharpoons H_2O \tag{1.3}$$

This reaction is similar to that of the combustion of H_2 in O_2 and produces energy as such, but as electrical rather than thermal energy [16]. This is due to the electrolyte being an electronic insulator, meaning that the electrons formed in reaction 1.2 is required to find another way to the oxygen electrode i.e. a circuit where they can be used as current. Combusting the H_2 using solid oxide fuel cells (SOFCs) is furthermore more efficient than doing it in a internal combustion engine due to the reversibility of the combustion in the SOC [30].

SOCs, can if applied with a potential work against the chemical potential of the combustion reaction and produce H_2 from H_2O [31]. This means that the SOC can be used as a electrochemical device for electrolysis, a Solid Oxygen Electrolysis Cell (SOEC) [16].

The reversible nature of SOC operation means that they can be used for stabilising the energy supply from solar and wind power both during daily fluctuations , or during seasonal changes [32, 33]. Where other energy storage technologies such as batteries have limited capacity based on their materials, this is not an issue for SOCs. Because SOCs do not have to store the energy they converts, they can work continuously so long that they are fed with the appropriate gasses. This, however, also mean that they are reliant on an external supply of gas.

The majority of previous studies on SOCs have been into either fuel cell [34–39] or electrolysis cell [40–45] operation producing H_2 as energy carrier. SOCs are however versatile in the type of fuel it uses, due to its chemical resistance to deactivation from chemical species of which other fuel/electrolysis cell technologies are less tolerant towards [46]. These alternate energy carriers include CO [47], NH_3[48], CH_4 and other short-chain carbon hydrides/alcohols/ethers [49–52].

Production of CO occurs during the fuel electrode reaction

$$2CO_2 + 4e^- \rightleftharpoons 2CO + 2O^{2-} \tag{1.4}$$

combining reaction 1.4 and 1.1 and normalising for CO/CO_2 gives the total reaction:

$$CO_2 \rightleftharpoons CO + \frac{1}{2}O_2 \tag{1.5}$$

This means that SOECs provides a method for dealing not only fluctuations in the power supply, but can also be used to utilise CO_2 which is mainly seen as a waste product. The produced CO can be combined with H_2 to form synthesis gas (syngas), which can be made into fuels or chemicals [53, 54]. SOECs in combination with other technologies have hence garnered the title Power-to-X (P2X/PtX) [54].

1.2 The Fuel Electrode

The fuel electrode of SoA SOECs does, as described previously, consist of a porous Ni/YSZ cermet. In some cases, as during this project, the fuel electrode furthermore acts as structural support [17]. This type of cell is called an anode or fuel electrode supported cell (ASC), based on SOFC naming convention [17]. This means that the fuel electrode consists of a mechanical support layer of 200-1000 μm wide layer

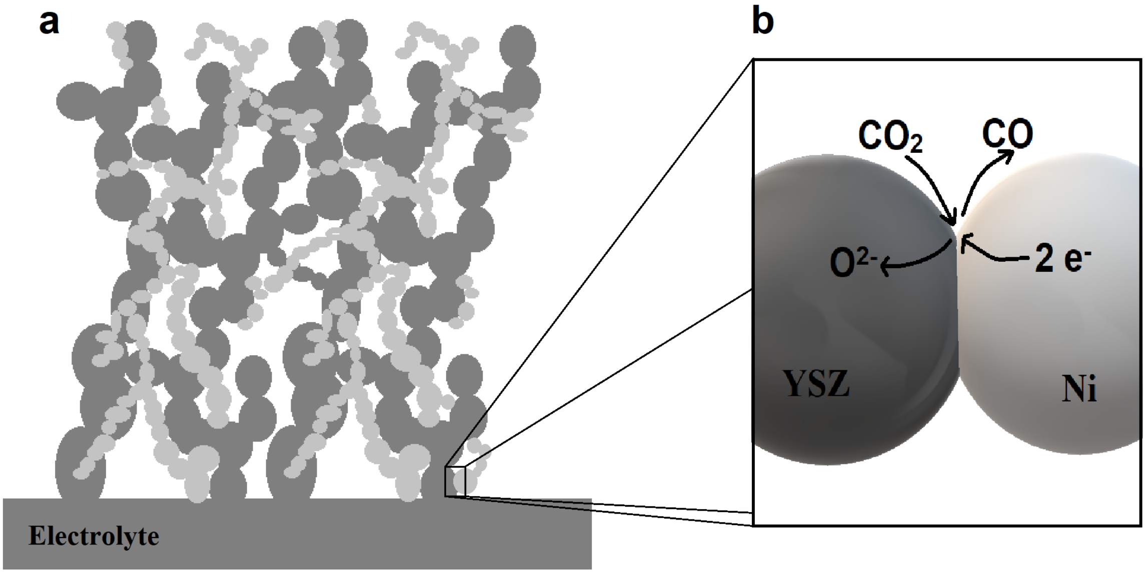

Figure 1.2: a) Sketch of Ni/YSZ electrode near the electrolyte, YSZ - Dark Grey, Ni - Light Grey. b) Sketch of TPB

of 3YSZ (3% Y_2O_3 content), and an active fuel 8-10 μm 8YSZ (8% Y_2O_3 content) closest to the electrolyte, where the Y_2O_3 contents have been chosen to optimise mechanical strength and ionic conduction for the two layers respectively [17, 35].

One advantage of the SOEC technology has when compared with the Proton Exchange Membrane (PEM) technology is the use of cheaper materials, where SOECs due to their high operation temperature (600-1000 °C) can use a non-noble metal Ni as an electro-catalyst for H_2/CO production [55]. Noble metals are however required for PEM cells due to the lower temperature, and the acidic conditions of the oxygen electrode [56].

Figure 1.2 a) depicts the porous fuel electrode near the electrolyte. The Ni/YSZ SOEC fuel electrode does as in the figure consist of interconnected Ni and YSZ networks [16]. Figure 1.2 shows a zoom in on where Ni and YSZ networks meet with the gas phase, this point is called the Triple Phase Boundary (TPB), and is the active site for the fuel electrode reaction [16].

Alternatives to Ni/YSZ fuel electrode are other cermets such as Ni/Scandia Stabilised Zirconia (Ni/SSZ) [57] and Ni/Gadolinium doped Ceria (Ni/CGO) [23].

1.3 Degradation of the Ni/YSZ Fuel Electrode

The major challenges for SOECs' include the various degradation mechanisms that shortens the lifetime of the application. While degradation occurs for various components, the focus here will be on those mechanisms that occur in the Ni/YSZ Fuel electrode.

1.3.1 Ni Coarsening and Ni Migration

The high operating temperature of SOECs means a higher mobility of the Ni-component of the fuel electrode [58]. Ni coarsening is a well known cause of degradation [58, 59]. Ni coarsening leads to growth of Ni particles, and from this growth follows loss of contact between the Ni particles and hence breakage of the conductive percolating network [58]. Coarsening furthermore causes a decrease in TPBs which results in reduction of the electrochemical performance [60–62].
Migration of Ni away from the fuel electrode is another consequence of the increased Ni mobility [61, 63]. Migration of Ni away from the electrolyte effectively thickens the electrolyte, since O^{2-} then has to travel further between the fuel and oxygen electrode [64]. This is of impact due to the significantly lower conductivity of YSZ compared with Ni [58].
Ni coarsening and migration are described and discussed in more detail in chapter 5.

1.3.2 Carbon Deposition

A major cause of degradation in SOECs during CO_2 electrolysis is carbon formation [65]. This carbon can either deposit through electrochemical reduction [66].

$$CO_2(g) \rightarrow C(s) + O_2(g) \tag{1.6}$$

$$CO(g) \rightarrow C(s) + \frac{1}{2}O_2(g) \tag{1.7}$$

Or through the Boudouard reaction [67]

$$2CO(g) \rightleftharpoons CO_2(g) + C(s) \tag{1.8}$$

Carbon deposition in the fuel electrode is an issue as it, unlike CO/CO_2, is a solid, and fills the pores which can lead to a variety of damages [68]. This damage includes detachment between particles, through a mechanism where carbon dissolves in Ni, and is subsequently ”extruded” as carbon nano tubes (CNTs) [68, 69]. The pressure from the CNTs may also lead to de-lamination between the fuel electrode from the electrolyte in severe cases [70].
The onset for carbon formation should theoretically be possible to calculate thermodynamically from the Boudouard reaction from the macroscopic gas composition, though previous studies have shown carbon deposition in SOECs operated at mac-

roscopic ”safe” conditions, where carbon was not expected to form [71]. In these studies microscopic conditions such as local gas composition [72] or temperature deviations [67] from the expected (macroscopic) conditions have been claimed to be the cause of carbon formation.

1.3.3 Sulphur Poisoning

Carbon capture and sequestering from the atmosphere is very expensive, and is not projected to become affordable anytime soon [73]. Industries such as steel and cement production, or biomass combustion on the other hand provides a cheap source of highly concentrated CO_2 for use in SOEC. Using the cheap CO_2 would be the most economically sound choice, in addition to mitigating the produced CO_2 from the atmosphere. This, however, brings its own challenges, such as CO_2 contains various impurities, including sulphur containing species. This is an issue since sulphur containing species have been reported to poison the Ni in the fuel electrode both during fuel cell [74–79], and electrolysis cell operation[72, 80, 81].

The poisoning of the Ni occurs when S chemisorps to the metal, leading to a change in the surface energy and subsequently the reaction pathway, which decreases the catalytic activity [82, 83].

Studies have shown that the degradation rate of SOCs increases with the concentration of S-containing species in the gas stream [65, 74]. Temperature has furthermore been shown to be a variable in Ni poisoning, with degradation having a larger impact at lower temperatures [74], which is in line with the S-sorption isotherms described by Bøgild [84].

While sulphur poisoning has a detrimental effect in large quantities in both modes of operation, a limited amount of S has been shown to be advantageous for SOFC operation, as it inhibits carbon formation through decreased catalytic ability, which decreases carbon formation [85]. This is less so the case in SOEC [86], whereafter the reductive conditions during electrolysis operation reduce sulphur-species into sulphur where it deposits and inhibits the TPBs [80]. SOECs have hence been shown to degrade at an increased rate with down to 15 ppb of S-containing species in the CO_2[65]. The mode of SOC operation is therefore a parameter when considering degradation from S-poisoning.

1.4 Motivation and Scope of Thesis

The potential future of the SOEC technology is looking promising, though it still have some hurdles to cross. While the global goal is to achieve independence from fossil fuels for electricity production, they are still the main source for modern amenities such as medicine and plastics, in addition to fuel for aviation which have proved difficult to electrify. This means that enabling SOECs for CO_2 electrolysis would mean one more step towards independence of fossil fuels, as it could lead to the production of synthetic fuels which could be used for the hard-to-electrify sectors, and complex chemicals for medicine and other modern amenities.

1.4.1 Current State of the Art SOEC Fuel Electrode for CO_2 Electrolysis

Currently what is holding back the SOECs is limited durability [21] and performance [27], where a lifetime of 50kh (5+ years) has been determined to be expected for the technology to become commercially viable [21, 87]. One aspect of achieving this is to improve long-term performance by mitigating degradation during CO_2 electrolysis operation either partly or completely.

A lot of effort is currently being put towards fuel electrodes of perovskite-type (ABO_3) materials including but not limited to materials such as LSTs ((La/Sr)(Ti)O_3)[88, 89], LSFs ((La/Sr)(Fe)O_3) [90, 91], and SFMs ($Sr_2Fe_{1.5}Mo_{0.5}O_{6-\delta}$) [92, 93]. These materials shows promising results for both performance and tolerance towards carbon deposition, despite this few are shown to operate more than 200h [27], whereas SOECs with Ni/YSZ fuel electrode has been demonstrated to last up to 10 kh ($\approx$ 1 year)[21]. Furthermore many of the perovskite type fuel electrode show an improved electrocatalytic activity when Ni is introduced to the material, though to a much lesser extent than in Ni/YSZ [91, 94]. Ni/YSZ fuel electrodes however are still the most used type of fuel electrode among commercial producers such as Elcogen [95] due to Ni being the the material demonstrating the best lifetime during steam electrolysis [22]. Ni/YSZ fuel electrodes are hence, still being researched to mitigate degradation and improve performance of the SOECs [96–98].

1.4.2 Scope of PhD Project

The question: *”What does carbon tolerant mean?”*[99, 100] have previously been raised. This can be extended to: *How should it be determined?* Current experimental work often determines tolerance towards carbon deposition based on whether or not it is observed after operation [96, 101, 102]. In case of observed carbon it can be concluded that carbon did deposit during operation. Though the lack of observed carbon does not indicate when or whether it will occur 200 or 20000 h down the line. The scope and purpose of this project has been to improve performance of SOECs with Ni/YSZ fuel electrode through an increased understanding for the degradation mechanisms carbon deposition and Ni coarsening/migration.

Structure of Thesis

To this end the thesis has been structured as stated below:

Chapter 2 introduces the concepts behind the experimental methods for testing and characterisation of SOECs. Description of the experimental procedures and setups carried out during the PhD at the Technical University of Denmark.

Chapter 3 studies the impact of the test parameters current density and CO_2 utilisation on the electrochemical performance. Nine single cell Ni/YSZ fuel electrode supported SOECs were tested during CO_2 electrolysis operation whilst monitoring their electrochemical performance with EIS. Post-test SEM and Raman spectroscopy was used for correlating electrochemical performance and carbon deposition.

Chapter 4 studies whether fuel electrode modification through wet-infiltration of CGO can improve the electrochemical performance and increase tolerance towards carbon deposition. Two single cell Ni/YSZ fuel electrode SOECs were infiltrated and tested during CO_2 electrolysis operation. The SOECs were characterised using EIS during electrolysis testing, whereas SEM and Raman spectroscopy was used similarly to the previous chapter to correlate carbon and electrochemical performance.

Chapter 5 studies microstructural changes of the cell in chapter 3 and 4. The chapter is based on SEM micrographs of SOEC pieces embedded in epoxy.

Chapter 6 presents the results from the external stay in the Walker group at Montana State University. Attempts at correlating carbon deposition and electrochemical performance through *In-operando* studies. Describes the set-up used for the studies, what went wrong, and how to improve.

Chapter 7 summarises, compares, and discusses the results from all the previous in an overall discussion. **Chapter 8** concludes and gives an outlook to further worthwhile endeavours.

Chapter 2

Characterization Techniques and Experimental Set-ups

2.1 Electrochemical Impedance Spectroscopy

The electrochemical performance of the SOEC in this project, was characterised using Electrochemical Impedance Spectroscopy (EIS). It was used due to its applicability testing electrochemical devices, including *in-operando* during the durability tests carried out during this project. This section will include a brief background of the technique, how it was used, and a description of the general setup used.

Background and Graphical Presentation of EIS

Impedance is the relationship between current and voltage, and can be defined by the formula:

$$Z = \frac{E}{I} \tag{2.1}$$

Where E, I and Z is the voltage, current and impedance respectively. When measuring EIS, the voltage is perturbed and the current response is measured in potentiostatic EIS, whereas it is the other way around for galvanostatic EIS. Figure 2.1 depicts the voltage and current, plotted as the sinusoidal functions:

$$E(t) = E_0 \sin(\omega t) \tag{2.2}$$

$$I(t) = I_0 \sin(\omega t + \phi) \tag{2.3}$$

The impedance arises from the phase shift ϕ, which is the only difference between E and I in this example. E_0 and I_0 is the amplitude, and ω is the angular frequency

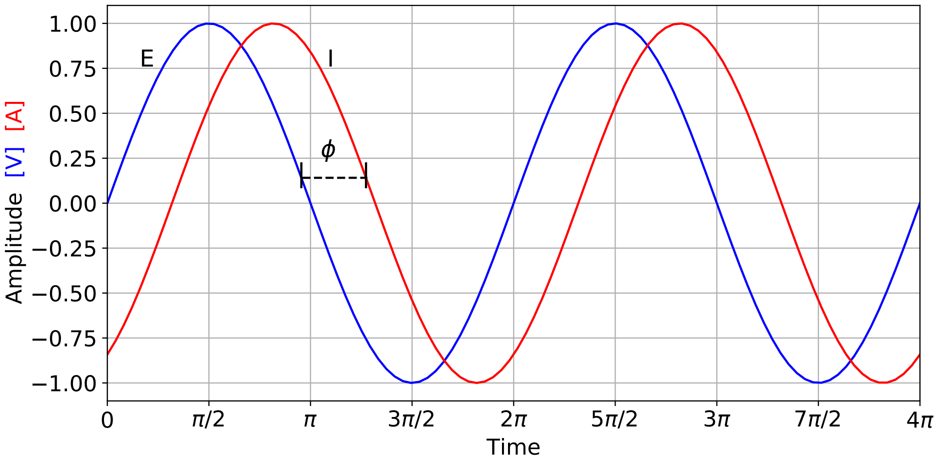

Figure 2.1: Phaseshift between E (blue) and I (red) over time.

($\omega = 2\pi f$). From this, impedance can be more elaborately defined using complex numbers, by combining the equations 2.1, 2.2, 2.3 and Euler's formula $e^{j\phi} = \cos(\phi) + j\sin(\phi)$, where $j^2 = -1$ [103].

$$Z = \frac{E_0 \sin(\omega t)}{I_0 \sin(\omega t + \phi)} \tag{2.4}$$

$$Z = Z_0 e^{j\phi} = Z_0(\cos(\phi) + \sin(j\phi)) \tag{2.5}$$

$$Z = Z_R + jZ_{Im} \tag{2.6}$$

When defined such, Z_R is known as the real part, and Z_{Im} is known as the imaginary part.

Figure 2.2 shows two graphical presentations of EIS data; a Nyquist plot (a) and a Bode plot (b). The Nyquist plot has Z_R along the x-axis, and $-Z_{Im}$ along the y-axis. Note that the $-Z_{Im}$ is plotted rather than Z_{Im}, this is done to plot in the first quadrant of the coordinate system. The total resistance as seen in the Nyquist plot, can be further split up into the ohmic resistance; R_Ω, and the polarization resistance; R_p. R_p can be split further to determine the resistances from individual processes e.g. diffusion, gas conversion, and the electrochemical reactions occurring in the SOEC. The advantage of the Nyquist plot is that it shows both R_Ω and R_p. The Bode plot is depicted with f (frequency) along the x-axis, and $-Z_{Im}$ along the y-axis. It is also possible to make a Bode plot with Z_R along the y-axis, though less relevant for this project. From the Bode plot, the frequency of the different processes occuring in the SOEC can be more easily be determined. The mass transfer processes are typically slow (i.e. in the lower frequencies), and the electron transfer processes are typically fast (upper frequencies). For more extensive description of the background and graphical presentation of EIS, the reader is referred to the work by Orazem and

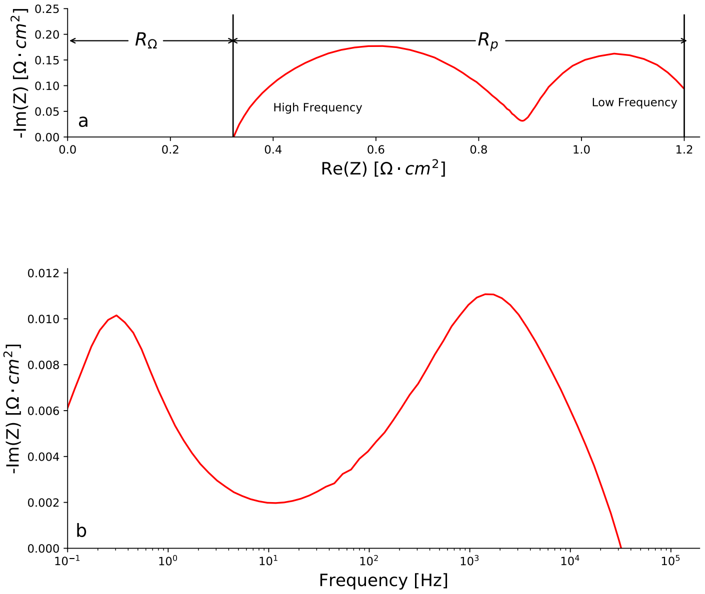

Figure 2.2: Nyquist(a) and Bode(b) representation of EIS data

Tribollet [104]

EIS Analysis

The total impedance of an electric device, can as described above, be broken down into contribution from different elements. To identify the contributions from the elements, an equivalent circuit model(ECM) can be fitted to the data using complex-nonlinear-square (CNLS) regression. An ECM representing the components/elements in the device is required to achieve results representative of the device. Figure 2.3 depicts the ECM for SOECs used to fit to the data throughout this study. The ECM used during this project consists of four different elements:

L Inductor: $Z_L = j\omega L$ - This element accounts for the inductance of the wires in the test setup. This element is part of the ECM to take the setup into consideration.

R Resistor: $Z_R = R$ - The simplest element, in that it is independent of the frequency. Z_R can be determined from the Nyquist plot as $Z_R = R_\Omega$.

G Gerisher: $Z_G = \frac{Z_0}{\sqrt{k+j\omega}}$ [105] - The Gerischer element is used for the oxygen

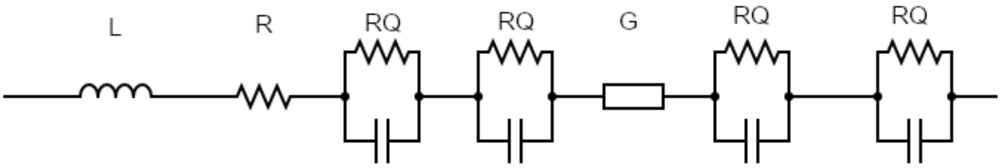

Figure 2.3: ECM used for the investigated SOEC in this project.

Table 2.1: Number of repetitions at EIS frequency ranges

Upper range	**Lower range**	Repetitions
96 kHz	6.7 Hz	200
6.6 Hz	0.67 Hz	90
0.66 Hz	0.06 Hz	40

evolution reaction in the oxygen electrodes [36, 106].

RQ Resistor and CPE in parallel: $\frac{R}{1+R\cdot Q_0(j\omega)^n}$ - This element is a resistor and a constant phase element (CPE) in parallel. When $n = 1$, Q is a perfect capacitor, which is used to represent charging and the formation of double-layers at the electrode interfaces, whereas when $n = 0$, Q is an ideal resistor. The RQ element is used instead of the RC element, due to the uneven electrode areas in the SOECs.

This ECM was previously applied by Hauch et. al. characterisations of SOECs used for steam electrolysis [107]. Before applying the ECM for CO_2 electrolysis, its applicability was confirmed by a similar process to the one by Kromp et. al. [38], where the changes to the EIS at different fuel and oxygen electrode gas compositions, in addition to various temperatures, and flow rates, were used to assign the individual impedance elements to ECM components. Fitting of the ECM to the data was done using the in-house developed Python-based software Ravdav [108]

EIS Acquisition

The EIS measurements were carried out using various Solartrons (1252A, 1255B, 1260), though in all cases the measured frequency range was the same. The impedance response was measured in the 96 kHz - 0.06 Hz range, with 12 points per decade. Furthermore the acquired data was based on multiple repetitions at each point based on the frequency range. The number of repetitions for the three frequency ranges can be seen in table 2.1.

2.2 Raman spectroscopy

Raman spectroscopy was used for carbon detection in the long-term tested SOECs at DTU, in addition to *in-operando* monitoring of carbon deposition in the cells. The latter experiments were carried out at Montana State University in collaboration with Tanner Henning.

Background

Raman spectroscopy is used for identifying the characteristics of chemical bonds, because these give insight into the structures they are a part of. A chemical bond can be represented by a mass on a spring, where the displacement can be described by Hook's law:

$$\frac{m_1 m_2}{m_1+m_2}\left(\frac{d^2x_1}{dt^2}+\frac{d^2x_2}{dt^2}\right)=-k(x_1+x_2) \tag{2.7}$$

$$\mu\frac{d^2q}{dt^2}=-kq \tag{2.8}$$

Where m_1 and m_2 represent the masses at each end of the spring, the xs represent the displacement of said masses, and k represents the bond strength. The equation has been simplified in eq. 2.8: using μ for the reduced mass, and q as the total displacement. Solving for eq. 2.8 q gives

$$q = q_0 \cdot cos(\omega t) \tag{2.9}$$

$$\omega = \sqrt{\frac{k}{\mu}} \tag{2.10}$$

From eq. 2.9 and 2.10 it is inferred that molecular vibrations are described by a cosine wave, with the frequency being proportional to the bond strength and inversely proportional to the reduced mass. Each bond will hence have a unique vibration dependent on the elements forming the bond and the bond strength.
The vibrational frequencies can be determined by Raman spectroscopy, where the electrical field from the bond (eq. 2.11) is perturbed by irradiating light in the UV-Visible range to induce an electrical dipole (eq. 2.12):

$$E = E_0 cos(\omega_0 t) \tag{2.11}$$

$$P = \alpha E = \alpha E_0 cos(\omega_0 t) \tag{2.12}$$

Where α is the polarisability. When the vibrational amplitude q_0 is small, the polarisation α can be described as a linear function of the displacement q:

$$\alpha = \alpha_0 + q\left(\frac{\delta\alpha}{\delta q}\right)_{q=0} + \cdots \tag{2.13}$$

Combining eq. 2.9, 2.12, and 2.13 gives:

$$P = \alpha_0 E_0 cos(\omega_0 t) + E_0 cos(\omega_0 t) \cdot q_0 cos(\omega t) \cdot \left(\frac{\delta\alpha}{\delta q}\right)_{q=0} \tag{2.14}$$

The second term in eq. 2.14 defines the Raman scattering, where the molecular vibrations give rise to a shift in frequency of the incident light. The first term describes Rayleigh scattering.
Figure 2.4 shows the quantum interpretation of the Rayleigh and Raman scattering (Stokes and Anti-Stokes). In the case of Rayleigh scattering, an electron is excited to a virtual state by a photon. Shortly after, it relax back into its original state, emitting a photon with the same amount of energy. Stokes scattering occurs when the electrons relaxes to a real state with a higher energy than the ground state, which leads to the emission of a photon with less energy than the original. Finally, in Anti-Stokes scattering, the electron starts in a higher level state, but relaxes to the ground level after having been excited. This transition emits a photon with higher energy than the exciting photon.

For a vibration to register in Raman spectroscopy, it needs to change the polarisation within the molecule upon a displacement.

$$\frac{\delta\alpha}{\delta q} \neq 0 \tag{2.15}$$

An example of a molecule with both Raman active and in-active vibrations is CO_2. CO_2 as a molecule is made up of three atoms and hence has 3 vibrational modes, which can be calculated using the general formula: 3N-6, where N is the number of atoms, and the -6 is due to 3 translational modes and 3 rotational modes [109]. Figure 2.5 shows the 3 vibrations of a CO_2 molecule: (a) symmetrical and anti-symmetrical stretching and, (b) bending. The two stretching vibrations are Raman active as they change the polarisation of the bonds, while the bending does not. This makes IR spectroscopy a suitable additional method of characterisation, as IR spectroscopy detects based on an induced change to the dipole-moment, which occurs in the bending vibration. It should be stated that while molecular vibrations are mutually exclusive for IR and Raman spectroscopy in this case, it is not always so, since this property arises from the inversion center symmetric element of CO_2.

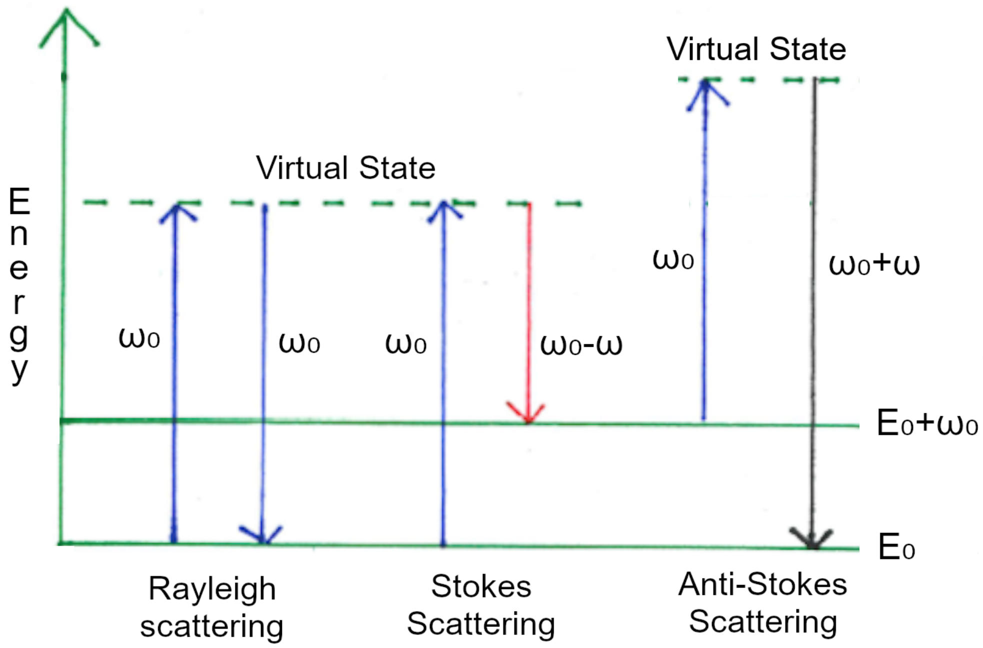

Figure 2.4: Jablonski diagram of energy transition for Rayleigh, Stokes, and Anti-Stokes scattering.

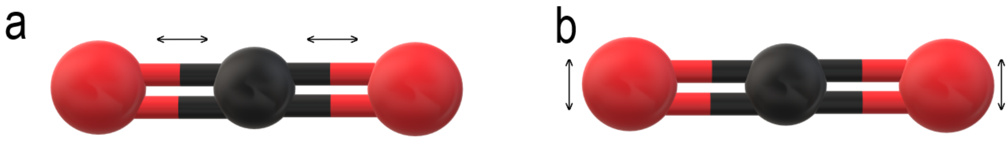

Figure 2.5: Vibrational modes of CO_2

While the vibrations in CO_2, a simple molecule, are easily found, larger molecules contain more vibrational modes, and as such identifying is a time consuming task. To simplify the search for Raman active modes, molecules can hence be grouped into point-groups with similar vibrational modes, based on their symmetry using group theory [110]. Furthermore, efforts by George Socrates and Lafuente et. al. has resulted in large libraries/databases of Raman spectra as reference for solid-state Raman spectroscopists [111, 112]

Raman measurements and Graphical Presentation

During the Raman measurement, the sample is irradiated by light, usually a laser, to excite electrons within the sample, as described in the previous section. The light perturbs the content of the sample, emitting photons which are then detected. Lasers are used as a light source, since they provide a large amount of focused photons, and the wavelength of the light can be controlled. A large amount of photons are required, since most photons results in Rayleigh scattering and only about 1/10^6 photons result in Raman scattering. The specificity in wavelength of the incident light makes it easier to measure the deviations from the Raman scattering. In Raman measurements, wavelengths between the UV (ultra violet) and IR (infra red) are used, as these correspond to photons with the required energy to excite electrons in the molecular bonds. In this project, wavelengths within the visible range have been used, as it yields sufficient Raman responses, also the ability to register the light increases the ability to avoid it and makes it easier to focus the laser beam on the target.

Figure 2.6 shows a drawing of a Raman spectrum, with signal intensity in arbitrary units along the y-axis, and the frequency shift between the absorbed and emitted light in wavenumbers, for which the unit is cm^{-1} along the x-axis. The frequency shift can alternatively be plotted in Hz. The figure also shows the relative positions of Rayleigh, Stokes, and Anti-Stokes Scattering. Rayleigh scattering, as seen in the middle, is usually filtered out, as it does not provide any useful information related to Raman. Stokes and Anti-Stokes scattering is located equidistant from the incident light, frequency, as expected from eq. 2.14. The ratio between the Stokes and Anti-Stokes feature is given by the Maxwell-Boltzmann distribution.

$$\frac{P_{v=1}}{P_{v=0}} = e^{-\Delta E/kT} \tag{2.16}$$

Where $P_{v=x}$ is the population of the x-th exited stated. From the Boltzmann distribution it is hence apparent that the lower energy species must be most abundant, and therefore the Stokes feature will be largest, though it will decrease at increasing temperature. Only the Stokes scattering has been studied in this project. For more extensive theory on Raman spectroscopy, the reader is referred to the work by Nakamoto [113]

Raman equipment

Raman investigations of the long-term tested SOEC, were carried out using a Renishaw InVia Reflex Spectrometer system with a 532 nm laser. Measurements were done with a 3x10s exposure time, 1 µm beam spot size on the sample, and a laser power of <8 mW. The sample preparation consisted of breaking an appropriated piece off the tested cell. The Raman spectroscopy was then carried out in the cross section of the piece.

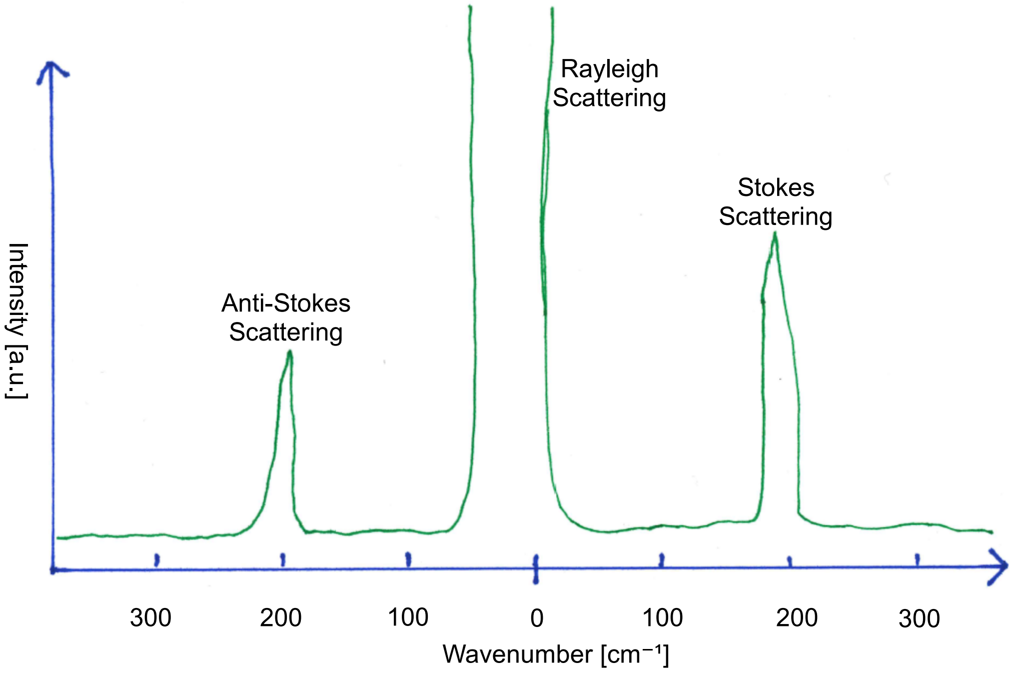

Figure 2.6: Drawn example of Raman data including Anti-Stokes, Rayleigh, and Stokes scattering.

2.3 Scanning Electron Microscopy

Scanning Electron Microscopy (SEM), like optical microscopy, is based on the reflective properties of a sample, but uses electrons rather than photons. The shorter wavelength of electrons compared to photons in the visible spectrum, allows for detection of submicron species, which is where optical microscopy falls short. SEM also allows for depth of focus, which makes it an optimal technique for studying surface features i.e. texture and topography in the 10^2-10^{-2} μm range.

A SEM largely consists of an electron source, lenses, and electron detector. The electron source produces electrons, e.g. through a Tungsten filament from which electrons are accelerated by a high voltage field [114], or a field-emission gun [115]. The electron beam is then focused through a magnetic field acting as lenses, after which it impacts with the surface of the sample, is reflected, and then picked up by a detector. For a more detailed description on the workings of the SEM parts, the reader is referred to chapter 5 in the work by Goodhew et. al. [116].

Figure 2.7 shows a sample being impacted by an electron beam where the electrons penetrate the sample, in what is called the interaction volume. After penetrating, the electrons with the lowest energies (SE) will only be able to escape from the surface, whereas electrons at higher energy levels (BSE) can escape from further within the interaction volume. Finally X-rays created by the electron bombardment can escape

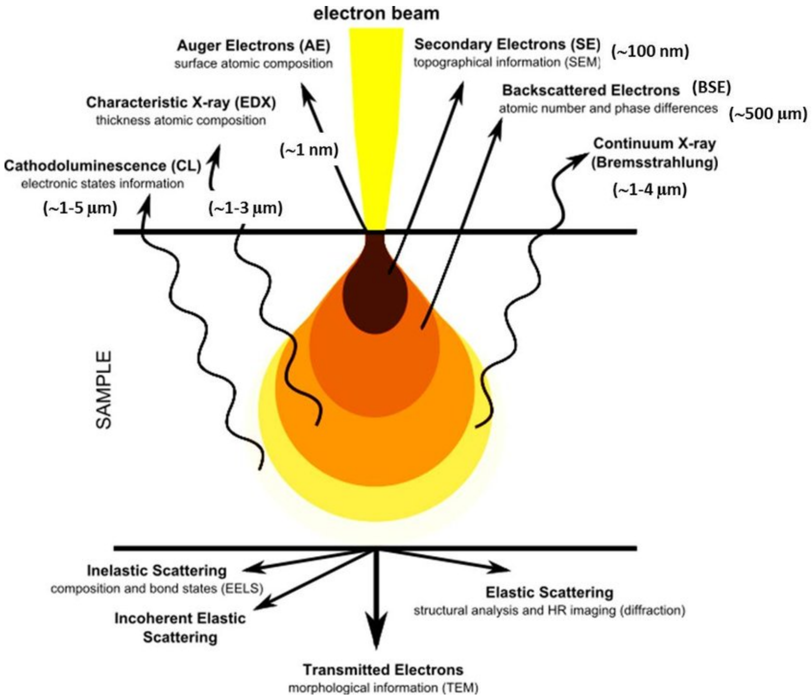

Figure 2.7: Different signals emitted from the interaction volume, which is formed upon impact between the electron beam and sample during SEM microscopy. Reproduced from [117]

Table 2.2: Overview of the investigated data types obtained from SEM during the project.

Scattering Depth	**Signal**	**Information obtained**
In-elastic scattering $< 100nm$	Secondary Electrons (SE)	Topography & Morphology
Elastic scattering 1< μm	Back Scatter Electrons (BSE)	Differentiation of materials
Characteristic X-rays $\approx 10\mu$m	X-rays	Elemental composition

from even further inside the interaction volume. Table 2.2 gives an overview of the types of data that the SEM investigations have yielded in this project. For more extensive description on electron microscopy the reader is referred to the work by Goodhew et. al. [116]

Sample preparation

Five $\approx$ 1 cm pieces of the tested cells (2 × inlet, 1 × middle, 2 × outlet) was cold vacuum embedded in EpoFix from Struers®, in a manner where the cross sections faced upward. The embedded samples were grinded using SiC-paper, and subsequently polished using diamond suspensions from Struers® with grit size: 9, 3, an 1 μm.

The epoxy sample was usually left uncoated to enable investigation of Ni-percolation at low acceleration voltages (0.95 kV) as described in the next section, where car-

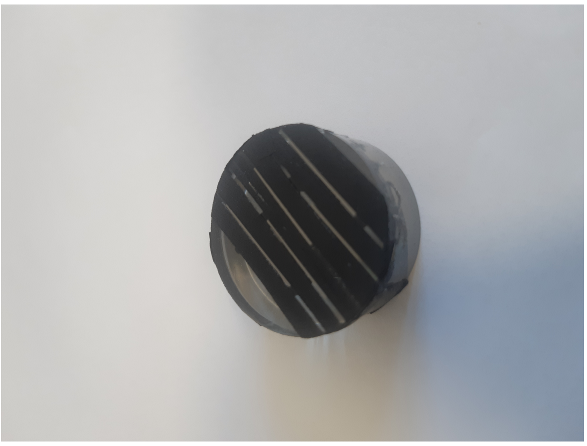

Figure 2.8: Sample prepared for low acceleration voltage SEM to investigate Ni-percolation

bon tape was used to achieve conductivity of the surrounding epoxy instead to avoid charging artifacts. Figure 2.8 shows the prepared sample for Ni-percolation investigation. Carbon tape was applied to increase conductivity of the sample, while allowing charging of the percolating Ni-particles. It was attempted to place the carbon tape as close to the cells in the sample, whilst avoiding covering them. This was done to minimise the charging of the epoxy around the sample, while still being able to see the sample.

The sample was coated in carbon before investigating the microstructure using high acceleration voltage (10-15 kV).

Quantifiable Microstructural changes using Embedded Samples

Embedded samples were used for investigating qualitatively and quantitatively changes in the microstructure. The quantitative changes being the changes of the Ni and Pore components of the structures, e.g. ”particle”-size distributions and component fraction. For investigation of the Ni characteristics, the sample was investigated uncoated. It was more specifically the percolating Ni that was investigated using the method described by Thydén et. al. [118]. This method relies partly on the backscattering coefficients between YSZ and Ni, diverging at low acceleration voltages (< 5 kV). This is accentuated of the charging of the sample, which is a even more essential part of the technique. Upon charging, the insulated and non-conductive parts of the sample will not be able to ”resupply” secondary electrons, whereas the percolating Ni-network will be getting electrons from its network. This will result in the percolating Ni-network lighting up.

To record the said micrographs, an inlens SE detector on a Zeiss Ultra equipped with a Gemini Field emission gun was used. The micrographs were captured at a

working distance of 3.5 mm and an acceleration voltage of 0.95 kV.
The pore characteristics, in addition to a general characterisation of the structure were investigated using a carbon-coated sample at a high acceleration voltage (15 kV) and a working distance of 8.5 mm, using the same microscope as used for the Ni characterisation, but using a Everhart-Thornley SE detector instead of the inlens detector.
For the quantification, a minimum of 1000 particles of the two phases to achieve a statistically significant value. The phases were quantified by their contrast; Ni from low voltage SEM, and pores from high voltage SEM, using the ”Analyze particle” function of the image software ImageJ [119].

Fractured surface studies

A Zeiss Merlin equipped with a Gemini Field emisssion gun was used for studying fractured SOECs (non-embedded samples). The samples were mounted on SEM stubs with the cross section facing upward. The samples were investigated using a working distance of 3.5 mm and an acceleration voltage of 1.9 kV.

2.4 Cell Specifications

The cells used during this project were all from the same production batch. They were of the type ”planar fuel electrode supported cells”. The fuel electrode support consisted of 350 μm Ni/3% Yttria Stabilised Zirconia (3YSZ), an 8 μm Ni/8% Yttria Stabilised Zirconia active fuel electrode, a 10 μm 8YSZ electrolyte, a 5 μm $Ce_{0.9}Gd_{0.1}O_2$ (CGO) interdiffusion/oxygen electrode protection layer, and a 25μm $La_{0.6}Sr_{0.4}Co_{0.2}Fe_{0.8}O_{3-\delta}$ (LSCF)/CGO composite oxygen electrode. The cells were cut to the dimensions 5.3 × 5.3 cm^2. A 30 μm $La_{0.85}Sr_{0.15}MnO_3$ (LSM) oxygen electrode contact layer was applied, in a 4.0 × 4.0 cm^2 square at the middle of the oxygen electrode by screenprinting, followed by drying at 90 °C overnight. Figure 2.9 shows in picture (a) and (b) a SEM micrograph of the cross sections of the cells used in the project, both with the oxygen electrode facing upwards.

2.5 Cell tests

Cell Mounting in Test House

The cells were mounted in an alumina cell test house as shown in figure 2.10. The cell test house consisted of two alumina blocks. The main part (bottom part fig.

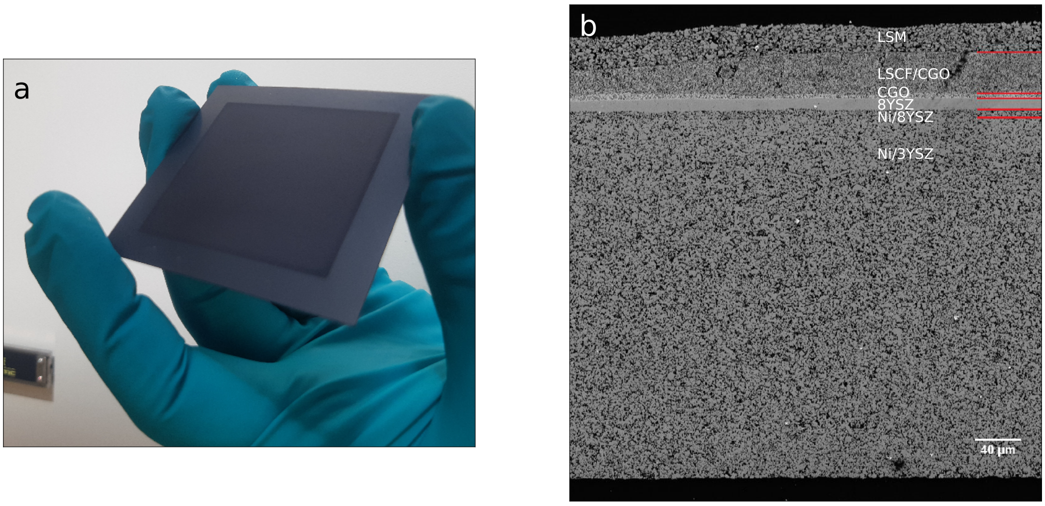

Figure 2.9: a) Picture of a SOC as used during this project. b) SEM micrograph of SOC cross section.

2.10 a)). Additionally the main part consisted of a block with two pipes attached, which served as fuel in- and outlet respectively. Both the inlet and outlet pipes were equipped with pO_2 sensors and thermocouples to monitor the gas composition. The inlet tube was furthermore equipped with a manifold to allow the addition of various gasses. The pipes were attached to the main block, where a channel had been carved out to allow gas flow through to the SOEC, and exit at the outlet. The main block was equipped with two Au current leads and four Pt voltage leads, attached to a Ni-plate in the middle of the house. A flow field/current collector was made out of two pieces of Ni-mesh, a coarse one, which were corrugated to a height 0.65-0.85 mm, and a fine 0.20 mm mesh. Both meshes were cut into 4×4 cm^2 squares. A 0.08 mm Au-frame was placed around the current collector. The SOEC was placed with the fuel electrode facing downward in a manner where the oxygen electrode contact layer was aligning with the current collector. A square alumina block with a square hole was then placed on top of the main alumina house. An Au-mesh-wrapped alumina flowfield with the dimensions, 4×4 cm^2, with two Au and Pt wires for current and voltage leads respectively, was placed on top of the oxygen electrode contact layer.

Test rig

Figure 2.11 shows a) the cell test house mounted in the furnace of the test rig, and b) the test rig. The cell test rig setup consisted of:

1. Pot furnace

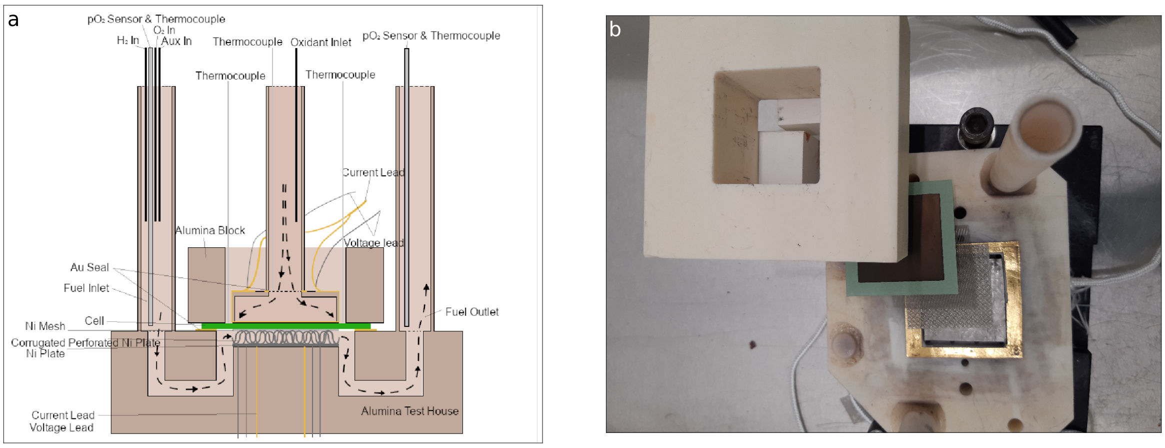

Figure 2.10: Cell test house used for mounting at DTU a) Schematic of cell test house. b) Top view of cell house illustrating the layering of current collectors, flow-fields and sealing during mounting.

2. Power supply unit
3. Gas supply
4. Safety measurements
5. Test management software

Pot Furnace: The heat to the cell was supplied to a Pot furnace controlled by two eurotherm controllers (2416 and 2416i), connected to the test management software.

Power supply unit: The cell test rig was equipped with a Delta Elektronika Power Supply SM15-100 galvanostat, for supplying power to the cell. The power supply unit was connected to the test management software.
The rig was furthermore equipped with a relay allowing one to switch the direction of the current, and hence enabling alternations between electrolyser and fuel cell operation.

Gas supply The test rig was able to supply air, N_2, and O_2 to the oxygen electrode. To the fuel electrode, the test rig was able to supply H_2, O_2, CO_2, CO, N_2, CH_4, and 5% H_2 in N_2. All of the gas, except the CO_2 and CO flows, were controlled by Brooks 5850R/S mass flow controllers (MFCs). The CO_2 and CO flows were controlled by MKS MFCs, as these allowed for more precise flows at the volumes used in this project.

Safety measurements The test rig was equipped with safety measurements partly to protect the sample, but mainly to protect the personnel/operator. This was done using a so called ”safety box” that shut off the current and gasses, with the exception of 5% H_2 in N_2 and air to the cell, if triggered by several detectors in the rig. These detectors included two gas detectors: One for CO and a second for H_2 to avoid build-up of toxic or explosive gas. A third detector, an air flow detector, was mounted at the ventilation to ensure proper through flow. Temperature limits through the furnace controllers were established, a lower (600 °C) and upper (1050 °C) limit for furnace temperature. The lower limit was chosen to avoid a build up of an explosive atmosphere[120], while the upper limit was chosen to avoid the Au-seal melting (1064 °C [121]). Finally the rig is equipped with a door switch, that triggers upon opening the doors to the rig. A more extensive description of the safety box can be found in the work by Mogensen and Hendriksen [122]

Test management software The test was managed using an in-house built software made by Søren Koch and Bjørn Sejr Johansen. The software allowed for controlling the test parameters such as gas flows, furnace temperature, and current. Furthermore, it could initiate EIS measurements. The software also logged data every 5 min from various sensors including gas flows, temperatures, pO_2 measurements, current, potential, and power supply settings, to be stored on a Linux server.

For a more extensive description of the test rig the reader is referred to the works by Hauch and Jensen [123, 124]

Mounting the cell house in the rig

The cell test house was mounted in the furnace on four ≈2.5 cm tall spacers of alumina. The alumina spacers were adjusted until the test house was resting on all of the spacers without rocking. An alumina tube was put through scaffolding on top of the rig onto the Au-sealed inset on the top of the oxygen electrode flow field. The tube and house was adjusted until it was perpendicular to level. Gas for the H_2, O_2 and auxiliary gasses, were connected to the fuel electrode manifold, while the oxygen electrode gasses were connected to the oxygen electrode gas inlet. The thermocouples and pO_2 sensors at the in- and outlets were connected, and air was led to the pO_2 sensors. T-type thermocouples were placed on the top of the cell, between the oxygen electrode flow field and the top part of the house; one at the over the fuel electrode inlet, and one over the fuel electrode outlet. The voltage and current leads were attached to the circuit. The furnace was closed of by porous alumina blocks, and further insulated using Superwool$^{®}$. A 4 kg weight load was

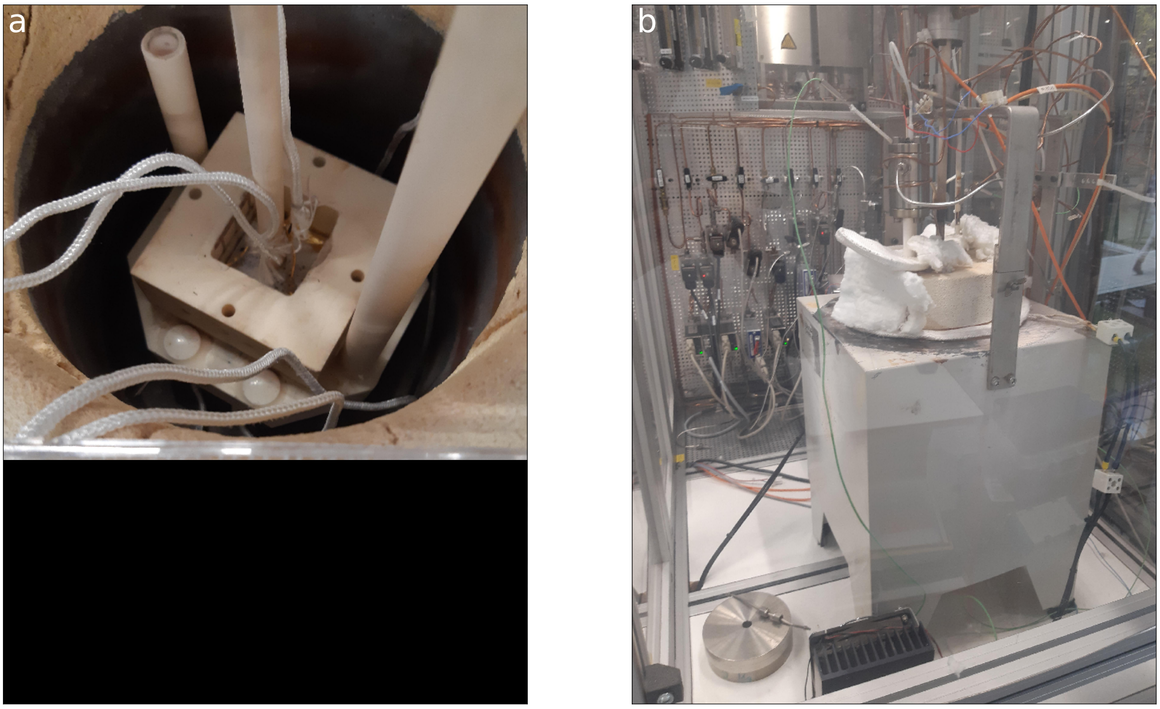

Figure 2.11: Test rig used for testing at DTU a) Picture of cell test house in furnace. b) Picture of test rig.

added to the cell, by placing it on top of the aforementioned alumina pipe on top of the oxygen electrode.

Gas cleaning

Gas cleaning was used in one instance in chapter 3. The CO_2 and CO was cleaned by leading it through $\approx$ 4 g of 400-500 μm diameter Ni/8YSZ particles heated to 650 °C in a 0.5 cm diameter tube furnace (Inner tube diameter). After this it was led to the inlet for auxiliary gasses on the fuel electrode manifold. The gas cleaning material was made by crushed and sieved Ni/8YSZ fuel electrode.

NiO reduction protocol

The test was started by heating the test house to $\approx$ 850 °C with a heating rate of 60 °C min^{-1}. Applying 20 l/h air to the oxygen electrode, and 20 l/h N_2 to the fuel electrode during heating. After reaching 850 °C, the NiO in the fuel electrode was reduced by applying 20 l/h 5% H_2 in N_2 for 2 h, after which the gas was changed to H_2 with an initial flow rate of 4% l/h. The H_2 flow rate was increased with 4 l/h every 10 min until it reached a total flow rate of 24 l/h H_2, at which point 0.5 l/h O_2 was added to the fuel electrode to reach a gas composition of 4% H_2O in H_2. The cell was then left to reduce in this atmosphere for 1 h.

Table 2.3: Test conditions for initial electrochemical characterization of cells. Total flow for the fuel electrode gasses was 24 l h^{-1} and 20 l h^{-1} when using H_2O:H_2 and CO_2:CO respectively, the gas flows at the oxygen electrode were kept at 140 l h^{-1}. In the last column "+" and "-" indicates fuel and electrolysis mode during the iV curves respectively

Fuel Electrode	**Oxygen Electrode**	**Temperature**	**Characterization**
4:96 – H_2O:H_2	Air/O_2	750/700 °C	EIS, +iV
20:80 – H_2O:H_2	Air/O_2	750/700 °C	EIS, +iV
50:50 – H_2O:H_2	Air/O_2	750/700 °C	EIS, +/-iV
90:10 – H_2O:H_2	Air/O_2	750 °C	EIS
50:50 – CO_2:CO	O_2	750/700 °C	EIS
50:50 – CO_2:CO	Air	750 °C	EIS
90:10 – CO_2:CO	O_2	750/700 °C	EIS
90:10 – CO_2:CO	Air	750 °C	EIS

Initial characterisation

The SOECs were characterised using EIS and iV curves before and after the durability tests. Test conditions and characterisation techniques for the initial characterisation can be found in table 2.3. The test conditions post test were limited to the CO_2:CO containing conditions to avoid removal of carbon. The tests including CO_2:CO did not include iV curves as these had aged the cell prematurely in earlier tests.

Durability tests of SOECs

The specifics on durability tests of the SOECs can be found in their respective chapters.

Chapter 3

Performance and Carbon Deposition in Solid Oxide Electrolysis Cells During CO_2 Electrolysis Operated at Various Current Densities and Fuel Utilisations

3.1 Introduction

SOECs are as established previously (Chapter 1), energy conversion devices that can electrolyse CO_2 into CO. This conversion comes with risk of various detrimental reactions leading to to faster degradation of the device, which can lead to a lower efficiency, or complete failure [65, 69, 81, 125–127]. While SOEC pilot plants has started appearing [43, 128–130], development/understanding of SOECs are still required to reduce and avoid degradation [87], to achieve longer lifespans and hence lower costs of SOECs.

In this study several single cell SOECs are tested galvanostatically at different current densities and and different degrees of CO_2 utilisation during CO_2 electrolysis. To investigate the onset of carbon deposition. One of these SOECs are tested using gas cleaned upstream by running it through gas cleaning where it can adsorp before reaching the SOEC. The cells electrochemical performance are monitored in-operando using EIS, which are de-convoluted by CNLS. The microstructure of the SOECs are characterised using SEM, and Raman spectroscopy is used for detection of carbon in the cells.

Table 3.1: Test conditions for the tests in this chapter. Naming convention: Current density - Low(29%)/High(58%) Utilisation - GC: gas cleaning applied, ”1” & ”2” denominates test iteration.

Internal Reference	**Name** [A cm^{-2}]	**Current Density**	**CO_2 Utilization**	**Gas Cleaning**
5test139	04HU	0.375	58%	No
1test181	05HU-1	0.5	58%	No
1test187	05HU-2	0.5	58%	No
1test173	05HU-GC	0.5	58%	Yes
5test126	06HU-1	0.625	58%	No
5test127	06HU-2	0.625	58%	No
1test169	06LU-1	0.625	29%	No
5test128	06LU-2	0.625	29%	No
5test129	08LU	0.75	29%	No

3.2 Experimental

Experimental cell test set-up and test protocols for initial characterisation is described in detail in chapter 2.

During the durability tests the SOECs were supplied with a 10/90 CO/CO_2 atmosphere to the fuel electrodes, and 50 l/h O_2 to the oxygen electrode. Table 3.1 lists the parameters for the tests carried out in this study. One of the tests were carried out using gas cleaning. In this test the gasses to the fuel electrodes were cleaned upstream by passing them through crushed fuel electrodes (Particle size: 500-600 μm) heated to 650 °C. The tests were monitored applying EIS as described in section 2.1. Tests with the internal reference starting with ”5” were tested with a slightly different geometry, as the test house did not have a depression as shown in figure 2.10. The flow field was instead made within a rise consisting of an alumina spacer between two gold seals.

After the tests the cells were characterised using Raman spectroscopy and SEM. Furthermore, the utilisation of 06LU-2 was increased to 58% after around 600 h of electrolysis testing.

Duplicate tests

Some tests were made in duplicate as seen in table 3.1, each for different reason. The reasons being:

1. 05HU: The first test iteration was found to leak. This was caused by fuel starvation due to the current leads being connected erroneously (in reverse). Figure 3.4 illustrates this through the OCV.

2. 06HU: The initial was thought to behave unexpected in the long-term test, and was hence ended early. The second test behaved similarly. This can be seen in figure 3.5.
3. 06LU: The 06LU-2 (first test to be carried out) was found to leak, which lead to the decision of changing the CO_2 utilisation from 29% to 58% (fig. 3.5) with the purpose of investigating the effect of such a change.

3.3 Results & Discussion

3.3.1 Initial Characterisation

Figures 3.1, 3.2, and 3.3 show the initial characterisation of the tests included in this chapter. It is seen that iV and/or EIS are missing for some conditions in some of the tests, which was due to faulty logging caused by system or user mistakes during the tests.
Figure 3.1 shows iV curves carried out in a 50/50 H_2/H_2O fuel electrode atmosphere. It is seen that the slopes of the iV curves vary significantly with the largest and lowest ASR being 0.725 (05HU-2) and 0.346 (08LU) Ω cm^2 respectively (calculated at -0.5$\pm$ 0.16 A cm$_2$). It is also noted that the intercepts with the y-axis (OCV) vary slightly. The different set-up might be part of the explanation, as the slope for the group 06HU-1+2 and 06LU-2 all were tested on the alternate set-up.
Figure 3.2 and 3.3 show EIS recorded at four different gas compositions during the initial characterisation. The aforementioned variety in performance is also seen in the EIS, where R$_s$ lies within 0.13-0.28 Ω cm^2 for the cells which is not insignificant. Comparison of the R$_p$(fig. 3.3) shows that 06HU-1+2 has about twice as large an impedance around 1 kHz, when compared with the other SOECs, in all gas compositions. This frequency region has previously been linked to the charge transfer process at the TPBs [131], which would indicate a weakening of said element, possibly due to a lower performing fuel electrode. A very large low frequency contribution is observed for 06LU-2 in fig. 3.3 d). The most likely cause for this would be a leak. This is indicated by Nernst equation, where a change in a minority species lead to a large change in free energy/potential. Since the low frequency contribution (conversion) is based on the tangent to the function, this would lead to a larger peak due to the steeper slope of the Nernst equation upon a decrease in a minority species. Similar, though smaller low frequency responses are seen for 04HU and 05HU-2 3.3 d) which may indicate slight leaks. An investigation of the outlet gas during the long-term test by the pO_2 sensor shows a decrease in potential. This means that an increase in pO_2 is expected in the fuel electrode outlet gas. This indicates that

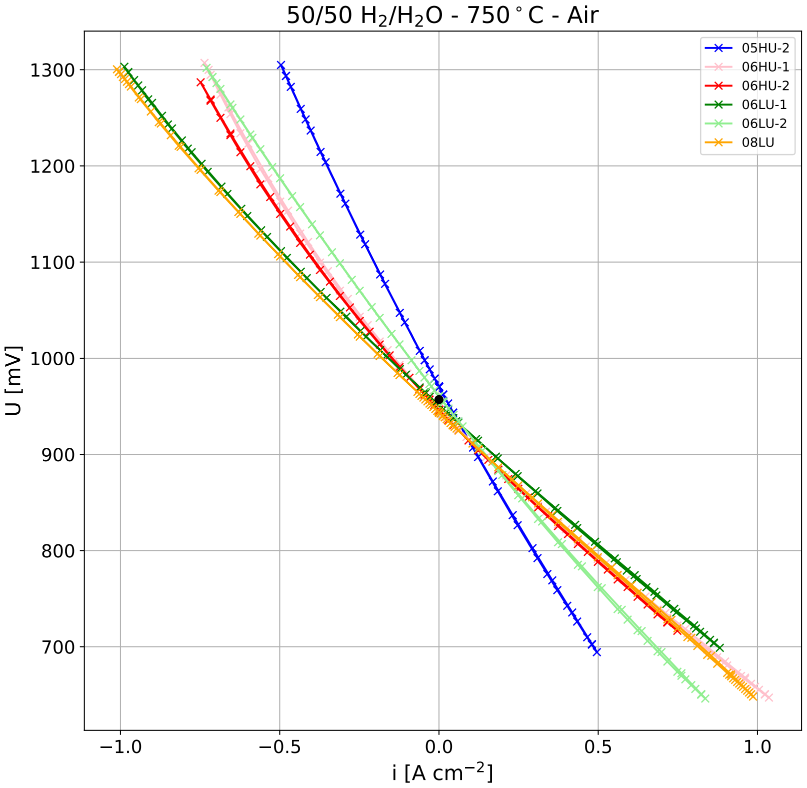

Figure 3.1: iV curves for the tested cells prior to the long-term durability test. The iV curves were recorded in a 50/50 H_2/H_2O fuel electrode inlet gas, with air to the oxygen electrode, at 750 °C. Black dot at 957 mV indicates EMF value calculated based on Nernst equation.

the leak of the SOEC increases over time. The other variations of the EIS are relatively slight compared to the mentioned ones, and are assumed to be based on the variance seen in the iV curves (fig. 3.1).

3.3.2 Current-voltage response in CO/CO_2

Figure 3.4 shows the current-voltage response for the increase in current, during start-up of the long-term durability tests. The iV-curves generally behave as expected, in that the iV-curves for the high-utilisation tests have a steeper slope than the ones for low-utilisations, with ASRs of 1.055 (06HU-1) and 0.413 (06LU-2) Ω cm^2 (calculated based on all points for their respective curves.). It is also noted that there is a spread in the cell voltages for the same test parameters. This might be due to a combination of factors. The spread in initial performance as seen in the EIS (fig 3.2), might also be ascribed to leak in the cells. A leak is most easily determined for test 05HU-1, as the OCV is significantly lower than the expected 908 mV, which is more than a ±1% variation in the gas components, which might occur due to rounding errors, caused by precision of the MFCs. The 05HU-1 SOEC was

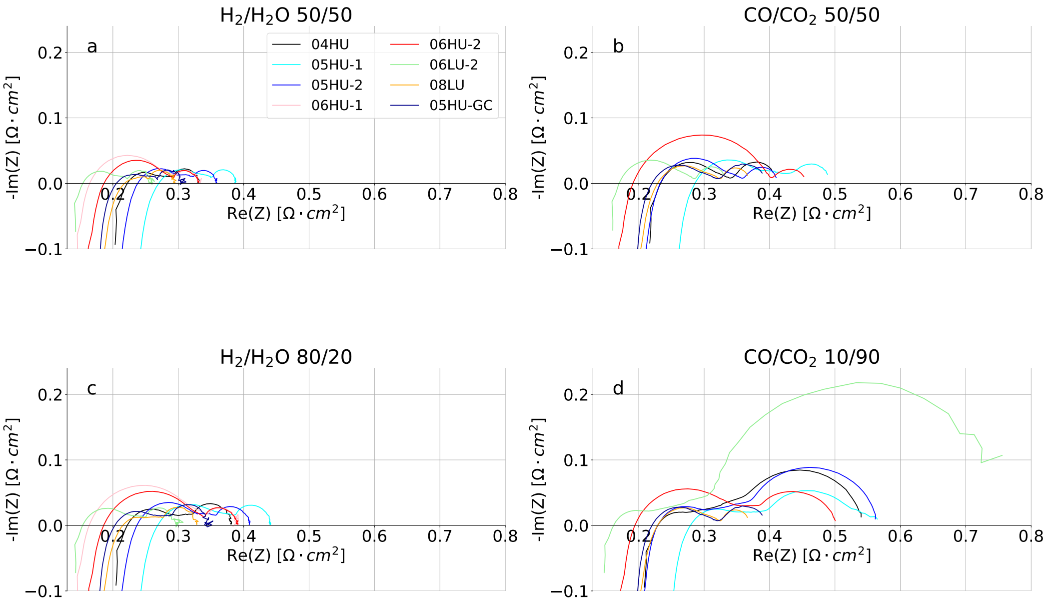

Figure 3.2: Nyquist plots of the initial performance of the tested cells in various gas compositions. Fuel electrode gas composition is given by the header for the subfigures, while oxygen electrode composition was O_2. The EIS were recorded at 750 °C.

therefore determined to leak, which is why the test was done in duplicate. The leak is further supported by the slope of said iV-curve (05HU-1), as it overlaps the one for 06LU-1, a test with lower degree of utilisation.

Of greater interest is the non linearity of the iV-curves for the two 06HU experiments, where the steepness of the curves increases when going beyond -0.5 A cm^{-2} or at 1288 and 1355 mV for 06HU-1 and -2 respectively. A similar bend in the iV-curve was reported in previous work [132] (fig. 2a). Here the iV-curve which reaches 29% utilisation at 1 A cm^{-2} deviates from linearity between 0.95 and 1 A cm^{-2}, corresponding to a bend around 1375 mV, which is only 20 mV apart from the bend seen in the iV-curve for 06HU-2. Fuel starvation was ruled out in this case due to the limited utilisation. While the case as shown in figure 3.4 operates with a 58% CO_2 utilisation, it is still unlikely to be caused by fuel starvation, since the iV-curves for the other tests with 58% utilisation do not show this increase when nearing the target current density.

Furthermore, the bend in the prior study also led to a hysteresis effect in the iV-curve [132]. This is indicative of carbon formation in the cell, as shown by Skafte et. al. [72], where the iV-curve for a cell that had been exposed to carbon formation was shown to have a hysteresis.

Another cause of the bend in the iV-curves might be the partial reduction of ZrO_2 to metallic Zr, and subsequent dissolution into Ni to occur at or below $pO_2^{TPB} = 3.2 \cdot 10^{-29\pm3}$ bar as predicted by Chen et. al. [125]. This will lead to the formation

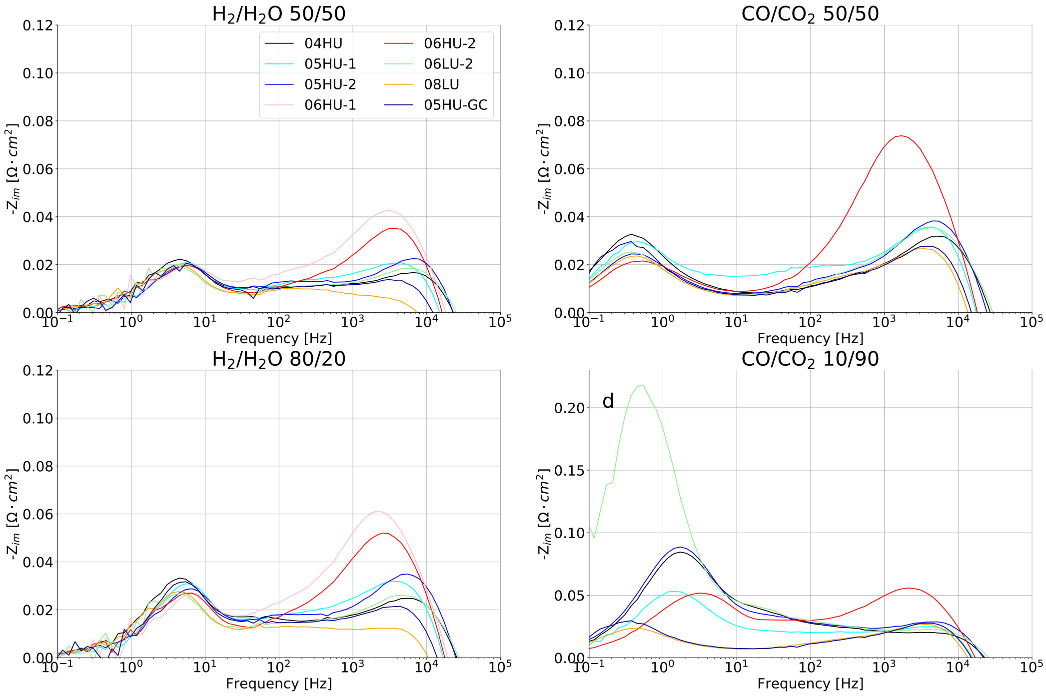

Figure 3.3: Bode plot of the initial performance of the tested cells in various gas compositions. Fuel electrode gas composition is given by the header for the subfigures, while oxygen electrode composition was O_2. The EIS were recorded at 750 °C.

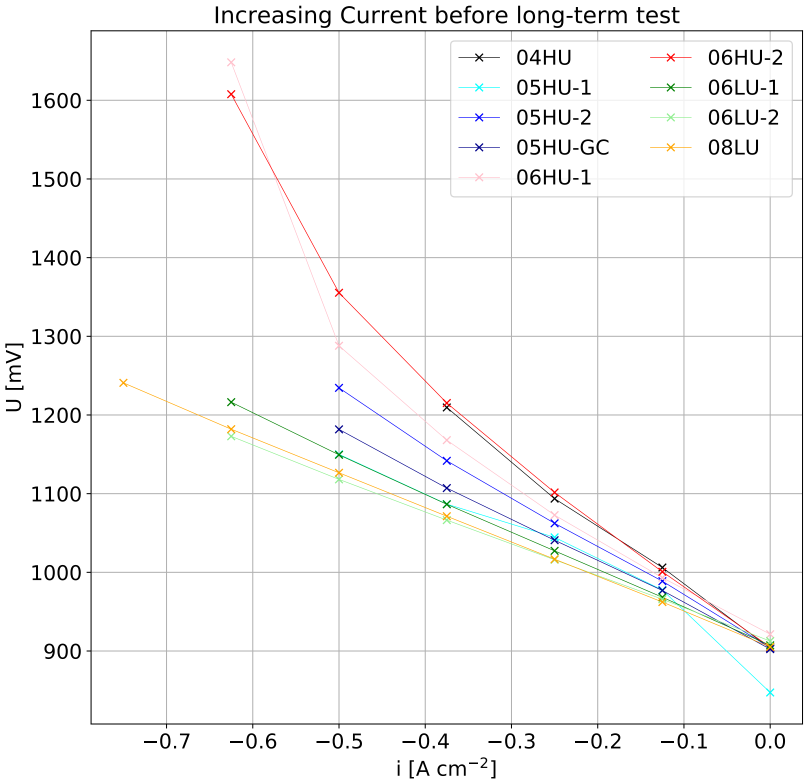

Figure 3.4: iV curves for the tested cells. The iV curves were recorded in a 10/90 CO/CO_2 fuel electrode composition, with O_2 to the oxygen electrode, at 750 °C. The iV curves were recorded as current were increased prior to the long-term tests.

of ZrO_2 nano-particles on the Ni-backbone after which the Zr has migrated through the Ni and exsolved at another point where the local pO_2 is sufficiently high for it to oxidise. Calculation of the expected pO_2 was done using the expression;

$$\eta_{TPB} = \frac{RT}{4F}\ln\frac{pO_2^{OE}}{pO_2^{TPB,local}} \tag{3.1}$$

where η_{TPB} is the overpotential at the TPB found by CNLS fitting (described in a later section), where R is the gas constant, T is the temperature in Kelvin, F is Faraday's constant, and $pO_2^{OE}/pO_2^{TPB,local}$ is the ratio between oxygen electrode and local TPB partial pressure of oxygen respectively. Using the overpotential at 0.625 A cm^{-2} for test 06HU-1, gives pO_2^{TPB}= $3.0\cdot10^{-28}$ bar, against pO_2^{OE}=1.013 bar (1 atm). This value is within the uncertainty reported by Chen et. al. [125], and hence the bend in the iV curve could also be caused by a reduction of ZrO_2. This is however less likely due to ZrO_2 nano-particle formation being an all solid state reaction, and would not be expected at this timescale. Hence onset of carbon deposition was deemed the most likely cause. This would also mean that carbon is formed during start-up of the 06HU tests.

3.3.3 Performance during long-term durability testing

Figure 3.5 shows the development in cell voltage for the duration of the durability tests. The tests have been split up to compare durability at different current densities at low a) and high b) CO_2 utilizations. Figure 3.5 c) compares the performance of cells operated at the same current density, but different utilisations. Finally fig. 3.5 d) shows the effect of cleaning the gas upstream. Bar plots within subfigure 3.5 a), b), and d) refer to degradation rates for the tests within their respective figures at 150, 500, and 650 h where applicable. The degradation rates were determined by linear regression, which are shown as line-segments on top of the measured data in the relevant figures. A figure with all tests included in a single graph can be found in appendix B.

Fig. 3.5 a) compares SOECs tested at varying currents and 29% utilisation. From this figure and the embedded subfigure, it can be seen that the degradation rate (dV/dt) after 150 h for the tests operated at 0.625 (06LU) and 0.75 A (08LU) cm^{-2} are both $\approx$ 200 mV kh^{-1}, and hence degrade at a similar rate. The degradation rate then speeds up for the test at 0.75 A cm^{-2} (08LU) as it has doubled to $\approx$ 400 mV kh^{-1}, whereas the degradation rate of the 0.625 A cm^{-2} test has only increased by 50 mV kh^{-1} at 500 h, and barely reaches 400 mV kh^{-1} at 650 h.

Fig. 3.5 b) compares SOECs tested at varying currents and 58% CO_2 utilisation. The difference in degradation rate is already quite apparent from the cell voltages, where it increases with the current density. This figure shows the highest and lowest degradation rates of all of the tested cells at 650 h: 851 mV kh^{-1} and 19 mV kh^{-1} for 06HU-1 and 04HU respectively. The high rate of degradation in the SOECs tested at 0.625 A cm^{-2} is likely due to carbon formation from the beginning of the durability test. These operating parameters are therefore determined to be non-viable for operation. The test 05HU-2 carried out at 0.5 A cm^{-2} shows a stable if not sligtly decreasing degradation rate. The test shows an increase in cell voltage of 30-40 mV during the first 50-100 h, after which it increases linearly with a rate of $\approx$ 120 mV kh^{-1} from 150 h, and decreases to 113 mV kh^{-1} after 650 h of testing. The test at 0.375 A cm^{-2} starts out with an activation, previously ascribed to activation through Ni-relocation [124]. The rate of degradation later becomes positive, with a magnitude of 18 mV kh^{-1} after 650 h. This is, as mentioned previously, the lowest rate of degradation at 650 h observed in this study. This indicates the operation parameters to be ”safe” for long-term operation. Though while being the lowest of the studied cells, it is still 20x larger when compared with the general target for EC degradation rate 0.8 mV kh^{-1} [133]. The rate of degradation seen in this study is, however, better than the degradation rate seen by Hu et. al. [134], which shows 38 mV kh^{-1} with a 16 % utilisation at 800 °C at experimental cells.

Figure 3.5 c) shows the cell voltage for the SOECs tested with different CO_2 utilisations at 0.625 A cm^{-2}. This figure highlights the large difference between testing at 29% and 58% CO_2 utilisation. When comparing these tests, the observations from the iV-curves in fig. 3.4 should however be restated: the cell voltages for the high-utilisation tests do not behave linearly, at the test conditions which are indicative of carbon deposition [72] (or reduction of ZrO_2 [125]) taking place from the onset of the long-term durability test. It is seen from the figure that changing the utilisation of 06LU-2 from 29% to 58% drastically increases the cell voltage, to a point where it is comparable with those of the SOECs tested at a high utilisation throughout. Comparison of the change in degradation rate in figure 3.5 a) and b), shows a faster acceleration for the tests carried out at high current and low utilisation, whereas the degradation rate for the tests with low current and high utilisation keeps constant. While the degradation rate is assumed to be dependent on the current density, it is also observed that an acceleration in degradation occurs around a cell voltage of 1350-1375 mV, most clearly illustrated in the bar plot for 06LU-1 (fig. 3.5 a)) where a larger increase is seen between 500 and 650 h, compared with the difference in degradation rate between 150 h and 500 h. A similar increase was seen in a previous study [132] (or appendix A), where the degradation rate went from 252 to 467 mV kh^{-1} before and after reaching a cell voltage of 1375 mV. Furthermore, this also coincides with the voltage region in the iV-curves, wherein the bend occurs (fig. 3.4). Hence, it is likely that this point indicates carbon formation, a point that will be discussed further in a later section. Figure 3.5 d) compares the performance of SOECs tested at 0.5 A cm^{-2} with a CO_2 utilisation of 58%, with the parameter being the presence or absence of up-stream gas cleaning. 05HU-1 was (as described in another section) leaking, which is why this comparison will focus on the two other tests. The degradation rate of the SOEC tested with gas cleaning is seen to be much lower than those of the SOEC tested without gas cleaning. This indicates similarly to the findings of Hauch et. al. [65], that sulphur containing impurities in the CO_2 is the cause of increased degradation in SOECs. This would indicate that the gasses fed to the SOECs during the tests might also have contained impurities, which will be discussed in a later section. The cell voltage development for the SOEC tested without gas cleaning differs from the majority of the other SOECs tested in this study by having a concavely shaped development in the cell voltage compared to the convex shape of all but 06HU, and which is not the case for the leaking test 05HU-1. Also 05HU-2 starts off at a cell voltage +50 mV compared with the test with gas cleaning. This would be indicative of its iV behaviour when compared with the iV-curve made during the initial characterisation (fig. 3.1). While the bend seen in the iV-curves during start-up was not ascribed to the reduction and dissolution of ZrO_2, due to this reaction occurring at a longer timescale, it cannot be excluded as a factor of degradation during the 06HU tests as seen in figure 3.5.

3.3.4 Electrochemical Performance - Break down of cell resistance contributions

The long-term durability tests were monitored using EIS, which the ECM: R$_{\Omega}$-RQ$_{ion}$-RQ$_{TPB}$-G-$_{o}x$.-RQ$_{diff}$-RQ$_{conv}$ was fitted using complex-non-linear-square (CNLS) regression, employing the Python based in-house-developed software RavDav [108], as described in chapter 2, as it was previously shown to be suitable for this type of tested SOEC [20]. The guesses and boundaries used for localising minima through the algorithm, were determined based on the initial characterisation, where gas composition and temperature were varied to determine the location of the ECM elements in a similar manner as described by Padinjarethil et. al. [23] and Leonide et. al. [135].

Example of EIS fitting

Figure 3.6 shows examples of the R$_{\Omega}$-RQ$_{ion}$-RQ$_{TPB}$-G$_{ox}$-RQ$_{diff}$-RQ$_{conv}$ ECM fitted to the initial (a,c) and final (b,d) EIS recorded during test 06LU-1 presented as Nyquist (a,b) and Bode (c,d) plots. The figure shows that the impedance increase is mainly caused by the increase of R$_{p}$. The increase of R$_{p}$ can be further broken down into the components used in the ECM. This "breakdown-of-losses" shows RQ$_{TPB}$ to be the main contributor to the increase in impedance during the test. It is furthermore observed that the peak frequency of the RQ$_{TPB}$ element decreases, as expected from the expression $\frac{R}{1+R\cdot Q_0(j\omega)^n}$ where R and CPE are the resistance and capacitance, $j\omega$ is the angular frequency. $j\omega$ is correlated with the frequency (descibed in chapter 2). The movement of RQ$_{TPB}$ over time means that it will pass over the elements G$_{ox}$ and RQ$_{diff}$. If the software cannot differentiate between the elements, some or all of the contribution from one element might be mistaken as coming from the other. The risk of this happening is largest when passing over G$_{ox}$. To minimise this effect, the boundaries for the G$_{ox}$ and RQ$_{diff}$ was hence kept constrained during fitting to avoid "theft" between components. This choice were supported by the data where the change in G$_{ox}$ and RQ$_{diff}$ was very small at the time scale of the $\approx$ 1000 h duration of the tests. This was further supported by literature where application of the same/similar ECM showed low to no significant changes to the G$_{ox}$ element [136]. While a small change in RQ$_{diff}$ is expected in case of carbon deposition inhibiting the pores, the RQ$_{diff}$ contribution is of sufficiently low frequency that this would add to the RQ$_{conv}$. This would result in an overestimation of RQ$_{conv}$, this risk

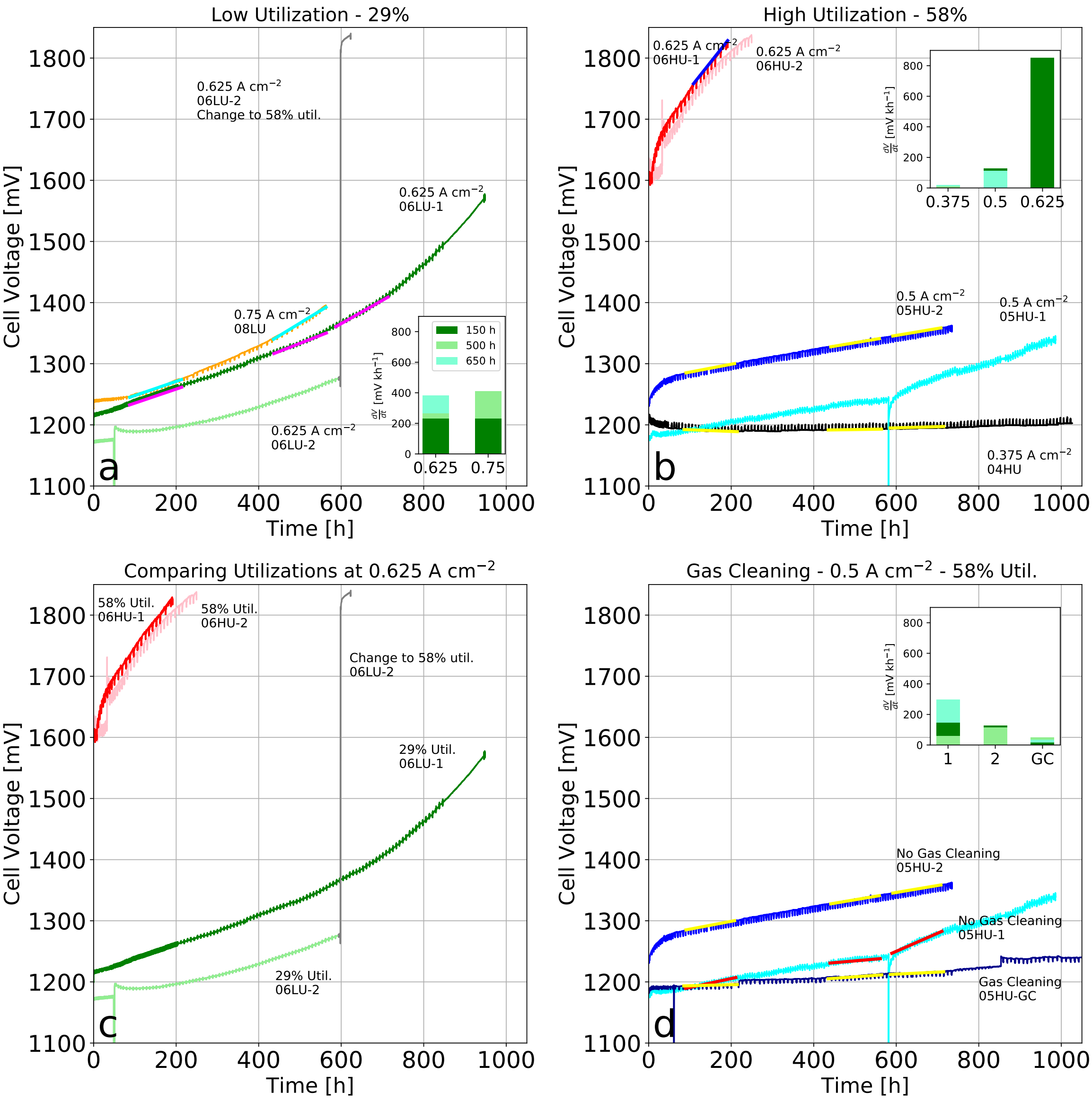

Figure 3.5: Cell voltages measured during the durability tests, line colours are consistent across subfigures. a) Comparison of cells tested at 29% CO_2 utilization, b) comparison of cells tested at 58% CO_2 utilization, c) comparison of cells tested at 0.625 A cm^{-2}, d) comparison of cells tested with and without gas-cleaning. High colour contrast lines in the subfigures refer to degradation rates determined at 150, 500, and 650 h where applicable. Bar plots within figures refer to said degradation rates.

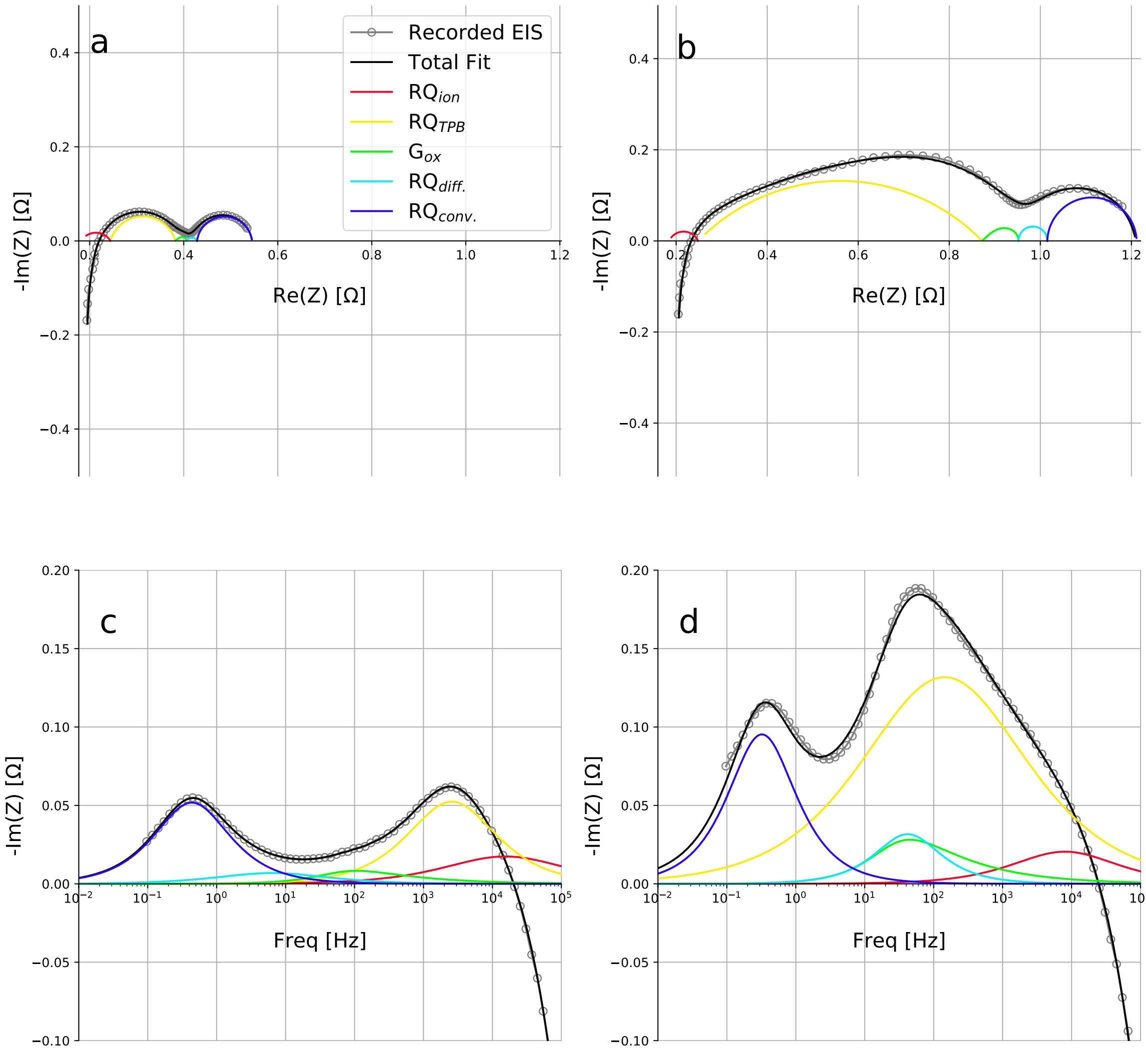

Figure 3.6: Recorded data (grey), total simulated fit (black), and component fit(various colours) of the initial (a,c) and final (b,d) EIS during the 06LU-1 durability test. The legend in a) is shared for all subfigures. i:0.625 A cm^{-2}, T:750 °C, Fuel electrode: 10/90 CO/CO_2, oxygen electrode: O_2

is however deemed worthwhile when focusing on the RQ$_{TPB}$. Hence, the growth in RQ$_{conv}$ should also be assumed to include some of the impedance arising from diffusion, as it would not be expected to increase significantly by itself as discussed by Sun et. al. [136].

Fitted test results

Figures 3.7 and 3.8 show the respective Nyquist and Bode plot for the EIS recorded every 50 h during the long-term durability tests. The colouring goes from red at time 0 h (defined by reaching the operating current), the colour then moves towards blue/violet over yellow, orange and green in the given order. The colours in the various subfigures correspond to the same times across the different tests. The black line in subfigure g) in both fig. 3.7 and 3.8, shows the EIS after the increase in CO_2 utilisation from 29% to 58%.

Figure 3.9 shows the result of the CNLS fit to the data shown in figure 3.7. Hence, it is possible to follow the development of the resistances obtained from ECM. Note that this figure does not include a fit of the EIS after changing utilisation in 06LU-2. The figure shows that RQ_{TPB} is the cause of the largest increase in impedance over the 1000 h duration of the test.

The peak frequency for RQ_{TPB} is seen to decrease over time along with its increase in magnitude. The increase in RQ_{TPB} is seen to be fastest in the tests with the harshest test conditions (high current and/or CO_2 utilisation), which indicates that a high current density and subsequently polarisation leads to accelerated degradation, which is in line the studies of previous workers, be it in steam, co-, or CO_2-electrolysis[132, 137, 138].

Comparison of the cell voltage developments in figure 3.5 showed test 04HU (b) and 05HU-GC (d) as lowest rate of degradation and hence longest expected lifetime. This is supported by EIS, data and fitting results (fig. 3.8 and 3.9), where both these tests mainly show increases in the high-frequency region and no peak frequency decrease of RQ_{TPB}.

Other observations of note is the very large low-frequency response of 04HU (fig. 3.7 a)), likely caused by a relatively small total flow of 4.8 l/h, which in case of a lack of gas convection, diffusion takes over mass transport [139]. Comparison of the cell voltages in figure 3.5 and fits in figure 3.9, correspond better when excluding RQ_{conv}. RQ_{conv} is given by the tangent to the change in Nernst potential that occur during EIS. Since the perturbing current is the same magnitude for all experiments, this will lead to a relatively larger change in gas composition for the tests using a low flow rate when compared with those using a high flow rate. In the end this will mean an expectedly larger RQ_{conv} for the tests using a low flow rate. In the end this is a consequence of the set-up, where the working and reference electrodes are in different atmospheres [140]. The reason for this component to be excluded when comparing cell voltages is that the change in gas composition is already included in the EMF, which differs depending on the change in average gas composition across the SOEC upon applying current.

Comparison of the EIS in figure 3.7 and the results of the CNLS fitting (fig. 3.9), generally shows a larger variety between tests with different operation parameters, than the duplicate tests, despite indicated leaks in some. This observation also holds in the case of 06LU-2 (g in fig. 3.7/3.8) upon increased utilisation to 58%, after which it acts as a 06HU test (d/e), though with a shifted peak frequency for RQ_{TPB}. The final peak frequency for RQ_{TPB} is lower for test 06LU-2, when compared to those of

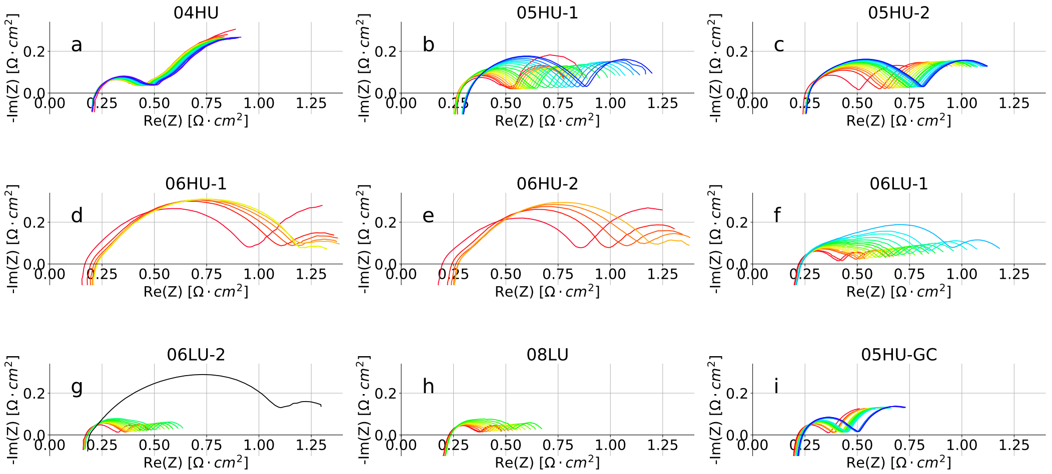

Figure 3.7: Nyquist plots of EIS recorded every 50 h during the long-term durability tests. Data colouring: red: 0h going towards blue over time. Same colours corresponds to approximately the same time. The black line in subfigure g) symbolises EIS after change from 29% to 58% utilisation in test 06LU-2. Test conditions are summarised in table 3.1.

the 06HU tests. This is explained by the longer duration of 06LU-2, and would be indicative of where the peak frequencies for RQ_{TPB} in the 06HU tests would have been, had the tests not been ended.

3.3.5 Distribution of Carbon

Figure 3.10 a) and b) shows the Raman spectra for the active fuel electrode near the CO2 inlet and outlet for test 06LU-1. Figure 3.10 b) have been split in two: An upper part, for which the Raman spectra was recorded at a part of the cell near the CO/CO_2 outlet that did not experience current during operation, and a lower part which did. The peak at 615 cm^{-1} is assigned to YSZ [141]. Three signals are seen for carbon: That of disordered carbon at 1345 cm^{-1} (D), and two for ordered carbon; a large signal at 1585 cm^{-1} (G_1) and a small shoulder at 1610 cm^{-1} (G_2) [142]. The G_1 and G_2 signals have previously been assigned to originate from 2D and 3D structures respectively [143]. The presence of the G_2 signal indicates the formation of a 3D structure of carbon in the fuel electrode. In combination with the other carbon signals, this growth indicates that the carbon in the cell forms as carbon nanotubes (CNTs), as reported by Duesberg et. al. [142].
From fig 3.10 a) and b) it is apparent that the presence of carbon is largest at the fuel electrode/electrolyte interface of the CO/CO_2 inlet and decreases when moving away from the electrolyte towards the fuel electrode support and the outlet.
In a cell operated like here, the current density will decrease from inlet to outlet as discussed by Chen et al. [144] and Sun et. al. [145]. Effectively the current col-

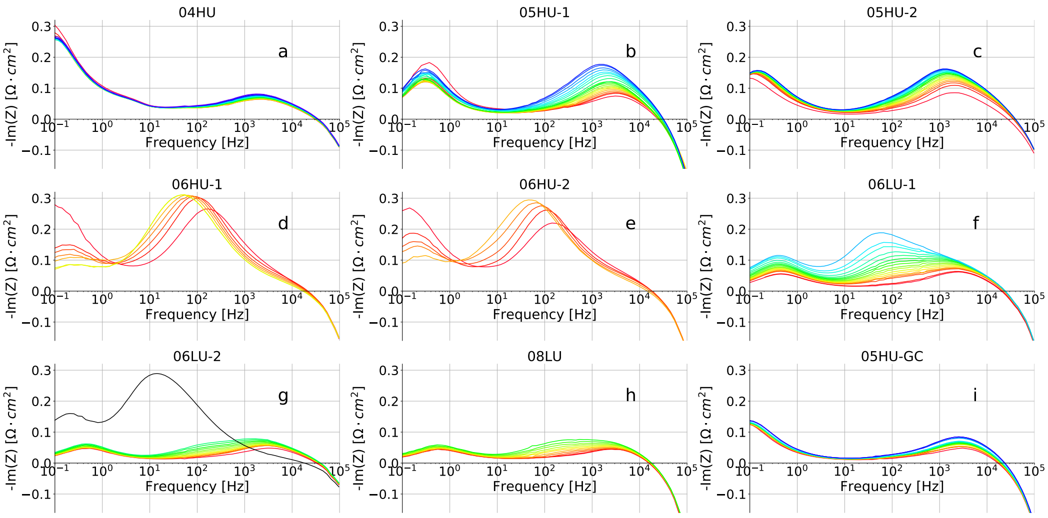

Figure 3.8: Bode plots of EIS recorded every 50 h during the long-term durability tests. Data colouring: red: 0h going towards blue over time. Same colours corresponds to approximately the same time. The black line in subfigure g) symbolises EIS after change from 29% to 58% utilisation in test 06LU-2. Test conditions are summarised in table 3.1.

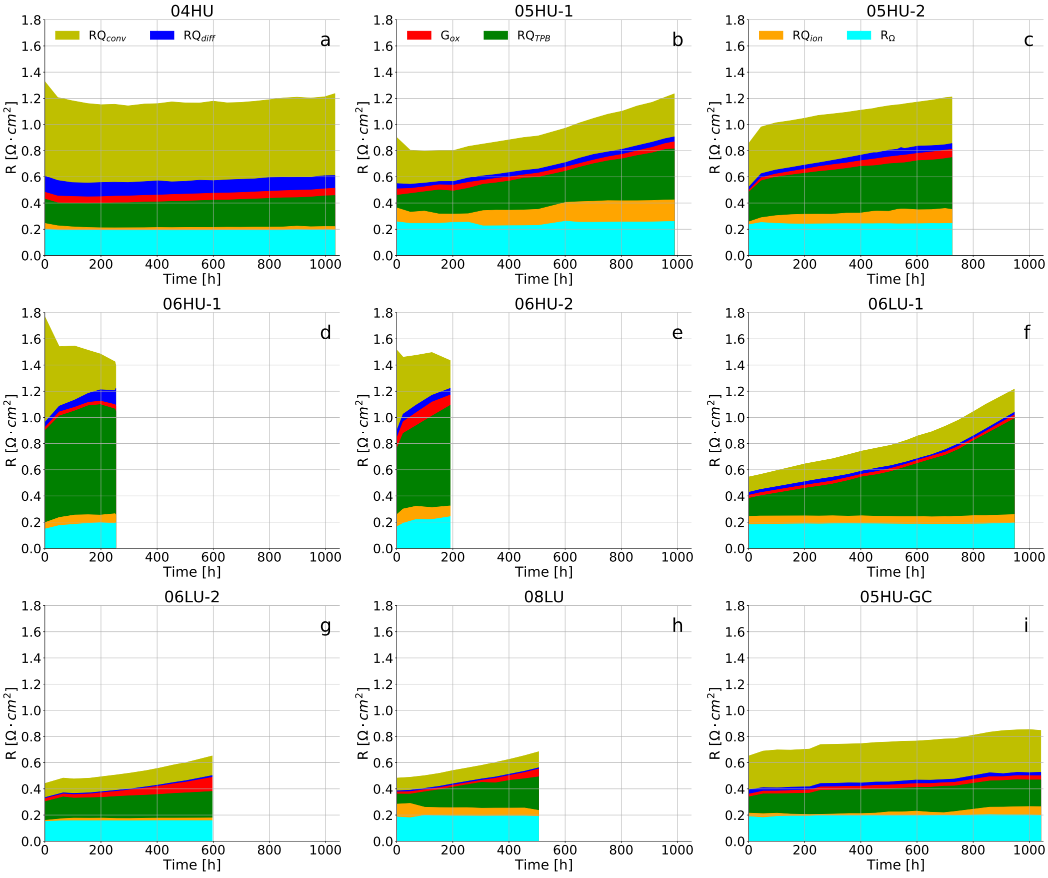

Figure 3.9: CNLS fitting results of the EIS recorded during the durability tests shown in figure 3.7 and 3.8. The resistance contributions seen in the figure corresponds to the ECM components: R_{Ω}-RQ_{ion}-RQ_{TPB}-G-$_{ox.}$-RQ_{diff}-RQ_{conv}. Test conditions are summarised in table 3.1.

lection grids define a fixed potential, and as EMF increases from inlet to outlet, the current driven by (U-EMF) will decrease. Similarly, the carbon signals are most intense at the electrolyte/fuel electrode interface and decrease moving towards the support layer. These observations show that there is a correlation between carbon deposition in the fuel electrode and the local overpotential, since the highest local η_{TPB} will be near the electrode/electrolyte interface, from where it will decrease moving towards the support layer. The absence of carbon in the Raman spectra for the part of the cell that has not experienced any current (fig. 3.10) b upper), confirms that carbon deposition is not caused by the macroscopic gas composition. These findings are well in line with the observed carbon depositions previously reported by Hauch et. al [65].

Expecting carbon near the gas outlets on both the air and fuel electrodes, rather than the fuel electrode inlet as observed in this study, Navasa et. al. [67] suggests carbon deposition to occur due to insufficient diffusion, and cooling from the endothermic electrolysis reaction, leading to carbon deposition through the Boudouard reaction. Despite the conflicting results on the location of carbon formation between this study and that by Navasa et. al.[67], the limited diffusion observed in the latter would lead to a build-up of CO at microscopic level would add to the tendency to form carbon. The cooling effect reported by Navasa et. al. [67] at the most effected areas, ranges from 25 °C, for heat flux (experimental conditions) to 43 °C thermal insulation (perfectly insulating) boundary conditions respectively. In both cases the areas most affected by cooling are away from the air and fuel electrode inlets.

These temperature differences are not enough to favour chemical carbon deposition macroscopically. Microscopically a ΔT of -25 °C at the operation temperature used during the tests means going from requiring p(CO)=0.8 to p(CO)=0.72 for carbon deposition to occur. With an expected macroscopic outlet composition of 54/46 CO/CO_2 in the high utilization tests, this would equate to carbon activities of 0.21 and 0.34 for 750 and 725 °C respectively. The described uneven current density, would therefore in combination with the endothermic electrolysis process and lack of diffusion, favour carbon formation near the CO_2 inlet as observed in figure 3.10 a) and b).

Figure 3.11 shows SEM micrographs of the fuel electrodes of the tested SOECs. Figure 3.11 a) shows the micrograph of test 08LU where fibrous/tubular structures can be seen at the electrolyte/fuel electrode interface highlighted by a yellow circle. Growths like these have previously been identified as CNTs by Tao et. al. [69] and the claim is further backed by the presence of the G_2-carbon peak observed with Raman spectroscopy [142].

The CNTs are similarly present in the micrographs for test 06LU-1 both at the electrolyte interface (b) and out to the active electrode/electrode support interface. The

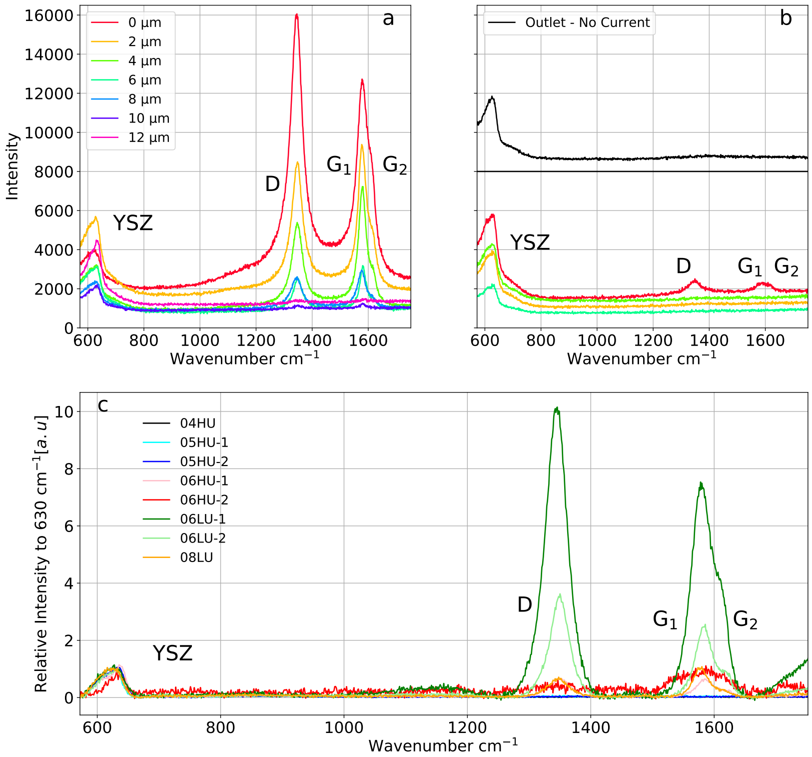

Figure 3.10: Post-operation Raman spectra near the fuel electrode/electrolyte interface. a) Raman spectra recorded at the CO$_2$ inlet of test 06LU-1, legend denotes distance from the fuel electrode/electrolyte interface, and is shared with lower part of b). b) Raman spectra recorded at the CO$_2$ outlet of test 06LU-1, lower part was recorded for the part of the cell having experienced current, the upper part was recorded at the CO/CO$_2$ outlet of the SOEC not having experienced current. c) Raman spectra for the tested SOECs recorded at the CO$_2$ inlet, 0 μm from the fuel electrode/electrolyte interface.

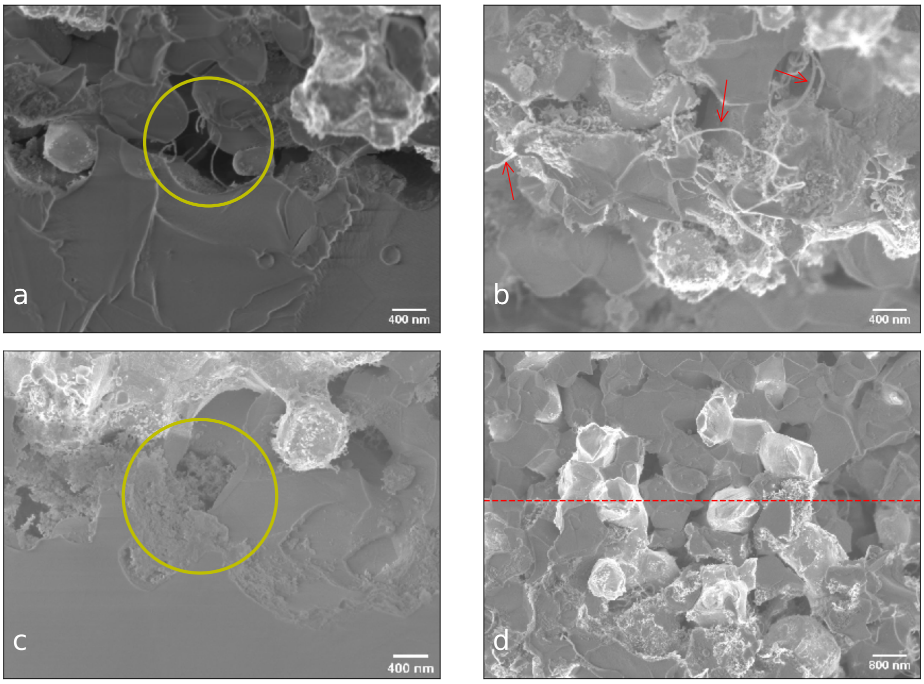

Figure 3.11: SEM micrographs of the fuel electrode near the CO_2 inlet post-test. a) Fuel electrode/electrolyte interface of test 08LU, b) Fuel electrode/electrolyte interface of test 06LU-1, c) Fuel electrode/electrolyte interface of test 06HU-2, d) Interface (red dashed line) between active(8YSZ) and support(3YSZ) part of the fuel electrode from test 06LU-1.

red dashed line in figure 3.11 d) highlights the transition from active fuel electrode (8YSZ) to electrolyte support (3YSZ). This transition is also highlighted by the sudden decrease to absence of carbon 1 μm into the support layer, whereas it is clearly visible in the active electrode.

These observations supports the diminishing presence of carbon moving away from the electrolyte observed in the Raman spectra (fig. 3.10c)).

3.3.6 Electrochemical Threshold for Carbon Formation

Table 3.2 and 3.3 show the results of the values of R_Ω, R_p, and η_{TPB} determined by the CNLS fit to the used ECM model R_Ω-RQ_{ion}-RQ_{TPB}-G_{ox}-$RQ_{diff.}$-$RQ_{conv.}$ for the first and last EIS recorded during the tests. Table 3.2 and 3.3 furthermore show the cell voltages recorded prior to the EIS measurements, and table 3.3 also includes the time of the final EIS measurements with respects to the first (0 h), i.e. the duration of the specific test. The tables include the calculated carbon activities (a_C). The procedure for calculation of carbon activities can be split up into 3 steps:

1. Calculate EMF+η_{TPB}.
2. Calculate ratio of CO/CO_2 that would give rise to said potential.

Table 3.2: Cell voltage, cell resistances: R_{Ω} ,R_p, triple phase boundary overpotential η_{TPB}, expected carbon activity a_C calculated using the thermodynamical database NIST[146], for the initial EIS during each test.

Test	**U [mV]**	**R_{Ω} [Ω cm^2]**	**R_p [Ω cm^2]**	**η_{TPB} [mV]**	**a_C**
04HU	1210	0.202	1.126	70	0.07
05HU-1	1150	0.257	0.644	48	0.03
05HU-2	1234	0.235	0.620	113	0.32
05HU-GC	1182	0.189	0.462	62	0.05
06HU-1	1648	0.148	1.622	439	891
06HU-2	1608	0.165	1.351	315	53
06LU-1	1216	0.182	0.364	86	0.13
06LU-2	1173	0.151	0.290	107	0.26
08LU	1240	0.186	0.297	58	0.05

3. Calculate the expected carbon activity from the Boudouard reaction by isolating a_C in the expression $K_{Boudouard} = \frac{pCO_2 \cdot a_C}{pCO^2}$ where $K_{Boudouard}$ is the equilibrium constant for the Boudouard reaction, and pCO_2/pCO are the partial pressures of CO_2 and CO respectively.

The thermodynamic data used for calculating the activity of carbon was found in the NIST database [146]. Carbon is expected in the fuel electrode when $a_C > 0$.

The values for 06LU-2 in table 3.3 are the values before increasing the CO_2 utilisation from 29% to 58%.

From the fits of the initial EIS (table 3.2) it can be seen that carbon is not expected initially in any of the SOECs except for the ones tested at 0.625 A cm^{-2} at 58% utilisation. These test are further differentiated from the other tests by the very high initial degradation rates. At the other end of the test (table 3.3), where all but test 04HU and 05HU-GC show carbon activities above unity. Finally table 3.3 gives an overview of which SOECs wherein carbon was detected, and to which extent. Two cells were oxidised after the long-term durability test, which is why the result for these are non-applicable in regards to determining the presence of carbon.

Figure 3.10 c) shows the Raman spectra for all tests except 05HU-GC. All spectra in the figure were recorded at the electrolyte/fuel electrode interface near the fuel gas inlet. 05HU-GC was left out of the figure since it was oxidised by accident during the post-durability-test characterisation, to an extent where the majority of the Ni was turned into NiO, determined by the fuel electrode of the SOEC having turned green after the test. The presence of NiO was also observed by Raman spectroscopy, but this has not been included.

Figure 3.12 shows the micrograph for tests 05HU-1 a) and 05HU-2 b). A growth of tubular morphology is clearly seen in the micrograph for test 05HU-2 (fig 3.12 b)) that looks like entangled CNTs (highligted by red arrows). In the micrograph for

Table 3.3: Cell voltage, cell resistances: R_Ω ,R_p, triple phase boundary overpotential η_{TPB}, expected carbon activity a_C calculated using the thermodynamical database NIST[146], for the final EIS during each test, in addition to the extent of observed carbon in the cell. n/a in the last column means that it was not possible to carry out determination of carbon due to oxidation.

Test	**Time [h]**	**U [mV]**	**R_Ω [Ω cm^2]**	**Rp [Ω cm^2]**	**η_{TPB} [mV]**	**a_C**	**Carbon**
04HU	1034	1208	0.194	1.043	89	0.14	n/a
05HU-1	989	1338	0.260	0.975	195	3.2	Traces
05HU-2	725	1356	0.246	0.965	198	3.4	Traces
05HU-GC	1041	1235	0.198	0.648	102	0.22	n/a
06HU-1	253	1834	0.195	1.202	493	3034	Fluffy Mass
06HU-2	190	1829	0.243	1.192	480	2259	Fluffy Mass
06LU-1	947	1571	0.194	1.022	458	1371	A lot
06LU-2	786	1278	0.158	0.494	152	1.0	None
08LU	506	1395	0.190	0.494	192	2.9	Some

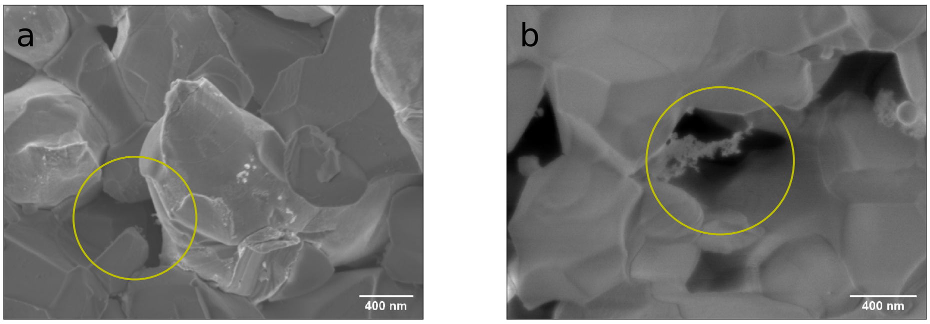

Figure 3.12: SEM micrographs of the fuel electrode near the CO_2 inlet post-test. a) Fuel electrode/electrolyte interface of test 05HU-1, b) Fuel electrode/electrolyte interface of test 05HU-2.

05HU-1 small tubular growths are highlighted by the yellow circle.
Comparing these observations with the the Raman spectra for said tests (fig. 3.10), it is seen that no carbon signals are present in the spectra. The reason for this might be that carbon was present below the detection limit for Raman spectroscopy, and/or highly localised. The second case was observed to be true, since when investigated with SEM the observed carbon was few and far between. The nature of the SEM enabled ”browsing” the sample for carbon, which is not the case for Raman spectroscopy since the CNTs is not visible by light-microscopy available at the Raman spectrometer. The presence of carbon is hence established for the 05HU tests.

Comparing the presence of carbon across the SEM micrographs (fig. 3.11 and 3.12) and Raman spectroscopy (fig. 3.10) the smallest quantities are seen for test 05HU-1 and 2 in SEM, and it does not even register in the Raman spectra. This indicates that the carbon/CNT formation is likely expected to occur closer to η_{TPB} of $\approx$ 190 mV, than the $\eta_{TPB} = 102$mV where no carbon is seen for the 05HU-GC test, since the CNTs are barely present. This is backed up by the iV-curves (fig. 3.4) where the bend of the curve occurs at a similar cell voltage as seen during the long-term durability tests.

The presence of Ni, as stated in the introduction, in the Ni/YSZ SOEC fuel electrode has been assumed to be part of the reason for carbon formation, due to its well known catalytic ability to form CNTs [147]. Lately Tao et. al. [69] have shown the ZrO_2 nano particle to be a catalytic reagent for CNT formation in SOECs. Tao et. al. reported CNT formation to occur at the mass transport limiting step in cells operated at an electrolysis current density of 2.25 A cm^{-2} and temperature of 875 °C [69]. While not reported, the η_{TPB} and hence pO_2 near the TPBs are assumed sufficient for ZrO_2 nano-particles have been formed as described earlier [125]. The pO_2^{TPB} was hence calculated for the tests using the previously stated expression (eq. 3.1). Figure 3.13 shows the calculated pO_2^{TPB} during the long-term tests plotted over time. The highlighted area shows the expected pO_2 threshold for ZrO_2 to partly reduce, leading to the formation ZrO_2 nano particles, according to Chen et. al. [125]. In this figure it is observed that 06LU-1 and the 06HU tests reaches a sufficient low pO_2^{TPB} for the formation of ZrO_2 nano-particles to occur. Due to the stochastic nature of chemical reactions, the probability of ZrO_2 nano-particle formation is expected to increase with a decreasing pO_2^{TPB}. More nano-particles will mean more nucleation sites, and hence more CNT growth. With spacial restrictions, as in the porous structure of a SOEC, it will mean that beyond a certain point, each additional ZrO_2 nano-particle/CNT will take up space from the other. This might lead to the formation of shorter, entangled, or clumped up CNTs. This is speculated to be the cause of why the pores in the fuel electrode of test 05HU-2 is filled with some spongy/fluffy looking mass in figure 3.11 c), while the test 08LU shows fewer, but longer CNTs (3.11 a)). This would however need to be confirmed by EDS. In between is test 06LU-1 which shows long CNTs, which might have formed initially, where the spongy mass could have formed once ZrO_2 nano-particles started forming. While this is only speculation, and further investigations would be required for explicit proof, it is a possible explanation for the findings.

While ZrO_2 nano-particles may accelerate the carbon deposition, it is not the cause of it. In a previous study a similar increase in the cell voltage degradation was seen upon reaching a cell voltage of about 1375 mV [132], similarly to 06HU-1 in figure 3.5 a). This cell voltage increase is assigned to the onset of carbon formation. This is the case because the formation of ZrO_2 nano-particles can be ruled out, due to insufficient η_{TPB} and hence too high pO_2^{TPB} for this to occur according to the findings from figure 3.13 and Chen et. al [125]. In a study by Navasa et. al. [67] the tendency of carbon formation was linked to the Boudouard reaction, rather than

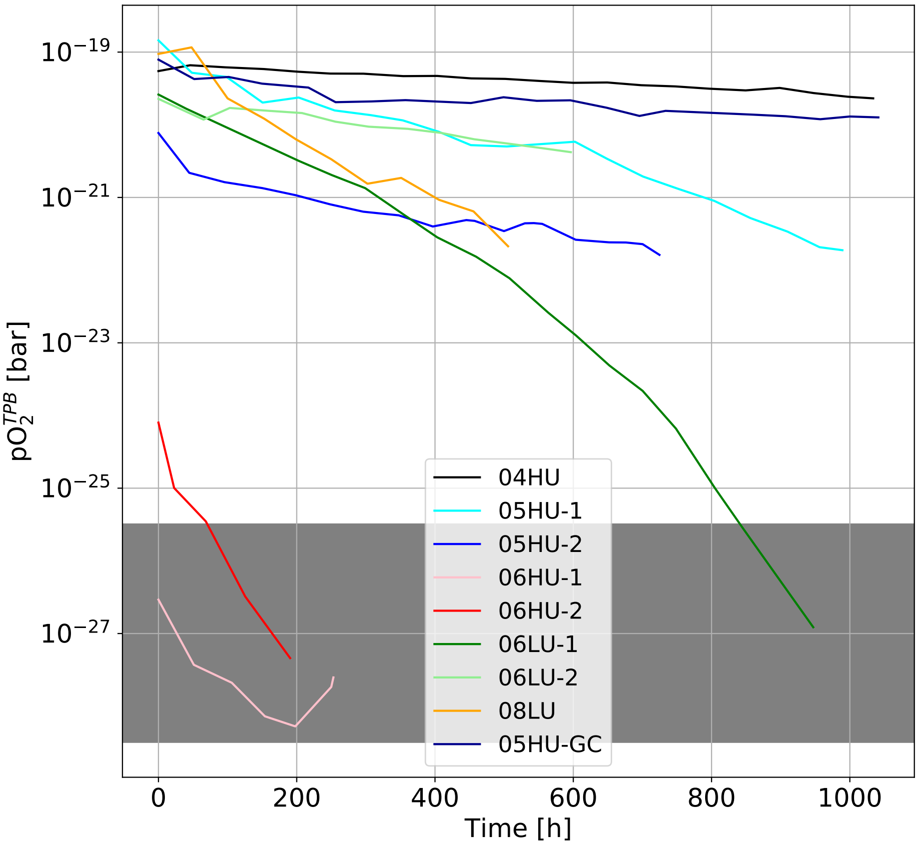

Figure 3.13: Local pO_2s at the TPBs estimated from the CNLS fit of the EIS recorded during the long-term durability tests. Highlighted area depicts expected onset of ZrO_2 reduction according to Chen et. al. [125]

electrochemical reduction, which is why the carbon activities were calculated from the Boudouard equilibrium constant in tables 3.2 and 3.3. The carbon deposition is thus thought to occur due to a lack of convection/diffusion at the local TPBs, which leads to a build up of the product, CO, and subsequently carbon. This will further lead to an increased polarisation at nearby TPBs, enabling further carbon deposition, until cell failure.

Based on these results it is observed that CNTs start forming in the fuel electrode upon reaching an TPB overpotential of ≈ 190-200 mV. The formation of ZrO_2 nanoparticles upon reaching a sufficiently low pO_2^{TPB} is furthermore speculated to increase carbon formation by acting as nucleation sites.

Carbon may already be dissolved in Ni at this potential, having caused irreversible damage to the cell according to Skafte et. al. [71]

3.3.7 Gas cleaning

Hauch et. al. [65] have previously shown gas impurities in the CO_2 feed, such as sulphur, to have detrimental effect at concentrations down to 15 ppb. Even before that, it has been used as a ”catch-all” reason for otherwise unexplainable/non-assignable degradation, which it might have been [148]. Test 05HU-GC was tested using gas cleaning consisting of crushed Ni/YSZ fuel electrodes with a particle-diameter of 500-600 μm. The gas cleaning was only heated to 650 °C, to ensure better adsorption than at the operating temperature to retain gas impurities [149]. This cell, as described previously, shows to be more durable than the cells at the same operational parameters in regards to rate of degradation (fig. 3.5) and η_{TPB} (table 3.3), which indicates gas impurities in the used CO and/or CO_2 for the test. It has however not been prioritised to determine the levels of said impurities.

The most discussed impurity during CO_2 electrolysis is sulphur, as it is a well known impurity during SOFC operation with hydrocarbons and for metal catalysts in general [40, 149]. Impurity sensitivity is larger during SOEC operation since sulphur species are reduced to elemental sulphur due to the operating potential, which leads to physi/chemi-sorption on the Ni-particles leading to deactivation of the TPB [149, 150].

Assuming that the impurity level remains constant in the gas over the duration of the test, and all of the impurities (or a constant fraction) adsorps to the Ni [150], it will lead to a linear increase in the number of sulphur species inhibiting the TPBs. From this a linear increase in η_{TPB} (and cell voltage) over time would be expected [84]. This increase is seen due to the galvanostatic testing, since whenever a TPB is inhibited from partaking in the electrolysis, the nearby/remaining TPBs takes over. With a constant current and a decreased reaction surface, this will lead to an increase in the current density of the remaining surface area [84].

A tendency is seen, as discussed previously, where the SOECs in figure 3.5 degrades linearly versus time up until a cell voltage of about 1375 mV, whereafter it accelerates, indicating the onset of an additional degradation mechanism. Based on this, in addition to the observations of the test where gas cleaning was applied, it is highly likely that a significant part of the initial linear degradation can be assigned to gas impurities.

3.4 Conclusion of Chapter

SOECs tested for CO_2 electrolysis have been tested at various current densities and CO_2 utilisations for ≈ 1000h. The rate of degradation has increased with harsher operating conditions. CNLS fitting of EIS recorded during tests have shown η_{TPB} to be the main cause of the increase in the cell resistance and cell voltage during operation at the given time scale and test conditions.

Carbon deposition has been observed in the fuel electrodes of SOEC reaching

$\eta_{TPB} \approx 192$ mV during CO_2 electrolysis. The extent of carbon formation furthermore seems to be dependent on the cell voltage or overpotential. ZrO_2 nano-particles are speculated to accelerate the carbon formation upon reaching polarisation/local pO_2 at the TPBs necessary for the reduction of ZrO_2, leading to formation of said nano-particles.

Post-test characterisation of the tested SOECs by SEM and Raman spectroscopy have shown the depositing carbon takes the form of CNTs with the highest presence at electrolyte/fuel electrode interface for the gas-inlet, and reduces moving towards the support layer/gas-outlet.

Cleaning of the CO and CO_2 up-stream has shown great effect in decreasing the rate of degradation during test.

Chapter 4

$Ce_{0.8}Gd_{0.2}O_{1.9}$ Infiltrated SOEC Fuel Electrodes for Improved Carbon Tolerance During CO_2 electrolysis

4.1 Introduction

SoA Ni based fuel electrode supported SOECs' proneness to carbon deposition in the fuel electrode when used for CO_2 electrolysis is a limiting factor for the technology to achieve widespread use. As seen in the previous chapter it is possible to avoid carbon deposition by operating at low current density or cleaning the gas. Since electricity cost accounts for ≈70% of the operation cost of SOECs [151], it is of interest to maximise production/turnover when electric power is cheap. Increasing the carbon deposition tolerance of SOECs for CO_2 electrolysis would hence mean a higher turnover during periods with cheap power, and hence decreased net operational costs.

A possible solution, which lately has gained significant attention is to adjust the electrodes by infiltration [152–156]. Infiltration is a method of modifying the surface of the electrode [152], to increase catalytic [157] and conductive properties [158], in addition to increasing the active surface area of the electrodes [159]. The general process for infiltration consist of 3 steps and is shown in figure 4.1, the first being acquiring a porous backbone for infiltration e.g. a reduced Ni/YSZ fuel electrode. The second step is to apply a precursor solution, which during the third step decomposes to the target infiltrate during heat treatment [160]. The most used/studied group of materials used for infiltration in SOC electrodes is the Mixed Ionic and Electronic Conducting (MIEC) materials [24, 25, 161–165]. Using a MIEC means that the gas phase only needs to be in contact with one material component, compared with two in the Ni/YSZ backbone leading to the formation of double phase boundaries (DBPs). The advantage of DBPs over TPBs as the former is measured in area per electrode-area, and the latter in length per electrode-area [159]. The infiltration method also provides a way to introduce a catalytically active species which is neither suited as a structural component, or where a difference in thermal expansion coefficients would lead to mechanical strain if used in larger quantities, but is viable in small amounts. Finally the temperature of the heat treatment for decomposition is typically in the 300-500 °C range, meaning that potentially detrimental reactions between the SOC components and the MIEC at high temperature is avoided, so is large scale sintering usually leading to the infiltrate occurring as nano-particles in the cell.

Ceria containing material has previously been shown to increase the performance and durability of SOECs during steam electrolysis [166, 167] and according to the review, of its material qualities, by Sala et. al. is also a promising candidate for use in CO_2-electrolysis operation [158]. This is due to ceria not only showing a high ionic conductivity compared to YSZ, but also a catalytic activity towards the reduction of CO_2 [168, 169], in addition to suppression of carbon deposition during said reduction [66, 70, 170]. Furthermore, it has been shown to increase the resistance towards gas impurities, such as sulphur when operated in fuel cell mode [171, 172]. The carbon tolerance of ceria can, according to Wang et. al. [98], be further improved by the introduction of the non-catalytic element Gd. The carbon deposition mechanism in ceria is caused by Ce^{+3}-Ce^{+3} pairs at which carboxylates forms. By introducing Gd^{+4} these Ce^{+3}-Ce^{+3} pairs are split as Gd coordinates between the Ce ions in the scaffold, Ce^{+3}-Gd^{+4}-Ce^{+3}, and hence impedes carbon deposition. The introduction of gadolinia to the structure also leads to an increased number of oxygen vacancies, improving the oxygen-ion conductivity of ceria further.

The material; gadolinia-doped-ceria (CGO), has hence shown great promise, both as a fuel electrode material and infiltrate due to its ionic conductivity. This has led to an extended lifespan of SOECs, when compared with that of Ni-YSZ for steam and co-electrolysis [23, 28]. Most of these studies have however, been for H_2O electrolysis and/or co-electrolysis, while only a limited amount of studies have been made into the effects of CGO containing SOECs during CO_2 electrolysis of full cells [28, 173], and even fewer for tests lasting +500h [163].

The purpose of this study has been to study the long-term ($\approx$ 1000 h) durability of CGO infiltrated Ni/YSZ fuel electrode supported SOECs during CO_2 electrolysis. To this end, two SOECs with different loadings of CGO infiltrate were studied to determine whether there is any significant change to the performance or durability of the cells, and whether CGO increases the tolerance towards gas impurities and carbon deposition, when compared with a non-infiltrated cell tested under the same conditions.

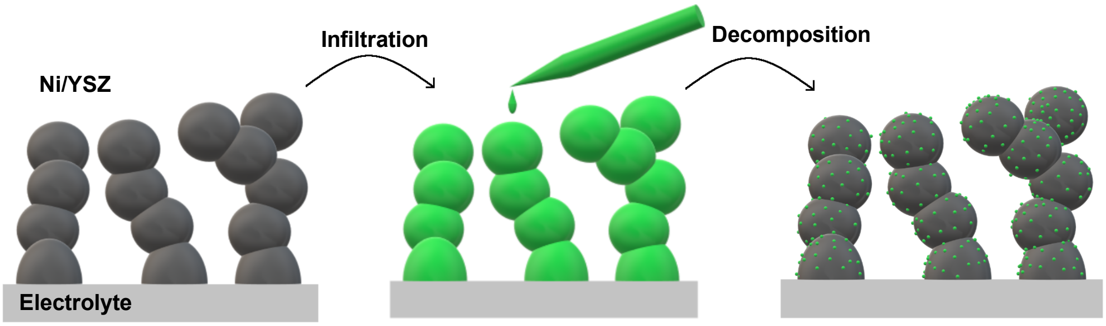

Figure 4.1: 3-step infiltration process.

4.2 Experimental

4.2.1 CGO infiltration

Reduction The cells were reduced prior to infiltration. The reduction was carried out in a tube furnace, the cells were hence reduced in a one-atmosphere set-up at ambient pressure. The cells were heated to 850 °C with a heating rate of 180 °C/h in a 8 l/h N_2 atmosphere. Once at the 850 °C, the gas composition was changed to 5% H_2 in N_2 and was led through a humidifier kept at room temp. this lead to a H_2O content of ≈ 4 %. This gas composition and temperature were kept for 4 h, before cooling down to room temp. The humidifier was bypassed before cooling down to avoid/minimise phase transformation in the 3YSZ fuel electrode support as reported by Khajavi et. al. [174]

Precursor-solution 8.685 g $Ce(NO_3)_3 \cdot 6\,H_2O$ (Alfa Aesar) and 2.259 g $Gd(NO_3)_3 \cdot 6\,H_2O$ (Alfa Aesar) was dissolved in 25 ml de-ionised water while stirring in a beaker. After having dissolved the salts, 0.258 g of the surfactant P123 (Sigma Aldrich) was added to the water. The beaker was covered with parafilm, and the solution was heated to 40 °C while stirring. It was left to stir for 3 days, to dissolve the surfactant.

Infiltration The SOECs were infiltrated by adding the CGO-nitrate precursor to the reduced fuel electrode drop-wise with a pipette. The precursor solution was distributed over the fuel electrode by a small sponge-swab, making sure it did not go over the edges of the cell. The solution was left to infiltrate into the fuel electrode for ≈ 2 min, after which excess solution was removed carefully with a fine tissue,

Table 4.1: Test number(internal reference), test name(referred to as hence forward), and CGO loading of the three tested cells in this study.

Test Number	**Test Name**	**CGO loading [mg cm^{-3}]**
1t169	CGO-0	0
1t182	CGO-2	127.5
1t183	CGO-4	225.3

once again making sure not to get precursor-solution over the edge of the cell. The cell was entered into a chamber furnace set to 200 °C. Once in the furnace it was heated to 300 °C with a heating rate of 300 °C h^{-1} to decompose the precursor-solution into CGO, the cell was removed after 35 min in the furnace (20 min heating + 15 min at 300 °C). This process was repeated 2-4 times. After the last repetition the cell was left in the furnace for 2h for a final extended decomposition. The cells were weighed initially, and after each repetition to determine CGO loading.

4.2.2 Cell tests

Three SOECs were investigated during this study, as shown in table 4.1, which includes the test number as internal reference, the name by which it will be called hence forward, and the CGO loading. It should be noted that CGO-0 is also seen in the previous chapter under the name 06LU-1.

The cells were tested using the test set-up and initial characterisation protocol described in chapter 3. The SOECs were tested for CO_2 electrolysis in a 10/90 CO/CO_2 fuel gas composition and O_2 to the oxygen electrode. The tests were all carried out with a current density of 0.625 A cm^{-2} and 29% fuel utilisation at 750 °C. The duration of the tests were $\approx$ 1000h.

4.2.3 Post test characterisation

The SOECs were characterised by SEM and Raman spectroscopy as described in chapter 3 after the tests.

4.3 Results & Discussion

4.3.1 Cell reduction and infiltration

The one-atmosphere cell reduction protocol was inspired by the work of Tong et. al. [175]. This method did however make the cells brittle, and prone to break during

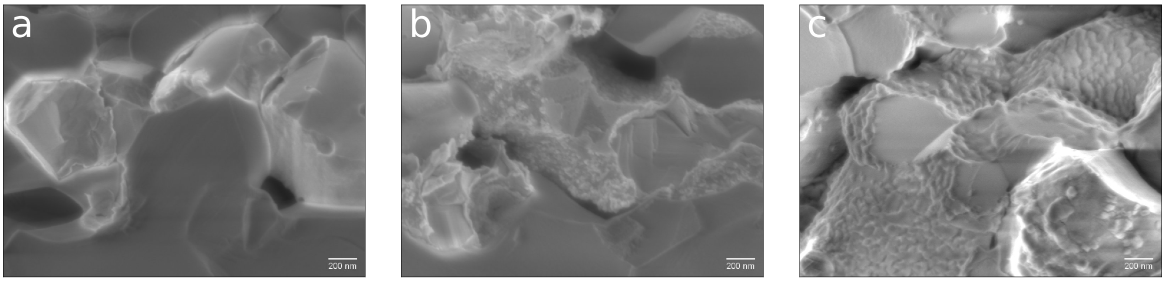

Figure 4.2: SEM micrographs of non-tested samples with CGO loadings of: a) 0 mg cm^{-3} (CGO-0), b) 120.2 mg cm^{-3} (CGO-2), and c) 267.1 mg cm^{-3} (CGO-4) corresponding to the CGO loadings of the tested samples.

the start-up of the test. The failure during start-up was speculated to be caused by the formation of monoclinic 3YSZ during cooling down from reduction, or during infiltration, due to exposure to moisture in the 80-200 °C temperature range. This has previously been shown to be where phase transformation is most prone to occur by Khajavi et. al. [174]. The humidifier was hence bypassed during cooling down to 600 °C. The humidifier was originally included to help protect the oxygen electrode from a too reductive atmosphere, as degradation in LSCF was previously observed due to thermal expansion mismatch with the YSZ electrolyte [167].

This also led to a change in temperature ramp during the infiltration from 200 to 300 °C/h, to reduce the time at critical temperatures.

The slower reduction protocol as described in the previous section was implemented to avoid failure during start-up, so was waiting with applying the weight on top of the cell until the SOEC was hot, and more flexible.

4.3.2 Initial fuel electrode structure

Figure 4.2 shows SEM micrographs of cells infiltrated with 0 (a), 120.2 (b), and 267.1 (c) mg CGO cm^{-3} which has not been tested. The microstructure of the cells in fig. 4.2 are hence comparable to the initial microstructures of the studied cells. Fig. 4.2 a) shows an un-infiltrated cells with a comparatively smooth electrode surface, whereas the particles in fig. 4.2 b) and c) show the microstructure of CGO infiltrated cells with increasingly rough and covered electrode surfaces, upon and, with increasing CGO loading, similarly to the observations by Tong et. al. and Ramos et. al. [175, 176].

4.3.3 Initial Performance

Figure 4.3a shows an iV curve recorded during the initial characterisation for the three cells. The iV curve shown in fig. 4.3a was recorded with a 50/50 H_2/H_2O fuel

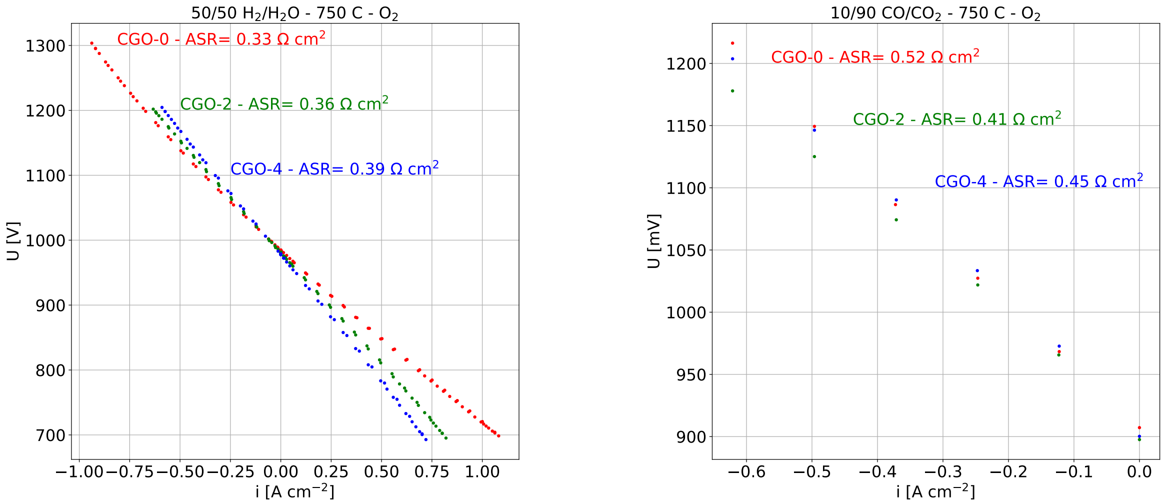

(a) Fuel gas composition 50/50 H_2/H_2O (b) Fuel gas composition 10/90 CO/CO_2

Figure 4.3: iV curves recorded as part of the initial characterisation. Both curves were recorded at 750°C, with O_2 to the oxygen electrode. Dots represent data, and lines represents the linear fit for determining ASR, which was calculated between -0.34 and - 0.66 A cm^{-2}

gas composition, and O_2 to the oxygen electrode at 750 °C. The ASR was determined in the range -0.34 to -0.66 A cm^{-2}, and shown beside the plotted data. Figure 4.3b shows an iV curve recorded with another fuel gas composition: 10/90 CO/CO_2, but otherwise the same conditions. The iV curve in fig. 4.3b corresponds to the increase in current before the long-term test, as iV curves in CO/CO_2 were otherwise left out due to previous experiences where the cells were aged prematurely. The iV curves in fig. 4.3a show a very slight advantage in ASR of the non-infiltrated cell compared with the infiltrated cells which shows increasingly larger ASR along with the increase in CGO loading. These differences are however so slight that they could just as well be due to variations of the initial (pre-infiltration) microstructures. The ASRs of all the tested SOECs are furthermore rather large compared to SoA cells, where an ASR of 0.15 Ωcm^2 was been previously achieved [44].
Comparing the ASRs seen in the iV curves in CO/CO_2 from fig. 4.3b with the ones in steam shows the opposite tendency, where the infiltrated cells have the lower ASR compared to the non-infiltrated one, though not completely opposite tendency, as also here the twice infiltrated cell performs better than the quadruple infiltrated cell.

Figure 4.4 shows the Nyquist plots of impedance spectra recorded during the initial characterisation of the three cells, operated at four different gas compositions to the fuel electrode: a) 50/50 H_2/H_2O, b) 50/50 CO/CO_2, c) 10/90 H_2/H_2O, and d) 10/90 CO/CO_2, all with O_2 to the oxygen electrode at 750°C. All of the EIS was recorded at OCV. Finally table 4.2 shows the R_Ω and R_p for the EIS measurements in fig. 4.4 and 4.5. From fig. 4.4 it can be seen that the R_Ωs are lowest for the non infiltrated cells, with little-to-no variation based on gas composition. Whereas, the R_Ω for the infiltrated cells in most cases increases with the number of infiltrations, and gas composition. The increase in resistance between the non-infiltrated cell and infiltrated cells might be caused by the introduction of CGO to the YSZ, as elemental interdiffusion between these phases have been known to decrease conductivity when sintered together [177, 178]. The discrepancy might also be explained by the conditions of the fuel electrode reduction or infiltration, in that for a duration of both the cell was exposed to a humid atmosphere below 400 °C. These conditions can, according to previous studies, induce a phase changes within 3YSZ to go from a tetragonal to a monoclinic unit cell [174, 179, 180]. This would then mean that a crack has formed in the support layer and propagated into or through the active layer, although this is quite unlikely. The microstructure might also have been damage though rapid cooling from 300 °C when the cells were removed from the furnace during the infiltration process [181].

Comparing the R_p in table 4.2 shows a relative decrease in resistance is seen between the non-infiltrated and infiltrated cells for the 50/50 fuel gas compositions, similar values for the 10/90 H_2/H_2O composition, and an increase during operation in 10/90 CO/CO_2.

Figure 4.5 shows the DRT plots corresponding to the EIS measurements shown in fig. 4.4. The lines for both infiltrated cells are similar to each other, but generally differs from line for the non-infiltrated cell in two aspects across the four fuel gas compositions: Firstly the line for the non-infiltrated cell is shifted towards the higher frequencies, secondly the non-infiltrated cell has a large frequency response at 10kHz, which is very diminished for the infiltrated cells. Assigning the peaks similarly to the previous chapter (chapter 3), it is assumed that the high frequency peak corresponds to the O^{2-} transport through YSZ and CGO [167]. Since CGO is a better O^{2-} conductor than YSZ at the operation temperature [182], covering the fuel electrode (fig. 4.2) with CGO will lead to a decrease in resistance.

An increase is seen in the low frequency region for the infiltrated cells of the EIS in fig 4.4/4.5, this most pronounced in the gas composition 10/90 CO/CO_2 (fig 4.4/4.5). While CGO has been reported to have a low frequency response [23], previous studies of CGO infiltrated fuel electrodes of similar cells did not show a similar increase in the low frequency region upon infiltration, though it did show a similar shift in peak frequency [137]. The most likely explanation for the increase in the low frequency response is that the cell might be leaking, since a leak in the cell might lead to a decrease of the least populous gas species and hence an increased slope of the tangent in Nernst equation [140, 183]. The data for a down stream sensor have shown that the gas composition contains less than 10% CO at the start of the test at 0.625 A cm^{-2}, when 39% CO is expected. Despite the apparent gravity of this leak,

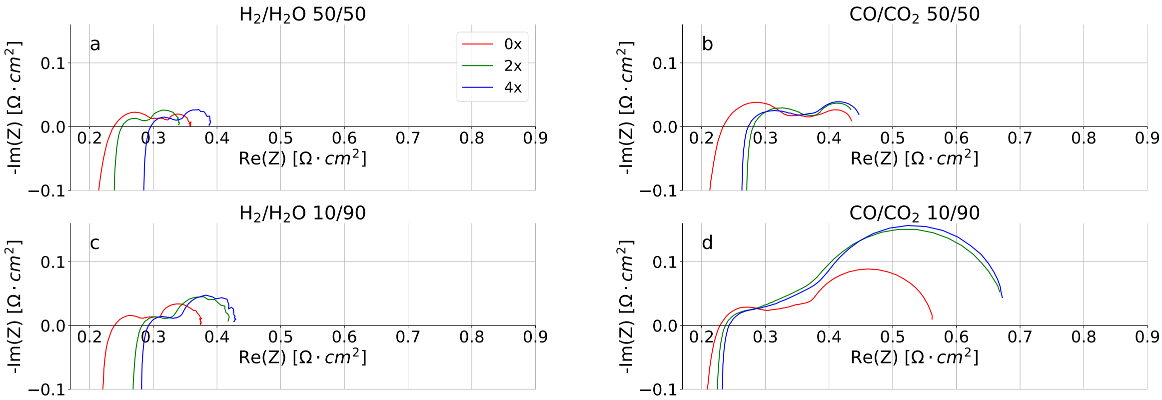

Figure 4.4: Initial characterisation of the tested cells in various fuel gas composition. Line colours are consistent across subfigures: red - CGO-0, green - CGO-2, blue - CGO-4. Headings of subfigures describe fuel gas composition. All tests were carried out at 750 °C, with O_2 to the oxygen electrode.

Table 4.2: R_Ω and R_p for the tested cells at the gas conditions shown in figures 4.4 and 4.5. All resistances in the table is given in $\Omega \cdot cm^2$

	50/50 H_2/H_2O		**50/50 CO/CO_2**		**10/90 H_2/H_2O**		**10/90 CO/CO_2**	
Test	**R_Ω**	**R_p**	**R_Ω**	**R_p**	**R_Ω**	**R_p**	**R_Ω**	**R_p**
CGO-0	0.21	0.15	0.21	0.20	0.22	0.15	0.21	0.35
CGO-2	0.24	0.10	0.27	0.16	0.27	0.15	0.22	0.45
CGO-4	0.28	0.10	0.26	0.16	0.28	0.14	0.23	0.44

visual inspection of the cells after the test did not show any cracks. Additionally, when comparing the cell voltages during the start of the test (at OCV) they were only differing with 10 mV (2% CO). It is hence estimated that the leak occurs near the edge of the cell, and while having a small effect it is minimised by the geometry of the test setup. This is backed up by the cell voltage during the tests, since a leak of this size would have led to a significant reduction of this parameter.

Figure 4.6 shows Arrhenius plots for the resistances R_Ω (a+c) and R_{TPB} (b+d) in fuel gas compositions corresponding to the inlet (10/90 CO/CO_2) (a+b) and outlet (39/61 CO/CO_2) (c+d) during the long-term durability test. The values used in the figure was determined from CNLS fitting of the model R_Ω-RQ_{ion}-RQ_{TPB}-$G_{ox.}$-$RQ_{diff.}$-$RQ_{conv.}$ as described in previous chapter (chapter 3). RQ_{TPB} is here used interchangeably for the Ny-YSZ charge transfer process whether it is for a three phase boundary (non-infiltrated) or two phase boundary (infiltrated) SOEC. The EIS used in the figure were recorded in the temperature range 675-850 °C. Table 4.3 shows the activation energies calculated from the slopes of the linear regression in fig. 4.6 in addition to the activation energy for the whole cell. Comparison of the E_a for the non-infiltrated cell, to those of the infiltrated cells shows a decrease for all but for the $E_a(\Omega)$s which are 0.63 eV ±5 at both inlet and outlet gas compositions. The invariant $E_a(\Omega)$ values indicates that the electrolyte has not been damaged during

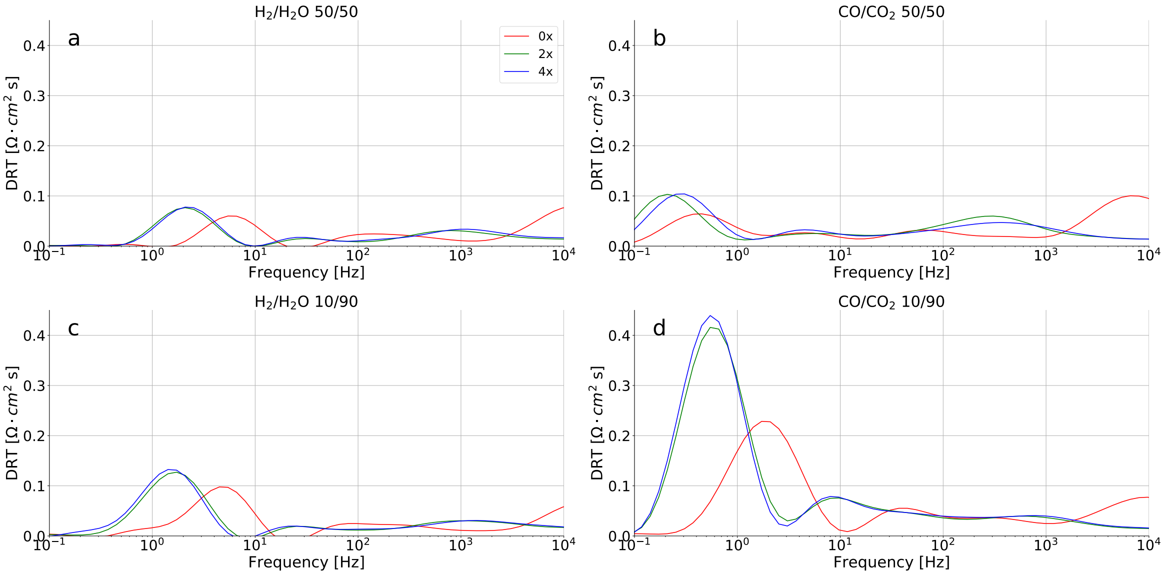

Figure 4.5: Initial characterisation of the tested cells in various fuel gas composition. Line colours are consistent across subfigures: red - CGO-0, green - CGO-2, blue - CGO-4. Headings of subfigures describe fuel gas composition. All tests were carried out at 750 °C, with O_2 to the oxygen electrode.

infiltration, since the infiltrate is not expected to affect the R_Ω. The activation energies being lowered for the infiltrated cells shows that infiltration of CGO improves the performance the tested cells in a CO/CO_2 atmosphere, which can be explained by CGO's well-known ability to catalyse the CO_2 reduction reaction [158, 159, 168]. This improvement is seen in the E_a(TPB) which shows the largest decrease for the infiltrated cells, further establishing the advantageous effect of CGO for CO_2 reduction.

Table 4.4 shows the activation energies for R_Ω and R_{TPB} as investigated in this study. Due to the limited amount of studies done on activation energy on full cells in a CO/CO_2 atmosphere [184, 185], values determined in a H_2/H_2O composition have been included. Comparing the H_2/H_2O and CO/CO_2 ratios it is seen that the reduced species(H_2) is most prevalent for the former composition, while the oxidised species (CO_2) is favoured in the latter. The reason for this is that more research has been done for SOFC than SOEC (1.2 M vs 0.14 M articles on google scholar as of November 1st 2022) where a large H_2 content corresponds to operation conditions for SOFC [186]. Furthermore during operation in CO/CO_2 an excessive concentration of CO would lead to carbon deposition in the fuel electrode through the Boudouard reaction [67], though this is most prevalent at lower temperatures.

A large variation in activation energy is seen when comparing the values for R_Ω in H_2/H_2O atmospheres in the referenced literature, these cells were however based on different electrode structures, indicating that R_Ω is dependent on more than solely the resistance of the electrolyte. Comparing the value $E_a(\Omega)$=1.23 eV which was re-

Table 4.3: Activation energies for the processes concerning R_{Ω}, R_{TPB}, and the total cell resistance at fuel electrode gas composition corresponding to what the inlet and outlet of the SOECs experience during operation of the long-term test. The activation energies was calculated on the slopes in figure 4.6. All activation energies in the table are given in eV.

	Test	E_a Ω	E_a TPB	E_a Total
	CGO-0	0.68	0.22	0.38
In	**CGO-2**	0.6	0.06	0.23
	CGO-4	0.64	0.01	0.22
	CGO-0	0.62	0.68	0.65
Out	**CGO-2**	0.58	0.21	0.40
	CGO-4	0.61	0.33	0.47

corded in a C-containing gas composition [184], with the range of values for the H-containing gas compositions, and the corresponding $E_a(\Omega)$ found in this study, it is seen that this $E_a(\Omega)$ is rather large. Furthermore, it does not follow the tendency of $E_a(\Omega)$ in table 4.3 where the gas composition has little to no effect. This would indicate a significantly improved structure of the cells tested in this study, when compared to the cells tested in the literature, this may be due to a larger YSZ grain size used for the electrolyte [187].

The determined E_a(TPB,Tot) are dependent on gas composition, as seen in table 4.3. Comparison between the literature values, and results from this study will therefore be primarily based on the outlet conditions as these correspond better to the CO/CO_2 gas compositions found in table 4.4. It should also be noted that different fuel electrodes have been used in the case of CO/CO_2, which were furthermore infiltrated in the case of Yue and Irvine [185].

The infiltrated cells from this study performs well across the board in comparison to the corresponding E_as found in table 4.4, while the non-infiltrated cell generally performs worse in CO/CO_2. An exception for this is E_a(TPB) for CGO-2 (1.02 eV) is slightly larger than than the cell tested by Leonide [184] (0.95 eV), while CGO-4 is still smaller (0.65 eV). It is still, however, a massive improvement when compared with the un-infiltrated cell (1.78 eV).

4.3.4 Long-term durability tests

Figure 4.7 shows the cell voltage during the long-term durability tests for the cells tested in this study. From the figure it is seen that the CGO-0 degrades faster than the infiltrated cells, where CGO-4 degrades faster than CGO-2. The drop in cell voltage during CGO-2 was caused by a gas supply issue during which operation was stopped, and the cell was left at OCV in 5% H_2 in N_2 to the fuel electrode and air to the oxygen electrode. Before restarting operation the cell underwent the start-

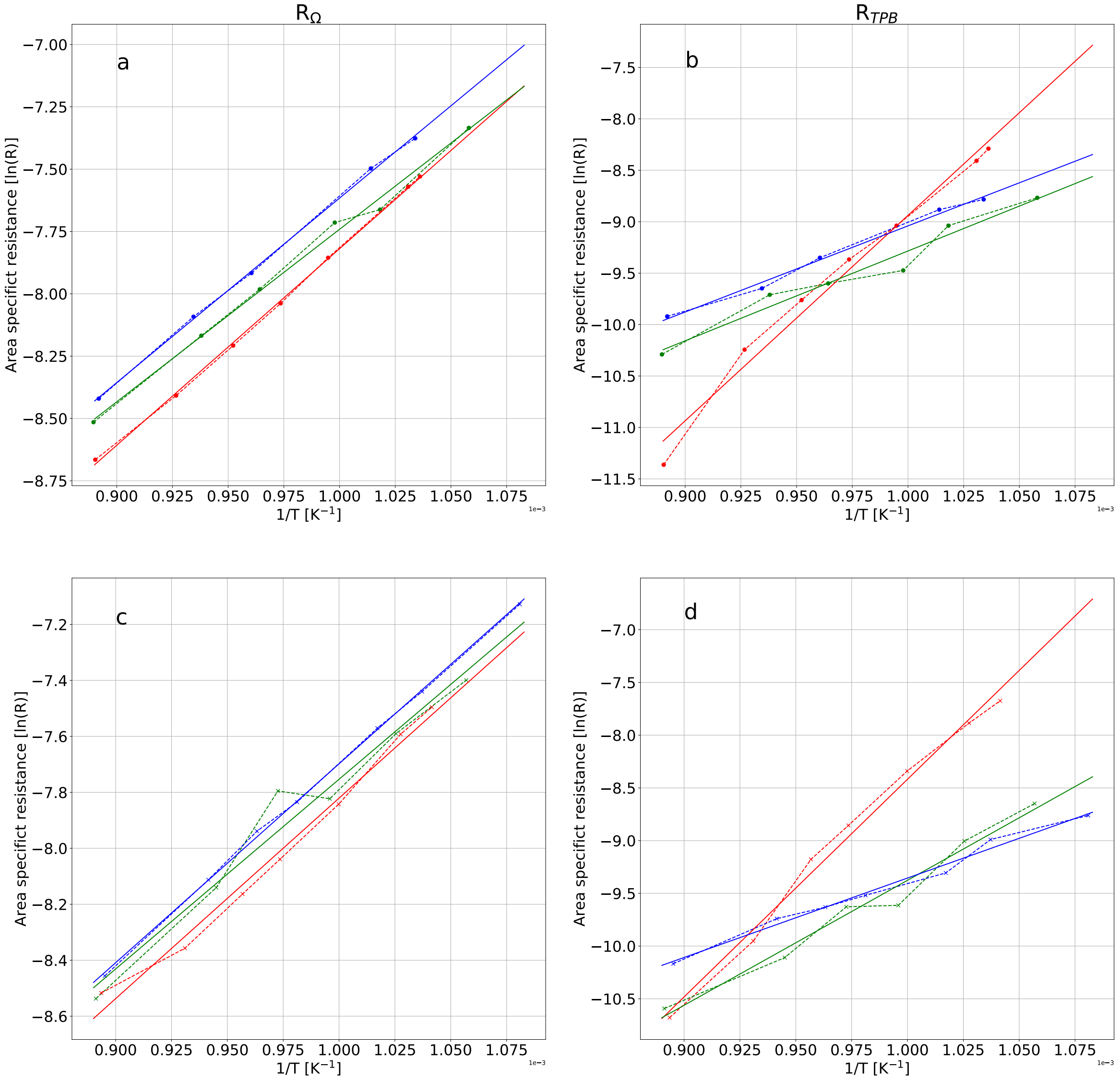

Figure 4.6: Arrhenius plots for : red - CGO-0, green - CGO-2, blue - CGO-4. Test conditions: (a+b) Gas composition corresponding to fuel electrode inlet - 10/90 CO/CO$_2$, (c+d) Gas composition corresponding to fuel electrode outlet 39/61 CO/CO$_2$, O$_2$ was applied to the oxygen electrode throughout, EIS was recorded at OCV.

Table 4.4: Activation Energies in eV found in litterature for similar resistance components as shown in table 4.3. The column ”Gas” denotes whether the E_as where determined in ”H”: H_2/H_2O or ”C”: CO/CO_2, with the ”Gas comp.” column stating the ratio between the gasses. ”Fuel elec.” describes the used fuel electrode material for the test.

Component	**E_a**	**Gas**	**Gas comp.**	**Fuel elec.**	**Source**
R_Ω	0.83-0.95	H	98/2	Ni/8YSZ	[188]
R_Ω	0.5-1.6	H	97/3	Ni/8YSZ	[189]
R_Ω	1.23	C	40/60	Ni/8YSZ	[184]
R_{TPB}	1.09	H	80/20	Ni/8YSZ	[131]
R_{TPB}	0.95	C	40/60	Ni/8YSZ	[184]
R_{Tot}	0.52-0.78	H	100/0	Ni/8YSZ	[190]
R_{Tot}	1.31-1.43	H	98/2	Ni/8YSZ	[188]
R_{Tot}	1.02-1.17	H	98/2	Ni/YST	[188]
R_{Tot}	0.57	C	30/70	LSCM/8YSZ	[185]
R_{Tot}	0.60	C	30/70	LSCM/CGO	[185]

up reduction protocol as described in the experimental chapter. This was chosen based on experience with other infiltrated cells breaking during the reduction, which was ascribed to too fast increase in flow-rate of H_2 to the fuel electrode. After one hour in H_2 the test was re-initiated. It is apparent that the performance of CGO-2 had worsened during shut-down or restarting of the cell.

Figure 4.8 shows the development in EIS over the duration of the test from: red corresponding to 0 h, to magenta depicting the last EIS during the long-term durability test. The time between each EIS is ≈50 h, and the colours correspond to the same time between the tests. The columns of the figure correspond to each test, while the rows from top to bottom are the Nyquist plots(a-c), DRT plot (d-f), and the resistances of the components comprising the ECM, plotted as function of time during the durability test(g-i). The highlighted areas in the DRT plots (fig 4.8 d-f) show where the respective elements of the ECM are expected in the EIS.

The data for the lines plotted in fig. 4.8 a-c were recorded 50 h apart, and show, similarly to fig. 4.7, that the degradation rate accelerates during the tests, though it is fastest for the non-infiltrated cell. The largest increase in the impedance across the tests occurs in the high-frequency arc. The DRT plots in fig. 4.8 d-f furthermore determines said increase being caused by RQ_{TPB}, which is the electron transfer resistance for the reduction reaction [191], which not only increases in magnitude, but also decreases in peak frequency. Another component where an increase is also seen is, $RQ_{conv.}$, which about doubles during the test, whereas RQ_{TPB} increases three to fourfold during the test. This combined loss indicates the main degradation being loss of TPB density/area, since the decreased TPB area would then experience a larger current density and polarisation, which would lead to a change in the surrounding gas composition [140].

The decrease in peak frequency for RQ$_{TPB}$ leads to the RQ$_{TPB}$ overlapping with G$_{ox}$ and RQ$_{diff}$ on its way down in frequency. This meant a risk of a partial or complete absorptions of these components, to avoid/minimise this effect, G$_{ox}$ and RQ$_{diff}$ were kept within tight boundary conditions during the fitting, with G$_{ox}$ being kept constant as it was not expected to degrade significantly in this time scale based on the results shown in fig 4.8c-f, and RQ$_{diff}$ kept within ± 2-4% of the previous result in the time series. This further avoided RQ$_{diff}$ taking too much of the RQ$_{TPB}$ on its way down in frequency, though this risks RQ$_{TPB}$ absorbing potential increases to RQ$_{diff}$ or G$_{ox}$. The peak frequency of RQ$_{diff}$ was also limited from increasing from its initial value, though it was allowed to decrease. This was done despite introducing a risk of RQ$_{diff}$ absorbing some of RQ$_{conv}$.

The impedance development of the various ECM components are shown in fig. 4.8 g-f. Here the tendency in the development of RQ$_{TPB}$ starts with a linear increase turning into a non-linear increase around 600 h. This matches the increase seen in the cell voltage for CGO-0 (fig. 4.7). From these figures it is seen that the increase of the RQ$_{TPB}$ element during the test is slowed by the introduction of CGO into the fuel electrode by comparing the non-infiltrated cell with the infiltrated ones. Comparison between the infiltrated cells, CGO-2 and CGO-4, shows that the CGO loading is only helpful up to a point, after which the performance worsens.

Table 4.5 shows the initial and final cell voltages, TPB overpotentials and carbon activities based on said η_{TPB}s for the tests in this study. The carbon activity was calculated based on η_{TPB}+EMF (908 mV in 10/90 CO/CO$_2$ against O$_2$, 750 °C). This value was used to determine the CO/CO$_2$ ratio that would give rise to said value. Finally the carbon activity was determined from the gas composition in the Boudouard reaction calculated using the thermodynamic data from the NIST database[146]. Carbon is expected in the cell when a$_C > 1$.

Based on the values from table 4.5 carbon is not expected in any of the tested cell initially, based on the η_{TPB} contribution. It is also seen that the infiltrated cells show a 59 and 30 mV lower initial η_{TPB} when compared with the non-infiltrated cell, which is slightly made up for by a larger contribution from $\eta_{conv.}$ in the cell potential for the infiltrated cells, when comparing initial cell potentials. After long-term testing, only test CGO-2 has a a$_C < 1$, whereas carbon is expected in the other cells. Comparing the two infiltrated tests, CGO-2 and CGO-4, shows a significant larger η_{TPB} for the latter. The η_{TPB}s of the infiltrated cells are 77 and 216 mV for CGO-2 and CGO-4 respectively, this is a 139 mV difference. Initially the difference between the infiltrated cells were 39 mV, which indicates a faster degradation rate and/or worse performance of CGO-4. This further shows that an optimum CGO loading exists, and that the loading of CGO-2 is closer than that of CGO-4, to an extent where the

Table 4.5: Cell voltage, determined η_{TPB}, and theoretical carbon activity for the tests in this study. The calculated values were based on the initial and final EIS and calculated using values from the NIST database[146].

	Initial			**Final**			**Observed**
	U [mV]	η_{TPB} **[mV]**	**a**$_C$	**U [mV]**	η_{TPB} **[mV]**	**a**$_C$	**Carbon**
CGO-0	1216	86	0.13	1571	458	1391	A lot
CGO-2	1171	27	0.013	1341	77	0.096	None
CGO-4	1204	56	0.040	1380	216	5.3	A bit

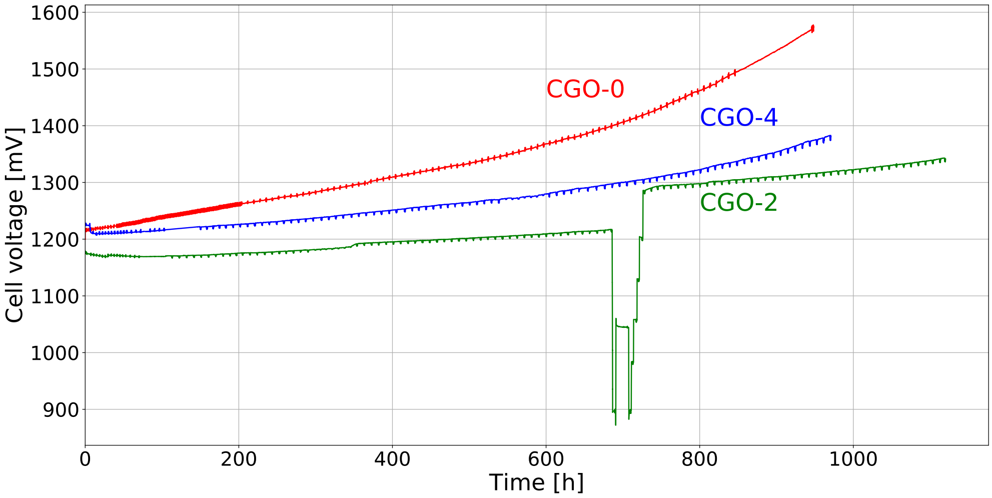

Figure 4.7: Cell voltage development over time during the long-term durability test. All tests were carried out at 0.625 A cm^{-2} with 29% fuel utilisation in 10/90 CO/CO$_2$ to the fuel electrode, O$_2$ to the oxygen electrode at 750 °C. Red - CGO-0, green - CGO-2, blue - CGO-4.

CGO-2 cell still performed better after what likely is loss of contact during the restart, as seen in fig. 4.7, though this might also have lead to a less reductive atmosphere. A sudden increase in impedance/resistance is seen across the figures for CGO-2 (fig. 4.8 b,e,h). This was caused by restarting the test as discussed previously. It is seen that the impedance of all components increases including R$_\Omega$ which indicates loss of active area. While visual inspection of the cell after the test ruled out large cracks of the cell, slight cracks leading to loss of contact might have occurred.

4.3.5 Carbon Deposition in the fuel electrode

Figure 4.9 shows the Raman spectra recorded at the fuel electrode/electrolyte interface for the tested SOECs post-operation. The spectra were recorded at the fuel inlet as carbon previously has been shown to be most prevalent here, for this type of cell [132]. The intensity (y-axis) has been normalised to the signal at 620 cm^{-1}. Four

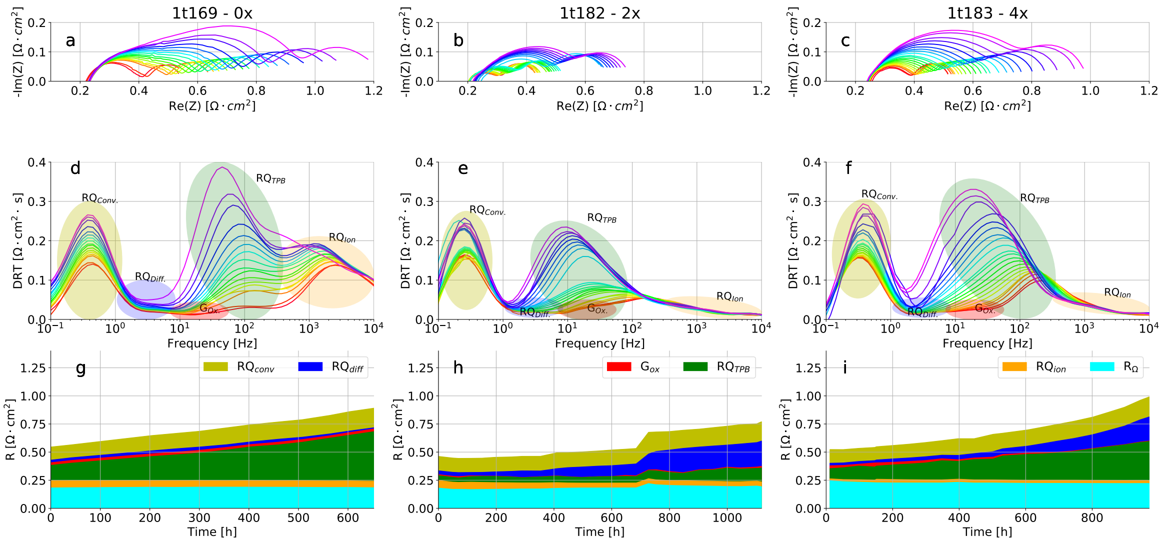

Figure 4.8: Performance during long-term durability tests of CGO-0 (a,d,g), CGO-2(b,e,h), and CGO-4(c,f,i). a-c) Nyquist plots of EIS recorded during the test, colours go from red (0h) to magenta (end). d-f) DRT plots of EIS recorded during the test, colours go from red (0h) to magenta (end). Highlighted areas are the regions assigned to the various components of the ECM: R$_{\Omega}$-RQ$_{ion}$-RQ$_{TPB}$-G$_{ox}$-RQ$_{diff.}$-RQ$_{conv.}$. g-i) Development in the total and relative resistances for the ECM during the long-term durability test.

signals, are seen in the figure. The first peak from the left is located at 615 cm^{-1} and is is assigned to YSZ [141], and is marked as such in the figure. The second peak is located at 1345 cm^{-1} and corresponds to disordered graphite [142], it is denoted as "D" in the figure. The two peaks denoted "G$_1$" and "G$_2$" are located at 1585 cm^{-1} and 1610 cm^{-1} respectively. Both of these peaks have previously been assigned to the ordered graphite structure. The G$_1$ and G$_2$ peaks differ in the structural information contained within them, as they correspond to 2D and 3D dimensional structures respectively [143]. Presence of the G$_2$ peak has previously been linked with the presence of carbon nano tubes (CNTs) by Duesberg et. al. [142].

Figure 4.10 shows SEM micrographs of the tested cells: a) CGO-0, b) CGO-2, and c) CGO-4 post-mortem. Tubular growths are seen in the cell (CGO-0) in fig. 4.10 a). These are identified as CNTs based on the presence of the the G$_2$ peak seen in fig. 4.9, and by the fact that Ni is a known catalyst for CNT formation [192]. Furthermore, CNTs were previously identified in the fuel electrode of SOC by Tao et. al. [69]. The micrograph for CGO-2 after testing (fig. 4.10 b) is similar to the micrograph for the non-tested cell with the approximately same loading (fig. 4.2 b)) meaning that the carbon is absent and that the cell backbone is covered by the infiltrate. The absence of carbon is backed up by the Raman spectrum for the cell. The carbon shown in the micrograph for test CGO-4 (fig. 4.10 c)) looks like a a net, or multiple short tangled up CNTs, similar to some of the carbon observed for 06HU-2 in chapter 3, although

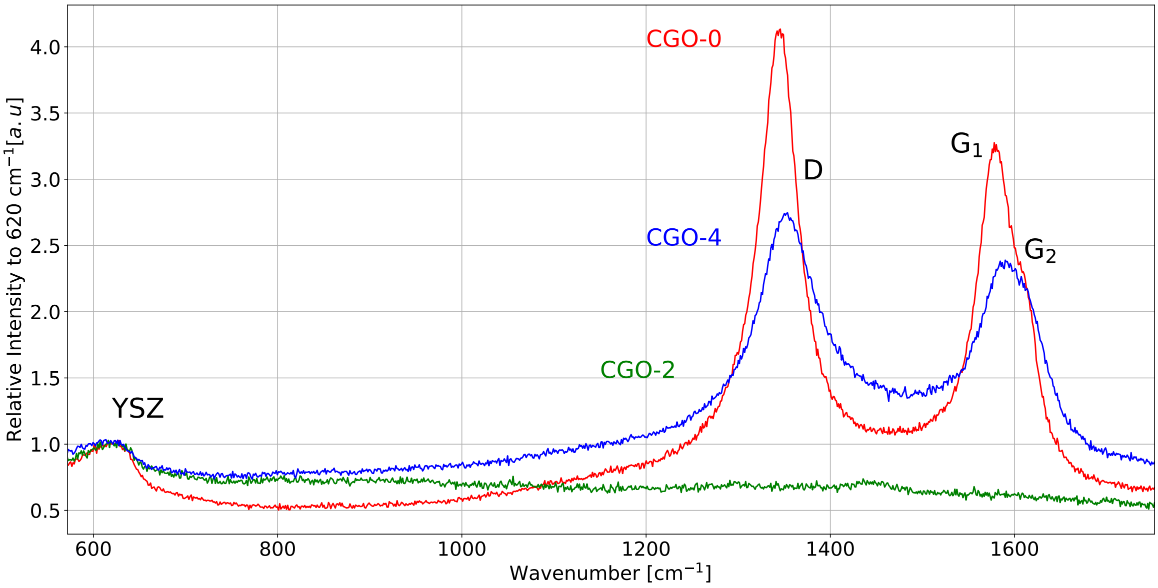

Figure 4.9: Raman spectra measured at the fuel gas inlet, fuel electrode/electrolyte interface. Red - CGO-0, green - CGO-2, blue - CGO-4.

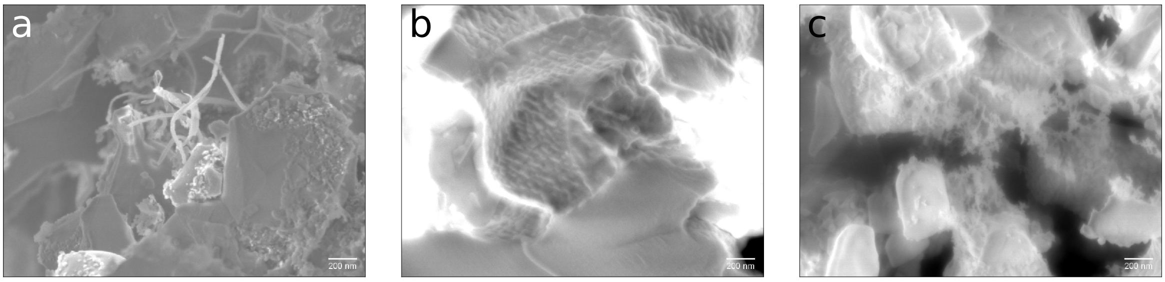

Figure 4.10: SEM micrographs recorded post-mortem of the tested cells: a) CGO-0, b) CGO-2, and c) CGO-4.

to a much larger extent for CGO-4 which is also evident from the Raman spectrum. Comparing values in a$_C$ found in table 4.5 to the post-test Raman and SEM characterisation, the values are found to be consistent with the expected presence of carbon in the fuel electrode. Carbon is hence observed at a similar η_{TPB} despite the introduction of CGO, as seen in the previous chapter for non-infiltrated cells.

4.4 Conclusion of Chapter

The results achieved through this study shows that the addition of CGO to the fuel electrode does not only improve the durability as expected, but also improves the performance. The results (fig. 4.7) show that an optimum CGO loading exists where the catalytic activity of the infiltrate makes up for the decreased porosity, and hence increased diffusion resistance. The results of this study have, however, also shown that while CGO increases the durability, it is very limited when compared to the target lifetime of 5-10 years. It is however suspected that a significant part of the initial degradation is due to gas impurities as seen in the previous chapter 3, since the degradation trend is similar, so too is the onset for carbon deposition. This likely means that the increased durability is mainly due to the impurity tolerance of CGO [171], though smaller for SOEC operation than for SOFC. It would therefore be necessary to redo the tests with gas cleaning to get improved insight into the cell performance and degradation thereof without the increased degradation caused by impurities.

The results suggests that the CGO infiltrate has not affected the threshold of carbon deposition, which was identified to be around a cell voltage of 1370 mV or η_{TPB} of 190-200 mV as seen when comparing the values/calculations in table 4.5 and the presence of carbon post-operation (figure 4.10 and 4.9). Further improvements regarding carbon deposition suppression would also be expected if one were to use a 1:1 Ce:Gd ratio, since this would lead to a minimisation of the Ce^{3+}-Ce^{3+} pairs in the structure, and hence the formation of carbon precursors [98].

Chapter 5

Characterisation of Microstructural and Compositional Changes during CO_2 electrolysis including the effect of CGO infiltration

This chapter pertains to the microstructural changes that occured during the tests described in the two previous chapters. The number of SEM micrographs have been limited in this chapter due to the amount of space they take up, though representative SEM micrographs have been included. The reader is referred to appendix D for a more extensive collection of micrographs for the samples discussed in this chapter. The reader should also be aware that details in the micrographs are lost upon printing, and therefore the best experience is achieved by referring to the micrographs in the digital version.

This chapter has been split into two topics: Microstructural changes characterised via SEM, and compositional changes of the YSZ support characterised by Raman spectroscopy.

5.1 Introduction

5.1.1 Microstructural changes during SOEC operation

Ni coarsening and migration have previously been described as an important phenomenon for SOC degradation, and is one of the main challenges to overcome for the technology to achieve a widespread use [193–195]. There are different hypotheses in the literature why this occurs [59, 64, 196]. The two phenomena: coarsening and migration, seem to be two separate mechanism [195], though they are interlinked as when Ni particles coarsens due to detachment from YSZ it also facilitates the Ni migration process.

A recent study by Shang et. al. [195] compared results for three SOECs in which coarsening occurs even for a cell that did not experienced operation under current, while migration of Ni only occured during electrolysis operation. Faes et. al. [197] has described the Ni particles to coarsen due to Ostwald ripening. Monaco [196] suggests the formation of oxide-vacancies ($V_O^{\bullet\bullet}$) in YSZ leading to Ni-YSZ detachment, with the fuel electrode overpotential dictating the rate of detachments through a definition relating $V_O^{\bullet\bullet}$ and fuel electrode overpotential. Breakage of Ni-YSZ interfaces would, when Ni minimises its surface energy leads to spherical particles, decreasing the chance for reattachment [58]. This effect is increased in the presence of impurities such as Si which can form as a surface film inhibiting continued Ni adhesion [175].
Migration of Ni away from the electrolyte has been shown to correlate with a decrease in cell performance, furthermore it occurs to a much larger extend during SOEC operation compared with SOFC operation [59]. Jiao et. al. [198] showed that the wetting angle of Ni is dependent on the local pO_2. Trini et. al. [59] have suggested a mechanism of migration based on the observations by Jiao et. al. [198], where a low wetting angle further from the electrolyte (caused by a higher pO_2), when compared with the operational area near the electrolyte would lead to migration of Ni towards the fuel electrode support. This is in opposition to the hypothesis by Mogensen [58], where volatile Ni species such as $Ni(OH)_x$ is the lead carrier of Ni during steam electrolysis, though this does not account for migration during CO_2 electrolysis where the volatile species are still unidentified [64].

The microstructure of the cells tested in the previous chapters have been analysed by SEM and EDS to determine the effects of the operational on microstructural changes. Furthermore the pore fractions of the SOECs have been quantified and compared with various test parameters, such as η_{TPB}, to determine whether or not a dependency exist.

5.1.2 YSZ degradation caused phase transformation

The SOECs tested during this project have been planar fuel electrode supported SOCs, with the support consisting of Ni/3YSZ. Using a mechanical support with similar composition as the active electrode and electrolyte (8YSZ) means that the thermal expansion coefficients (TECs) are expected to match, meaning less/no heating induced strain is expected at operation temperature due to TEC-mismatch [199]. In addition to its inherent mechanical toughness, 3YSZ can undergo transformation toughening [200]. Transformation toughening in YSZ means that it undergoes a phase transformation from tetragonal 3YSZ (YSZ_t) to monoclinic YSZ (YSZ_m) un-

der mechanical stress.
This would mean that if a small crack is formed the 3YSZ will undergo the 3YSZ$_t$ →3YSZ$_m$ transformation, where the formation of 3YSZ$_m$ creates a crack-closing compressing stress around the crack, hence impeding crack formation.
The transformation is possible due to 3YSZ$_t$ being metastable below the sintering temperature, the cause of which is the addition of Y_2O_3 as a stabilising agent, in addition to creating oxygen vacancies for improved oxygen-ion conductivity [200].
The phase transformation is, however, disadvantageous if it occurs spontaneously over a substantial part of the structure in cases where it occurs without the room a crack gives for expansion. Instead it might by itself strain the structure, and lead to the formation of cracks [201]. This could lead to catastrophic failure if these cracks propagate through the electrolyte, or the support disintegrates. Studies of YSZ show only minor rates of degradation when aged at conditions reflecting the operation condition of steam electrolysis ($H_2O/H_2 \approx 800$ °C) [174]. It is hence expected that SOECs operated for electrolysis will not show a large degree of thermal ageing, and what 3YSZ$_m$ would be detected will be due to mechanical stress.
This assumption would change for SOECs modified by wet infiltration. Here, phase transformation of 3YSZ is expected to occur due to low temperature degradation (LTD) as described by Lin et. al. [202]. LTD occurs within the range 50-400 °C, and is worsened in humid atmosphere [201], which resembles the conditions during infiltration of CGO as described in the previous chapter. 3YSZ$_m$ could thus be expected to be present in the infiltrated SOECs.

To test this hypothesis the fuel electrode support of the SOEC were long-term tested for CO_2 electrolysis with or without an infiltration treatment have been probed by Raman spectroscopy to analyse the relative amounts of 3YSZ$_t$/3YSZ$_m$.

5.2 Experimental

5.2.1 Microstructural Reference

A microstructural reference of the SOEC microstructure was established. A SOEC with the same specifications as the ones described in previous chapters was heated and reduced (chapter 2 section 2.5), whereafter it was cooled in 5% H_2 in N_2 to keep the Ni in a reduced state. This cell is here on forward referred to as SEM-ref

Table 5.1: Overview of SOECs studied with SEM. LTT: Long-term test

Test	**Internal reference**	***i*** **[mg cm^{-3}]**	**Utilisation [%]**	**CGO load [mg cm^{-3}]**	**Duration of LTT [h]**
04HU	5test139	0.375	58		1035
05HU-1	1test181	0.500	58		991
05HU-2	1test187	0.500	58		735
06HU-1	5test126	0.625	58		254
06HU-2	5test127	0.625	58		192
06LU-1	1test169	0.625	29		949
08LU	5test129	0.750	29		566
CGO-2	1test182	0.625	29	127	1080
CGO-4	1test183	0.625	29	224	973
SEM-Ref	16test78	0.000	0		0

Table 5.2: Overview of SOECs analysed with Raman spectroscopy. ”Cycles” refers to the number of infiltration cycles with CGO.

Test	**Internal reference**	**CGO Load [A cm^{-2}]**	**Cycles**	**Time T>650 °C [h]**
Ref	2t153			285
06HU-1	5t126			661
06LU-2	5t128			1221
I-Ref	1t174	112	2	176
CGO-2	1t182	127	2	1285
CGO-4	1t183	224	4	1199

Test overview

Table 5.1 shows an overview of the SOECs analysed using SEM, their test conditions, and whether or not they were infiltrated with CGO and how much. Naming convention: Current density rounded to one decimal + CO_2 utilisation e.g. the sample 06HU was tested at 0.6(25) A cm^{-2} with high CO_2 utilisation (58%). Low utilisation corresponds to 29%. CGO infiltrated cells were tested similarly to 06LU-1, and was infiltrated 2 and 4 times with a 1 M CGO-precursor solution respectively. For further information on specifications and the infiltration procedure the reader is referred to the two previous chapters (chapter 3 and 4).

Table 5.2 shows an overview of the SOECs analysed using Raman spectroscopy, along with the same information as above. Two references are seen in the table, one infiltrated: ”I-Ref”, and one not: ”Ref”. I-Ref was infiltrated as described in chapter 4, but only aged for a short period of 180h (the test was terminated during the initial characterisation due to a CO being detected in the rig, it was hence not exposed to a long-term test). Ref underwent the initial characterisation, after which it was cooled.

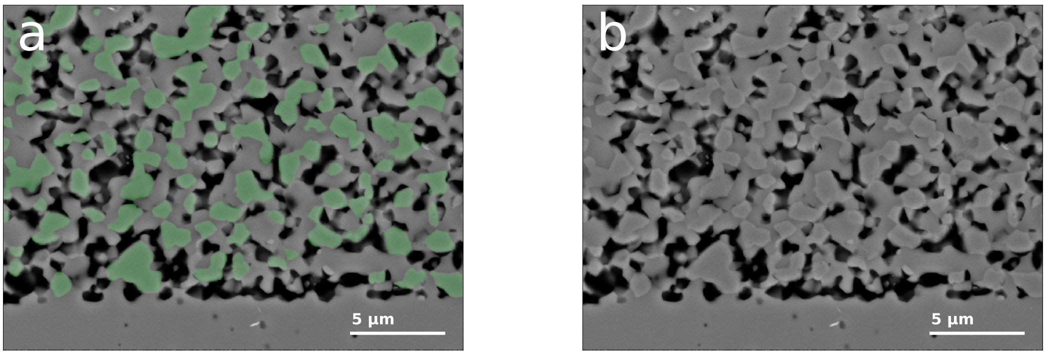

Figure 5.1: Example of a polished cross section SEM micrograph. a) Micrograph with Ni particles highligted in green. b) Original micrograph.

5.2.2 Polished cross section SEM

Pieces of SOECs tested in CO_2 electrolysis operation (chapter 3 and 4) were embedded in epoxy resin (EpoFix™) and analysed using a Zeiss Ultra FE-SEM, as described in chapter 2 section 2.3.

The pores and Ni particles was quantified using the method described in chapter 2 for the active electrode in the range 0-4μm from the electrolyte.

Raman spectroscopy

The fuel electrode support of tested and reference SOECs was investigated using Raman spectroscopy as chapter 2 section 2.2. The time for each acquisition was 3x30s.

5.3 Results & Discussion - Microstructural Changes

5.3.1 Microstructural changes along the direction of the fuel gas flow within an individual cell

Figure 5.1 shows the polished cross section of an embedded SOEC. The micrographs contains three phases: The pores which are ”transparent” allowing for a depth of view until they turn black), along with two grey phases YSZ and Ni. The Ni particles have been highlighted with a green overlay in figure 5.1 a), whereas the b) is the original.

Figure 5.2 shows SEM micrographs of 05LU-2 (a-c) and SEM ref (d). An example of the transparent pores are illustrated with the yellow circle in b). The Ni particles can furthermore be distinguished from the YSZ since it seems to be on top of the YSZ, furthermore some of the Ni particles have scratches in them from the sample preparation.

The area highlighted by the cyan ellipse in fig. 5.2 a) shows two Ni particles detached from the YSZ framework. The highlighted area in the red circles have a shape with corners indicating Ni particles once were located there, though it detached during the test [76]. It is hence not unlikely that the particles in the cyan area would have migrated away if test 05LU-2 been allowed to continue. Figure 5.2 a) and b) were recorded at the part of the electrode experiencing a current load, a) near the fuel gas inlet and b) near the outlet, while c) was recorded at a part of the cell without oxygen electrode contact layer, meaning that it did not experience any current. The SEM micrograph in fig. 5.2 d) was recorded for SEM-ref for which no long-term testing occurred. The quantitative analysis of the micrograph shows that the phase fraction of percolating Ni is 17% and 20% at the inlet (a) and outlet (b). This means that Ni content is lowest at the inlet where other Ni-YSZ detachments are seen along with multiple locations where Ni seems to have been located before migration. The outlet b) has experienced a slightly lower loss of Ni. The quantitative analysis of the Ni-particles also shows an $\approx$1.5x fold increase in average particle size between inlet and outlet with respective values of 1.09 and 1.58 μm.

A smaller loss of Ni is expected for the part that has not been under current load (c+d), though this has not been quantified. The expectation of the comparison of c) and d) one would expect a higher degree of coarsening of the Ni in c) due to its 1000+ h at operation temperature compared with SEM-ref's <100 h. While the amount and particle size of Ni seems too similar, the Ni particle shapes of some particles in d) is slightly less rounded (sharper edges) than for the ones in c). The difference in particle shape is even larger when comparing d) with the parts of 05LU-1 which has experienced current (a+b). The particle size is furthermore larger for a+b compared with c+d, indicating the effect of current, in agreement with the observation by Mogensen et. al. [64].

Based on the difference in the fraction and average particle size of the percolating Ni it is expected to see the observe most of the microstructural changes in SOEC is observed at the fuel gas inlet. For this reason SEM micrographs of the inlet will be used for the comparison between microstructural changes in the tested cells for this chapter.

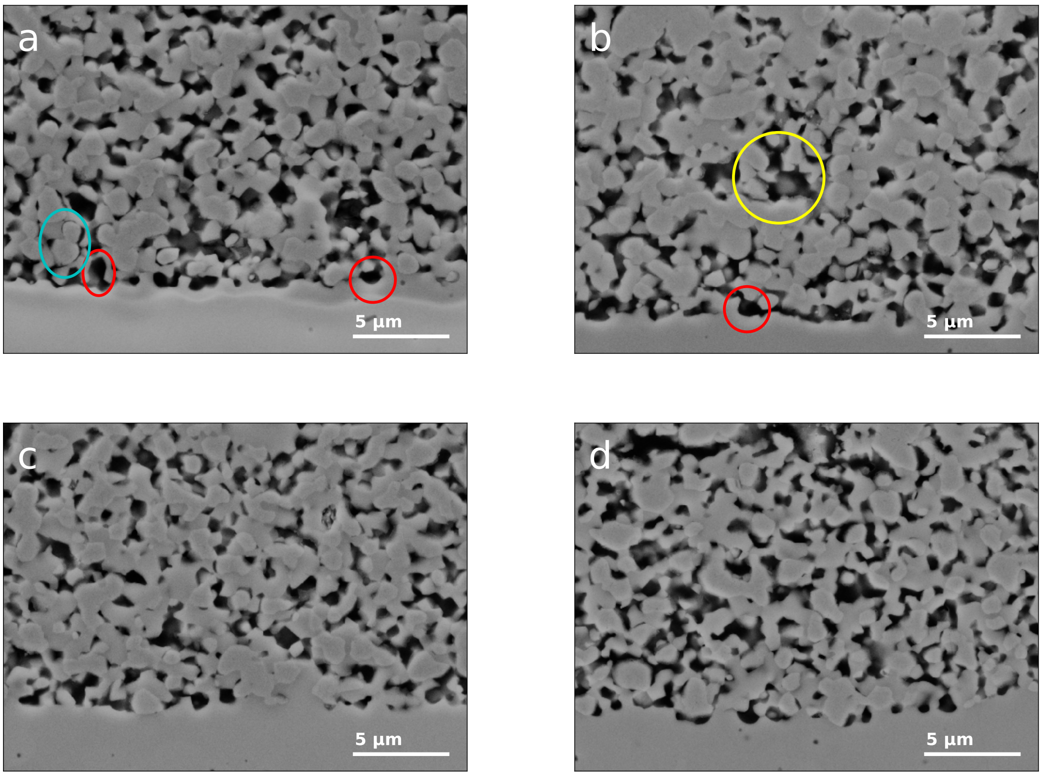

Figure 5.2: SEM micrographs 05LU-1 at the inlet a), outlet b), c) part without oxygen electrode contact layer. d) SEM micrograph of SEM-Ref. Contrast difference of electrolyte in a) is caused by charging.

5.3.2 Microstructural changes in non-infiltrated SOECs as effect of operating parameters

Figure 5.3 shows the SEM micrographs recorded at high SEM acceleration voltage for the four non-infiltrated samples a) 04HU, b) 08LU, c) 06LU-1, and d) 06HU-1. The micrograph for 04HU (a) shows an insignificant difference in microstructure when compared with SEM-ref (fig. 5.2 d), indicating it has been operated in a safe manner in regards to microstructural degradation. The SOECs having been operated at higher current densities (b-d) does however show considerable changes. A quantitative comparison of the Ni particle size across the samples ranks them in the following order 04HU<08LU<06LU-1≪06HU-1. While the Ni coverage in the active part of the electrode follows the order 04HU<08LU<06HU-1$\lesssim$06LU-1. The ordering coincides with the η_{TPB} found in the previous chapters (The results are repeated in table 5.3 in a later section). This also corresponds well with the hypothesis by Monaco [196], whom theorise that the rate of coarsening is dependent on η_{TPB}. In this hypothesis the Ni detaches from YSZ through the breakage of Ni-oxide bonds, due to the formation of oxygen vacancies in YSZ for which the concentration is based on η_{TPB} [58, 125, 196]. Whether it being the hypothesis of Monaco being true or not, the coarsening seems to follow the consensus among SOEC researches that η_{TPB} is somehow involved, either by itself [59], in defining the local pO_2 [203], or an effect of the application of current [195]. The same is however not the case for the presence of Ni closest the active electrode, where 06HU-1 (fig 5.3 c) has more Ni than is seen for 06LU-1 (fig 5.3 d). This indicates that while Ni coarsening and migration might be interconnected, one or more parameters exist that are unique for either.

One explanation for the significant larger Ni particles in 06HU-1 (fig 5.3 d) would be Ni-YSZ detachment due to the formation of a layer of impurities at the particle boundary [64]. This is likely due to the high η_{TPB} reached during the test, which is high enough (same local pO_2 required as for reduction of ZrO_2 [204]) to expect reduction or partial reduction of Al_2O_3 impurities in Ni to segregate [205]. The inclusions in the Ni particles of the same SOEC were confirmed to contain Al using EDS, the spectra of which which can be found in appendix D. It is worthwhile noting that the micrographs of 08LU (fig 5.3 b and appendix D) shows the largest amounts of Ni-YSZ detachments, some of which has been highlighted with red arrows. It has not been possible to find a suitable explanation for this since the reached η_{TPB} was rather low, and it was stopped before 600 h. It was however the test carried out at the largest current density, a parameter that by itself has not shown to be a major factor in the microstructural degradation.

Figure 5.4 shows the SEM micrographs recorded at low EHT using the technique by Thydén [118], to enable analysis of the percolating network of Ni for the four non-infiltrated samples a) 04HU, b) 08LU, c) 06LU-1, and d) 06HU-1. The white parts of the micrographs is the percolating Ni, the light grey - non-percolating Ni, dark grey - YSZ, and black - Pores. White lines are observed at the edges of YSZ particles near the electrolyte in fig. 5.4 c). These lines are very likely due to charging effects in the epoxy sample due to it being uncoated. While it is possible to determine the lines in the micrograph being a product of the charging due to the shape it is more difficult to distinguished whether the small round particles seen in the micrographs are a product of the charging effect or if it is in fact a Ni particle. This leads to an increase in the uncertainty of the quantitative results from the Ni-particle analysis.

Comparing the micrographs in figure 5.4 it is seen that the tendency for the amount of percolating Ni through the structure follows what is seen for particle size in figure 5.3 (Though with the opposite sign). This is in line with the hypothesis in a previous work by Mogensen et. al. [64], where the Ni-Ni connections are broken as part of the spherication of the Ni particle to achieve the lowest surface energy. Furthermore, in all micrographs but c) the non-percolating Ni is still present near the electrolyte, whereas it is not case for 06LU-1 where no/very small amounts of non-percolating Ni is observed near the electrolyte. This observation/difference does not

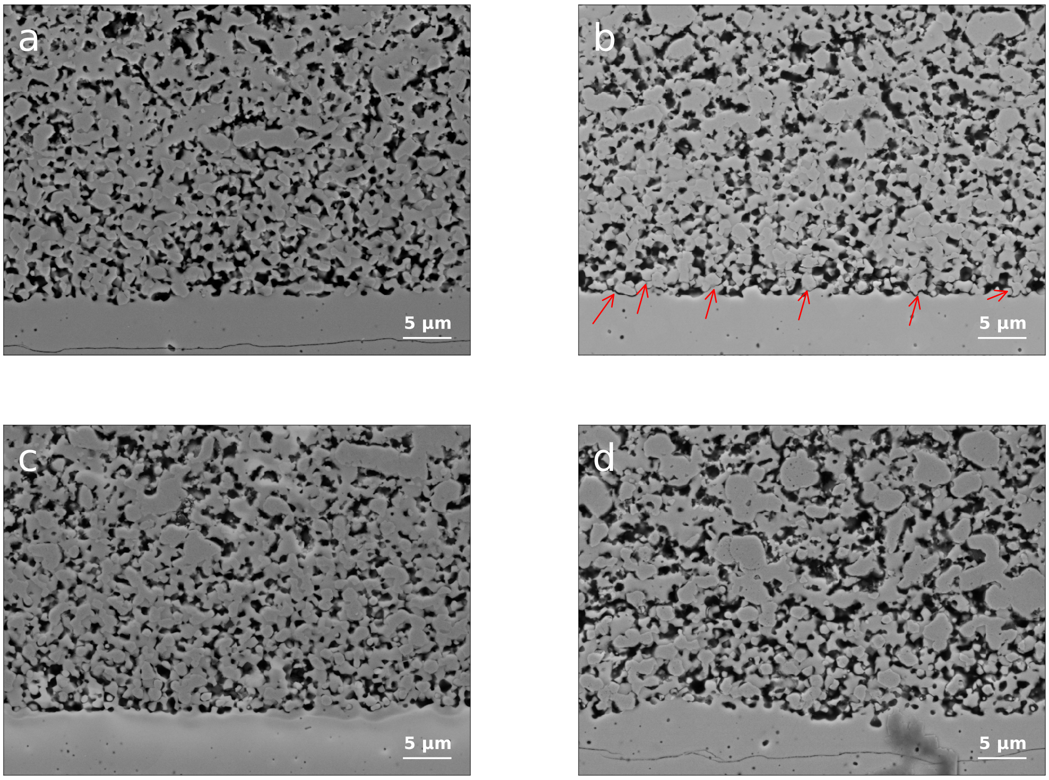

Figure 5.3: SEM micrographs of a) 04HU, b) 08LU, c) 06LU-1, and d) 06HU-1. Contrast difference of electrolyte in c) is caused by charging.

seem to be caused by the charging or slightly worse contrast, since particles of non-percolating Ni are observed in the support. Using the colour of non-percolating Ni, a few particles can be found in the active electrode. In addition to having retained most of its percolation, sample 04HU (fig 5.4 a) the percolation that have been lost looks to be evenly distributed along, and close to the electrolyte. The losses for the other SOECs are more localised and seem to reach deeper into the electrode. This might be caused by degradation of local TPBs, which then escalated to nearby TPBs.

The microstructural degradation for the non-infiltrated cells generally seems to be worst for the SOECs having experienced the harshest test conditions, which are in line with previous studies [20, 23, 195, 206]. This has lead to both damage of the Ni-Ni and Ni-YSZ connections, with the latter being of greatest importance since these defines the TPBs.

5.3.3 Microstructural changes in infiltrated SOECs

Figure 5.5 shows the microstructure parts of CGO-2 at the inlet with (a+b) and without (c+d) oxygen electrode contact layer. Comparison of the parts of CGO-2

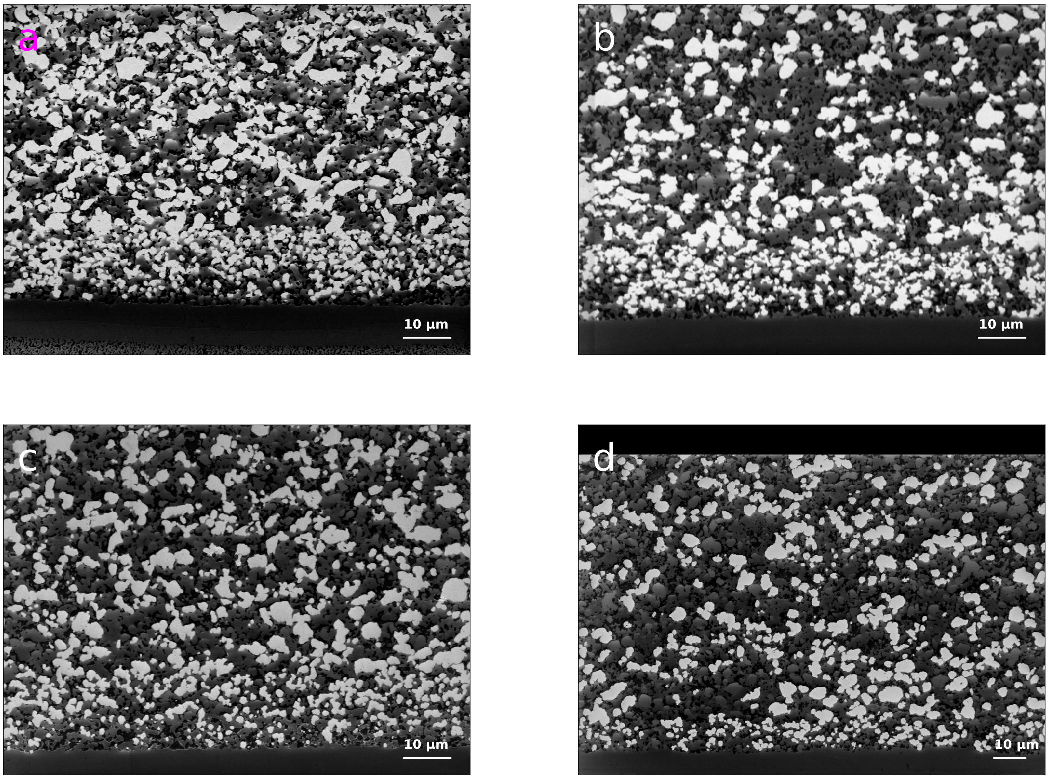

Figure 5.4: Low voltage SEM micrographs of a) 04HU, b) 08LU, c) 06LU-1., and d) 06HU-1. Black: Pores, Dark grey: YSZ, Light grey: Non-percolating Ni, White: Percolating Ni. Black box in top of d) has been added digitally for alignment purposes.

which have(a+b) and have not (c+d) experienced a current load shows only minor differences concerning relocation of Ni, with only a few Ni-YSZ detachments observed in a), and an even distribution of Ni particles of differing sizes including small ones. The main cause of degradation in CGO-2x is breakage of the YSZ network which can be seen for both areas of the SOEC as fracture lines through the YSZ. The breakage is slightly worse for the operational area (b) of the SOEC, it is however also seen for the non-operational area (d) to a lesser extent. Cases of high concentration of Ce can be identified by being slightly lighter in colour. This is an effect of the background electrons being picked up by the secondary electron detector due to its location in the electron microscope.

Figure 5.6 shows the microstructure of CGO-4x at the inlet with (a+b) and without (c+d) oxygen electrode contact layer. The microstructure of CGO-4x is damaged to a very large extent. Comparison between the operational (a+b), and non-operational (c+d) parts shows that the damage for the operational part extends out into the electrode support, while the damage for the non-operated part is confined to the outer area of the active electrode. The high magnification micrographs (b+d) show, similar to those of CGO-2x, that the YSZ is the damaged structural element though to a much larger extent for CGO-4.

The infiltrated SOECs did both leak to some extent which is indicated by the edges of some of the Ni particles being less sharp and taking on a ”fluffy” characteristic. The leak could hence have lead to redox cycling of the Ni-particles, where a repeated expansion/contraction could have lead to breakage of the YSZ structure. This is however deemed unlikely to have affected the Ni particles since similar observations would then have been expected for the non-infiltrated SOEC which may have leaked as well, which is not the case. Furthermore, the shape of the Ni-particles in the infiltrated cells are less rounded than those of the non-infiltrated cells. This is significant as rounding of the particles would be expected during redox cycling due to surface energy minimisation. Lastly the Ni would be expected to expand into the pores. The main difference between the infiltrated and non-infiltrated SOECs would be infiltration of CGO, this is hence speculated to be play a part in the damage to YSZ. The damage to the YSZ does not alone explain the absence of CGO and Ni in the micrograph. The absence of the YSZ and Ni in the structure is speculated to have been caused during preparation of the sample where pieces of the weakened structure may have been scratched away during grinding/polishing. Since no significant differences is observed between fig 5.6 b) and d). It is also noted that the microstructural damage in the inner part of the electrode (2-3μm closest to the electrolyte) looks slightly less severe than the rest. This damage is present across the cell (see appendix D)

Figure 5.7 shows the low voltage in-lens SEM micrographs of the infiltrated SOEC. The percolating Ni network is very extensive in CGO-2x (a), while it is damaged for CGO-4x (b). The damage to the percolating Ni in CGO-4x (b) is notably in the outer part of the active fuel electrode, whereas Ni have retained its percolation closest to the electrolyte. This is similar to the microstructural damage seen in the high voltage micrographs in figure 5.6. This might indicate that the loss of percolation was caused as a part of the breakage of the YSZ structure.

Figure 5.8 and 5.9 show EDS mappings of CGO-2x and CGO-4x respectively. It is seen that the microstructure and elements in the layered image (a) matches quite well with the corresponding SEM micrographs in fig. 5.5 and 5.6. Three elements have been included as subfigures: Ce (b), Ni (c), and Al (d). Ce was included as it is the main identifier of the infiltrated CGO. The Ce is generally seen in the whole electrode, along with a bit in the electrolyte. Ce is furthermore observed to accumulate in local areas, which are in line with the observation in the SEM micrographs for the infiltrated cells. This coarsening could be a cause for the breakage of the YSZ structure due to its larger coefficient of thermal expansion [207, 208]. The Ni in fig. 5.9 shows to be similarly affected by the microstructural damage of CGO-4x as seen by SEM (fig. 5.6 and 5.7 b). Despite the YSZ damage the Ni particles do not seem coarsened and they are evenly distributed, indicating that infiltration by CGO

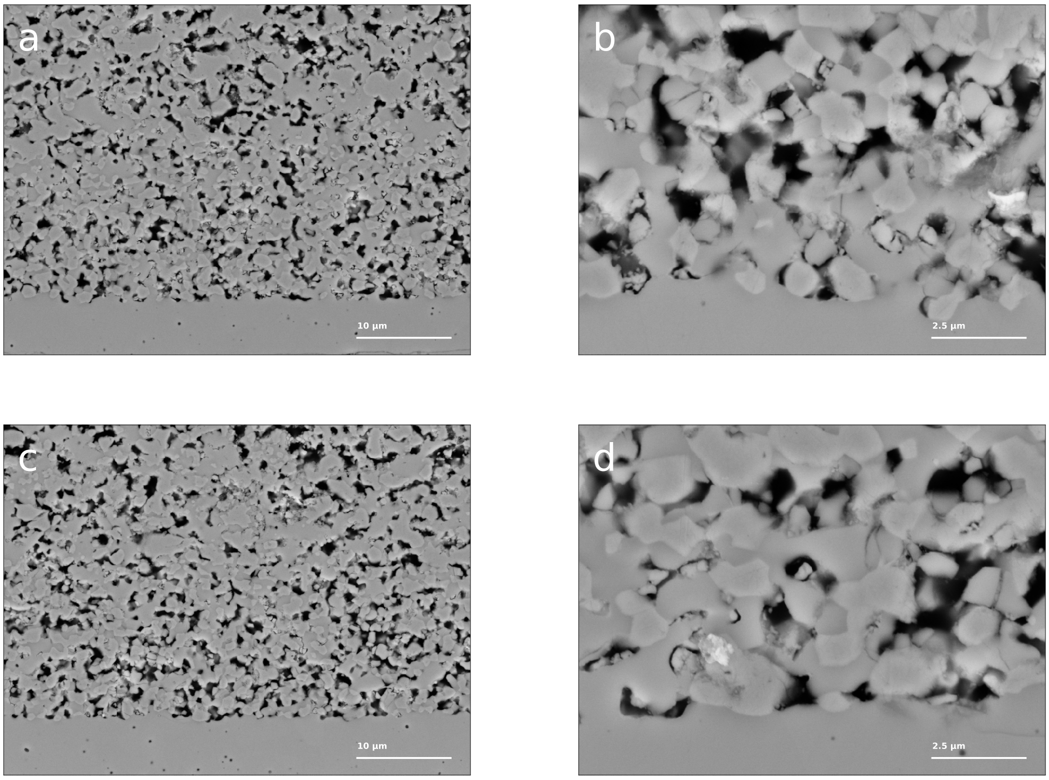

Figure 5.5: SEM micrographs of 2x CGO infiltrated SOEC at the inlet with (a/b) and without oxygen electrode contact layer (c/d).

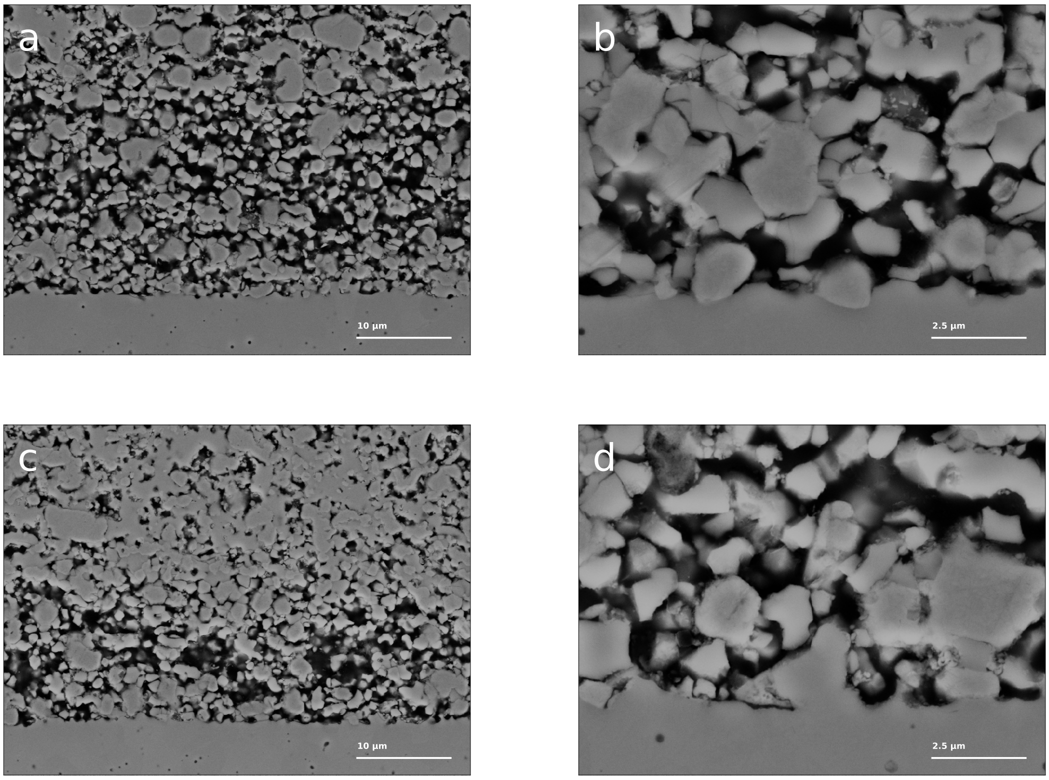

Figure 5.6: SEM micrographs of 4x CGO infiltrated SOEC at the inlet with (a/b) and without oxygen contact layer (c/d).

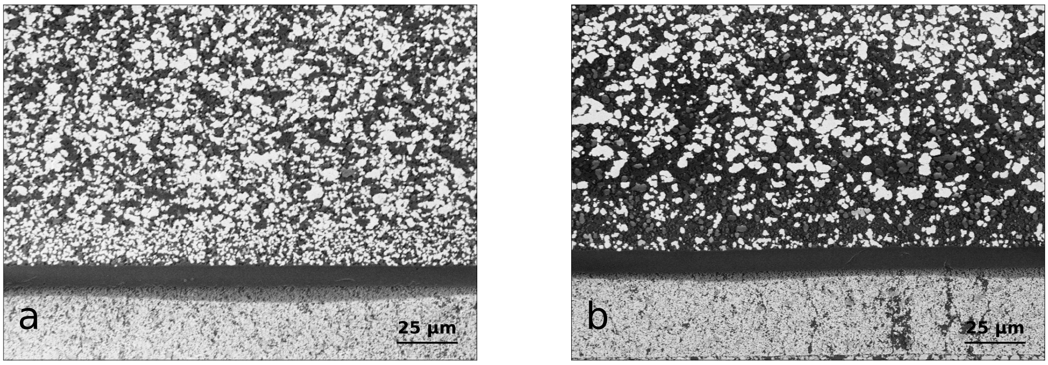

Figure 5.7: Low voltage SEM micrographs of a) CGO-2x and b) CGO-4x. Black: Pores, Dark grey: YSZ, Light grey: Non-percolating Ni, White: Percolating Ni.

may mitigate Ni migration. This is even more so the case for CGO-2x where Ni is present throughout the span of the fuel electrode (fig. 5.8 c). The location of Al (fig. 5.8 d) in the fuel electrode is observed to be rather random. Its presence is due to Al_2O_3 being a common sintering aid during the manufacturing of SOC [209]. The observation of Al in the EDS mappings seen in this chapter is characteristic of all of the SOECs (see appendix D), the impact of which has not been investigated further in this project.

5.3.4 Comparison between infiltrated and non-infiltrated SOECs

Porosity and retention of Ni Comparing the microstructure of CGO-2 (fig 5.5 and 5.7) and non-infiltrated (30-39%) (fig 5.3) SOECs shows that the porosity is lower for CGO-2 (24%) as expected due to infiltration. With a average porosity 0-4μm from the electrolyte for the non-infiltrated cells 34%, whereas it is only 26% for CGO-2 (both numbers have been corrected using the method described in section 5.3.5). What it also shows is, that the Ni has been retained to a larger extent in the infiltrated SOEC, in addition to the Ni particles seemingly being smaller by qualitatively looking at the SEM/EDS data. Though this is also the case for the quantitative analysis of the Ni particles 0-4μm from the electrolyte where the average Ni particle size for is 0.46 μm^2 and 0.72 μm^2 for CGO-2 and non-infiltrated cells (average across all cells) respectively. This indicates that the addition of CGO leads to increased retention of Ni. While not favouring any of the hypotheses to the mechanism of Ni migration, it is in accordance with most of them, e.g. that for Trini et. al.'s [59] where the wetting angle of Ni at low pO_2 would lead to coarsening and migration. Infiltration with CGO would, however, be expected to counter this effect due to improved Ni wetting through a lowered interaction energy [58, 210]. The increased Ni-YSZ wetting will also counteract the spherification of the Ni particles occuring as one of the first

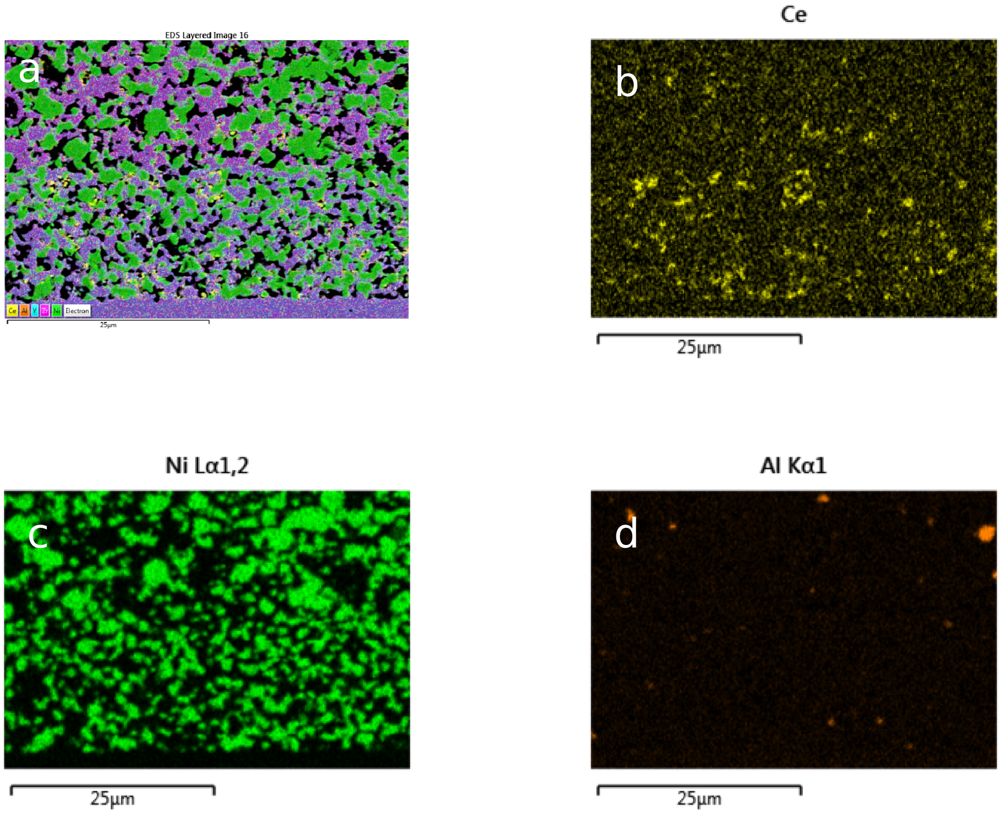

Figure 5.8: EDS of 2x CGO infiltrated SOEC. a) Layered image, b) Ce, c) Ni, d) Al.

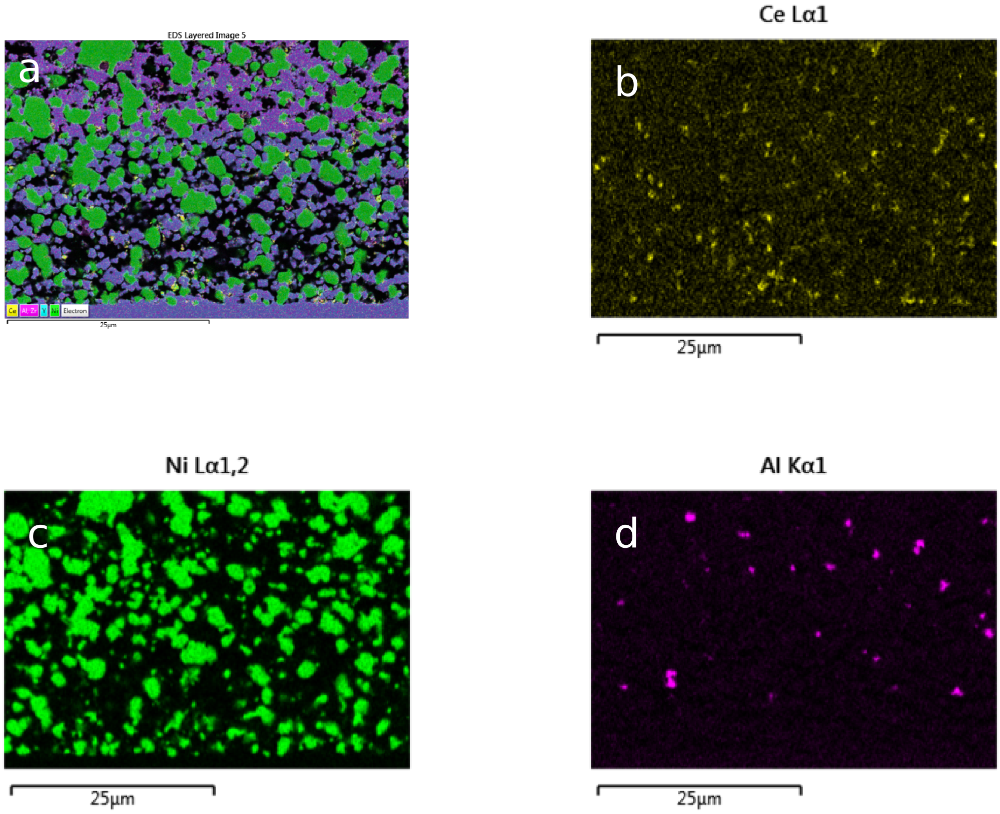

Figure 5.9: EDS of 4x CGO infiltrated SOEC. a) Layered image, b) Ce, c) Ni, d) Al.

steps of coarsening [210], leading the breakage of Ni-YSZ connections [58]. This will typically start as a rounding of the Ni particles. Comparison of the SOECs investigated in this chapter (fig. 5.3 and5.5) shows that the Ni in the infiltrated SOEC are generally of a less round character when compared with the non-infiltrated SOECs. This is observed in the EDS figures highlighting Ni (fig. 5.8/5.9 c) and in appendix D, along with the SEM micrographs where the Ni-particles for the infiltrated cells generally show to have more corners, whereas the corners have been rounded for the Ni particles in the non-infiltrated cells. The observations in fig. 5.7 a) support the hypothesis of a decreased wetting angle of Ni upon infiltrating with CGO [210], since this would lead Ni to be present at more locations. The increased percolation can also be excluded to be a direct effect of the presence of CGO, as this phase is not electronically conducting at room temperature [118].

The increased Ni retention of CGO-2 indicates that less migration away from the electrolyte has occurred, furthermore the smaller average particle size indicates less coarsening. This at indecates that Ni migration is more likely to occur in tandem with Ni coarsening, and while the two phenomena might be due to different mechanisms, the impeded Ni coarsening upon CGO infiltration also seems to impede Ni migration.

Structural damage of YSZ The structural damage of YSZ for CGO-4 is, as discussed previously, seen in figure 5.6 where most of the active electrode and the inner part of the support lies scattered. The high magnification micrographs fig. 5.6 (b+d) shows that the damage have mainly occured to the YSZ backbone. The onset of similar, though significantly more limited damage to YSZ is also seen for CGO-2 (fig. 5.5) where fracture lines are marked in figure 5.5 b) by the arrows. Some damage is seen for 06LU-1 and 08LU (appendix D), the damage for these tests is located around the fuel electrode-electrolyte interface, which indicates another cause for the damage, likely the high current for an extended amount of time these cells have experienced. The difference in damage between the infiltrated and non-infiltrated SOEC, increases the likely hood for former to be caused by the introduced component, CGO. During electrolysis operation Ce^{4+} may be reduced to Ce^{3+} by the negative potential [158], which will lead to an expansion of the CGO due to the increased ionic size of Ce^{3+} [211]. This expansion have previously been reported to be 1-2vol% by Bishop et. al. [212] and Wang et. al. [213]. This expansion is however unlikely to have caused the YSZ damage since CGO could easily have expanded into the pores.

In addition to containing CGO in their electrodes, the infiltrated SOECs also have another thermal history than the non-infiltrated cells, in that the former underwent the heating/cooling from the infiltration process. During this process the cells were rapidly heated to 200 °C from room temperature when entered into the furnace for the decomposition of the infiltration precursor. The infiltration cycles also included rapid cooling from 300 °C when the cells were removed from the furnace, which might induce thermal shock in the YSZ, thereby weakening it [181]. This would hence lead to the observations where a sample exposed to four cycles of this treatment would show more structural damage than the samples exposed to two.

The infiltrated SOECs was determined to leak in the previous chapter. Further investigation of the test history for CGO-4 shows that the down stream pO_2 periodically reached the required level for oxidisation of Ni in the final characterisation of the cell. It is hence possible that the structure could be caused by a redox effect [82]. The extend of the damage is however unique to the infiltrated cell, whereas non-infiltrated cells where leaks were determined did primarily present with NiO in the fuel electrode. The observed damage in the infiltrated cells is therefore likely caused by a combination of a thermal shock and expansion of Ni during oxidation. This damage is only seen due to the lack of YSZ in it structure, and while it is not expected to migrate as Ni, it may have been torn apart during the grinding/polishing part of the sample preparation.

Summary remarks The results indicates that CGO reduces Ni migration, which has also previously been shown by Tong et. al. [175], where a cell with CGO infiltrated fuel electrode also showed a better retention of Ni, when compared with a cell that had not been infiltrated. Based on the observations in figure 5.5 and 5.6 and following discussion infiltration should be done carefully to avoid thermal shock during decomposition of the precursor solutions.

5.3.5 Impact of Test Parameters on Pore fractions

Data correction

The pore-size distribution and fraction was investigated as described in chapter 2 using the secondary electron detector with an acceleration voltage of 15 kV.

Figure 5.3 b) shows a micrograph recorded at previously stated settings. A yellow circle in the figure highlights an issue, the structure beneath the surface of the cross section is visible, due to the epoxy filled pores being transparent.

This depth of view can be recognised by the human eye since it it is based on texture and context. This is however not the case for the image analysis software imageJ [119], which was used for discerning the pores based on a contrast thresholding method. Using the recorded pictures for determining the fraction of pores and the

Table 5.3: Data used for plotting figure E.1.

Test	Pore Fraction Corrected	Test duration [h]	Current density [A cm^{-2}]	η_{TPB} [mV]	Charge [C$\cdot 10^6$]
04HU	0.30	1035	0.375	88.91	22
05HU-1	0.35	991	0.5	194.94	29
05HU-2	0.33	735	0.5	198.21	21
05HU-GC	-	1051	0.5	102.21	30
06HU-1	0.35	254	0.625	493.30	9
06HU-2	-	192	0.625	479.80	7
06LU-1	0.39	949	0.625	458.24	34
06LU-2	-	624	0.625	-	22
08LU	0.32	566	0.75	192.20	24
CGO-2	0.26	1080	0.625	76.79	39
CGO-4	0.37	973	0.625	216.04	35
SEM-Ref	0.24	0	0	-	0

pore size distribution would hence lead to an underestimation of both. This issue was unfortunately discovered too late in the project to redo the microscopy for all samples.

This means that the results for the individual pore sizes are wrong, and hence also the size distribution thereof. An attempt has been made to correct the phase fraction of the pores. The method of which is described in appendix E.

All of the following fractions are corrected based on this method.

Time & Current

Figure 5.10 a) and b) shows the the pore fractions plotted against the test duration and current density respectively. Table 5.3 shows the data used for plotting the graphs 5.10.

In both fig. 5.10 a) and b) a very weak correlation can be seen, when excluding the infiltrated cells. It is however, also clear that time or current alone does not seem to be the cause of the increase in pore fraction. Fig. 5.10 b) also shows inconsistent pore fractions for the tests tested at the same current density(06LU/06HU). It is also worthwhile noting that the test with the lower pore fraction at 0.625 A cm^{-2} is the one tested using a larger utilisation (06HU-1) and η_{TPB}. The infiltrated SOECs were plotted as a separate series due to having been modified (blue), and may thus be expected to behave differently, as discussed above.

η_{TPB} & Charge

Figure 5.10 c) shows the dependency of the pore fraction on the final η_{TPB}. The figure furthermore shows two lines based on linear regression of the non-infiltrated cells either including (green line) or excluding (red line) the data for test 06HU-1 (orange/yellow highlight). The lines are denoted with the R- and p-values. Where the R-value denoting goodness-of-fit, and the p-value denotes the probability of whether the null-hypothesis is true. The p-value is hence the probability of random values resulting in the given distribution. Hence a low p-value indicates probability of correlation, for more on this the reader is referred to [214] or other work on statistical analysis. The motivation for excluding 06HU-1 is based on it being an outlier in 5.10 d), and the rationale being its electrochemical performance/history being differing significantly from the rest of the cells (chapter 3). The 06HU tests are also the only tests with large inclusions of glass-phase Al in the Ni-particles (fig. 5.3). While the line excluding 06HU-1 statistically is a better fit, the excluded test does not look like an outlier from the green line.

Figure 5.10 d) shows the correlation between the pore fraction at the inner 4 μm of the active electrode and the total charge passed through the cell during long term testing. Linear fits have been made for this correlation similarly to η_{TPB} (fig. 5.10). A secondary axis has been included in the graph, since the chosen parameter for the x-axis is proportional with the total amount of product, CO, produced during the long term test. Whereas neither the current or the test duration alone seemed to have a correlation to the pore fraction, the product of the two forms a linear trend. By using this parameter it is possible to compare the test across different test durations and current densities. In this case the porosity of all but one non-infiltrated SOEC correlate to the amount of charges passed during the test. Here 06HU-1 is an outlier to much a larger extent than in fig. 5.10 c). This means that excluding it has a much larger impact on the fit, especially the p value changing the fit to be statistically significant. The reasoning for the exclusion is the same as before.

Electron Transfer Energy

Figure 5.11 shows the comparison between the pore fraction and the total energy consumed for the electron transfer process during the long-term tests. The energy was calculated as the product of the integral of η_{TPB} during the tests (in steps of 50 h), and cumulated charge. The red line describes the fit to linear regression of all non-infiltrated cells. The data point for test 06HU-1 has been highlighted by an orange circle. From the figure it is seen that the energy correlates with the change in porosity, even for test 06HU-1 which was an outlier in the previous comparisons (fig. 5.10 c/d).

The correlation between the consumed energy for the electron transfer at the Ni-YSZ TPBs and pore fraction indicates that the loss of Ni 0-4 μm from the electrolyte

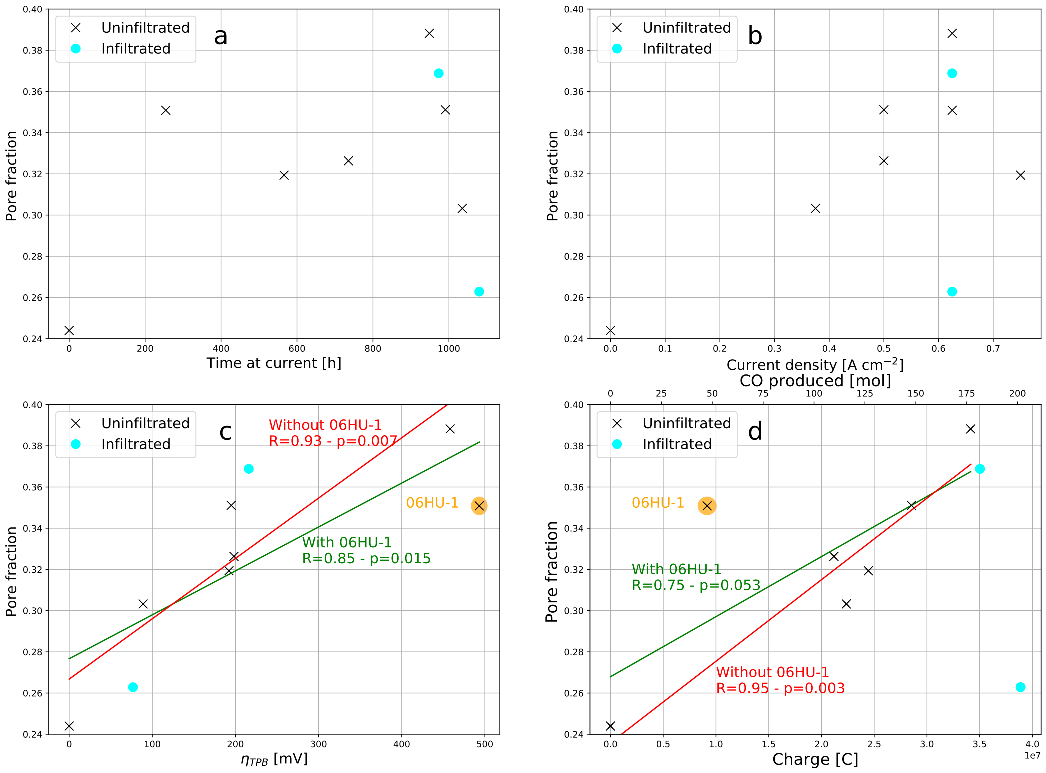

Figure 5.10: Pore fractions plotted against a) Time at current/duration of LTT, b) Current density during LTT, c) η_{TPB} at the end of test as determined in chapter 3 and 4, and d) the charge experienced during the LTT. The green and red lines in c/d) are linear regression made with and without the data point for 06HU-1 (marked in orange).

is linked to electrolysis operation. By comparison with figure 5.11 it is observed that both the charge and overpotential at the TPB contribute to the increase in pore fraction, and does so in different ways as seen by their individual correlations in figure 5.10 c) and d).
The correlation between charge and pore fraction in figure 5.10 d) indicates a part of the Ni migration is governed by charge. This is in agreement with the mechanism suggested by Monaco [196], where the formation of $V_O^{\bullet\bullet}$ would lead to to detachment between Ni and YSZ. In the original work the $V_O^{\bullet\bullet}$ concentration was described to be dependent on η_{TPB} [196], though the total number of $V_O^{\bullet\bullet}$ during a test would be proportional with the total charge. Similarly to the hypothesis by Monaco [196], a larger number of $V_O^{\bullet\bullet}$ would lead to more Ni-YSZ detachments due to the stochastic nature of chemical reactions. Subsequent reattachment is unlikely to occur due to spherification of the Ni particles through surface energy minimisation [64].
The observation from figure 5.11 indicates that η_{TPB} is enough of an equaliser to make up for the lower cumulative charge for the outlier 06HU-1 in figure 5.10. This might indicate that the contribution from η_{TPB} reaches a threshold where it does not contribute linearly due to the onset of secondary reactions e.g. CNT formation or partial reduction of Al_2O_3 and ZrO_2 leading to nanoparticle formation, as another ”migration” mechanism.
Comparing this hypothesis with the observations of the infiltrated SOECs shows that CGO-4 (pore fraction of 37%) is on the calculated line (figure 5.11). This is the case due to the very damaged fuel electrode structure of CGO-4. The pore fraction of CGO-4 would hence be expected to lie below the line if not for the structural damage, and it is deemed a coincidence for it to lie abone the linear regression for the non-infiltrated cells. Test 06HU-1 lies above the linear fit in figure 5.10 d), which is not the only case where this cell has stood out, as described previously. Furthermore the average pore size for this cell was determined to be the largest of the non-infiltrated SOECs 0.93 μm^2, whereas the average size across the other non-infiltrated SOECs were 0.66 μm^2. The sizes have not been corrected, though the ≈40% size difference is still indicative of the difference. The pore fraction of CGO-2 is quite low compared with the non-infiltrated SOECs, this is partially explained by the pores being filled with CGO, but also a better retention of the Ni as discussed previously.

If the tendency in fig. 5.11 was to continue linearly, Ni/YSZ SOEC would be unlikely to achieve widespread commercial success due to complete loss of Ni. This does not seem to be the case according to The at. el. [215], where the increase in pore formation originating from Ni migration is observed to slow down after a few thousand

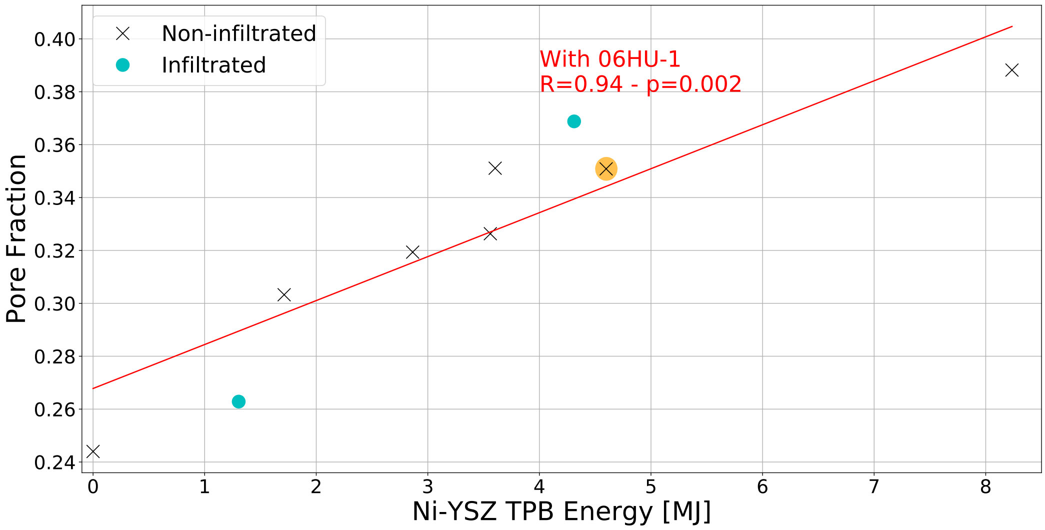

Figure 5.11: Pore fractions plotted against a) Time at current/duration of LTT, b) Current density during LTT, c) η_{TPB} at the end of test as determined in chapter 3 and 4, and d) the charge experienced during the LTT. The green and red lines in c/d) are linear regression made with and without the data point for 06HU-1 (marked in orange).

hours, which would similarly slow down pore formation. Such a phenomenon of decreasing rate of change would not be observed in this study due to the limited test duration (≈ 1000 h) of the test.

5.4 Results & Discussion - Compositional Changes in YSZ

Figure 5.12 shows the baseline-subtracted Raman spectra for 6 investigated SOECs. The embedded figure highlights the peaks used for determining the compositional ratio of tetragonal (t) and monoclinic (m_1 and m_2) in the fuel electrode support. The peaks were identified based on the findings by Kim et. al. [216], whom reported a peak for tetragonal YSZ at 148 cm^{-1}, while the two peaks at 180 and 192 cm^{-1} are assigned to the monoclinic structure. The ratio between the two phases is expressed in this chapter by

$$YSZ_{m/t} = \frac{I_{m_1} + I_{m_2}}{I_t} \tag{5.1}$$

where I is the integral of the peak I_x. This measure does not reflect the absolute amount of the phases, but rather is a measure for comparison between samples. Comparing these values with literature would require those values being determined using an identical approach.

The baselines were subtracted from the spectra using an asymmetric least squares smooth algorithm developed by Boelens et. al. [217], to account for non-identical baselines/background in the Raman data.

Table 5.4 shows the ratio of monoclinic to tetragonal YSZ in the structure for the investigated SOECs. Figure 5.13 shows a graphical representation of the ratio of monoclinic to tetragonal YSZ.

From the figures and table in this section it is immediate apparent that the Ref contains far the least monoclinic YSZ among the samples than any of the other characterised SOECs.

Figure 5.13 a) shows that the relative amount of monoclinic YSZ has increased for the SOECs that have been tested for a long time, this indicates that degradation occurs upon modification or operation of the SOECs. The likely causes for phase transition in the non-infiltrated tests are either aging [201, 202] or transformational toughening due to mechanical stress [200]. The similar $YSZ_{m/t}$ of the two tested SOECs makes it impossible to conclude on the effect of thermal aging on the system. If the SOECs however have behaved as expected, this meaning the cell tested for 661 h having degraded less than the 1221 h test, it would mean that 06HU-1 would have experienced more strain than 06LU-2 leading to a phase transition. Further adding to the complexity of the system is the risk of an athermal phase transition during cooldown of the SOEC after test [201], which would lead to an overestimation of monoclinic YSZ in case on an unsystematic transition between the SOECs.

Table 5.4: Overview of $YSZ_{m/t}$ for the SOECs

SOEC	Color	$YSZ_{m/t}$	Time above 650 °C [h]
Ref	blue	0.140149	285
06HU-1	red	4.063663	661
06LU-2	green	3.828985	1221
I-Ref	cyan	2.517086	176
CGO-2	magenta	0.843594	1285
CGO-4	orange	1.613391	1199

Figure 5.13 shows the $YSZ_{m/t}$ for the infiltrated cells. No clear link between either test duration and number of infiltration cycles in relation to $YSZ_{m/t}$ is seen. What is however observed is the difference between the non-infiltrated reference and the infiltrated reference. The $YSZ_{m/t}$ is significantly larger for the latter, despite it having been tested for the shortest time. The phase transformation of the infiltrated SOECs are hence likely due to be caused in part by the low temperature degradation (LTD) as reported by Chevalier et. al. [200]. LTD occurs in the temperature range between room temperature and 400 °C, where a humid atmosphere accelerates the phase transformation starting at the surface [200]. These conditions corresponds with the ones occurring during infiltration with an aqueous solution before it evaporates during decomposition of the precursor solution. Comparison between the various infiltrated SOECs in figure 5.13 does however show that the there is no apparent correlation between amounts of infiltration cycles and phase transformation, since I-Ref only have experience two cycles of infiltration. It is hence not possible to conclude anything on the effect of the number infiltrations in relation to phase transformation before more systematic experiments have been carried out. The only apparent result from this limited study into the degradation of the YSZ phase by phase transformation of the fuel electrode support is hence that a phase transition is seen to have occured in the fuel electrode support after operation whether or not infiltrated with CGO.

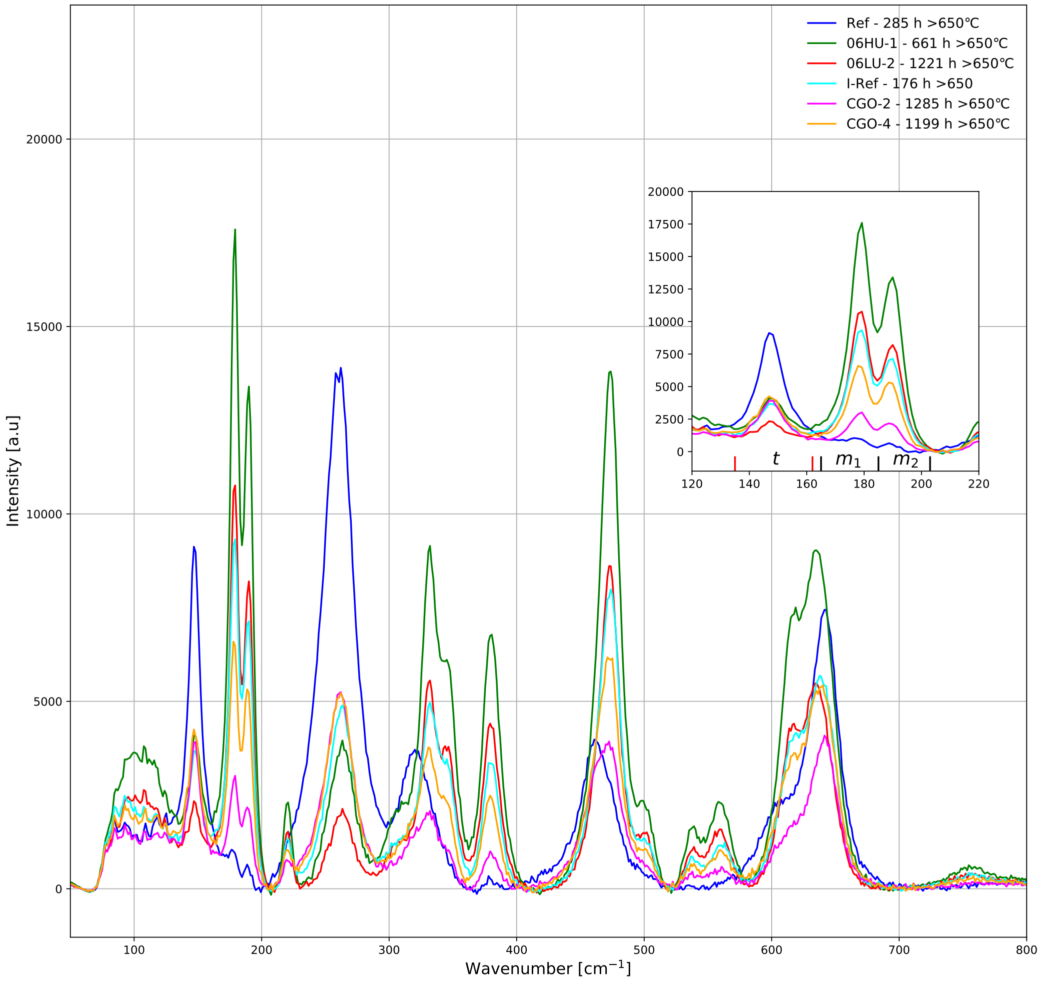

Figure 5.12: Raman spectra of YSZ, embedded figure highlights peaks used for determining ratio of tetragonal (t)/monoclinic (m) YSZ. Axes on the embedded figure share units with those the overall figure.

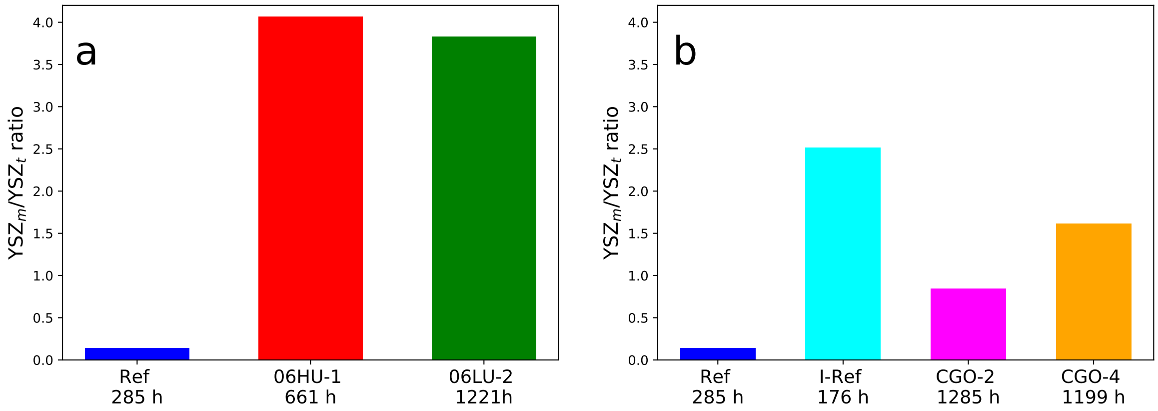

Figure 5.13: Bar plots comparing the YSZ_m/YSZ_t ratio of a) non-infiltrated SOECs, and b) infiltrated SOECs.

5.5 Conclusion of Chapter

Based on the twice infiltrated SOEC CGO-2, infiltration is seen to mitigate coarsening and subsequent migration of Ni or simply blocking Ni-surfaces slowing down transport. The infiltrated cell CGO-2 shows the most extensive network of percolating Ni throughout the fuel electrode.
Microstructural analysis of CGO-4 has shown that the thermal shock during the infiltration process and oxidative expansion of Ni can lead to extensive damage of YSZ.

Non-infiltrated SOECs have shown signs of ageing based on test parameters and the duration of exposure to these conditions. The Ni particles in test 06HU-1 has been identified as 33% larger than for those of the other non-infiltrated cells, and is speculated to being caused by a large η_{TPB} causing the formation of glassy phases to be formed on the surface Ni particles, this will be further discussed in the overall discussion (chapter 7).

Loss of percolating in the Ni is also seen to be dependent on test conditions, where SOECs tested at ”mild” condition (04HU) shows a thin, but evenly distributed layer of lost Ni near the electrolyte. ”Harsher” conditions (06LU-1) shows a distribution of deeper losses into the active electrode, these are less evenly distributed.

The change in pore fraction shows a correlation between the total amount of energy consumed for the Ni-YSZ TPB electron transfer process during the tests. A correlation with the pore fraction is also seen when compared with the cumulative charge for the process, though with 06HU-1 being an outlier due to a high inital η_{TPB}. This indicates that the Ni migration occurs due to the experienced energy at the Ni-YSZ TPB. The loss due to migration has been observed to increase per charge unit at high η_{TPB}. The correlation also means that the degradation is dependent on the total amount of produced CO during operation, unto a point where it is expected to level off.

Investigation of the fuel electrode support using Raman spectroscopy shows an tetragonal to monoclinic phase transformation of YSZ during operation, upon modification of the microstructure by wet infiltration of CGO.

Chapter 6

In-Operando Raman Studies of Carbon formation during CO_2 electrolysis

The results in this chapter was recorded during an external stay at Montana State University. All results in the chapter was achieved in collaboration with PhD student Tanner Henning, which is why some overlap between his and my thesis might occur. The purpose of the external stay was to link electrochemical performance(EIS) and carbon formation (Raman spectroscopy) to determine if a threshold for carbon formation could be proved. This was unfortunately was not achieved during the short external stay due to various reasons, which is explained and discussed in the chapter. The chapter furthermore attempts to come up with solutions to the problems, for making further attempt of the experiments more likely to succeed.

6.1 Introduction

It has previously been speculated/established that carbon deposits in the fuel electrode when a certain threshold or parameter is reached [65, 72, 132] . An exact value have however to be agreed upon. Identifying this value would provide knowledge of how to operate without carbon deposition, and hence extending the lifetime of SOECs for CO_2 electrolysis.

A major challenge in solving this issue is that the currently method of testing is: 1. Operate a SOEC for a time, 2. stop the experiment, 3. check for carbon formation. This method only provides information of whether or not carbon formation was achieved at the end, not when, meaning that only the parameters at the end of the test can be used, and even then the test history should also be considered. The issue using this method of testing for carbon formation can only be probed for at specific ”locations”, chosen wherever the light-source is pointed. The root of the issue is that only electrochemical data is measured while testing, while the presence

of carbon is not.
It is, however, possible to link electrochemical performance and carbon deposition as done by Welander et. al. [100] in SOFC operation with methane, here the carbon tolerance of various catalysts was determined *in-operando*.

In this study the set-up used in the work by Welander et. al. [100] is used in the attempt to determine the parameter(s) where carbon deposition occur during CO_2 electrolysis in SOEC, by linking carbon formation seen by Raman spectroscopy while monitoring the electrochemical performance with EIS.

6.2 Experimental

6.2.1 Infiltration

The SOECs used in this study were of the same type as described in chapter 3. They were laser cut into circles with a diameter of 28 mm. The SOEC was reduced prior to infiltration as described in chapter 4.

The SOECs were infiltrated with either CGO, Ni-CGO, or Cu-CGO. The infiltrated cells were infiltrated using the method as described in chapter 4, furthermore, the solution for the CGO infiltrated cells was the same as in chapter 4. The precursor solutions were made similarly to the CGO solution, but Ni/Cu nitrates was added to the respective solutions to reach 10wt% of the metal. The amount of reactants for the solutions can be found in table 6.1. All infiltrated SOECs was done so with four cycles.
Table 6.2 shows an overview of the SOECs and their infiltrate loadings investigated in this study.

Table 6.1: Component weights of Ni/Cu-CGO precursor solutions.

	Ni-CGO [g]	**Cu-CGO [g]**
$Ce(NO_3)_3 \cdot 6H_2O$	8.6848	8.6858
$Gd(NO_3)_3 \cdot 6H_2O$	2.2614	2.2573
$Ni(NO_3)_2 \cdot 6H_2O$	2.1609	
$Cu(NO_3)_2 \cdot 3H_2O$	1.6566	
P123	0.2542	0.2552
H_2O	21.5	22

Table 6.2: Infiltrate loadings in the fuel electrodes of the tested SOECs. Infiltrate is reflected by sample name.

Cell	Loading [mg cm^{-3}]
No-Load1	-
No-Load2	-
No-Load3	-
No-Load4	-
CGO-1	218.5535
CGO-2	231.0692
CGO-3	236.7925
CGO-4	247.4214
Ni-CGO1	245.4717
Ni-CGO2	271.5723
Ni-CGO3	266.2264
Cu-CGO-1	275.4717
Cu-CGO-2	296.8553
Cu-CGO-3	281.1321

6.2.2 The ”Rocket” Set-up

Figure 6.1 depicts the ”Rocket” set-up used for the *in-operando* Raman measurements. The ”Rocket” consisted of a main alumina tube with an outer diameter of 26-28 mm on which the SOC cut to the same measurement could be placed on top. An alumina tube was attached to the outside leading (Outer Gas Tube) the appropriate gas to the exposed side of the SOC, while a inner tube of alumina transported gasses to the downward facing side of the SOC. On the outside was furthermore placed a thermocouple with its end near the SOC, a short alumina tube as gas outlet, and a cooling element close to the bottom of the set-up. The cooling element was present to protect the rubber stopper from melting. The rubber stoppers was themselves used as gas seal between the scaffold tube and a outer quartz tube. The gas tubes, cooling element, current leads, and cooling element pipes went through holes in the rubber stopper. Superwool™was used as insulation between the two ends of the ”Rocket”, and furthermore was packed tightly in the holes in the stopper through which the gas tubes etc. went through to to avoid gas leakage. The inner rubber stopper contained two holes, one for the gas inlet, and one for gas outlet which was connected to a gas line leading directly to the exhaust. The gas outlet on the outside was also connected directly to the exhaust in a similar manner.

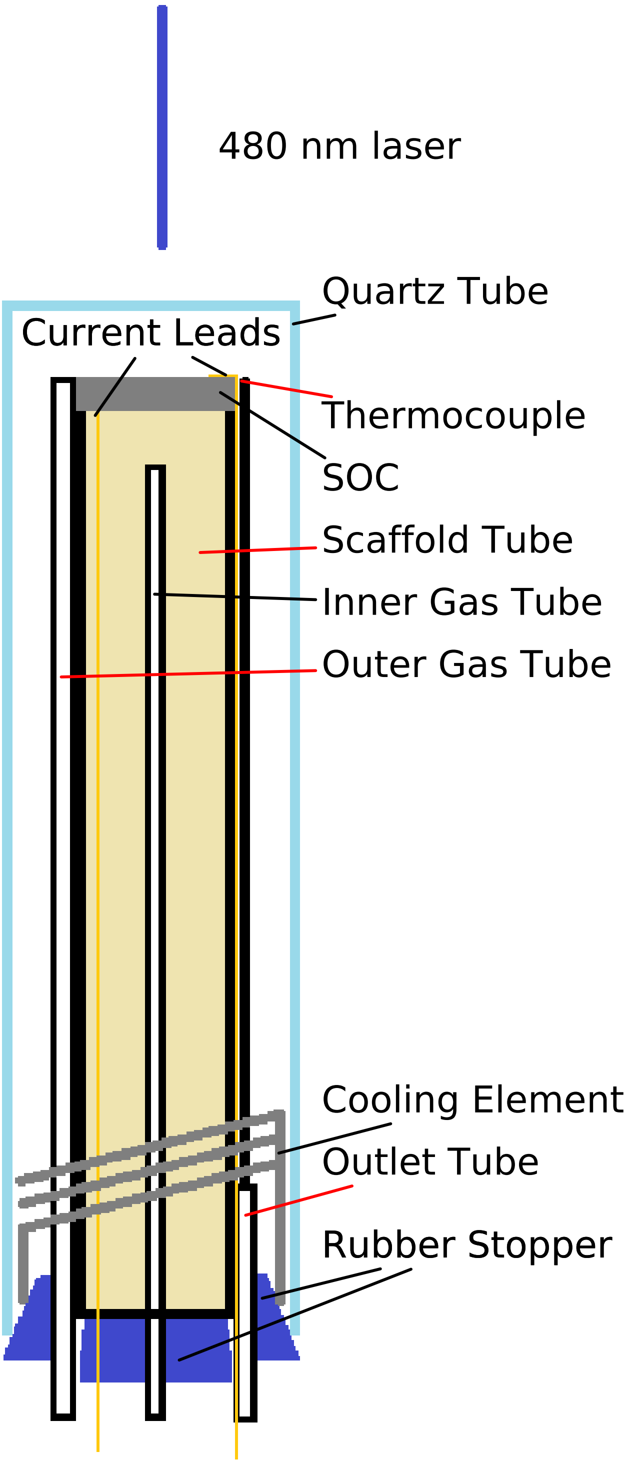

Figure 6.1: The ”Rocket” set-up, not to scale. See text for further description.

Mounting

Current collectors were attached to the fuel and oxygen electrodes. The current collectors consisted of 0.5×0.5 cm^2 Au gaze connected to a 5 cm piece of Au wire. The current collectors was attached using Au-paint, for further adhesion a small drop of alumina paste was dabbed into each corner of the current collectors. After the alumina paste had dried it was covered by Au-paint. The current collectors was then dried at 200 °C for 30 min.
The SOC was mounted on the scaffold tube oxygen electrode facing upwards. A thin layer of alumina paste was applied on the end of the tube as seal. Additional alumina paste was applied around the seal to improve gas tightness. 3-4 layers of alumina paste were added, each layer was left to dry at ambient temperature for 30 min. After the last layer the alumina was dried in an oven at 200 °C overnight, the heating and cooling was done in 50 °C intervals every 30 min. After drying the current collectors was attached to NiChrome current/voltage leads. The quartz tube was placed outside the other components. Superwool™was used as thermal insulation near the bottom, and the set-up was sealed with a rubber stopper, and copper gasket was added for additional gas seal around the edge of the quartz tube. The copper gasket was left to dry overnight at ambient temperature.

The ”Rocket” was mounted in a stand, to keep the set-up upright. The cooling element was attached to the coolant (ethylene glycol in water) loop. Gasses was attached to the appropriate inlet/outlet tubes. The setup was investigated for gas leaks using soapy water. A cylindrical (doughnut) furnace was placed around the ”Rocket”, the top was insulated with Superwool™to minimise heat loss, though with room for the Raman laser to access the sample. Further air cooling was added at the bottom of the set-up for cooling the rubber stopper. Air cooling was added on top of the set-up to cool the microscope objective from the Raman spectrometer. Raman was tested, to find focus on the sample before the objective was moved upward, away from the furnace, to avoid unnecessary exposure to heat. The furnace was heated to 750 °C at a rate of 60 °C h^{-1}. The fuel electrode was supplied with 4-5% H_2 in Ar_2 during heating

Operation

Continuous 5s Raman scans was used to obtain focus of the fuel electrode. The objective was adjusted to maximise the peak intensity of CGO 450 cm^{-1} [173], while minimising those from the perovskites (LSCF/LSM) in the oxygen eletrode [218, 219].
A Princeton Technology Corporation PSU was used to provide power for the SOCs.

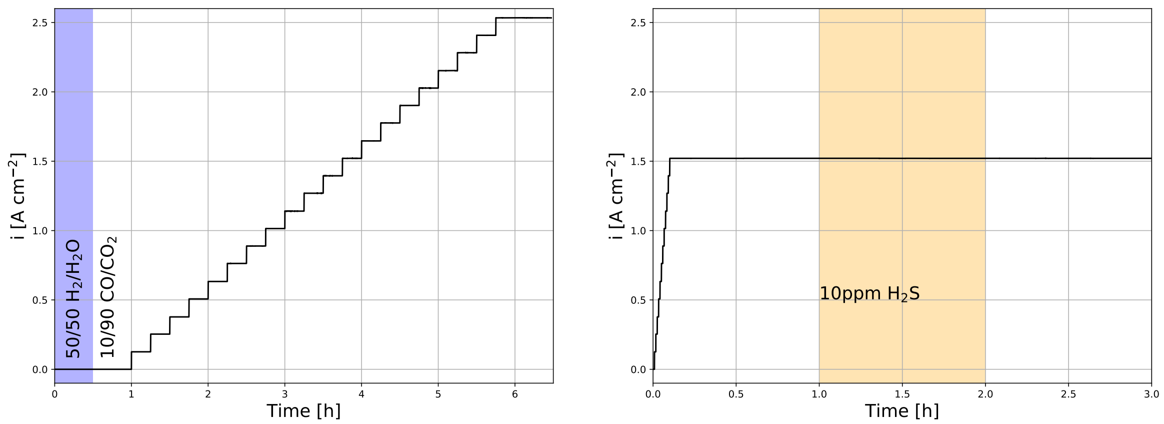

Figure 6.2: Graphical representation of the test protocols for the two experiments a) Stepwise increasing current, colours describe fuel gas composition, b) Constant current in a CO/CO_2 atmosphere, 1 h of H_2S exposure (coloured region).

Gas flows was controlled by ball flow meters. After the experiments the rig was cooled to room temperature at a rate of 60 °C h^{-1}. The fuel electrode was supplied with 4-5% H_2 in Ar_2 during cooling.

6.2.3 Test protocols

Figure 6.2 shows a graphical representation of the test protocols for the two experiments. Further details can be found in the following sections. The ”Increasing Current” experiment was made on day 1 and on the subsequent day ”Sulfur Exposure” was carried out. The fuel electrode was supplied with 4-5% H_2 in Ar_2 between experiments.

Initial Characterisation

An extended 3x30s Raman spectrum (100-3200 cm^{-1}) was recorded as initial characterisation. Electrochemical characterisation had been planned to be done using EIS, but failed due to nonsensical results (only noise).

Increasing Current

Figure 6.2 a) shows the test protocol for the first experiment, the test was carried out at 750 °C, and started at OCV with air to the oxygen electrode and a 50/50 H_2/H_2O for the first 30 min, after which it was changed to 10/90 CO/CO_2. The flow rates was 20/20 and 6/55 l h^{-1} for the gas compositions respectively. After 1 h the current density was increased by 0.125 A cm^{-2} every 15 min, until reaching 2.5 A cm^{-2} where the cell was left for ≈ h. The carbon formation was monitored with Raman in the range 260-1850 cm^{-1}, with 3×20 s scans.

Sulfur Exposure

Figure 6.2 b) shows the test protocol for the ”Sulfur Exposure” experiment. The experiment was carried out in 10/90 CO/CO_2 using the flow rates: 6/55 $l\,h^{-1}$ for the two gasses. The current density was initially increased stepwise to 1.5 $A\,cm^{-2}$. After 1 h the fuel electrode was exposed to 10 $l\,h^{-1}$ of 10ppm H_2S in H_2 for 1 h, after which it was turned off again. The SOC was left for 1 h thereafter. The carbon formation was monitored using Raman in the range 260-1850 cm^{-1}, with 3×20 s scans.

6.3 Method Development - Adaptation from SOFC to SOEC operation

Figure 6.3 a) shows a drawing of the SOC as in ”Rocket” used for previous studies [100, 220], where the set-up is reported to measure carbon formation in SOC during SOFC operation. This test geometry is possible since carbon forms on the gas/electrode surface during SOFC operation [100]. During CO_2 electrolysis the carbon forms at the fuel electrode/electrolyte interface as seen in figure 6.3 b and c), which is supported by the findings in chapter 3. It is hence necessary to investigate the fuel electrode/electrolyte interface instead of the fuel electrode surface, however this is not possible using the geometry in fig. 6.3 b). This is due to Raman mainly being a technique surface rather than bulk analysis, and the opaque fuel electrode support is way too thick (300μm) for the laser to penetrate through. The test geometry seen in figure 6.3 c) was suggested as a workaround for this, in this geometry the SOC is mounted oxygen electrode facing upwards. Before mounting a small hole ($\approx$ 100 μm diameter) is drilled in the opaque oxygen electrode, revealing the electrolyte which admits light due to its thinness (8 μm).
”Drilling” a hole in the oxygen electrode was done with the tip of a scalpel/exacto-blade, this method was possible since the hardness of the steel ”drill” is higher than that of the oxygen electrode (LSM/LSCF), but lower than that of the electrolyte (YSZ). The ”drilling” did however leave some particles of oxygen electrode in the hole after drilling. Figure 6.3 d) shows a top-down view into the hole drilled with a scalpel. The particle matter was tried removed with acid, though this was quickly discarded due to damage to the rest of the oxygen electrode causing the electrolyte to turn grey. The particle matter was also attempted to be removed by ablation using the ion beam in a FIB-SEM, or compressed air. Based on observations in Raman spectroscopy

ion-ablation was however discarded due to too little time-wise return-on-investment, since the compressed air worked well enough.

6.3.1 Carbon Detection Through the Electrolyte

Figure 6.4 shows the Raman spectra for the three steps proving the concept of carbon detection through the electrolyte. The peaks shown in the spectra are the D peak for disordered graphite, along with G_1 and G_2 peaks for ordered graphite[142], the latter has furthermore been associated with a 3D element as in the growth of carbon nano-tubes [143]. Step 1 in the proof was establishing carbon in a SOC that had been operated for CO_2 electrolysis, this is seen to be successful in the figure. Step 2 was to identify at which distance from the active area carbon stopped forming. Figure 6.4 a Raman spectrum recorded 300 μm away from the operational area with a oxygen electrode contact layer. This indicates that carbon is present 300 μm from the area with highest polarisation, which is 3 times the diameter of the hole in the cell. It should be stated that the intensity of the carbon peaks decreased away from the area opposite the contact layer, this was ”counter-acted” by increasing the scan time/repetition, the intensities are hence not comparable. Step 3 of the proof of concept was to identify carbon through the electrolyte, which it can be seen has been done in figure 6.4. It should therefore be possible to use this method for *in-operando* carbon detection using ”Rocket”.

6.3.2 Modifications to ”Rocket” Operation

The main operational difference compared to previous studies on SOFC using the set-up was that the oxygen electrode was facing upward during operation. From this follow a reversal of the inside/outside gasses, which improved safety around CO, as the inside of the scaffold tube was not observed to leak, whereas the outside part was more difficult keeping gas tight.

6.4 Results & Discussion

6.4.1 Observations - Intended Tests that did not Work

Due to issues with the power supply unit, or the inexperience of the operators it was not possible to measure any meaningful impedance. It was hence not possible to do the initial electrochemical characterisation or monitor performance during the experiments. The only measure that was achieved was voltage. Figure 6.5 shows the voltage over time for the tests of Ni-CGO3. A large fluctuation is seen in the

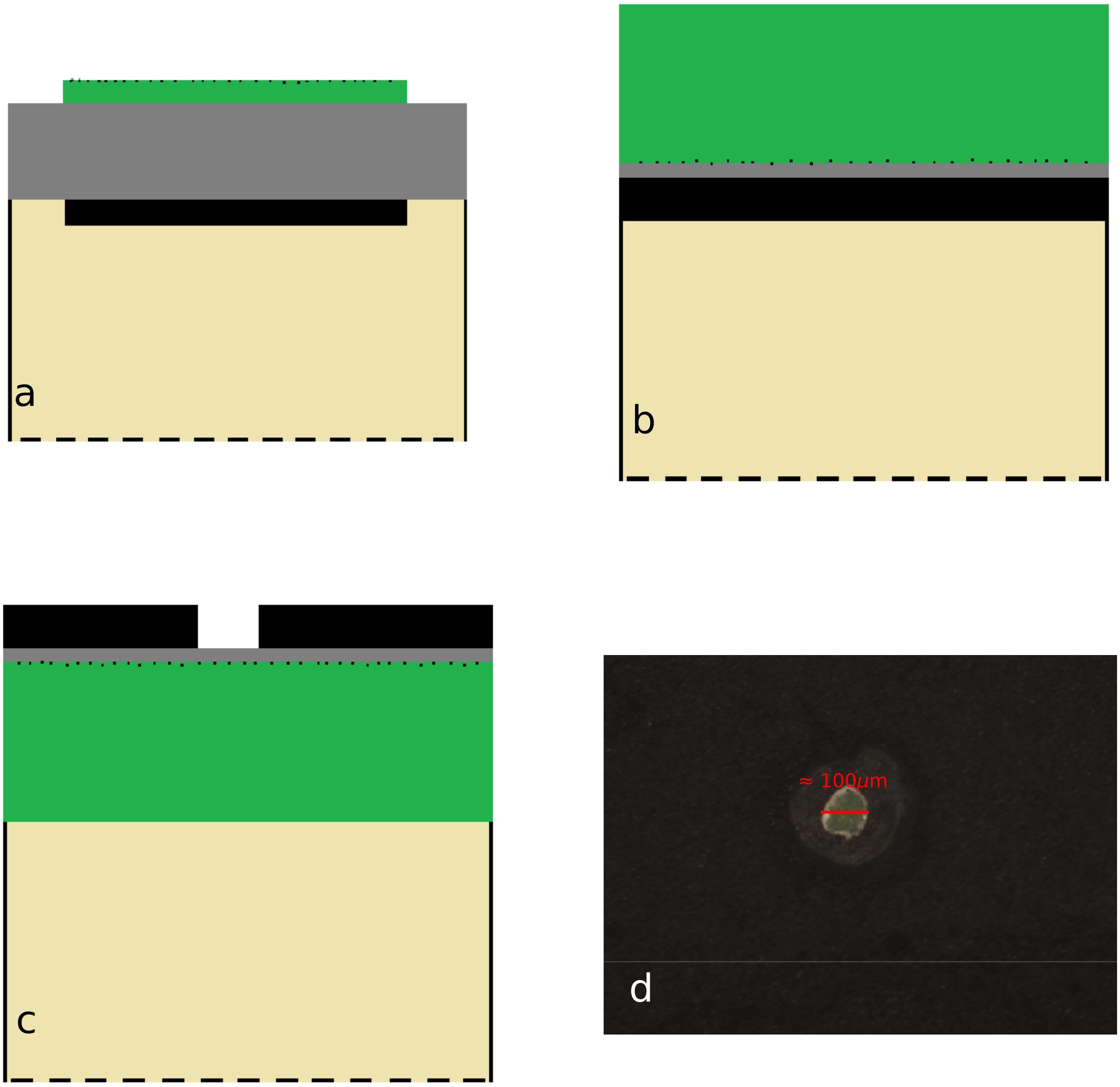

Figure 6.3: Three different test geometries a-c. a) Electrolyte supported SOC with fuel electrode facing upward, b) Fuel electrode supported SOC with fuel electrode facing upward, c) Fuel electrode supported SOC with oxygen electrode facing upward. In c) a hole has been drilled in the oxygen electrode. Colours: Beige - Alumina scaffold tube, Green - Fuel electrode, Grey - Electrolyte, Black - oxygen electrode, Black dots - Carbon. d) Top-down view of a hole drilled in the oxygen electrode with a scalpel.

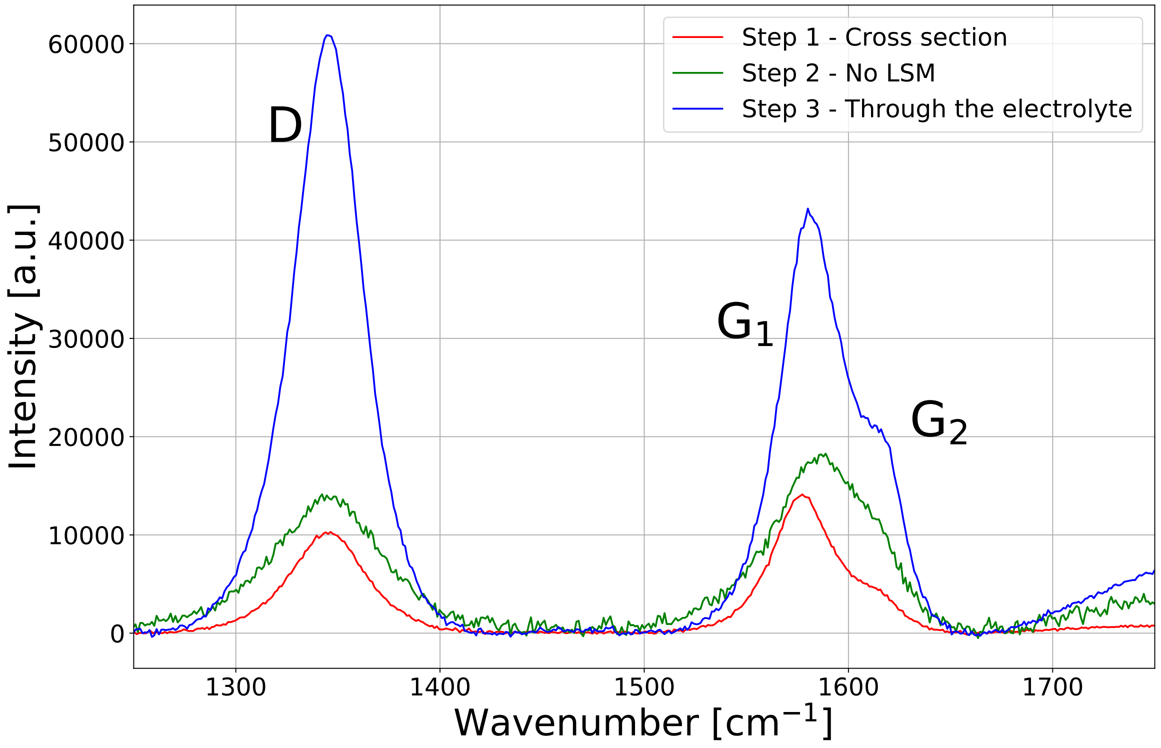

Figure 6.4: Raman spectra recorded at: ”Step 1” - SOEC cross-section at fuel electrode/electrolyte interface, ”Step 2” - SOEC cross-section at fuel electrode/electrolyte interface 300μ away from the edge of the oxygen ion contact layer towards the non-operated part of the SOEC, ”Step 3” - Through the hole in the oxygen electrode.

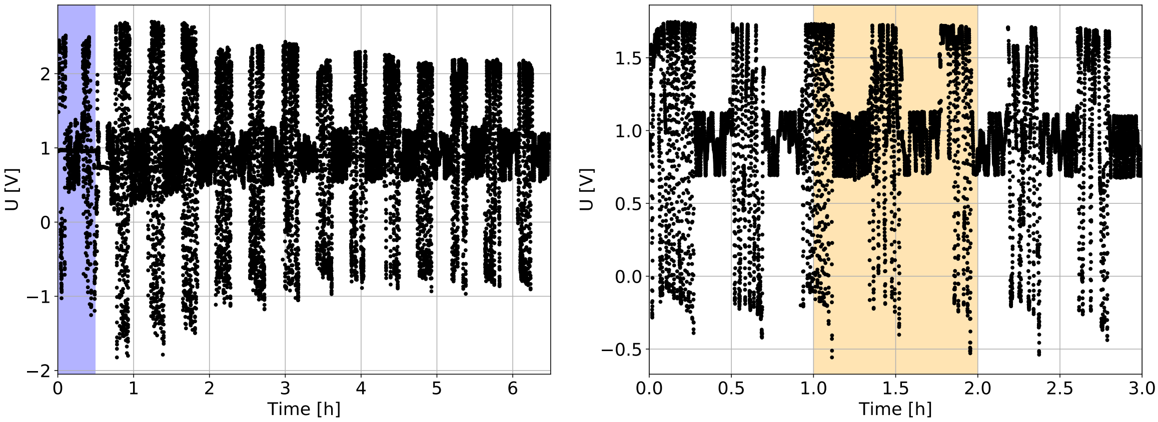

Figure 6.5: Voltage over time for the two *in-operando* experiments ”increasing current” (right) and ”sulfur exposure” (left). Colour coding can be seen in figure 6.2

voltage. The amplitude in the fluctuations is seen to change approximately every 15 min. Initially this corresponds with the increase in current in the ”Increasing current” experiment (right), but it continues after reaching maximum current density, and for the ”Sulfur exposure” experiment. This response was characteristic for all experiments.

6.4.2 Carbon Formation in tested SOECs

Figure 6.6 shows the Raman spectra recorded during the two different experiments, each for a different sample. Three peaks are present in the results from the ”Increasing Current” experiment at the wavenumbers 1545, 1590, and 1610 cm^{-1} which corresponds to the G$_1$, G$_2$[142], and peaks D’[221] respectively. These three peaks indicates the presence of carbon nano-tubes in the SOEC, and hence it has been possible to do *in-operando* Raman on a fuel electrode supported SOC. Furthermore, due to the low intensity of the peaks it is possible to differentiate them, where they are otherwise usually overlapping [143, 173, 221].

The caveat of this finding is that all peaks are present from the start of the ”Increasing Current” experiment, before the cell was exposed to a CO/CO$_2$ atmosphere, indicating an external carbon contamination. The results in figure 6.6 are characteristic for all tested cell in this study.

Figure 6.7 shows the peak carbon integrations for the ”Increasing Current” for Ni-CGO2, this indicates no systematic change in the peaks occurred during the tests, which is similar to what is seen in fig. 6.6. There is hence no significant increase in the presence of carbon during any tests in this study, and the infiltrate does not seem to have had an impact on whether carbon was observed. This raises two questions:

1. Where does the carbon contaminant come from?

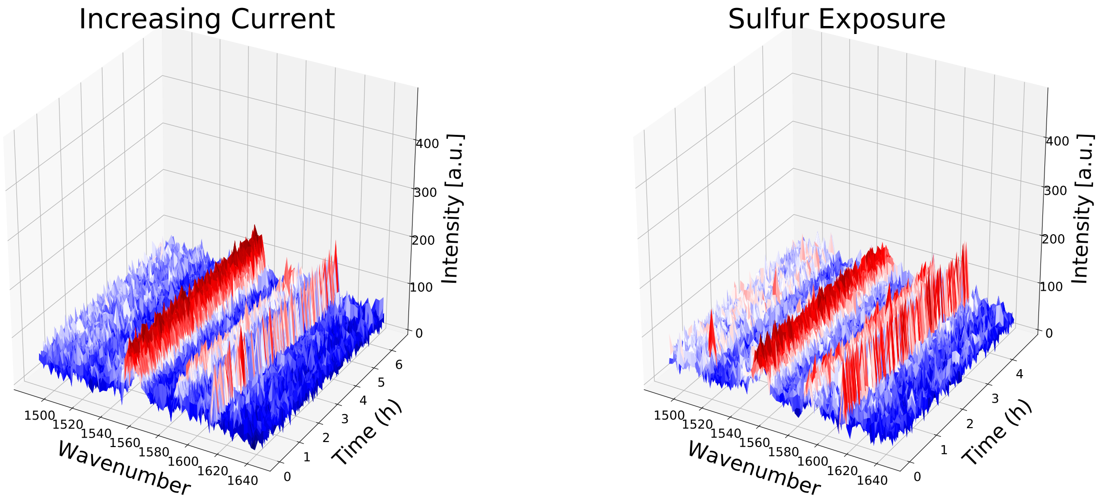

Figure 6.6: Raman spectra recorded during the experiments ”Increasing Current” (For Ni-CGO3) and ”Sulfur Exposure” (For Ni-CGO2).

2. Why does carbon not form during operation?

Carbon Contaminant The cell was exposed to a carbon containing species twice during preparation, the surfactant P123 while infiltrating and likely a binder in the Au paint as part of the mounting. Of these two the binder in the paint seems most likely as the current collector on the fuel electrode was placed at the location corresponding to the hole in the oxygen electrode. This would have lead to ”infiltration” of the binder into the fuel electrode, which would turn into carbon when heated to 750 °C carbon upon reaching the Boudouard threshold [204]. A similar explanation would be the case for the P123 used during the infiltration, though this was used in a much lower concentration. P123 was also used for the infiltration process in chapter 4, where carbon was absent in one of the tested SOECs.

No further carbon formation No significant/systematic carbon formation is observed after the initial in figures 6.6 and 6.7. Based on previous studies carbon formation in 10/90 CO/CO_2 was only seen after operation at current [65, 71, 72] and reaching a certain overpotential [132]. This would indicate that no reduction of CO_2 occurs in the hole, which is likely caused by the lack of oxygen electrode.
Figure 6.8 a) shows a sketch of the surroundings near the hole in the oxygen electrode. In the figure the resistance contributions from the polarisation is split into those from the oxygen (R_p^{OE}) and fuel (R_p^{FE}) electrode, which together gives the total polarisation resistance (R_p). R_Ω is marked as the electrolyte resistance, which will be the only contribution to the Ohmic resistance in this approximation. Furthermore, green markings have been made along the uncovered part of the electrolyte,

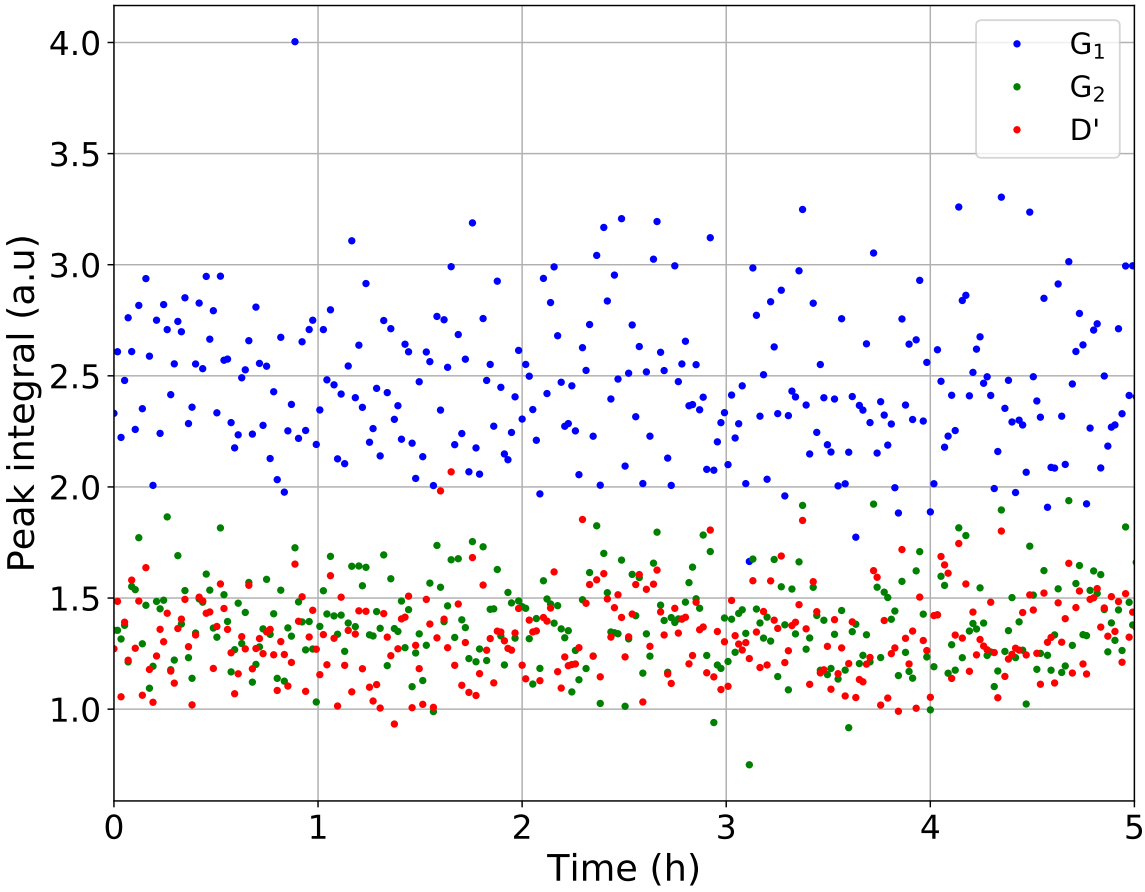

Figure 6.7: Peak integrals for the carbon peaks G_1, G_2 and peaks D' in "Increasing Current" for Ni-CGO2.

corresponding to the width of the electrolyte, the resistance between each marking will therefore be expected to be the same as across the electrolyte R_Ω.

Based on these statements the distribution of current inside the hole can be calculated. At distance 0 there is no hole and the current can be calculated by Ohm's law:

$$I_0 = \frac{U}{R_p + R_\Omega} \tag{6.1}$$

At n electrolyte widths from the edge I_n is:

$$I_n = \frac{U}{R_p + R_\Omega(1+n)} \tag{6.2}$$

Since U is assumed constant the ratio between the two is:

$$\frac{I_n}{I_0} = \frac{R_p + R_\Omega}{R_p + R_\Omega(1+n)} \tag{6.3}$$

Figure 6.8 b) shows $\frac{I_n}{I_0}$ as a function of ASC electrolyte distances ($\approx$ 8-10 μm) from the edge of the hole. It is seen from the figure that the non-infiltrated SOC retains the current better than the infiltrated SOC, this is due to the impact of the R_p/R_Ω ratio, the smaller it is the the quicker the current diminishes due to favouring transport through the electrodes compared to the electrolyte. The green dashed line in fig. 6.8 b) was calculated based on data found for an electrolyte supported cell in the work by Padinjarethil [222], while this cell was tested in a H_2/H_2O atmosphere the purpose of including it was to show how the increased R_Ω would lead to a better current retention. For ease of comparison between ASC and ESC the n in eq. 6.3 was multiplied by a factor of $\frac{1}{8}$ to compensate for the 8-fold difference in electrolyte thickness.

Assuming a 100µm hole in the electrolyte the greatest distance to the edge will be $\approx$ 5 electrolyte widths, which indicates a retention of $\approx$ 42 and 34 % current retained for the non-infiltrated and infiltrated SOC respectively, which indicates why no carbon formed. Figure 6.8 b) also indicates that an ESC would be better suited to this kind of experiment solely based on the current retention compared to the ASCs, though the transmittance of the material would decrease leading to less Raman signal.

6.4.3 Improvements

Based on the results in figure 6.8 two possible methods for improved results through increased retention of the current: 1) Use of ESCs instead of ASCs, 2) Raman operation close to the edge of the hole. Use of ESCs would, as described above, bring

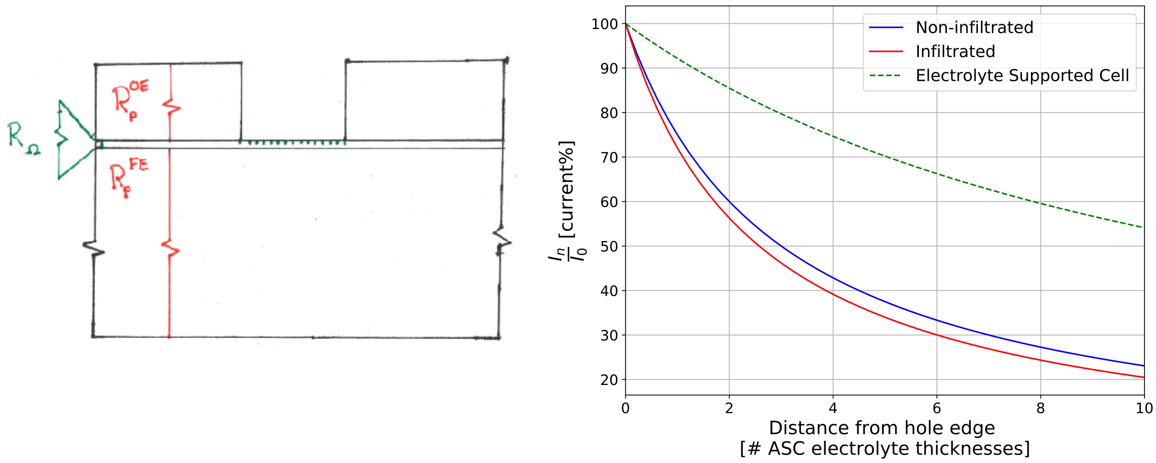

Figure 6.8: a) Zoom in on the hole in the oxygen electrode, R_p components marked in red, R_Ω marked in green. Green markings in the electrolyte marks distance corresponding to electrolyte thickness. b) Relative amount of current at location in the oxygen electrode hole compared to the edge for a non-infiltrated cell (blue), a infiltrated cell (red), and an electrolyte supported cell (dashed green, based on data from [222]) the thickness has been corrected to be comparable to ASC SOC.

its own challenges. Whereas the electrolyte is almost transparent in ASCs it is less so in ESCs due to it being thicker. For operation with ESCs it would therefore be necessary to investigate the absorbance/transmittance spectrum for YSZ to identify whether a suitable wavelength for penetrating the electrolyte, without loosing too much signal, exists.

Alternatively one would have to operate around one electrolyte width (8-10μm) from the hole. It was already attempted to operate as close to the hole as possible during this study. This was a challenge since the hole was hard to locate during operation, and horizontal movement of the sample was limited due to the furnace placement. Alternately the hole can be made smaller, while this would increase the challenge of locating them, some kind of identifier might help a bit. A patterned oxygen electrode might also be a solution. It could be made in a pattern which systematically exposed a electrolyte width of oxygen electrode, leading to only 80% current retention.

Furthermore it would also be necessary to achieve fruitful outputs from the impedance measurements.

6.5 Conclusion of Chapter

Carbon was observed in the Raman spectra for all samples before the SOECs were even supplied with a CO_2/CO atmosphere, the cause of which is likely the binder used as binder in the Au paste added as adhesive for the current collectors.

Due to the low intensity of of the Raman peaks it was possible to discern the D’, G_1,

and G_2 peaks.
No carbon formation was observed in the fuel electrodes other than the one from the paint, likely due to the SOECs lack of oxygen electrode oppositely of the investigated fuel electrode. This was also the case when the fuel electrode was exposed to a large amount of H_2S.

Chapter 7

General Discussion

This chapter references tests described in other chapters, for which test parameters and naming conventions can be found in table 3.1 on page 30 and 4.1 on page 56 for non-infiltrated and infiltrated cells respectively.

7.1 SOEC Degradation

The purpose of this project has been to study and mitigate carbon deposition in the Ni-YSZ SOEC fuel electrode during CO_2 electrolysis. This has been done by examining operation parameters along with the effect of gas cleaning in chapter 3 and infiltrating the fuel electrode with CGO in chapter 4. The microstructure has been investigated for the purpose of determining whether or not the different operation parameters have been able to achieve a more durable SOEC (chapter 5). Across these studies the resistance for the charge transfer process at the Ni-YSZ TPB, R_{TPB}, and the over-potential it gives rise to (η_{TPB}) have been identified as possible threshold for carbon formation. *In-operando* Carbon deposition was attempted monitored with the coupled use of Raman spectroscopy for determination of carbon formation and EIS for concurrent characterisation of electrochemical performance, though without success (chapter 6).

Figure 7.1 shows the R_{TPB} for the tested SOECs at the beginning (blue area), and end of the long-term durability test as dependent on the cumulative energy experienced at the TPBs during the test. The colouring and labelling of the individual tests are identical to the ones used in the previous chapters. Values for non-infiltrated cells have been marked with ”X”s, and the infiltrated cells with ”O”s. Using the cumulative energy converted by the cells, allows for comparison between cells tested at different current densities and durations. This also consider the non-identical developments of the η_{TPB} between tests. The energy was calculated by integrating

η_{TPB} in respects to charge $(i \cdot A \cdot t)$ converted during the tests. The R$_{TPB}$ values at the beginning of the tests are distributed within the range 0.05-0.23 Ω cm^2, with the exception of two 06HU tests, which showed a much greater R$_{TPB}$ due to the operation parameters. Though this behaviour was also seen in the iV characteristics for the tests in chapter 3. The variation of the R$_{TPB}$ values is partly ascribed to the different current loads and CO_2 utilisations (specially for the 06HU tests), though some of the variance is expected to stem from cell variance, contacting issues, and/or potential leaks based on the OCV performance seen in figure 3.3 (p. 34). The initial variation is significant since it spreads over approximately the same range as the tested non-infiltrated cells with the exception of 06HU and 06LU-1.

The distribution of R$_{TPB}$ values at the end of the tests shows a linear trend in regards to the experienced energy at the TPBs, the 06HU test are once again the exception to this behaviour. While these tests could be included in the trend line when comparing energy and porosity (fig. 5.11 p. 91), this is not the case in figure 7.1. This is indicative of a second process, in addition to the Ni migration, contributing to the large R$_{TPB}$ for these tests, which is likely due to the formation of carbon. The two 06HU tests are discussed further in section 7.1.1.

When comparing the 05HU tests, it is seen that the two tests without gas cleaning (05HU-1 and 05HU-2) share a position in the graph despite the differences in cell voltage (fig. 3.5 d) p. 39). Test 05HU-GC, carried out using gas cleaning shows a significantly smaller R$_{TPB}$. 05HU-GC is furthermore the only test of the ones operated at a 58% CO_2 utilisation having an R$_{TPB}$/TPB-energy ratio below the dashed trend-line in figure 7.1, which shows the positive impact of gas cleaning on cell durability.

The distribution of HU and LU (including CGO) tests above and below the trend-line shows that by minimising η_{TPB} through the reduction of R$_{TPB}$, leads to decreased degradation. This decrease could, as indicated by the trend-line be achieved by operating at a lower CO_2 utilisation, since this has shown to slow the increase in R$_{TPB}$ in this study. The trend-line also indicates that decreasing the parameters, i and t would mitigate degradation, though this is less relevant since this would also reduce the turnover rate.

From the figure, it can also be seen that the infiltration with CGO has, despite its inability to prolong the lifetime significantly as discussed in chapter 4 (fig. 4.7 p. 66), led to an ≈ 6x decrease in energy consumption for the process at the Ni-YSZ TPBs in the case of CGO-2, for approximately the same operation time when comparing with test 06LU-1.

Table 7.1 shows the data for figure 7.1 in its 1st part(not counting the test names). The total yield can be seen in the 2nd part of the table. Comparing the values from the first part of the table to the total yield and energy consumption, shows that CGO-

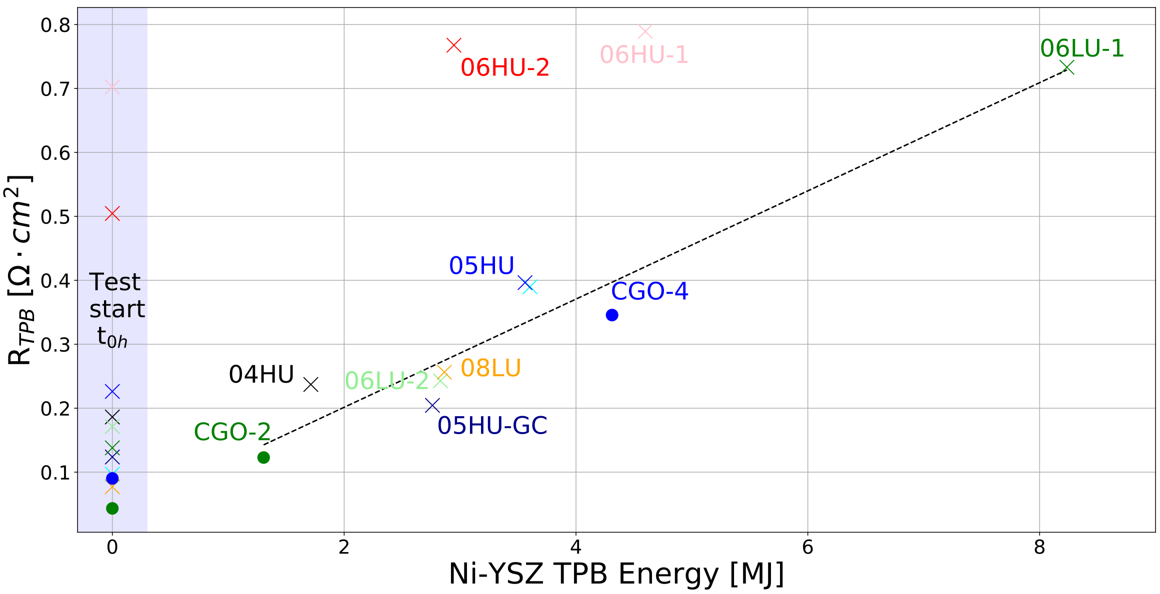

Figure 7.1: Determined values for R$_{TPB}$ in 10/90 CO/CO$_2$ (fuel electrode) and O$_2$ (oxygen electrode) at 750 °C based on the total consumed/experienced energy for the process at the Ni-YSZ TPB ($\int \eta_{TPB} dI \cdot t$) during long-term tested cells. The values included: Start of the test upon achieving operational current (Blue area), and at the end of the tests (White area). Colouring and labelling of the points are identical with those in chapter 3 and chapter 4. Non-infiltrated cells are marked with "X"s, and infiltrated cells "O"s. Dashed line: Linear regression for final R$_{TPB}$ values, excluding the 06HU tests. The initial R$_{TPB}$ values for the 06HU tests (red and pink) are outliers and matches what is seen in their iV characteristics. The data used for this plot can be seen in table 7.1

Table 7.1: The table is split into three parts. (1) Data for figure 7.1. (2) Energy specific yield, along with yield and total consumed energy. (3) Lifetime, defined as test duration before reaching η_{TPB}=190 mV. Linear regression was used for tests that did not achieve said overpotential during operation. Lifetime capacity: Expected total yield at end of life.

Test	**Total Energy Consumed at Ni-YSZ TPB**	**R$_{TPB}$**	**Yield**	**Total Consumed Energy**	**Energy Specific Yield**	**Lifetime**	**Lifetime Capacity**
	[MJ]	**[Ω cm^2]**	**[Nm^3]**	**[MJ]**	**[Nm^3 MJ^{-1}]**	**[h]**	**[Nm^3]**
04HU	1.71	0.237	2.6	26.7	0.097	6189.7	15.5
05HU-1	3.60	0.390	3.3	35.5	0.093	956.16	3.2
05HU-2	3.56	0.396	2.5	27.7	0.089	700.3	2.3
05HU-GC	2.76	0.204	3.5	36.3	0.097	3785.1	12.7
06HU-1	4.60	0.789	1.1	15.9	0.067	n/a	n/a
06HU-2	2.95	0.768	0.8	11.9	0.067	n/a	n/a
06LU-1	8.24	0.733	4.0	46.2	0.086	403.33	1.7
06LU-2	2.83	0.243	2.6	27.9	0.094	1367.8	5.7
08LU	2.86	0.256	2.8	28.7	0.099	505.69	2.5
CGO-2	1.31	0.123	4.5	49.8	0.091	4188.3	17.5
CGO-4	4.31	0.346	4.1	44.5	0.091	897.26	3.8

2 has the highest ratio between energy consumption at the Ni-YSZ TPB to yield ratio among all tests. The 2nd and 3rd best performing tests in this metric are 04HU and 05HU-GC respectively. Comparing the energy consumed at the Ni-YSZ TPB and total consumed energy, reveals a weakness in the previous comparison, in that the energy consumed at the Ni-YSZ TPB for the infiltrated cell CGO-2 only makes up 3% of the total energy, whereas the average across the non-infiltrated cells (excluding 06HU) is 11%. While the infiltrate might have improved the performance of CGO-2, the previous comparison does not take the energy used at the CGO double phase boundary into consideration, since this was not included in the ECM used for fitting the system. While this was chosen deliberately to enable to comparison between the cells using the same ECM, it does leave out some information. Another reason the CGO contribution was left out, was the difficulty fitting it due to its low peak frequency $\approx$ 1Hz, which leads to overlapping ECM components [23]. This means that the energy consumed at the CGO DPBs should be included in the ideal comparison of energy used for charge transfer processes.

7.1.1 06HU - The Outliers

Figure 3.5 c) (p. 39) showed the progression of the cell voltage for the two SOECs tested at 0.625 A cm^{-2} and 58% CO_2 utilisation (Tests 06HU), which is a deviationfrom the other tested SOECs. These tests showed both the highest initial cell voltage and the largest degradation rate. The variation seen for these tests were initially considered to be caused by their initial performance determined by EIS. The O6HU stood out due to a comparative large impedance contribution with a peak frequency of 1 kHz, a frequency associated with the charge transfer reaction in the Ni/YSZ electrode (RQ$_{TPB}$). While this large impedance contribution might have had some impact on the development in cell voltage over time, the observations from test 06LU-1 shows a similar cell voltage development, where a sharp increase is seen from $\approx$ 1300 mV to $>$1800 mV, upon the CO_2 utilisation change from 29% to 58%. This indicates that the test conditions are very impactful.

The η_{TPB} values for the 06HU tests at the beginning of the long-term tests, were determined to be above the threshold for carbon deposition, which is therefore expected to be a contributor to the increased degradation. 06HU-1, also displayed a η_{TPB} above the threshold for expected ZrO_2 nano-particle formation [125]. The initial R$_{TPB}$ values for the 06HU tests shown in figure 7.1 deviate from the rests of the tests. This deviation is ascribed to carbon formation as this tendency matches what is seen in the iV-curves (fig. 3.4 p. 35) in chapter 3). Due to the high initial η_{TPB} and expected carbon formation in the cells, it was not possible to calculate a non-zero lifetime capacity in table 7.1.

Furthermore, while microstructural changes might be contributing to the cell voltage increase, the fact that it deviates from the tendency line in figure 7.1 indicates degradation through other means, such as carbon deposition or ZrO_2 nano-particle formation [125].

7.1.2 The Overpotential at Ni-YSZ TPBs: η_{TPB} - A Factor for Carbon Deposition

The purpose of this project has been to increase the durability of Ni/YSZ ASC SOEC for CO_2 electrolysis operation. One of the causes for degradation during this type of operation is carbon deposition in the fuel electrode. The deposition of carbon damages the TPBs, either by blocking them or leading to disconnects in the percolating Ni-Ni network. Determining the threshold of when this occurs, is hence an important step towards mitigating degradation and prolonging the lifetime of SOECs.

Few studies have been made into carbon deposition during CO_2 electrolysis in SOECs, since SOEC technology has mainly been the focus of steam electrolysis, as reported recently in a review by Subotíc et. al. [223]. The few existing studies into this topic, measured carbon deposition at pCO lower than the thermodynamic Boudouard threshold, and defined it from this parameter [71, 72]. Navasa et. al. explained this carbon to be caused by diffusion limitation causing local build-up of CO, leading to the dissociation of CO to C and CO_2, through the Boudouard reaction [67]. In this project parameter η_{TPB} has shown to be indicative of carbon deposition during operation, carbon has specifically been observed in tests that achieved or went above $\eta_{TPB} \approx$ 190-200 mV during the particular operation conditions (gas composition) used in this project. Carbon was also here shown to deposit outside the conditions of what can be expected based on thermodynamic calculation of carbon activity for the Boudouard reaction. This confirms that carbon deposition likely occurs due to local variations in gas composition, which do not reflect the macroscopic test parameters. η_{TPB} might hence prove to be a metric that considers local gas composition at the affected TPBs despite it being an average across the cell.

In the previous discussion about figure 7.1 it was discovered that a low R_{TPB} is favoured for optimal performance. Minimising the initial value of R_{TPB} will have the advantage of a lower initial integral of η_{TPB}, hence allowing for a larger operational window for the cell to be operated under while still avoiding carbon formation. It also means that a low initial R_{TPB} will have a low initial η_{TPB}, which in turn will lead to a slow degradation, whereas a large initial R_{TPB} will degrade fast. The integral of $\Delta\eta_{TPB}$ (η_{TPB}-$\eta_{TPB-Init}$) for an large initial R_{TPB} will be greater than that of a low initial R_{TPB}.

The initial degradation during CO_2 electrolysis was in chapter 3 described to initially follow a linear trend, and was assigned to impurities in the CO_2/CO electrolysis feed gas, adsorbing to the Ni particles in the fuel electrode. Based on this hypothesis, a low initial R_{TPB}, and corresponding low η_{TPB} will increase the time in the linear region and time before carbon deposition.

Ni migration is another cause of degradation, as discussed in chapter 5, where the pore fraction correlated linearly with the Ni-YSZ TPB energy for the non-infiltrated cells. This is somewhat troubling, since it means that R_{TPB} impacts its own degradation. I.e. if the initial value of R_{TPB} is large, the η_{TPB}, and hence the energy ($\eta_{TPB} \cdot I \cdot t$), will be large, which will lead to increased degradation. It is hence doubly important avoid a large initial R_{TPB}, so as to prolong the lifetime and avoid carbon formation.

7.1.3 Impurity Tolerance - Gas Cleaning and CGO Infiltration

Figure 3.5 d) (p. 39) and 7.1 show that gas-cleaning impacts the cell performance during CO_2 electrolysis, which was also shown by Hauch et. al.[65]. Based on these findings all future tests/operation should optimally be carried out employing gas-cleaning to optimise operation.

In chapter 3 the initial linear degradation occurring for the tested SOECs was assigned the effect of poisoning. This would, however, only be a part of the initial degradation, as other degradation processes such as Ni migration and coarsening are also expected. This is based partly on previous findings [65, 75, 76], and the observations in figure 3.5, where the initial degradation rate is dependent on more than gas flow.

In case of the degradation solely being caused by poisoning, a more clear trend between the fuel gas volume through the fuel electrode and the cell voltage, would be expected from the results. Specifically, the low utilisation test would due to its higher gas flow rate be exposed to a larger cumulative amount of impurities, and would hence be expected to degrade faster than the cells with a lower gas flow rate. Similarly, tests carried out at high current would be exposed to more impurities than the tests carried out at low current. While this trend is only expected in the initial degradation before the Ni particles have been covered by a monolayer of chemisorbed impurity species, saturation is expected to take $\approx$ 500h since the impurities also adsorbs to the Ni surface area in the fuel electrode support layer which extends the poisoning effect as seen in previous studies by Ebbesen et. al.[148, 224]. In a recent study, Riegraf et. al. [225] studied the poisoning of ESC SOEC with Ni-CGO and Ni-YSZ fuel electrodes using an estimated 100 ppb of sulphur gas phase impurities in their feedstock (CO/CO_2). The findings from this study showed a Ni-saturation after $\approx$ 70 h, which was ascribed the lower number of Ni-surface sites in ESCs compared with ASCs [225], which is in line with the observations in this study. This trend is however not the case, as can be seen in fig. 3.5 p. 39, where the slope of the cell voltage developments for the 06LU tests are less steep in comparison with those of the 06HU tests, indicating that the degradation is caused by more than adsorption of gas phase impurities.

CGO was infiltrated due to its reported catalytic qualities, carbon tolerance and resistance towards impurities [158, 225]. Riegraf et. al. [225], reported in the study, introduced above, a cell voltage difference of 19 mV for a cell with a Ni-CGO fuel electrode before and after 55h exposure to gas impurities, whereas the cell voltage difference was 440 mV for the SOEC with Ni-YSZ fuel electrode. While the steepness of the initial linear degradation for the infiltrated cells were smaller than for the non-infiltrated cell shown in figure 4.7 (p. 66), the difference is less pronounced, even after the ≈ 500h that is expected to reach impurity saturation of the Ni surface [224]. This means, that while some of the improved performance is likely caused by increased impurity resistance, other factors such as the increased number of TPBs/DPBs, also factor into the performance. To study the impact of changing cell parameters and elements on impurity tolerance, it is hence recommended to use ESCs for reducing experiment time, by omitting the effect of also having to saturate the support layer [225].

7.1.4 Microstructure

Carbon deposition was previously determined to occur through the Boudouard reaction caused by a high concentration of CO near the TPBs due to insufficient diffusion [67], which indicates that a more porous structure might decrease the risk of CO build-up. Increased pore fraction would however lead to a decrease in TPB density and electrochemical performance [20]. The decrease in TPB density from increased porosity would lead to higher overpotentials at the local TPBs, which would increase the risk of carbon deposition. This does therefore not seem like the proper strategy, as the TPB density should ideally be maximised in the active fuel electrode area [16]. A linear correlation between the energy used for the process at the Ni-YSZ TPB and the pore fraction, was observed in figure 5.11. Similarly a correlation was observed between cumulated charge and pore fraction (fig. 5.10 d), though with the 06HU tests as outliers. The observations were explained by Ni migration (/increase in pore fraction) being dependent on the cumulatad charge, while the η_{TPB} is below ≈ 190-200 mV. Above this η_{TPB} threshold CNT and ZrO_2 nano-particle formation [125] are expected to occur, further accelerating microstructural degradation (fig. 7.1).

In this study the threshold for carbon deposition was found to be η_{TPB} ≈ 190-200 mV. Since carbon is caused by a high concentration of local CO [67], a different fuel electrode structure with increased mass transport, would be expected to be more tolerant towards carbon deposition. An example of this could be ESCs, where issues with diffusion is less of a problem in comparison with ASCs [225].

The degradation of the percolating Ni network can be seen in figure 5.3 (p. 79). Figure 7.2 shows sketches of the Ni-YSZ fuel electrode and electrolyte regions for two cases of operation: a) low η_{TPB}, b) high η_{TPB}. Colour coding: White - Fuel electrode with percolating Ni network, Black - Fuel electrode where the percolating Ni network is lost, Grey - Electrolyte. The tendencies sketched in figure 7.2 matches the observations in the micrographs in chapter 5, where cells that have experienced

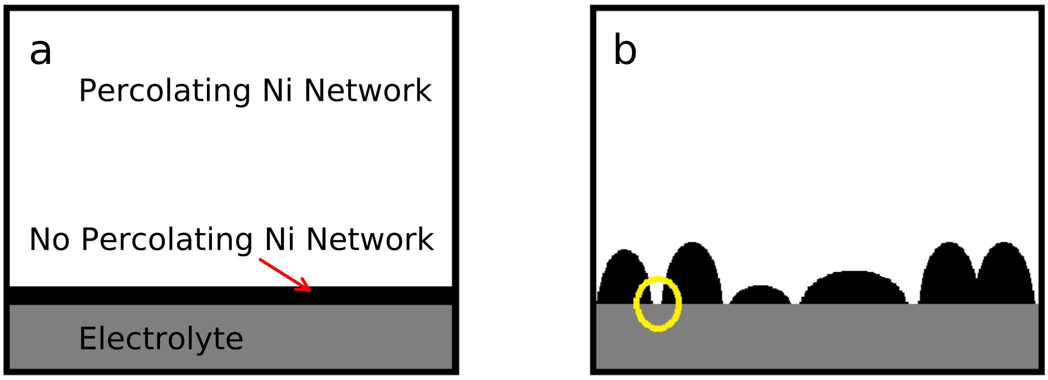

Figure 7.2: Sketch of fuel electrode and electrolyte part of an SOEC. Grey: Electrolyte. White: Fuel electrode with percolating Ni network. Black: Fuel electrode without percolating Ni network. a) Sketch of test carried out at low η_{TPB}. b) Sketch of test carried out at high η_{TPB}

a low η_{TPB} (a) show an evenly distributed loss of percolating Ni around the electrolyte, whereas cells having experienced a high η_{TPB} (b) shows an uneven loss. This uneven loss of percolating Ni for the high η_{TPB} tests, presents as thin Ni pathways (as seen in the yellow circle) to the electrolyte among areas with non-percolating Ni. Since the current will choose the path of least resistance, this will lead to an uneven current distribution, where electron transport through Ni will be favoured over ionic transport through 8YSZ, causing an increase in η_{TPB} near the electrolyte through the high current density. This can give rise to a local build-up of CO, or a sufficiently low pO_2 for partial reduction of ZrO_2 [125].

The infiltrated SOECs for the study in chapter 4 proved troublesome to test since they broke either during mounting, heating, or the initial reduction. This led to the implementation of a mild/slow reduction protocol used for this study. Across the studies two causes for this comes to mind: Either YSZ transformation [174] or thermal shock during infiltration [181]. In the study by Riyad et. al. [181], YSZ was shown to lose strength when cooled rapidly to room temperature from 300 °C. While the individual loss upon cooling is rather small, repeated thermal cycling, as experienced during infiltration, is expected to accumulate. The combination of these two factors in addition to a slightly bent cell after reduction, increased the risk of failure as a result.
Chapter 5 showed pronounced microstructural damage to the infiltrated cells, especially test CGO-4, which is inconsistent with the performance of the cells shown in chapter 4. It is hence likely that the cells were damaged after the long-term durability tests, either during the final characterisation, cooling, or sample preparation. Some of the damage to test CGO-2 might be caused during its re-reduction made

necessary due to a cut-off of the gas feedstock, after which the performance had decreased significantly (fig. 4.7 p. 66).

7.2 Discussing Energy Specific Yield and Lifetime Capacity

Table 7.1 shows, in its 2nd part, the energy specific yields for the tests in addition to the total yields, and total consumed energies used for calculating this. The yield assumes 100% faradaic efficiency. The total energy was calculated as the integral of the cell voltage curves (fig. 3.9 p. 43 and 4.8 p. 67) with respects to current and time. The best and worst performing cells in this metric have been highlighted by green and red respectively. The best performing test in this metric is test 08LU, with tests 04HU and 05HU-GC sharing the 2nd place. It is seen that the difference between the 06HU tests and the 2nd to worst performing test (06LU-1), is larger than the distribution of the other cells, which defines energy specific yield of the 06HU tests to be in its own group.

The 3rd part of table 7.1 describes lifetime and lifetime capacity. Lifetime is defined as the duration the cell can be operated without carbon deposition, defined as $\eta_{TPB} <$ 190 mV. In some cases, this matches the test durations. In others carbon is expected before or after termination. The lifetimes that exceeds the test durations was calculated through linear regression based on the fitted values of η_{TPB}. The lifetime capacity metric was introduced by Küngas et. al., and is defined as the total expected yield throughout the lifetime of a cell or stack [226]. Küngas et. al. [226] reports lifetime capacity to be independent of operation parameters, such that the operator can choose whether they want a short lifetime with high production rate, or long lifetime with a low production rate, with the caveat that this is within a certain window of parameters. Based on this report it must be assumed that the operation parameters during this project have been outside of the previously mentioned window, as the lifetime capacities seen in table 7.1 vary significantly based on operation parameters. For the non-infiltrated cells this varies between 1.7 Nm^3 CO for test 06LU-1 to 15.5 Nm^3 CO for test 04HU. The best over-all performing cell in this metric is the infiltrated CGO-2 with 17.5 m^3 CO produced. There is a correlation between R$_{TPB}$ and lifetime capacity, but this is expected since the former has been used to define the latter. The lifetime capacities of the tests 04HU, 05HU-GC, and CGO-2 stand out from the rest by exceeding 10 m^3 CO. This indicates that the lifetime capacity is extended when operated at a low electrolysis current below 0.5 A cm^{-2} (at 750 °C). The lifetime capacity can however be extended at higher current densities by gas cleaning or modification of the fuel electrode by infiltration of CGO. The possibility of a higher operation current in clean gas or with an infiltrated cell, means a larger operation window and hence greater flexibility for the operator [226].

The two best performing tests in this study considering lifetime capacity are 04HU and CGO-2. While CGO-2 has the largest lifetime capacity, 04HU is only 11% off and has a 7% higher energy specific yield. To determine the most profitable cell, when taking both metrics into consideration, the cost pr. Nm^3 is calculated. For this calculation the price of electricity 108.86 EUR/MWh is used (Danish electricity price the March 21st 2023 according to www.euenergy.live), which equals 0.031 $/MJ. For this calculation it is assumed that electricity makes up 70 % of the operation cost [151], and the cell cost makes up the remainder. This results in the production costs of 0.318 $ Nm^{-3} for 04HU at and 0.341 $ Nm^{-3} for CGO-2. It is hence most profitable to operate with 04HU, in which the calculation has not considered a potentially increased production cost involved with infiltration. The CO is furthermore more concentrated for this operation due to higher CO_2 utilisation. This means that less energy is required to a higher concentration.

While the calculation above shows that the 04HU test is most profitable, the infiltrated cell CGO-2 has the advantage of a larger operation window. This means that even if the lifetime capacity of CGO-2 does not increase by being operated under milder conditions. It has the advantage of regulating productivity dependent on the electricity price to a much bigger extent than 04HU.

It should be noted that test 08LU outperforms the two discussed tests on profitability, with 0.312 $ Nm^{-3}, only considering cell and electricity cost, it is however hypothesised that the much lower lifetime capacity would lead to a higher price due to maintenance costs.

Comparing the lifetime capacity of the tested cells in this study with the SOEC stacks in the study by Küngas et. al. [226], requires taking the larger active area of the latter into consideration. Doing this yields area specific lifetime capacities, which are 0.97 and 1.09 Nm^3 cm^{-2} for test 04HU and CGO-2 respectively. With an individual cell area of ≈ 110 cm^2 for the stacks tested by Küngas et. al., this corresponds to 0.38, 0.66, 0.57, and 2.07 Nm^3 cm^{-2} for stack S1 through S4 [226]. Comparing the area specific lifetime capacity for test 04HU and CGO-2 with the stacks, shows the single cells coming out on top in 3/4 cases. S4 however outperforms the tests 04HU and CGO-2 greatly, by having twice the area specific lifetime capacity. This comparison, and the results thereof should be taken lightly, as the lifetimes and hence lifetime capacities were found using different methods. Specifically the method of determining the lifetimes of the stacks/species, where they were determined to be the full duration of the tests for the stacks tested by Küngas [226], whereas they were found by extrapolation for the test 04HU and CGO-2.

7.3 Increasing Durability and Yield

Comparison of all the tested cells (fig. 3.5 p. 39 and 4.7 p. 66) shows that operation at a low current reduces degradation, leading to increased longevity. Infiltrating the fuel electrode with CGO has also shown to increase performance, though not to the extent where it could be operated under harsher conditions, and still perform better than the tests in chapter 3 operated at low current. Gas cleaning has in the case of test 05HU-GC shown to decrease degradation significantly, indicating that impurities in the fuel electrode gas exists and leads to degradation, and that this degradation can be mitigated through removal of said impurities up-stream. The test 05HU-GC performed similarly to 04HU, though slightly worse at the end. Based on these observations the optimal operation conditions for maximising longevity is to combine low current density, infiltration, and gas-cleaning.
Longevity matters because it is a factor in the lifetime capacity as seen table 7.1. It is hence also relevant to maximise the operational current and by extension yield thereof. In the window of operational parameters studied during this project, it is however expected that operating at a low current with infiltrated fuel electrode in cleaned gas would also lead to the best lifetime yield due to significantly smaller amount of degradation. Since carbon deposition has been observed to be dependent on R_{TPB}, operation at a higher temperature would lead to less carbon formation due to a decrease in R_{TPB}. Furthermore, the carbon deposition through the Boudouard reaction is also less likely to occur at a higher temperature [204]. Operation at a higher temperature might however lead to a faster microstructural degradation due to increased Ni mobility [227].
Another proposed method of mitigating carbon deposition is through the addition of Cu to the Ni [223, 228]. This was attempted shown in chapter 6, though no effect was shown due to the carbon contaminant discussed in said chapter. In a study by Skafte et. al. a SOEC of similar composition to the one in this project was infiltrated with Cu-CGO in the fuel electrode [72]. This study did however, not show any improvement towards carbon tolerance [72].
A study on SOFC run using a feedstock from biomass gasification by Mermelstein et. al. calculated that carbon formation could be avoided by providing enough O^{2-} for oxidising the deposited carbon at the fuel electrode [229]. This indicates that operating the SOC in reverse (FC mode) could be a method for *in-operando* carbon removal. A study by Königshofer et. al. where carbon had deposited during co-electrolysis, did not show any improvement in performance after fuel cell operation [230]. This, along with studies carried out with *in-operando* spectroscopy for carbon determination, indicates that the carbon formation occuring during fuel cell opera-

tion is reversible [231], whereas it is harder to reverse for carbon deposited during electrolysis operation, even in carbon tolerant SOECs [232]. Although harder, the previously mentioned study by Königshofer et. al. managed to show a regenerative effect by operating in steam electrolysis mode after carbon had deposited during co-electrolysis.

7.3.1 Determining SOEC Durability

Determination of the durability of SOECs is difficult, due to the complexity, a system that of consists of multiple interconnected parameters, whether they be external (gas feed, current density, microstructure) or internal (resistances and current distributions). The parameters considered in this study have mainly been current density, CO_2 utilisation, η_{TPB}, and infiltration. Another very significant parameter is time. Time is important due to the solid state nature of the system where degradation mechanisms, such as Ni migration/coarsening have a time element to them, as they do not occur instantly upon changing conditions. This means that tests with the purpose of determining the durability of SOECs, should be of a duration to account for this. During this project, this was considered when a test duration of $\approx$ 1000 h was chosen. This test duration allows for saturation of impurities on the Ni particles to occur, which as previously mentioned takes $\approx$ 500 h [224]. Ni migration has previously reported to diminish after a few kh [215]. Carbon deposition is by far the fastest of the degradation reactions as it has been shown to deposit in minutes during current-voltage response measurements [72]. The time-frames for the investigated degradation mechanisms in this project did hence allow for a resolution within the framework to display and highlight the impact of changing parameters, i.e. gas cleaning and infiltration. The short time-frame of carbon deposition did also allow for a more immediate reaction to this phenomenon. In a study by Ebbesen et. al. [148] the in-plane voltage of the fuel electrode was used to show the developing coverage of gas phase impurities. A similar investigation was also tried in this project, though without the same straight-forward tendency. It was, however, noted that the cells operated at low current and gas cleaning (04HU and 05HU-GC), were the only cells where this parameter was stable during the long-term test.

While this study sought to determine durability by investigating the onset of degradation, another approach is to study it by showing that no (or limited) degradation occurs during testing [20, 175]. While this approach can be used to show improved performance of the technology, it only provides the knowledge that no degradation occurred during the test duration. While tendencies in cell voltage or other metrics can be extrapolated to determine a total lifetime, this only works if the extrapolated parameter follows the model for extrapolation. This will not be the case if an unexpected threshold for degradation is met that shortens the lifetime.

With a SOEC lifetime goal of 5-10 years (45-90 kh) [87], it is not realistic/viable to test for the whole duration of all new SOEC materials and components. This means that as the SOEC technology keeps improving accelerated testing is required to show the effect of said improvements [233].

Chapter 8

Conclusion

Based on the results from testing and characterisation of ASC Ni/YSZ SOECs in the previous chapter the following conclusions can be drawn:

- The best performance was achieved for a SOEC operated at 0.375 A cm^{-1} with a 58% CO_2 utilisation, which showed a degradation rate of 38 mV kh^{-1}
- Low current operation is expected to optimise lifetime yield.
- Gas cleaning mitigates degradation significantly.
- Carbon has been observed to deposit when the η_{TPB} reaches 190-200 mV.
- Carbon deposition in the fuel electrode can be detected by a current/voltage response, which shows a sharp increase leading to a bend in the iV curve.
- The carbon deposited in the fuel electrode takes the form of filaments identified as carbon nano-tubes due to its G_2 peak from Raman spectroscopy.
- In the tested SOECs carbon mainly deposits through the Boudouard reaction due to local build-up of CO at the TPBs.
- Loss of percolating Ni network near the electrolyte is observed in all tested cells. In the SOECs tested at low current, this loss was distributed evenly near the electrolyte. The loss of percolating Ni in the SOECs tested at high current is distributed unevenly leading an uneven current distribution.
- The pore fraction of the fuel electrode 0-4 μm from the electrolyte, shows a correlation with the energy consumed for the electron transfer process at the Ni-YSZ TPBs.
- Infiltrating the fuel electrode with gadolinia doped ceria has shown to improve performance and durability.
- Gadolinia doped ceria infiltration does not impact the threshold for carbon deposition.

- It has been found that there exists an optimum infiltrate loading. The test results show that this is below 227 mg cm^{-3}, since the SOEC with 124 mg cm^{-3} fuel electrode infiltrate loading showed the better performance.
- The infiltrated SOECs have shown an improved percolating Ni-network.
- The infiltration process has led the infiltrated SOECS to show microstructural damage. Thermal shock during infiltration is expected to be the cause of this damage.
- Carbon was detected through the electrolyte with Raman spectroscopy.
- Continued Raman provided increased signal-to-noise ratio leading to all the peaks G$_1$, D’, and G$_2$ being discernible concurrently.

Finally, to achieve optimal durability the methods for improving SOEC performance should be combined such that infiltrated SOECs are operated with cleaned gas at a suitable current.

Chapter 9

Outlook

The transition away from the use of fossil fuels is under way. A contributor to this is the SOEC technology, which provides both a means of energy storage as well as sourcing of chemicals otherwise sourced from the petrochemical industry. While this project has studied some of the degradation mechanism of SOECs, challenges and questions about degradation still remain, such as:

- Does the rate of degradation continue to increase until total failure, or does it level out? If so, when? And is this determined by operation condition? And which ones?
- The threshold for carbon formation was determined to be η_{TPB} ≈190-200 mV. What would it be in a ESC where convection has a larger contribution to mass transport?
- How would the performance look for the test carried out at 0.375 A cm^{-2} and 58% utilisation if it had been allowed to continue for 2, 10, or 20kH? How long would it take for it to reach η_{TPB} ≈190-200 mV? Would this coincide with a cell voltage of ≈1350-1380 mV like in the other tests?

9.1 Further work

A project is never done, it runs out of time. This section includes ideas for continuing this line of research, in addition to the questions above, in addition to ideas for studies that were was not carried out due to lack of time.

9.1.1 Infiltration with TiO_2

A line of investigation that had been planned, but time did not permit, was the study of infiltration with TiO_2 in combination with CGO. TiO_2 has not by itself been shown to be catalytically active. Previous studies have however shown that TiO_2 improves the wettability between Ni on YSZ through surface energy minimisation [234, 235]. This means that TiO_2 can mitigate coarsening of the Ni particles [236], and increase the TPB density in the fuel electrode [237]. Inclusion of TiO_2 in the fuel electrode is hence expected to improve durability by retaining the Ni particles in the active electrode. In addition, the increase in TPB density will lead to decreased η_{TPB} at the specific TPBs. Care should however be taken when infiltrating with TiO_2, as studies where it was sintered with YSZ lead to decreased ionic conductivity [236, 238]. This decrease in conductivity is caused by a change in structure where the sixfold coordination of Ti induces a tetragonal structure and thereby reduces the oxide vacancies in the cubic 8YSZ [239]. Notably, this was seen in a study where the samples were sintered at ≥ 1300 °C, it might hence be possible to avoid this effect if the TiO_2 was to be introduced as an infiltrate.

9.1.2 Mass Transport Dependency of CO/CO_2 for Carbon Deposition

In a recent study by Riegraf et. al. [225], ESCs rather than ASCs were used because of their decreased proneness to local build-up of CO, and thereby carbon formation. This hypothesis seems sound due to the decrease in diffusion length when removing the 200-300 μm CO/CO_2 have to travel through in an ASC. While reasonable, there have been few studies comparing the effect that the presence of the fuel electrode support layer has on carbon formation. The proposed study for this would test four cells with different fuel electrode microstructure in 10/90 CO/CO_2 gas composition at 750 °C. The fuel cell microstructures would be:

1. Similar ASC to the ones tested in this study, as the threshold for carbon is known.
2. As above, but with a more porous active fuel electrode, inspired by the study by Hauch et. al. [20]
3. ESC with a dense fuel electrode similar to the active fuel electrode in ASCs
4. ESC with a porous fuel electrode.

The cells would be tested at a constant current, while being monitored with EIS until achieving η_{TPB}=200 mV, after which the cells would be probed for carbon using an appropriate method; e.g. Raman spectroscopy, XRF, or EDS.
This study could be accompanied with simulations similar to the one by Navasa et. al. [67].

9.1.3 Determination of Carbon Morphology During EC Operation

The carbon observed in this was determined to be CNTs, based on the presence of the G_2 peak observed by Raman spectroscopy [143] and the findings by Tao et. al., where the carbon was identified as multi-walled CNTs by TEM/EDS [69]. It would hence be relevant to confirm that the presence of carbon in the tested cells is indeed CNTs by TEM/EDS, or identify which other fibrous carbon species they might be. It is also relevant to identify the ”fluffy” mass observed near the electrode in the micrographs for the tests carried out at high current and CO_2 utilisation (06HU), to confirm if it is indeed deposited carbon. If this is the case, it would be relevant to determine whether it is an agglomeration of short CNTs or of another morphology. This could also lead to the determination of a threshold where the morphology of the deposited carbon changes. The suggested methods for this study are TEM/EDS similar to the study by Tao et. al. [69].

Appendix A

Preprint of article: "CGO-Infiltrated Ni-YSZ SOEC Fuel Electrodes for Increased Carbon Tolerance during CO2 Electrolysis"

Citation details: Clausen, A. K., Traulsen, M. L., Hendriksen, P. V., Sun, X., & Hauch, A. (2021). CGO-Infiltrated Ni / YSZ SOEC Fuel Electrodes for Increased Carbon Tolerance During CO2 Electrolysis. *ECS Transactions*, 103(1), 1945–1954. https://doi.org/https://doi.org/10.1149/10301.1971ecst

This is the version of the article before peer review or editing, as submitted by an author to ECS Transactions. IOP Publishing Ltd is not responsible for any errors or omissions in this version of the manuscript or any version derived from it. The Version of Record is available online at https://doi.org/https://doi.org/10.1149/10301.1971ecst

CGO-Infiltrated Ni/YSZ SOEC Fuel Electrodes for Increased Carbon Tolerance during CO_2 Electrolysis

A. K. Clausen, M. L. Traulsen , P. V. Hendriksen, X. Sun, and A. Hauch

Department of Energy Conversion, Technical University of Denmark, Fysikvej, bld. 310, 2800 Kgs. Lyngby, Denmark

Solid Oxide Electrolysis Cells (SOEC) have the ability to operate as CO_2 electrolysis cells, reducing CO_2 to CO. Applying SOEC for CO_2 electrolysis should be done carefully, since processes including carbon deposition lead to decreased life-time. This study is investigating the effect of the fuel electrode overpotential on carbon deposition in the Ni/YSZ fuel electrode, and the effects of CGO infiltration of the fuel electrode on carbon deposition, on performance during CO_2 electrolysis. Long-term durability test shows an increase in degradation rate from 252 mV/kh to 467 mV/kh over a ~50 h period at ~1375 mV. The carbon deposition threshold is investigated through the potential-current response, where a bend around 1375 mV in the iV-curve led to a hysteresis effect. Raman spectroscopy of the long-term tested cell shows carbon deposition; the largest quantities are found near the fuel gas inlet and the amount decreases along the gas flow direction.

Introduction

Solid oxide electrolysis cells (SOECs) enable production of syn-gas ($CO+H_2$) through co-electrolysis of CO_2 and H_2O. Syn-gas can, subsequently be used for production of hydrocarbons e.g. fuel and chemicals through the e.g. the Fischer-Tropsch process as an alternative to fuels sourced from the petrochemical industry. Using electricity from renewable sources and CO_2 of biogenic origin the fuels and chemicals can become CO_2 neutral. Hence, the SOEC technology has great potential for enabling the transition to renewable energy production due to the ability to close the carbon cycle, storing energy, and can thus play a key role in the balancing of intermittent electricity-generation from renewable sources. While the SOEC technology shows great potential, being able to electrolyze CO_2 to CO with high efficiency (1), long-term durability is still required to increase viability of the SOEC technology. One source of degradation causing insufficient durability is carbon deposition in the fuel electrode during electrolysis operation at an over potential below the thermodynamic potential for carbon formation (1). Impurities in the fuel gas such as sulfur is another cause of degradation, where concentrations down to 5 ppb has shown to have a harmful effect to the fuel electrode during CO_2 electrolysis (2). “Safe” operation conditions exists that makes it possible to operate an SOEC in CO_2 electrolysis mode for more than a year (1). However, reaching a year of operation requires carefully chosen operating conditions and a supply of clean CO_2, i.e. by cleaning the inlet gas. For more precise identification of what “safe” operating conditions are, it will be necessary to map the threshold of carbon deposition in the regime outside of the thermodynamic conditions at which carbon deposition. Furthermore, it is very attractive to modify the SOEC to achieve increased tolerance towards impurity poisoning and thereby extended safe operating window for CO_2 electrolysis where carbon deposition is avoided.

The aim of this study is investigating the threshold for onset of carbon formation in the Ni/YSZ based fuel electrode of SOEC. The investigation is carried out by carefully studying the current-voltage responses during recording of iV-curves in line with the study by Skafte et al. (3). And by thorough post-mortem analysis of tested SOEC. The carbon-deposition threshold will be investigated in a cell with and without infiltrated CGO in the Ni/YSZ electrode.

Experimental

Cell Specifications

The tested cells in this study were planar fuel electrode supported Ni/YSZ cells with the structure Ni/YSZ|YSZ|CGO|LSCF/CGO. The fuel electrode consisting of a Ni/3YSZ support layer, Ni/8YSZ active layer, an 8YSZ electrolyte, CGO barrier layer and an LSCF/CGO oxygen electrode. The cells had a footprint of 53x53 mm^2. With a 40x40 mm^2 LSM oxygen electrode contact layer which defines the active area Cells are similar to those reported by Trini et al. (4).

Infiltration

Ce- and Gd-nitrate were mixed in water in a 4:1 molar ratio to obtain a 1 M CGO ($Ce_{0.8}Gd_{0.2}O_{1.9}$) precursor solution. 1 wt% of the surfactant P-123 was added to the solution to improve wetting of the structure. The CGO-precursor solution was distributed over the surface of a reduced fuel electrode. Reduction of the fuel electrode was carried out as described by Tong et al. (5). Any remaining precursor solution was removed with a paper tissue. The infiltrated cell was placed in a chamber furnace heated to 350 °C and left for 30 min for the nitrate solution to decompose to CGO. The cell was infiltrated until a loading 250 mg cm^{-3} CGO was achieved, requiring 3-5 repetitions of infiltration and heating.

Cell testing and electrochemical characterization

The cells were tested using an in-house constructed test setup as described in previous work (Figure 1 Cell Assembly 2 in ref. (2)), using gold rather than glass sealant, and no sealing on the oxygen electrode side of the set-up. The procedure for test start-up, sealing and reduction at 850 °C is described elsewhere (6).

Table I describe the test conditions and applied characterization methods during the initial characterization. For long-term electrochemical performance test the cell was tested at a current density of -0.5 A cm^{-2} with a 58% CO_2 utilization at 750 °C for 1000 h. During the test mass flow controllers (MFCs) was programmed to supply the cell with a 10/90 mixture of CO/CO_2 to the fuel electrode, and O_2 (50 l/h) to the oxygen electrode. From pO_2 measurements by a sensor placed at the gas inlet the fuel gas composition was determine to vary +/- 1% in relation to the programmed gas composition during the test. The performance of the cell was monitored during the long-term tests by electrochemical impedance spectroscopy (EIS) every 8 h. Post-aging -characterization was done in CO/CO_2 at 750 °C and 700 °C, see table I for additional information.

The threshold for carbon deposition was investigated for two cells, a CGO infiltrated cell and a cell without infiltrate. The carbon deposition threshold was investigated at 750 °C with O_2 at the oxygen electrode and MFCs programmed to supply a 10/90 mixture of CO/CO_2 at the fuel electrode. These short tests focusing on characterization via i-V-curves were carried out using the same setup as described above. The initial characterization of the two cells used the investigations of the threshold for carbon depositions was shortened to only include measurements at 850 °C and 750 °C as specified in table I. The carbon deposition threshold was investigated for two different gas flows corresponding to a current density and CO_2 utilization of -0.5 A cm^{-2} with a 58% CO_2 utilization and -1 A cm^{-2} with a 29% CO_2 utilization at the programmed gas flows. The actual inlet gas composition fed to the cell during the iV-curves was calculated pO_2 sensors placed at the gas inlet. The fuel gas composition for the non-infiltrated cell was calculated to be to be 14/86 CO/CO_2 with <1% variation throughout the measurements. The fuel gas composition for the infiltrated cell was calculated to 5/95 CO/CO_2.

Electrochemical Impedance spectra (EIS) were recorded using a Solartron 1255 frequency analyzer. IS were recorded in the frequency range from 96 kHz to 0.1 Hz with 12 points per decade. The complex-linear-least-squares (CNLS) method was used to fit the equivalent circuit model: $L\text{-}R\text{-}RQ_{ion}\text{-}RQ_{TPB}\text{-}G_{ox}\text{-}RQ_{Diff}\text{-}RQ_{Conv}$ to the recorded EIS (previously described by Hauch et al. (7)). The CLNS analysis of the IS was done using the in-house developed Python-based software RavDav (8).

TABLE I. Test conditions for initial electrochemical characterization of cells. Total flow for the fuel electrode gasses was 24 l/h and 20 l/h when using $H_2O:H_2$ and $CO_2:CO$ respectively. In the last column "+" and "-" respectively indicates fuel and electrolysis mode.

Fuel Electrode	Oxygen Electrode	Temperature	Characterization
4:96 – $H_2O:H_2$	Air/O_2	850/800/750/700°C	EIS, +iV
20:80 – $H_2O:H_2$	Air/O_2	850/800/750/700°C	EIS, +iV
50:50 – $H_2O:H_2$	Air/O_2	850/800/750/700°C	EIS, +/-iV
90:10 – $H_2O:H_2$	Air/O_2	750°C	EIS
50:50 – $CO_2:CO$	O_2	750/700°C	EIS
50:50 – $CO_2:CO$	Air	750	EIS
90:10 – $CO_2:CO$	O_2	750/700°C	EIS
90:10 – $CO_2:CO$	Air	750	EIS

Post-mortem Raman characterization

A Renishaw InVia Reflex Spectrometer system with a 532 nm laser was used for Raman spectroscopy on fractured cross sections of the long-term tested SOEC. Measurements were done with a 10 s exposure time, 1 µm beam spot size on the sample, and a laser power of <8 mW.

Raman spectra were recorded of the Ni/YSZ fuel electrode 0-12 µm from the fuel electrode/electrolyte interface with a 2 µm step-size. Recalling the cell geometry; with a 40x40 mm^2 oxygen-electrode contact-layer printed on top the rest of the cell with an area of a 53x53 mm^2, leading to only the part of the cell with contact layer applied, experiencing a current load and subsequent polarization. The fuel electrode was characterized at parts of the CO_2 inlet with and without oxygen-electrode contact-layer. Similarly, characterization was done at the CO_2 outlet piece of the cell i.e. with and without oxygen electrode. Lastly, a part of the fuel electrode from the middle of the cell (in regards to gas flow direction) was characterized by Raman spectroscopy.

Results and Discussion

Cell Tests

Figure 1 shows the development of cell voltage over the duration of the long-term durability test and two lines representing the average degradation rate based on linear regression in the intervals 200-400 h and 600-800 h. The cell voltage degrades throughout the long-term durability test which is seen by the increasing cell voltage. After an initial rapid increase in cell voltage during the first ~50 h, the degradation rate (dV/dt) stabilizes at ~252 mV/kh, exemplified by the linear regression in the interval 200-400 h. This degradation rate is stable until the cell voltage reaches ~1375 mV at ~500 h into the test leading to a slight bend in the cell voltage curve. At this cell voltage, the degradation rate increases significantly over a ~50 h period, after which a less, but continuous increase in the degradation rate occurred lasting until the end of the test. The degradation rate after the significant increase is exemplified by the linear regression in the interval 600-800 h which results in a dV/dt of 467 mV/kh. The continuous increase of degradation rate is furthermore illustrated in the line, as it initially is above the measured data, and below the measured data in the end of the interval, whereas the linear regression between 200-400 h matches the measurements throughout the interval.

Figure 2a shows iV curves recorded in 14/86 CO/CO_2 at the fuel electrode, 50 l O_2/h, at 750°C reaching a 29% CO_2 utilization at the maximum current density: -1.0 A cm^{-2} for the red iV curve, and the blue iV curve reaching a 58% CO_2 utilization at its maximum current density: -0.5 A cm^{-2}. A sudden increase in cell voltage leading to a bend at ~1380 mV is observed in the iV curve reaching -1.0 A cm^{-2} (red).

The increase in cell voltage observed at ~1375 mV during both the long-term durability test (fig. 1) and in the iV curve in fig. 2a indicate a threshold for the onset of a degradation mechanism. The bend in the iV curve furthermore leads to an increased hysteresis effect, which has previously been shown to indicate the onset of carbon deposition in the fuel electrode by Skafte et al. (3).

The initial degradation rate observed in fig. 1 is roughly constant until the bend at ~500 h into the durability test. The initial degradation occurs despite carefully chosen gas composition that should not lead to thermodynamically favorable carbon.

Table II shows the gas compositions and the calculated carbon activities for the long-term durability test. Carbon activities was calculated in thermodynamic equilibrium with the gas-phase outside the electrode, considering the inlet gas composition and conversion of CO_2 to CO along the gas-flow direction as dictated by the current at the inlet, middle, and outlet of the cell. The calculations was based on an even current-distribution and gas flow throughout the cell. The initial degradation could therefore not be due to thermodynamically favored carbon deposition in the fuel electrode. The cause of the initial degradation could possibly be assigned to impurities in the inlet gas stream as no gas cleaning was applied.

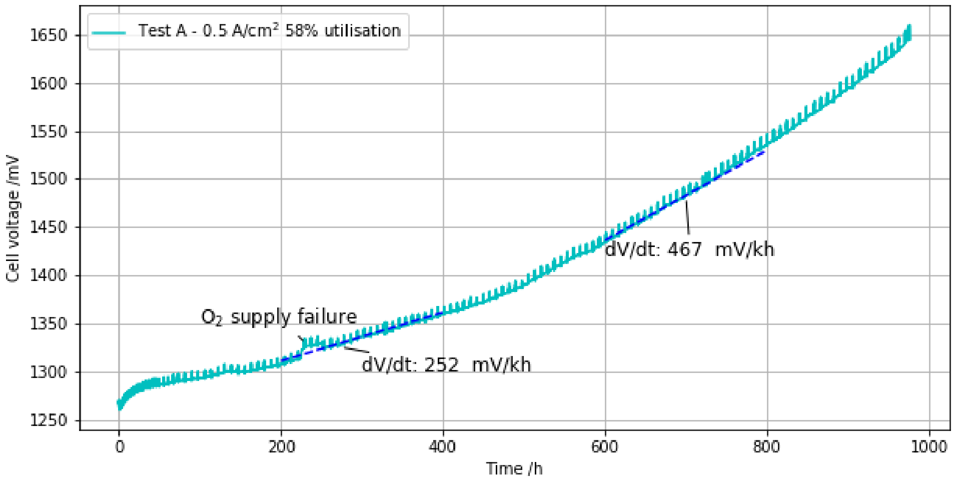

Figure 1: Development of cell voltage during the long-term electrolysis test conducted at 750 °C - 10/90 CO/CO_2 – 50 l/h O_2 at the oxygen electrode. Degradation rates (linear) were determined by linear regression in the intervals 200-400 h and 600-800 h are indicated in the graph and illustrated by dashed lines.

Figure 2b shows the iV curve for a cell with a 267 mg CGO cm^{-3} in the fuel electrode compared with the i-V curve for a cell without infiltrate. The OCV for the infiltrated cell in the beginning and the end varies from the expected OCV (900 mV vs O_2) and that of the non-infiltrated cell. Additionally, the OCV measurements at the beginning and end of the curve also deviate from each other. These deviations were caused by leakage in the cell, due to breakage near the edge during startup, allowing O_2 from the oxygen electrode side to react with the CO supply. The actual CO/CO_2 ratios have been calculated based on the Nernst equation and the measured OCV values. This suggest CO/CO_2 ratios of 5/95 and 2/98 at the beginning and the end of the recording of the iV-curve. Comparison of the two iV curves in fig. 2b should hence be done with care. Comparison between the iV curves shows that the infiltrated cell has lower electrochemical performance, than the cell without infiltrate. This is in line with the results from Skafte et al. who assigned the reduced performance to an increase in the diffusion resistance caused by infiltrate blocking the pores (3). Fitting the model L-R-RQ_{ion}-RQ_{TPB}-G-RQ_{Diff} -RQ_{Conv} via complex non-linear squares (CNLS) to electrochemical impedance spectra (EIS) recorded at 50/50 H_2/H_2O to the fuel electrode, O_2 to the oxygen electrode, at 750 °C for the cells represented in figure 2b, shows that this is also the case in for the infiltrated having nearly nine times as large R_{diff} compared to the non-infiltrated cell (9).

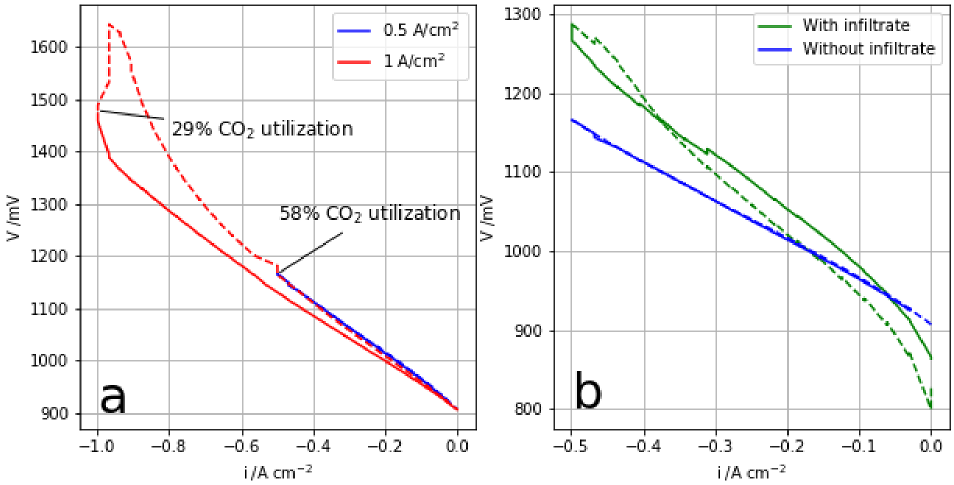

Figure 2 iV curves recorded in CO/CO_2 to the fuel electrode (gas inlet composition given in parantheses in the description of the individual iV curves) - 50 l/h O_2 at the oxygen electrode - 750 °C,. (a) Comparison between iV curves: with a 58% CO_2 utilization at -0.5 A cm^{-2} (14/86), and 29% CO_2 utilization at -1.0 A cm^{-2} (14/86), (b) Comparison between a cell with 267 mg cm^{-3} CGO infiltrated into the fuel electrode (5/95), and a cell without infiltration (14/86), both with a 58% CO_2 utilization at -0.5 A cm^{-2}. Full lines: Increasing electrolysis current, dashed lines: decreasing electrolysis current.

TABLE II. Gas composition at inlet, middle (average), and outlet and the thermodynamically calculated carbon activities at 750 °C during the long-term durability test.

	Inlet	**Middle**	**Outlet**
CO_2 [%]	90.0	67	46
CO [%]	10.0	34	54
Carbon activity	0.0036	0.056	0.22

Impedance Spectroscopy

Figure 3 shows the raw data (points) for the first and last EIS recorded during the long-term durability test (fig. 1) along with the CNLS fits (lines) applying a model described by the equivalent circuit L-R-RQ_{ion}-RQ_{TPB}-G-Q_{Diff}-RQ_{Conv} (7) to the EIS presented as Nyquist plots (top graphs) and Bode plots (middle graphs). Comparison of IS recorded at the start (Figure 3a) and at the end (Figure 3b) of the long-term test shows an increase of total polarization resistance (R_p) with the largest change occurring in the region 10 Hz-1kHz, as the resistance of the RQ_{TPB} element increases while its summit frequency decreases from ~1 kHz to ~100 Hz. RQ_{TPB} is of special interest since carbon formation occurs at the triple phase boundaries in the fuel electrode. The bottom graphs in fig. 3 is the error plot of the fit, showing the relative errors between the data and the fit.

Table III shows results of the equivalent circuit fits (Figure 3) in addition to the cell voltage and carbon activity at the beginning and end of test A. The carbon activity have been calculated from the inlet gas composition and the estimated fuel electrode overpotential assuming η_{TPB} to be dominating this (only contribution considered). Carbon deposition in the fuel electrode is expected from the start based on the calculated carbon activity of 1.2 in table III. The cause of carbon deposition is unlikely, considering the CO/CO_2 ratio in the gas-flow region when in equilibrium does not lead to carbon deposition as discussed earlier. While the carbon activities from table II would not cause thermodynamic carbon deposition based on the average gas composition throughout the cell, polarization at TPBs in the fuel electrode may change local conditions strongly enough for carbon deposition to occur.

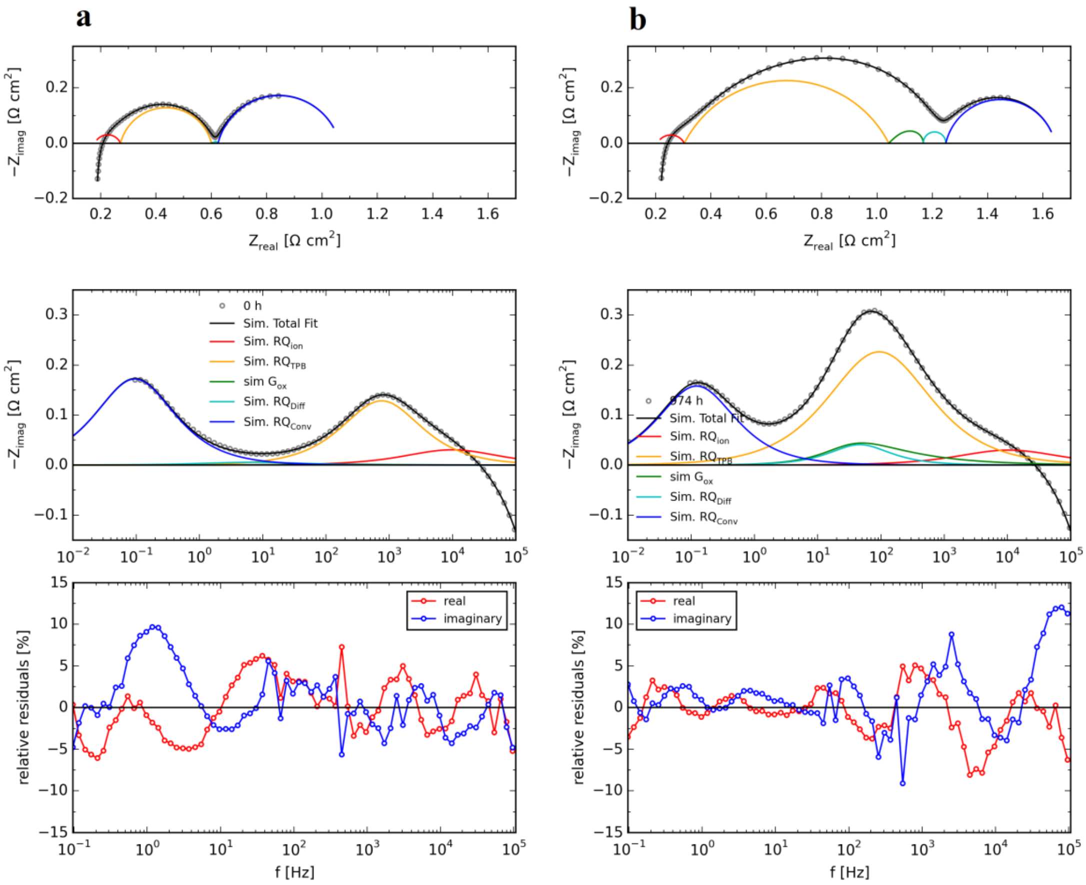

Figure 3 Impedance spectra (EIS) recorded during the long-term durability test at 0 h (a) and 974 h (b). The model L-R-RQ_{ion}-RQ_{TPB}-G_{ox}-RQ_{Diff}-RQ_{Conv} have been fitted to the EIS as described by Hauch et al. (7).

TABLE III. Results of fitting L-R-RQ_{ion}-RQ_{TPB}-G_{ox}-RQ_{Diff}-RQ_{Conv} to EIS recorded at 10/90 CO/CO_2 – O_2 ox. Electrode.- 750 °C – OCV to the CNLS model as described by Hauch et al. (7)

	Cell voltage (mV)	**R_s (Ω cm^2)**	**R_p total (Ω cm^2)**	**R_p(TPB) (Ω cm^2)**	**η_{TPB} (mV)**	**Calculated carbon activity (average over cell)**
0 h	1268	0.179	0.885	0.328	164	1.2
974 h	1647	0.206	1.438	0.739	369	163

Post-test analysis via Raman Spectroscopy

Figure 4a, b, and c shows Raman spectra obtained for the active fuel electrode for Test A. The peak at 615 cm^{-1} is assigned to tetragonal YSZ (9).The peaks at 1345 cm^{-1}, and 1585 cm^{-1} can be assigned to disordered (D) and ordered graphite (G), respectively (10). These peaks, hence, confirms the presence of carbon in the fuel electrode near the electrolyte. The carbon peaks are only observed in spectra for the part of the cell with oxygen electrode (fig 4a, b, c) i.e. where the cell has been subjected to a current load. This confirms that the carbon deposition is “driven” by the polarization of the fuel electrode. Figure 4d shows Raman spectra of parts of the cell (both inlet and outlet) that has not been subjected to a current load. These spectra have two peaks at 1090 cm^{-1} and 1490 cm^{-1} that can be assigned to the two-phonon and two-magnon scattering of NiO respectively (12). Which is not surprisingly as these edge parts of the cell can have regions with oxidized Ni (see specification to geometry and gas flows in (12)).

No carbon peaks are present in the spectra for the pieces of the cell that has not experienced a current load. This corroborates the findings that the carbon deposition observed in the long-term test is “driven” by the polarization. The presence of carbon in the cell is largest near the gas inlet and decreases towards the gas-outlet. In a cell operated like here the current density will decrease from inlet to outlet as discussed by Chen et al. (14). Effectively the current collection grids define a fixed potential, and as Emf will increases from inlet to outlet the current driven by (U-EMF) will decrease. Comparison of the carbon peaks in the spectra recorded at the gas-inlet and outlet parts of the cell (fig. 4 a, c) shows the highest carbon peak intensity near the electrode/electrolyte interface, and a decrease in intensity with increasing distance from the electrolyte toward the support layer. This indicates a correlation between carbon deposition in fuel electrode and the local over potential since the highest local η_{TPB} will be near the electrode/electrolyte interface and will decrease moving towards the support layer in a similar manner to the observed carbon deposition.

The fuel electrode for the non-infiltrated cell investigated in figure 2 was investigated using Raman spectroscopy at the same locations as the long-term durability test. No carbon was detected in the cell during Raman spectroscopy. This indicates that carbon does not instantly cover the fuel electrode, and that some exposure time, as well as a certain overpotential is required for carbon formation to occur.

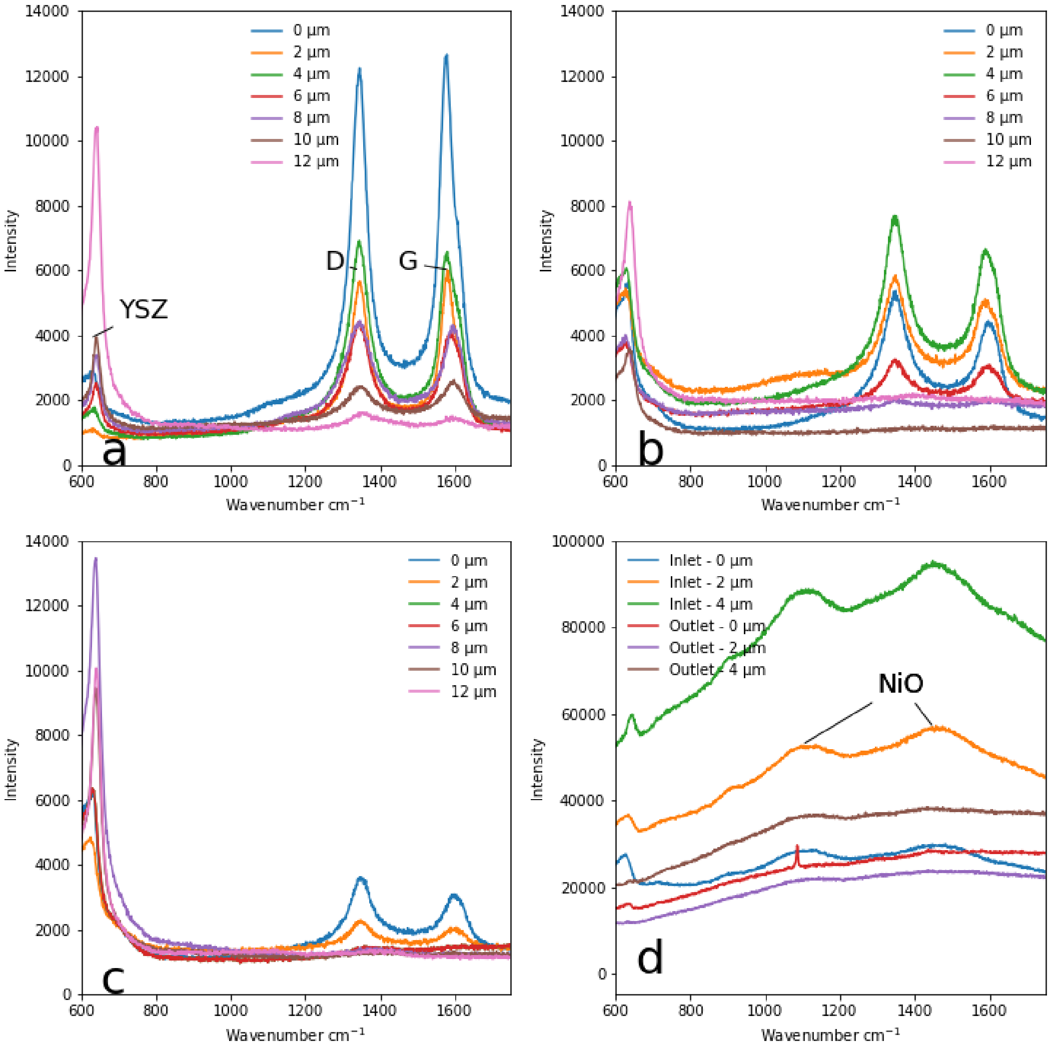

Figure 4. Raman spectra for the active fuel electrode-electrolyte interface at the: a) the CO/CO_2 gas the inlet, b) middle of the cell, c) CO/CO_2 gas outlet, d) gas inlet and outlet without oxygen electrode (ie. no current load). The legend indicates distance from the electrode/electrolyte interphase.

Conclusion

The long-term durability of an SOEC operated in electrolysis mode was tested for 974 h with the conditions: 10/90 CO/CO_2 gas composition at the fuel electrode, O_2 fed to the oxygen electrode at 750 °C.

From the long-term durability test it has been observed that; degradation rate during initially plateaus at 252 mV/kh until the cell potential reaches ~1375 mV where after it increases to 467 mV/kh over a ~50 h period after which it continues increasing. These findings are consistent with results of transient iV-curves, where the slope of the curves increase at 1375 mV leading to a bend in the iV-curve and a hysteresis, a behavior previously ascribed to carbon formation in the fuel electrode (3).

Estimated fuel electrode over potentials obtained through a ”break-down of losses” from the EIS data (recorded during aging) indicates that carbon deposits despite using gas compositions and temperatures at which carbon depositions should not occur according to thermodynamics.

Post-mortem Raman spectroscopy has shown carbon deposition throughout the cell tested for 974h. The relative amounts of observed carbon was largest near the gas-inlet and decreasing towards the gas-outlet.

Future Work

The work and results presented here represents the first set of data in this project, including CO_2 electrolysis long-term testing on a state-of-art SOEC and carbon deposition threshold investigation by detailed iV-curves and post-aging-test characterization by Raman spectroscopy. Next step is more tests and analyses for CO_2 electrolysis for similar cells with CGO infiltration with the aim of investigating the effects of the infiltrates on carbon deposition threshold and performance and durability. The tests will be carried out using gas cleaning to elucidate effects of impurities in the feed stream.

References

1. Küngas, R. . *J. Electrochem. Soc.* **167**(4), 044508 (2020).
2. Ebbesen, S. D., Graves, C., Hauch, A., Jensen, S. H., and Mogensen, M. *J. Electrochem. Soc.* **157**(10), (2010).
3. Skafte, T. L., Blennow, P., Hjelm, J., and Graves, C. *J. Power Sources* **373**, 54 (2018).
4. Trini, M. Hauch, A., Angelis, S. De, Tong, X., Hendriksen, P. V., and Chen, M. *J. Power Sources* **450**, 227599 (2020).
5. Tong, X., Hendriksen, P. V., Hauch, A., Sun, X., and Chen, M. *J. Electrochem. Soc.* **167**(2), 024519 (2020).
6. Hauch, A., Bowen, J. R., Kuhn, L. T., and Mogensen, M. *Electrochem. Solid-State Lett.* **11**(3), (2008).
7. Hauch, A., Marchese, M., Lanzini, A., and Graves, C. *J. Power Sources* **377**, 110 (2018).
8. Graves, C. RavDav Data Analysis Software, Ravdav, 2012Ver 0.97. (2012).
9. Clausen, A. K., Hauch, A., Hendriksen, P. V., Sun, X, and Traulsen, M. L. [Online], doi:https://doi.org/10.6084/m9.figshare.14593281.v1.
10. Feinberg, A. and Perry, C. H. *J. Phys. Chem. Solids* **42**(6), 513 (1981).
11. Pimenta, M. A. Dresselhaus, G., Dresselhaus, M. S., Cançado, L. G., Jorio, A., and Saito, R. *Phys. Chem. Chem. Phys.* **9**(11), 1276 (2007).
12. Mironova-Ulmane, N. N., Kuzmin, A., Steins, I., Grabis, J., Sildos, I., and Pärs, M. *J. Phys. Conf. Ser.* **93**(1), (2007).
13. Njodzefon, J.-C., Hjelm, J., Graves, C. R., and Weber, A. (2015).
14. Chen, M. Sun, X., Chatzichristodoulou, C., Koch, S., Hendriksen, P. V., and Mogensen, M. B. *ECS Trans.* **78**, 3077–3088 (2017).

Appendix B

Supporting Information for Chapter 3

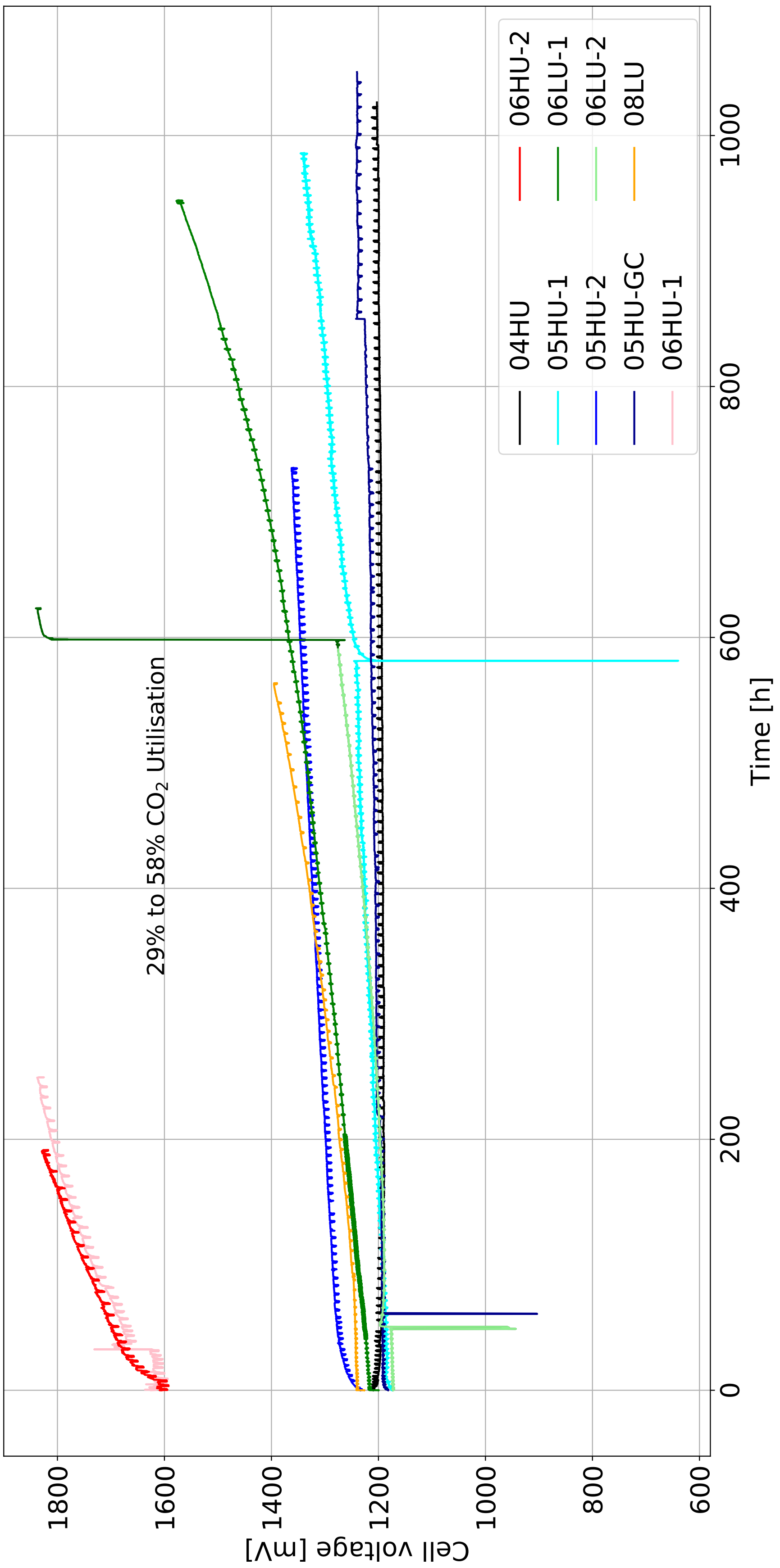

Figure B.1: Cell voltage development during long-term durability test in chapter 3. Test condition: 750 °C, 10/90 CO/CO_2, O_2. Specific test parameters can be found in table 3.1 on page 30.

Appendix C

Data for E_a determination

This appendix contains the data used to determine the discussed activation energies in chapter 4.

Table C.1: Resistances and temperatures for E_a determination for test CGO-0. Conditions: 10/90 CO/CO_2 vs. O_2

t °C	**R_Ω** $[\Omega \cdot cm^2]$	**R_{TPB}** $[\Omega \cdot cm^2]$
850	0.107	0.0091
806	0.129	0.0361
777	0.171	0.0363
754	0.200	0.0643
732	0.245	0.0715
697	0.326	0.1423
692	0.342	0.1609

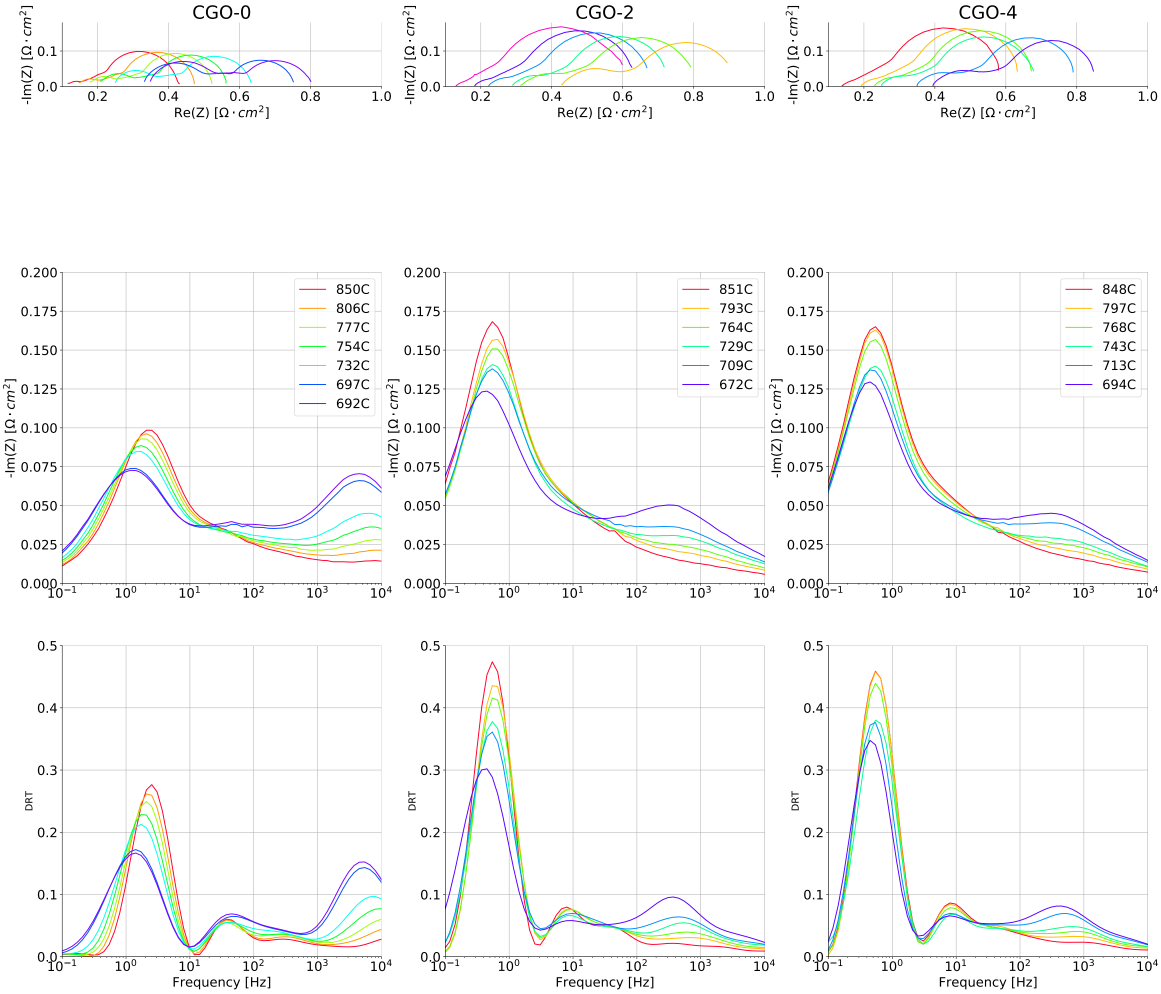

Figure C.1: Nyquist, Bode, and DRT plots for the three tested SOECs in test condition corresponding to inlet gas composition (10/90 CO/CO_2 vs. O_2). The tests are split into columns, from the left: CGO-0, CGO-2, CGO-4. Legend in the Bode plot (middle row) is representative for all plots in the column.

Table C.2: Resistances and temperatures for E_a determination for test CGO-0. Conditions: 39/61 CO/CO_2 vs. O_2

t °C	**R**$_\Omega$ $[\Omega \cdot cm^2]$	**R**$_{TPB}$ $[\Omega \cdot cm^2]$
846	0.125	0.0144
801	0.147	0.0298
772	0.178	0.0646
754	0.202	0.0891
727	0.245	0.1491
700	0.315	0.2352
687	0.347	0.2904

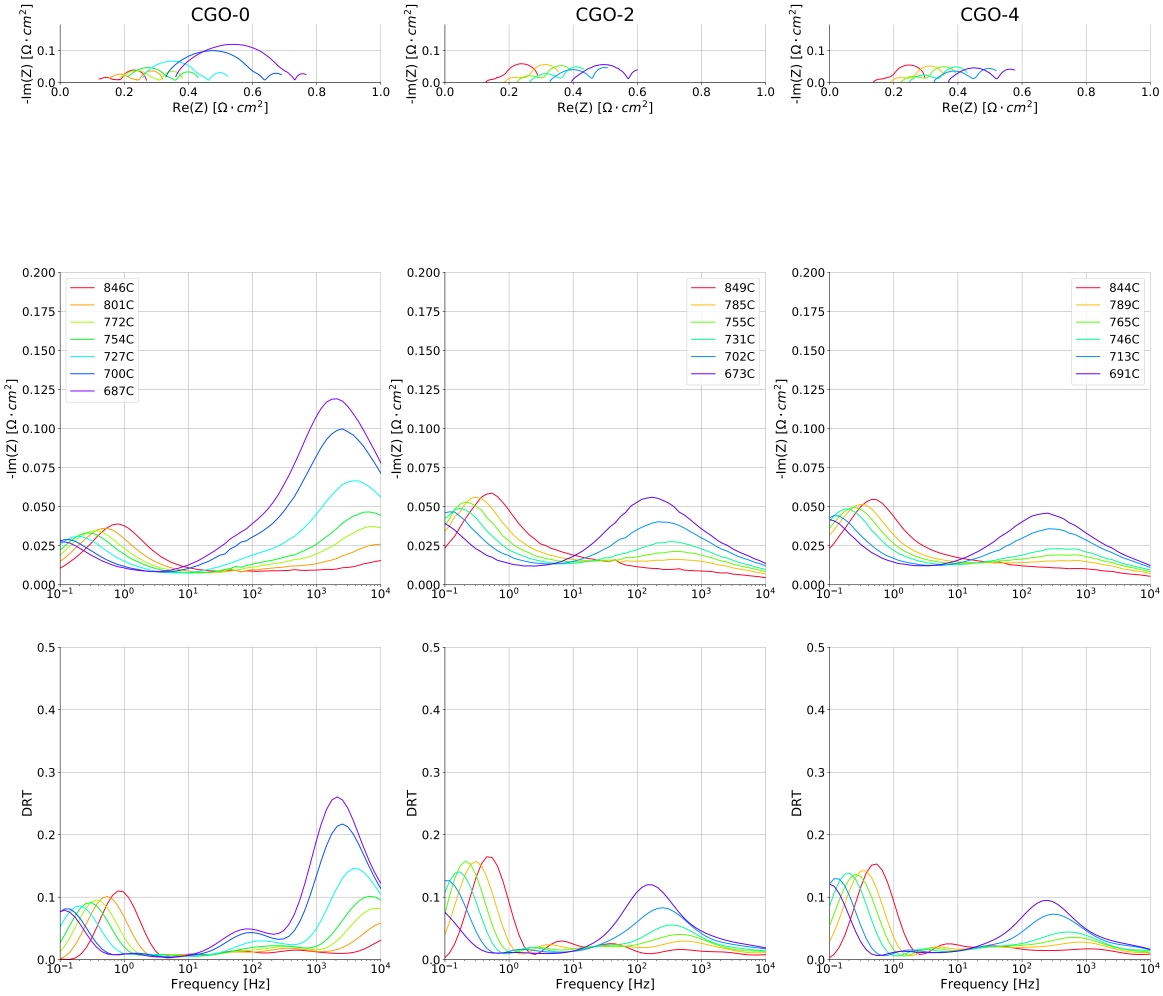

Figure C.2: Nyquist, Bode, and DRT plots for the three tested SOECs in test conditions corresponding to outlet gas composition (39/61 CO/CO_2 vs. O_2). The tests are split into columns, from the left: CGO-0, CGO-2, CGO-4. Legend in the Bode plot (middle row) is representative for all plots in the column.

Table C.3: Resistances and temperatures for E_a determination for test CGO-2. Conditions: 10/90 CO/CO_2 vs. O_2

t °C	**R**$_\Omega$ $[\Omega \cdot cm^2]$	**R**$_{TPB}$ $[\Omega \cdot cm^2]$
851	0.125	0.0212
793	0.177	0.0379
764	0.213	0.0423
729	0.279	0.0480
709	0.294	0.0742
672	0.408	0.0973

Table C.4: Resistances and temperatures for E_a determination for test CGO-2. Conditions: 39/61 CO/CO_2 vs. O_2

t °C	**R_Ω** $[\Omega \cdot cm^2]$	**R_{TPB}** $[\Omega \cdot cm^2]$
849	0.123	0.0157
785	0.182	0.0254
755	0.257	0.0412
731	0.250	0.0418
702	0.316	0.0768
673	0.382	0.1096

Table C.5: Resistances and temperatures for E_a determination for test CGO-4. Conditions: 10/90 CO/CO_2 vs. O_2

t °C	**R_Ω** $[\Omega \cdot cm^2]$	**R_{TPB}** $[\Omega \cdot cm^2]$
848	0.137709885	0.03072
797	0.191	0.0403
768	0.228	0.0543
713	0.347	0.0867
694	0.391	0.0958

Table C.6: Resistances and temperatures for E_a determination for test CGO-4. Conditions: 39/61 CO/CO_2 vs. O_2

t °C	**R_Ω** $[\Omega \cdot cm^2]$	**R_{TPB}** $[\Omega \cdot cm^2]$
844	0.133	0.024
789	0.187	0.0368
765	0.223	0.0410
746	0.247	0.0459
710	0.322	0.0568
691	0.367	0.0779
652	0.502	0.0979

Appendix D

Additional SEM and EDS

D.1 SEM

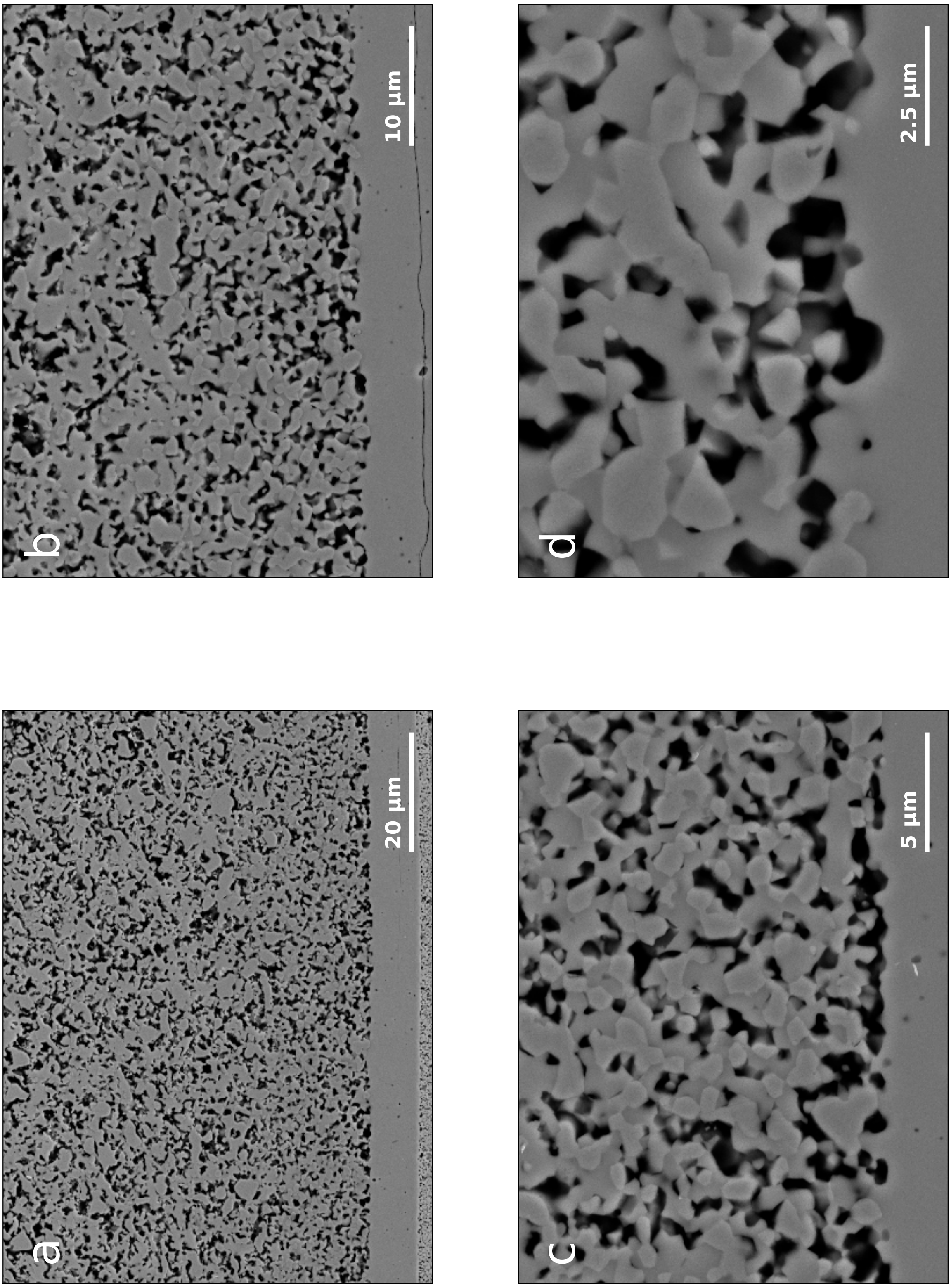

Figure D.1: 04HU in

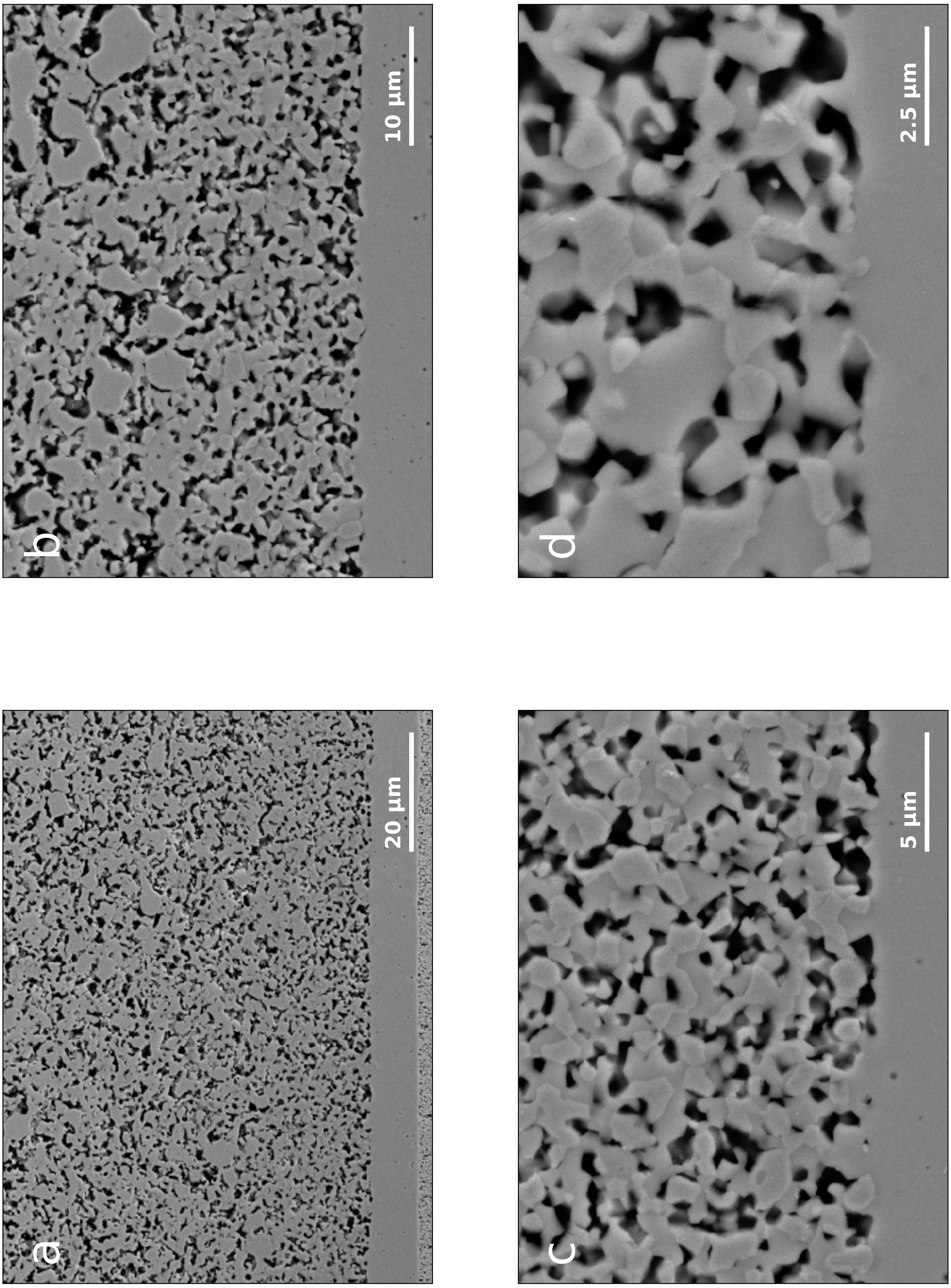

Figure D.2: 04HU out

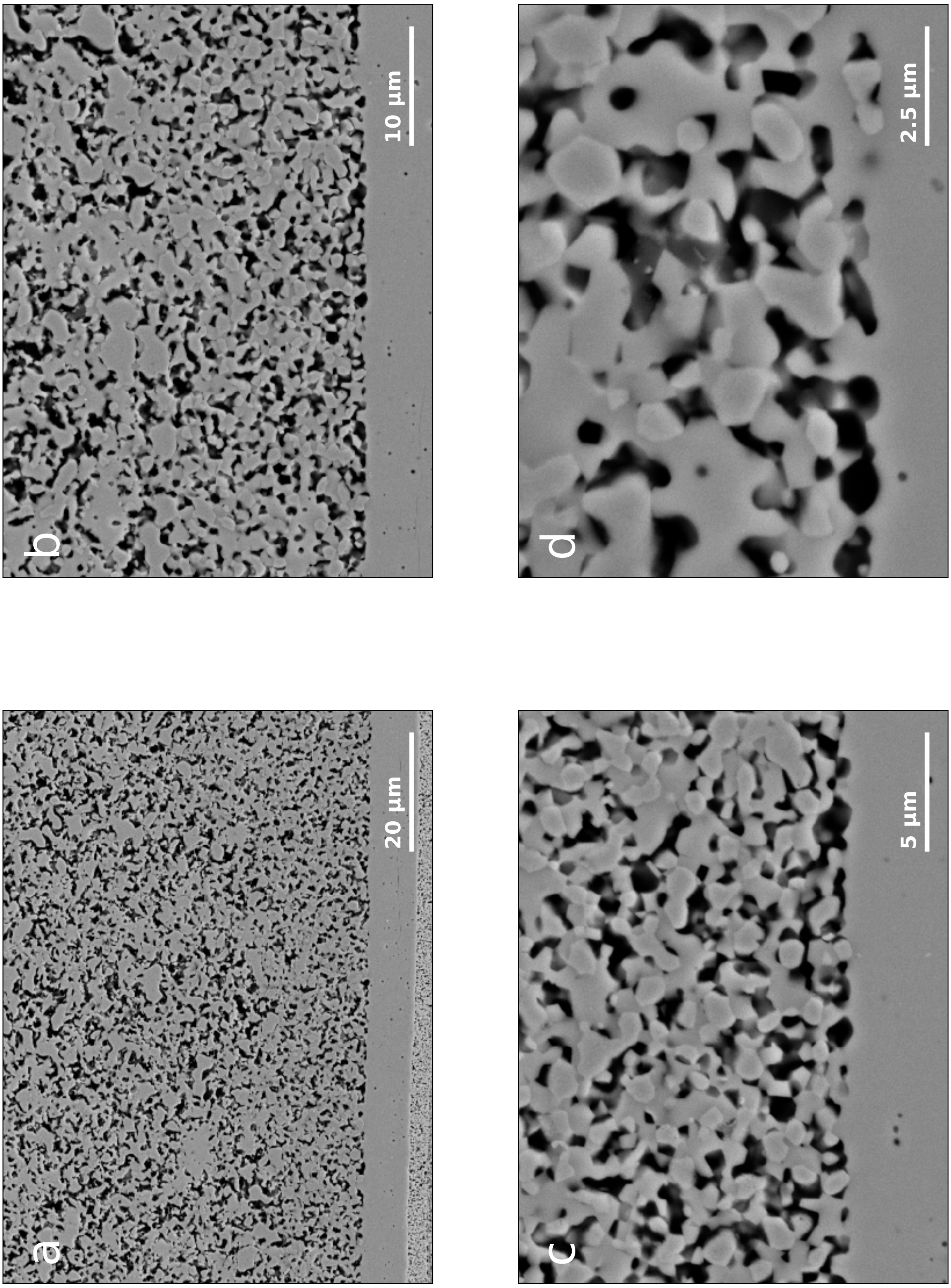

Figure D.3: 04HU without oxygen electrode contact layer

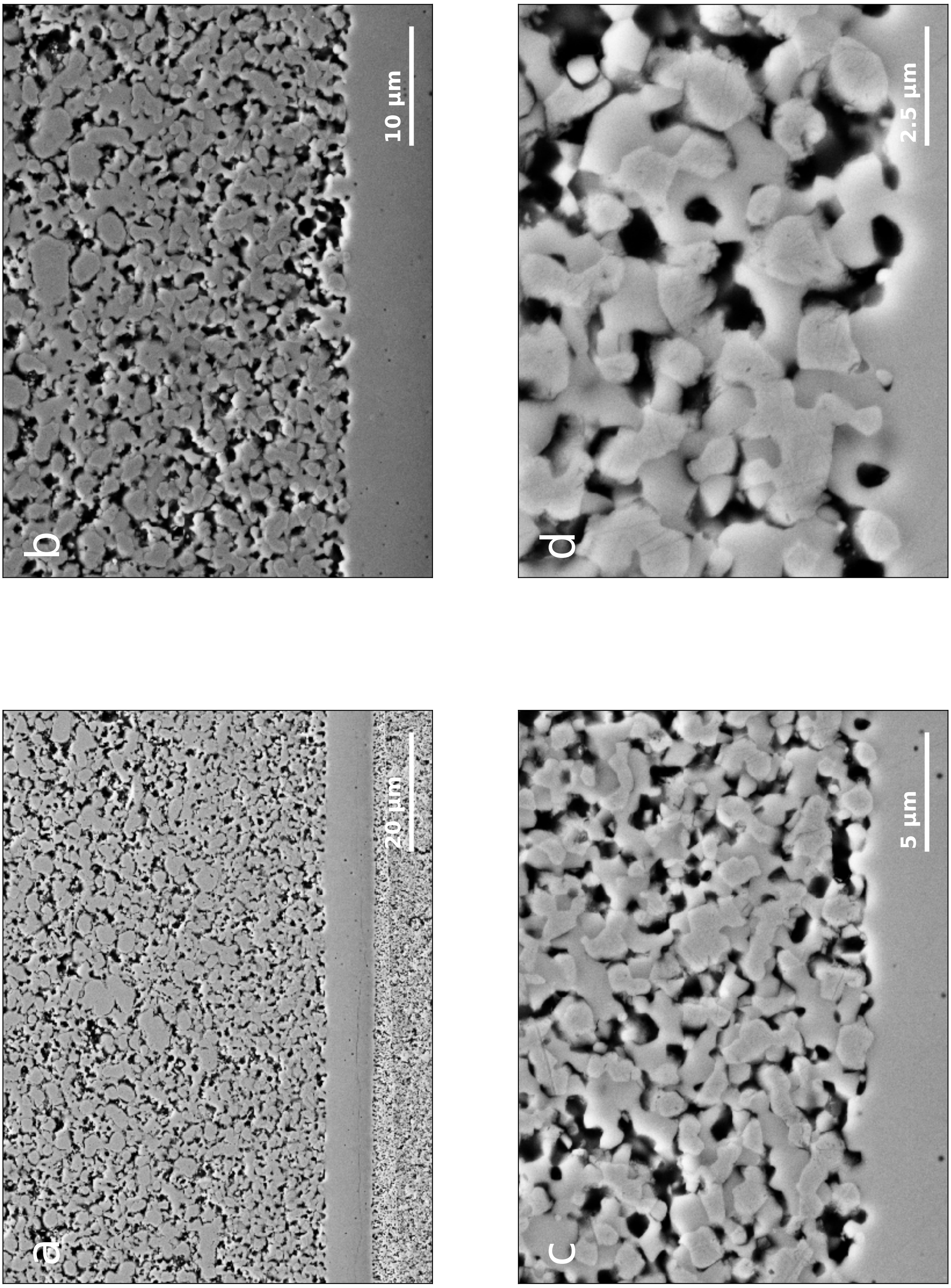

Figure D.4: 05HU-2 in

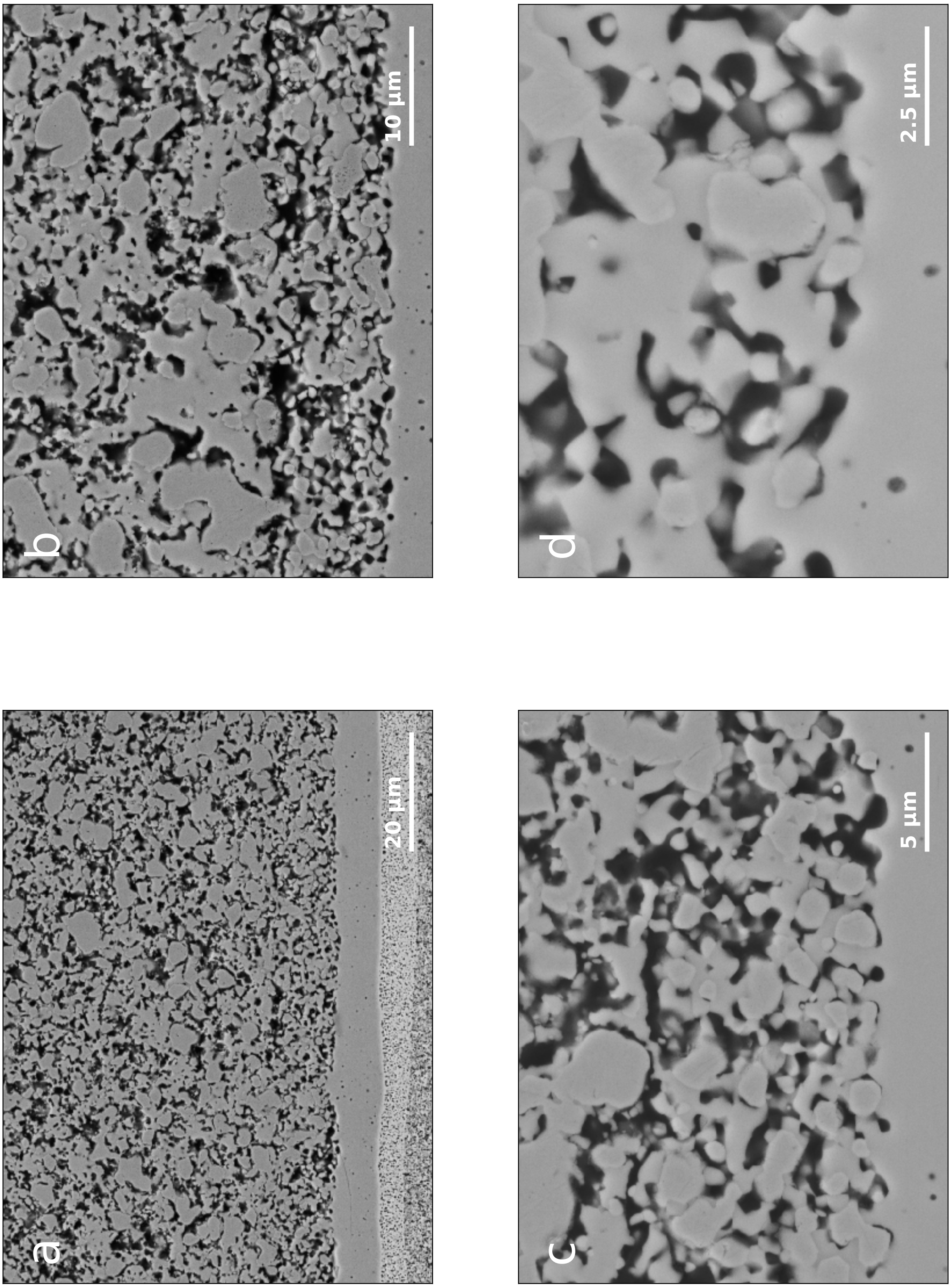

Figure D.5: 06HU-1 in

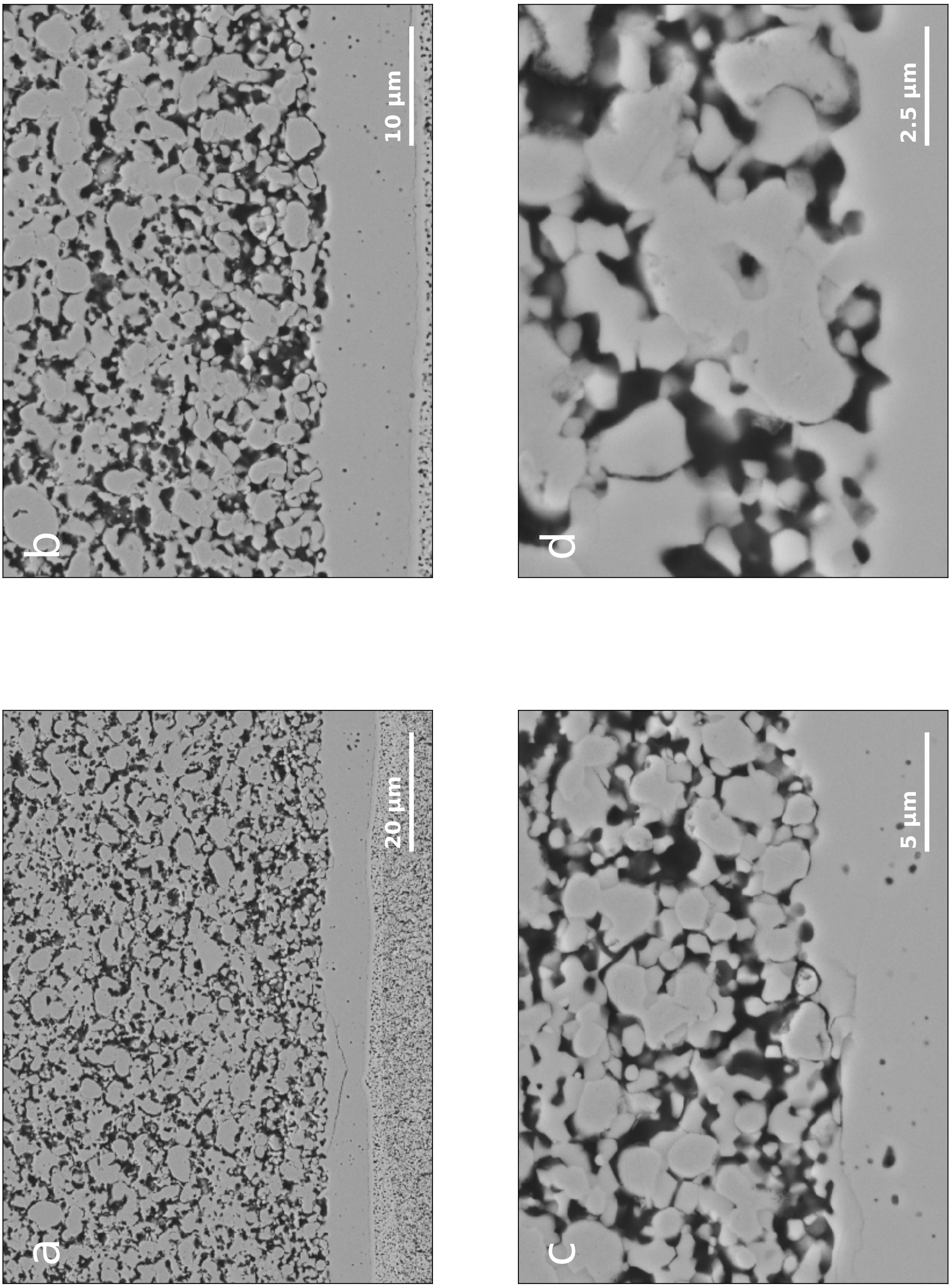

Figure D.6: 06HU-1 out

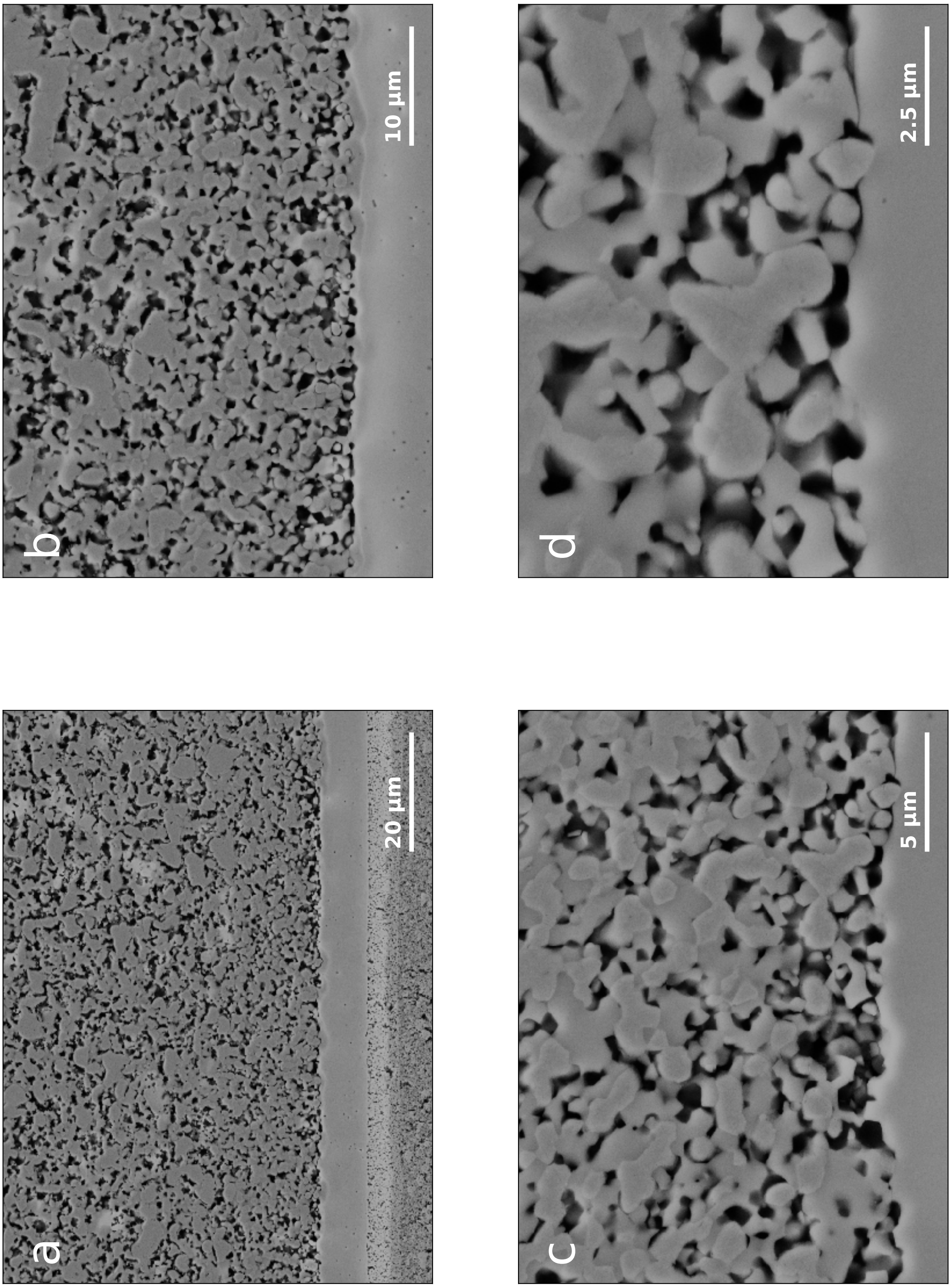

Figure D.7: 06LU-1 in

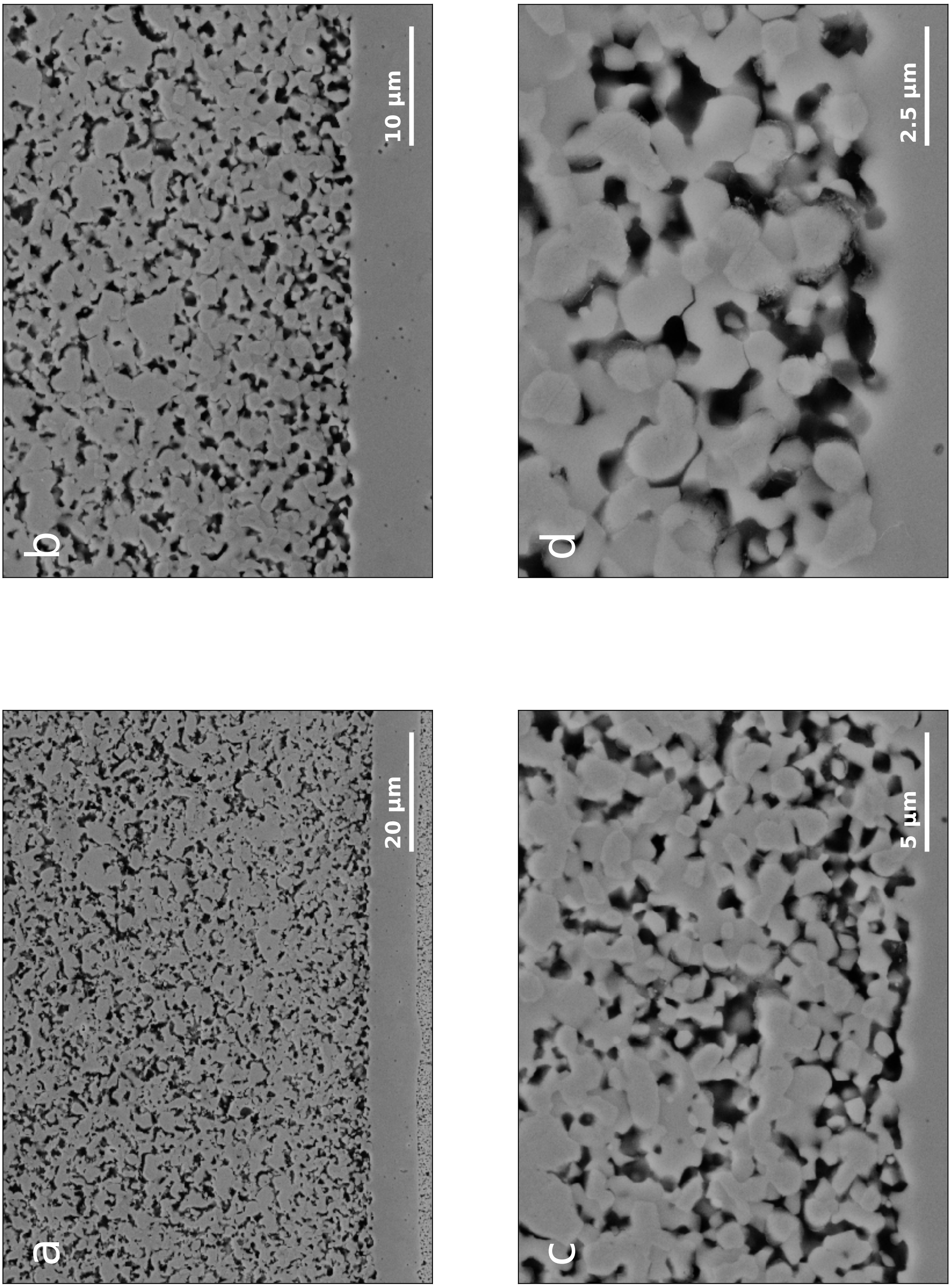

Figure D.8: 06LU-1 out

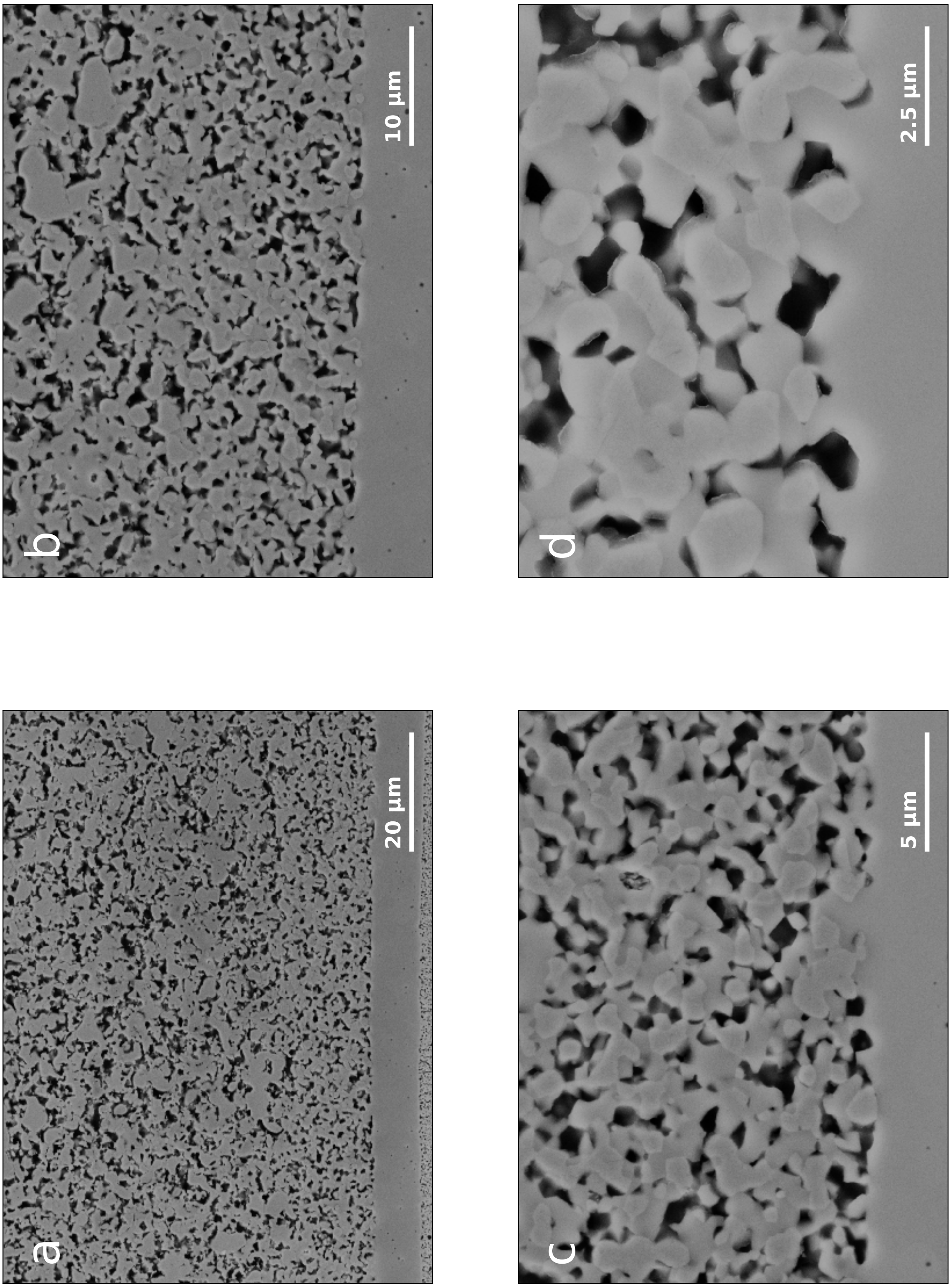

Figure D.9: 06LU-1 without oxygen electrode contact layer

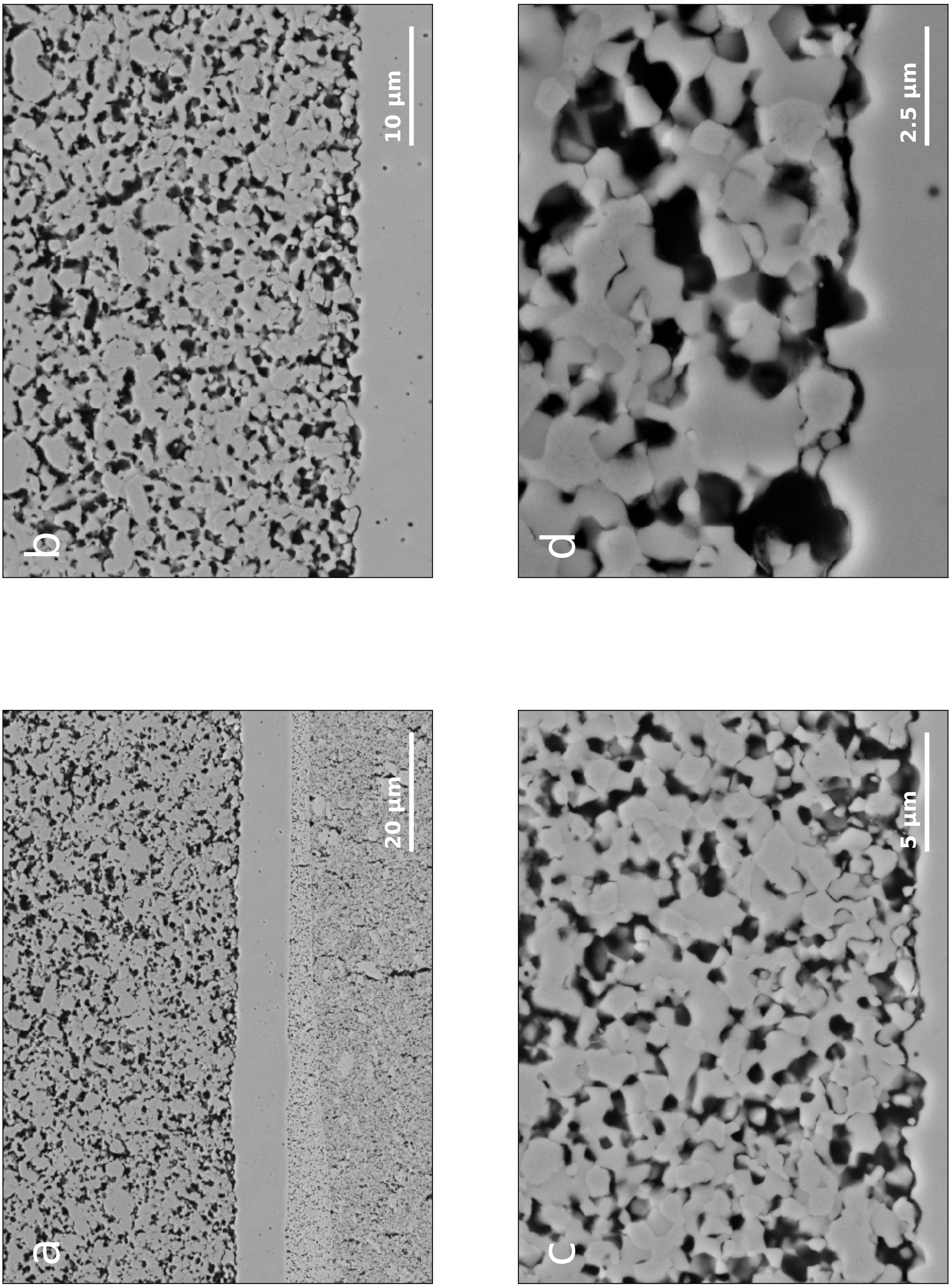

Figure D.10: 08LU in

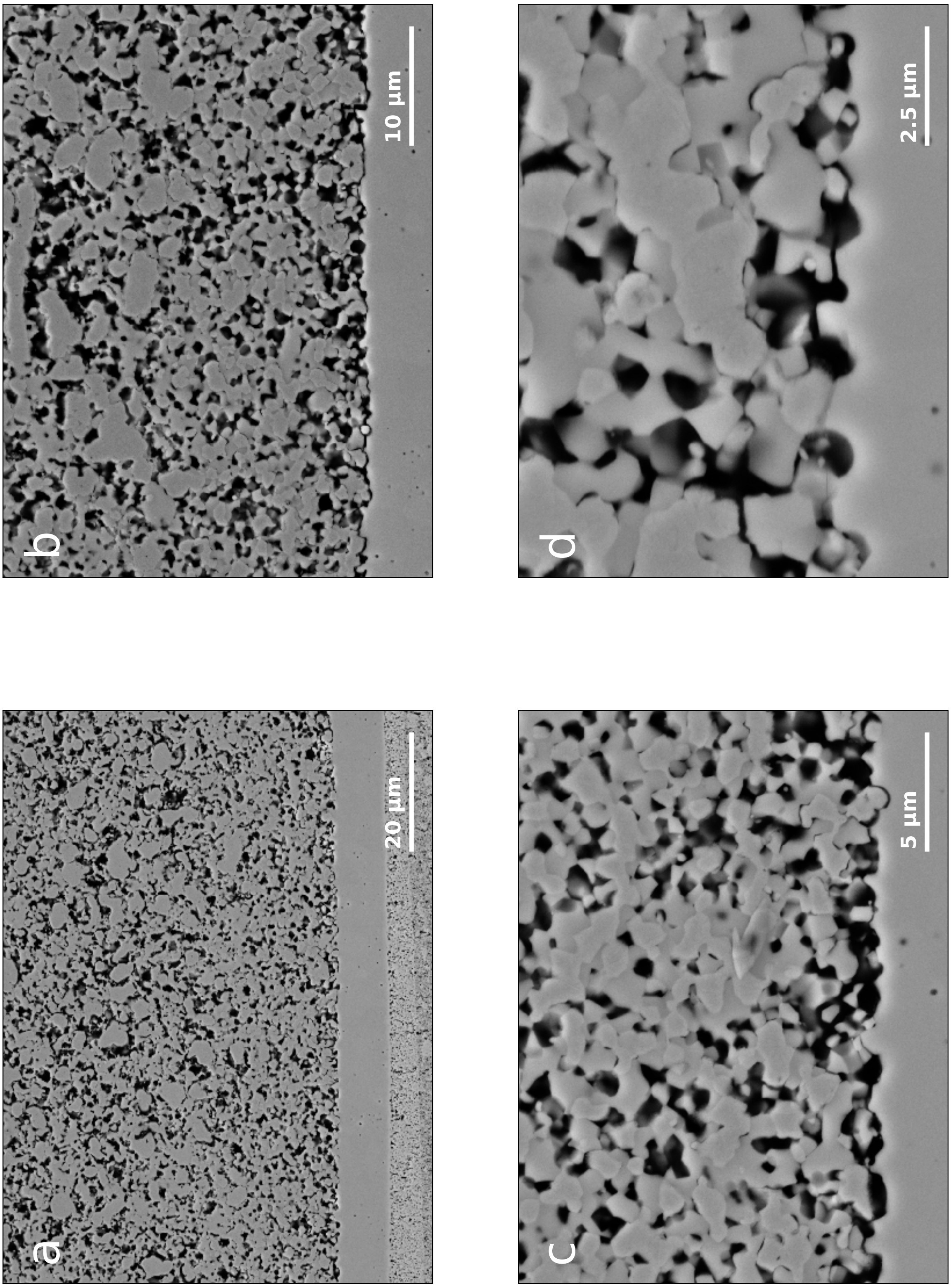

Figure D.11: 08LU out

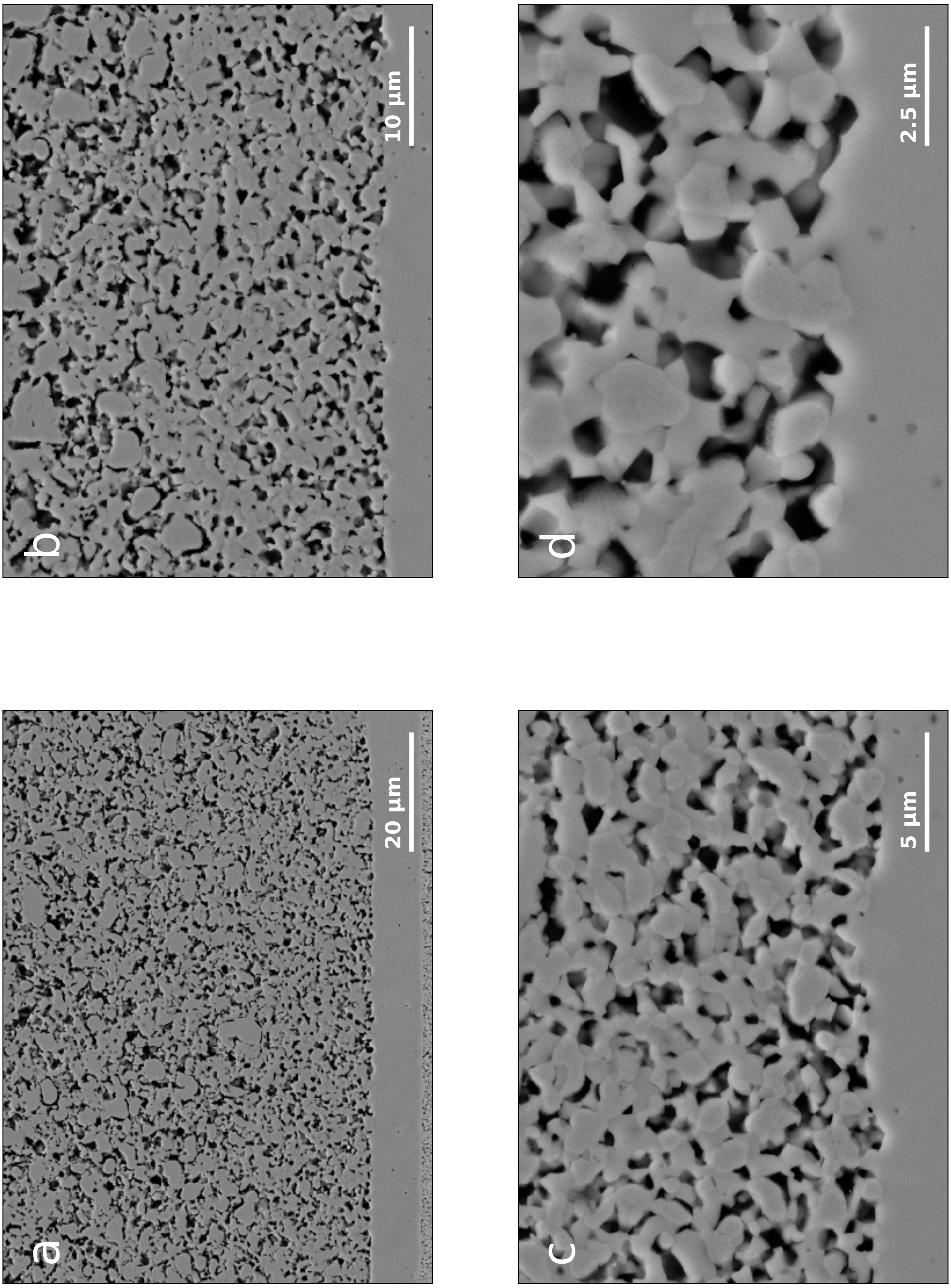

Figure D.12: 08LU without oxygen electrode contact layer

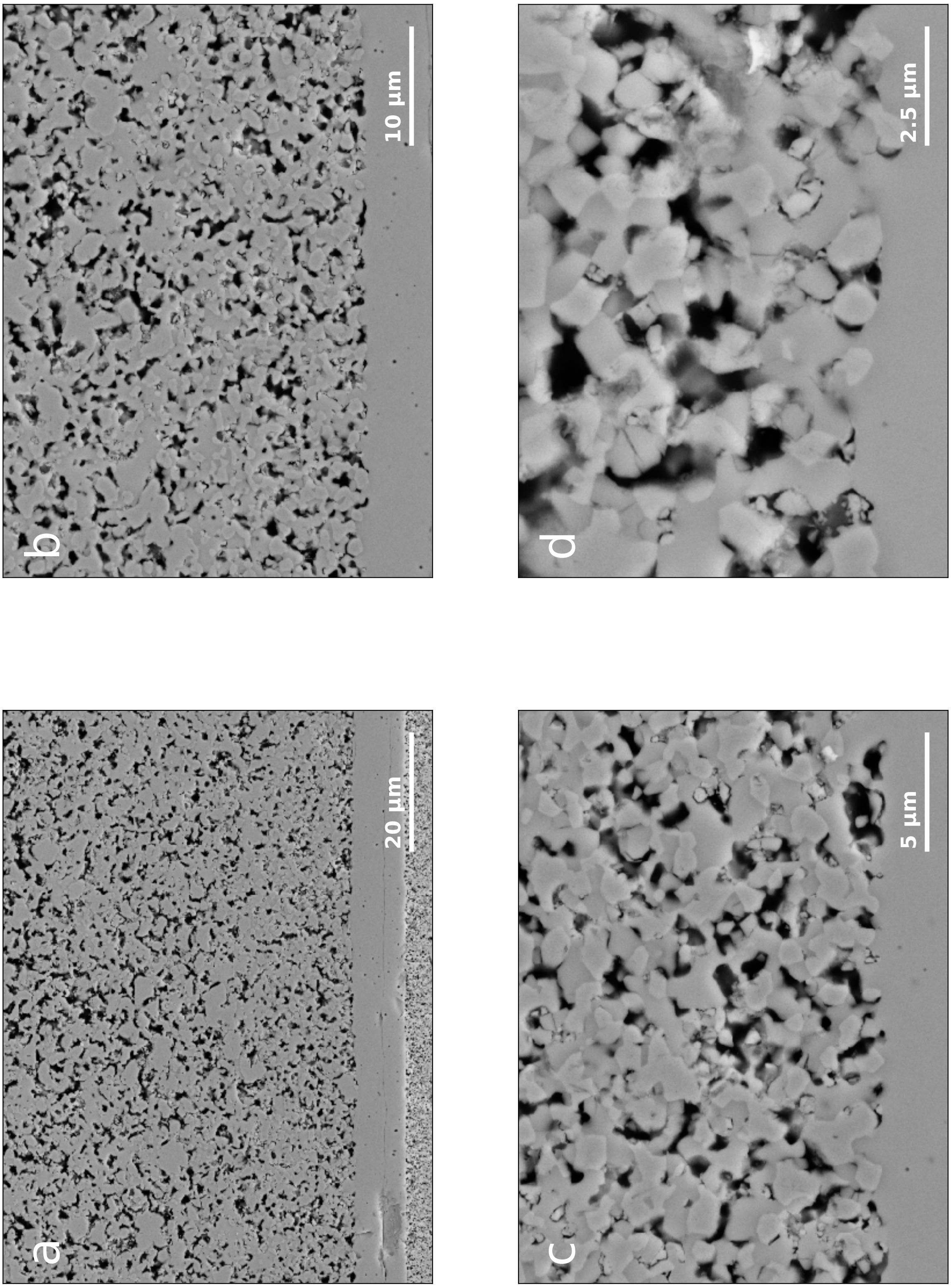

Figure D.13: CGO-2 in

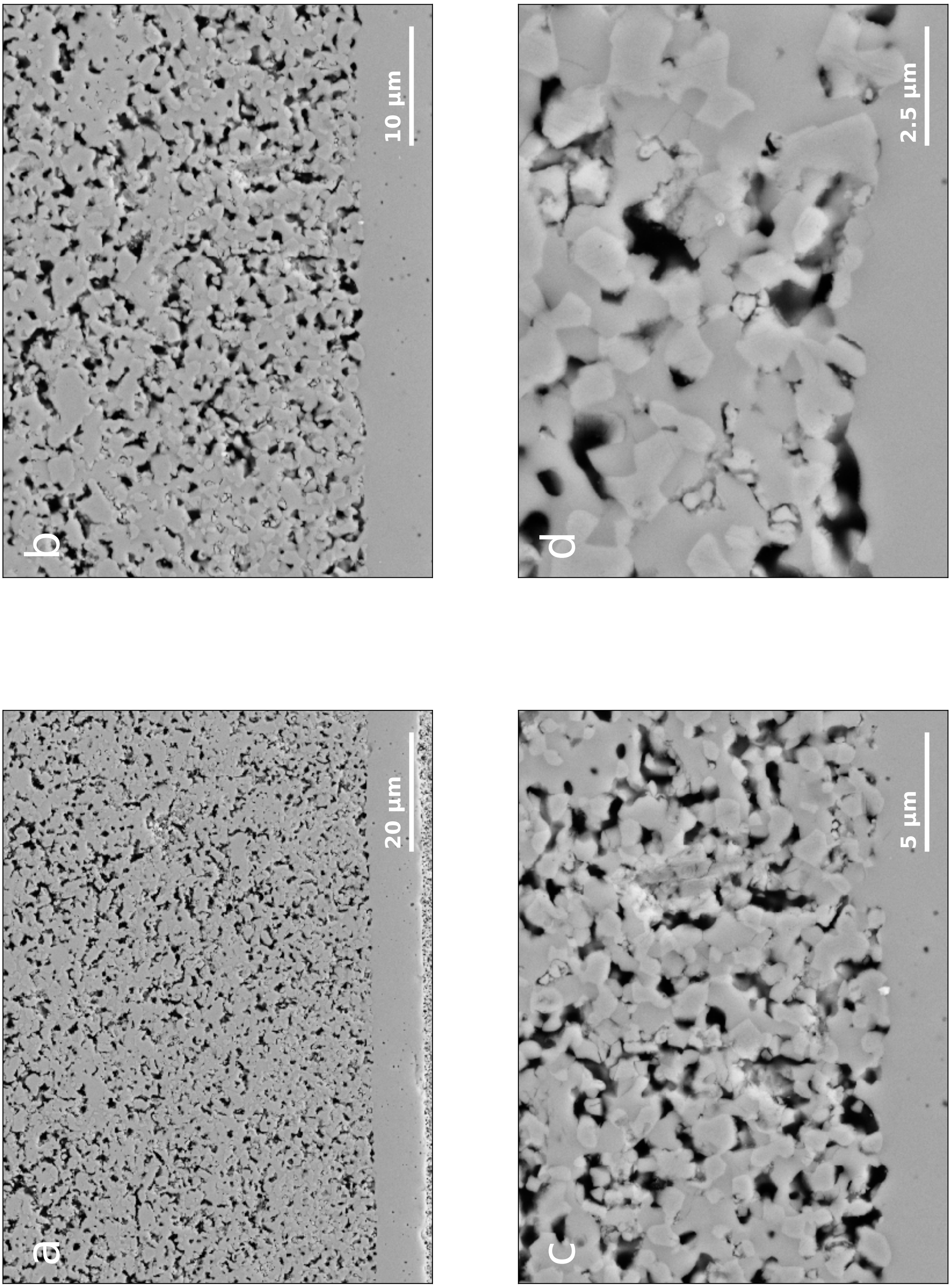

Figure D.14: CGO-2 out

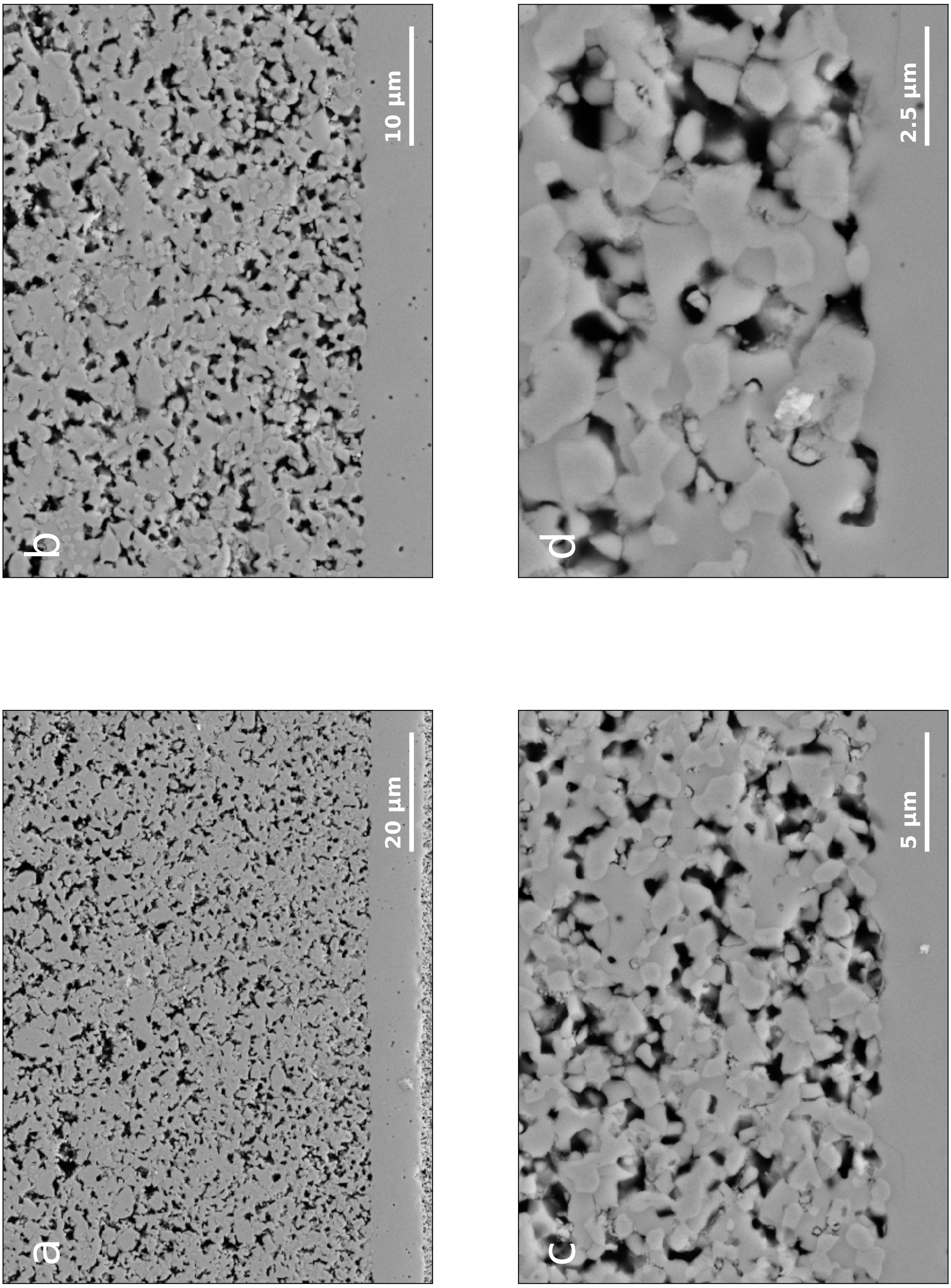

Figure D.15: CGO-2 without oxygen electrode contact layer

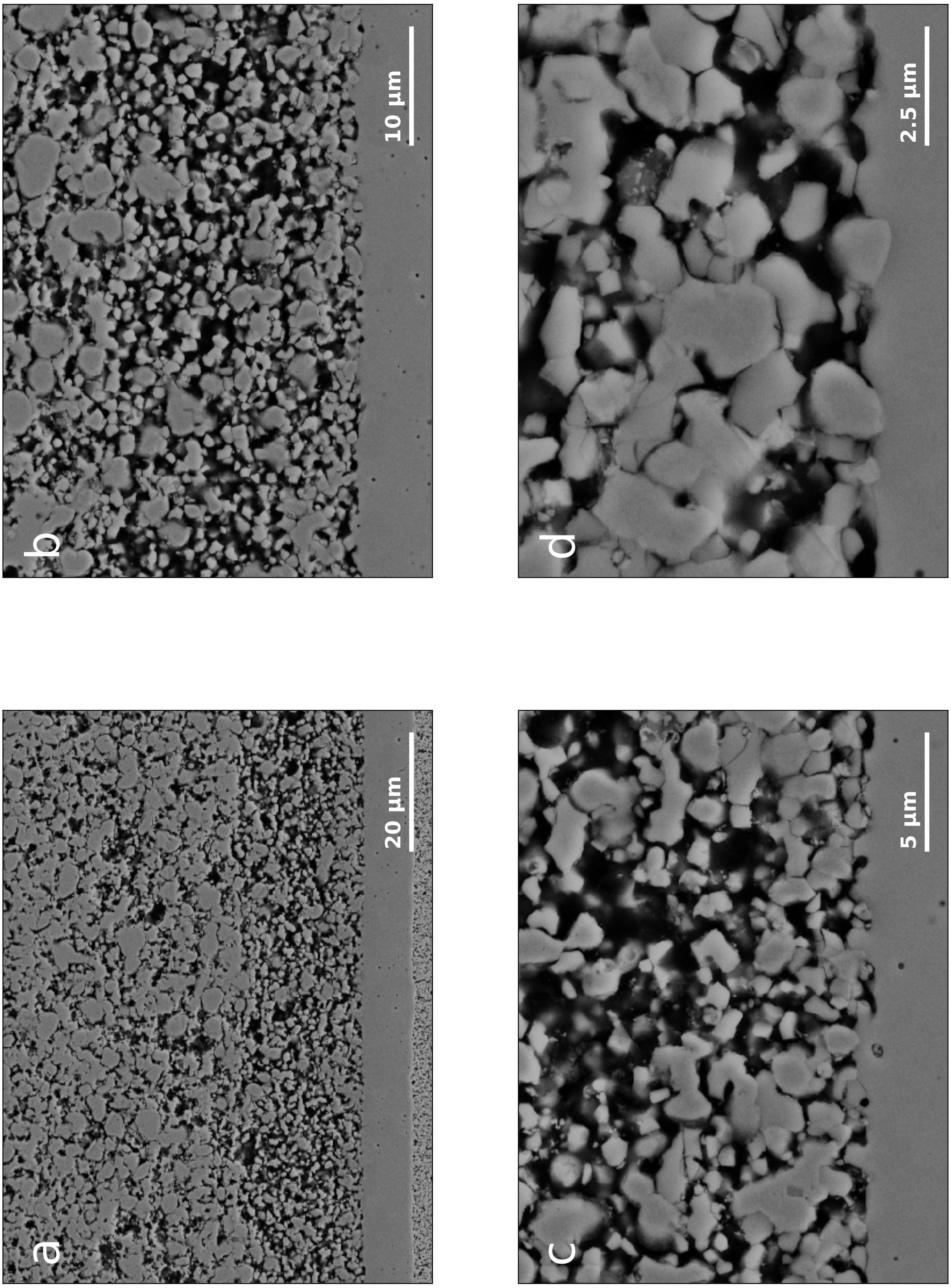

Figure D.16: CGO-4 in

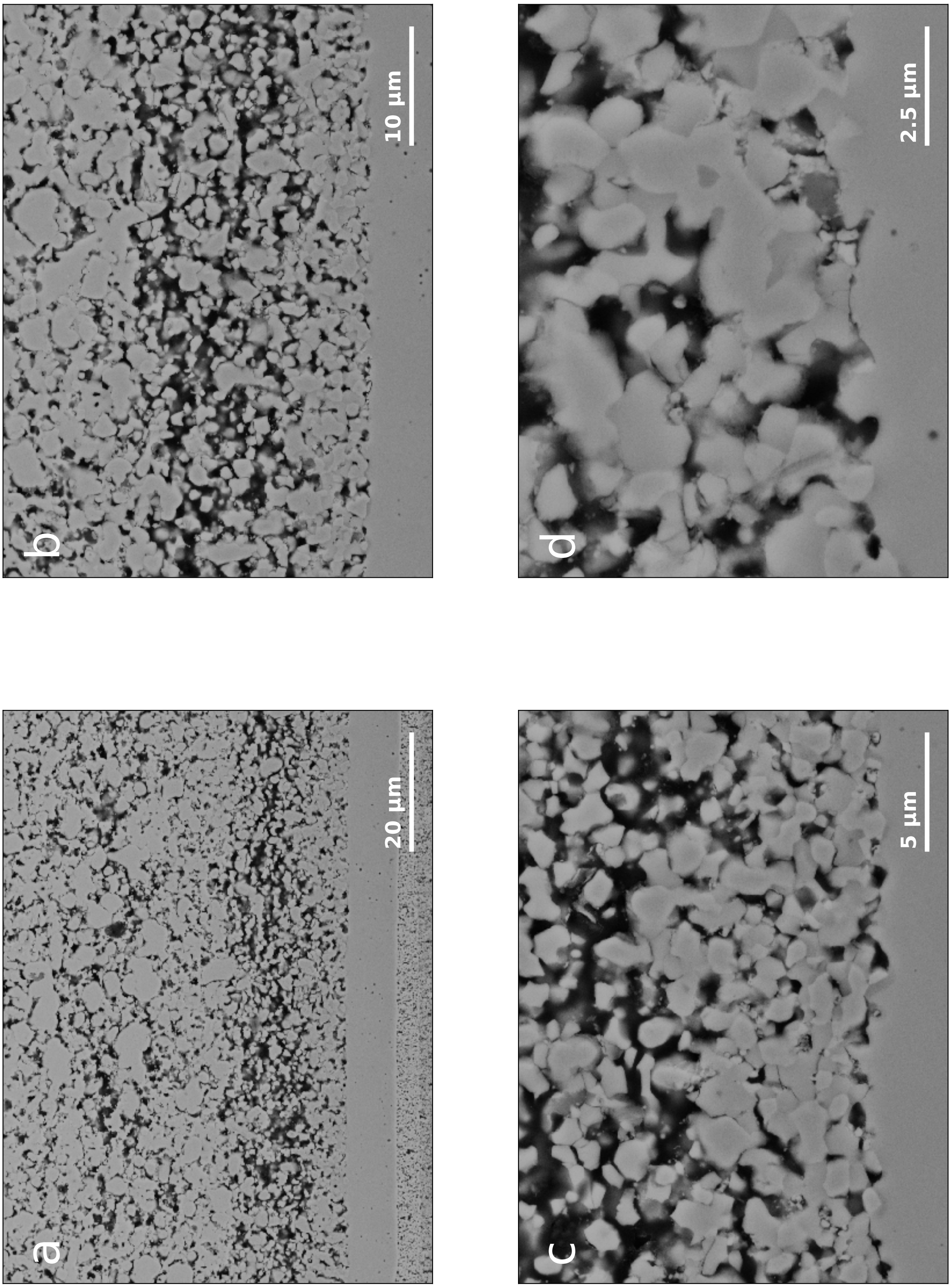

Figure D.17: CGO-4 out

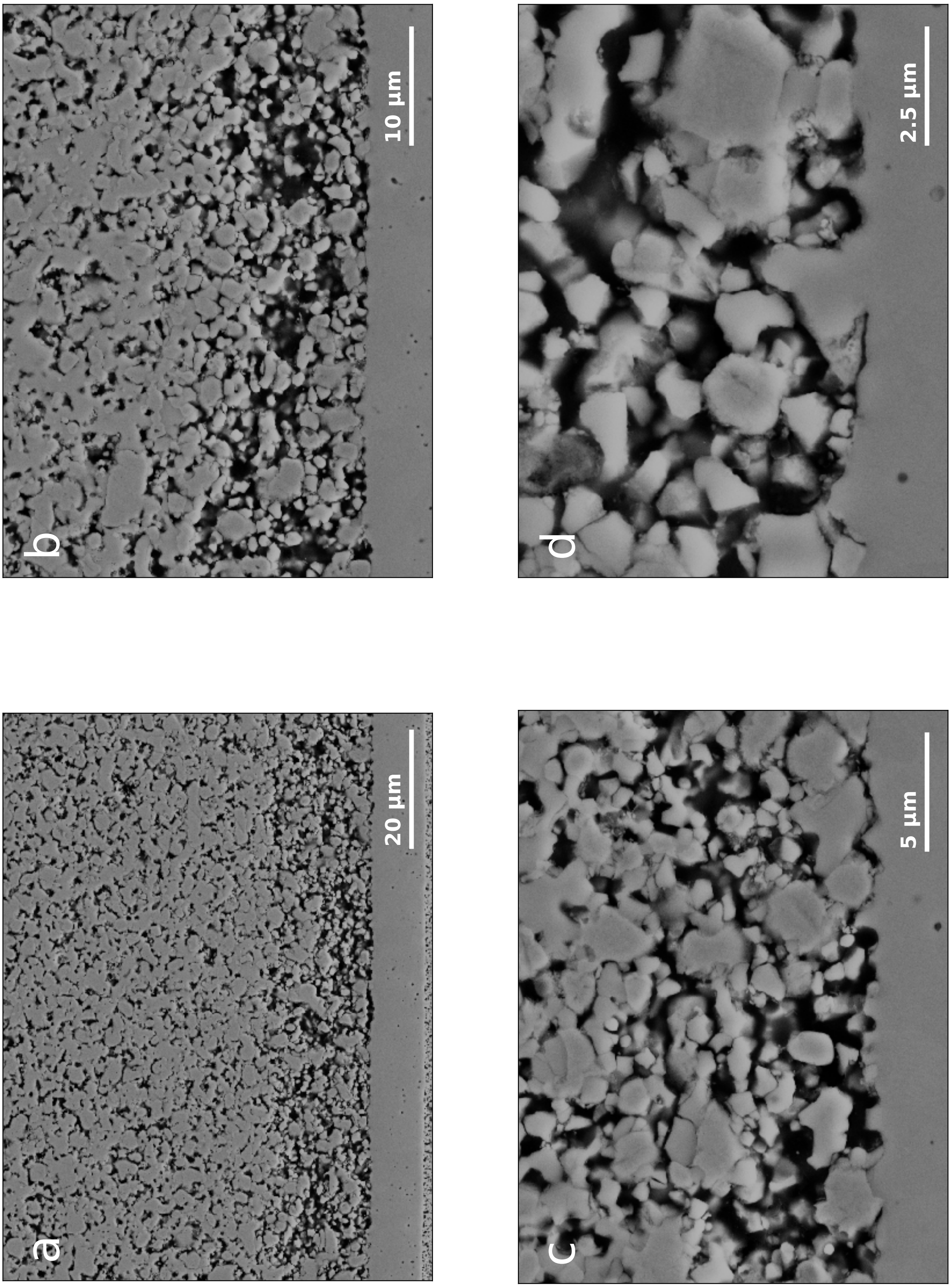

Figure D.18: CGO-4 without oxygen electrode contact layer

D.2 EDS

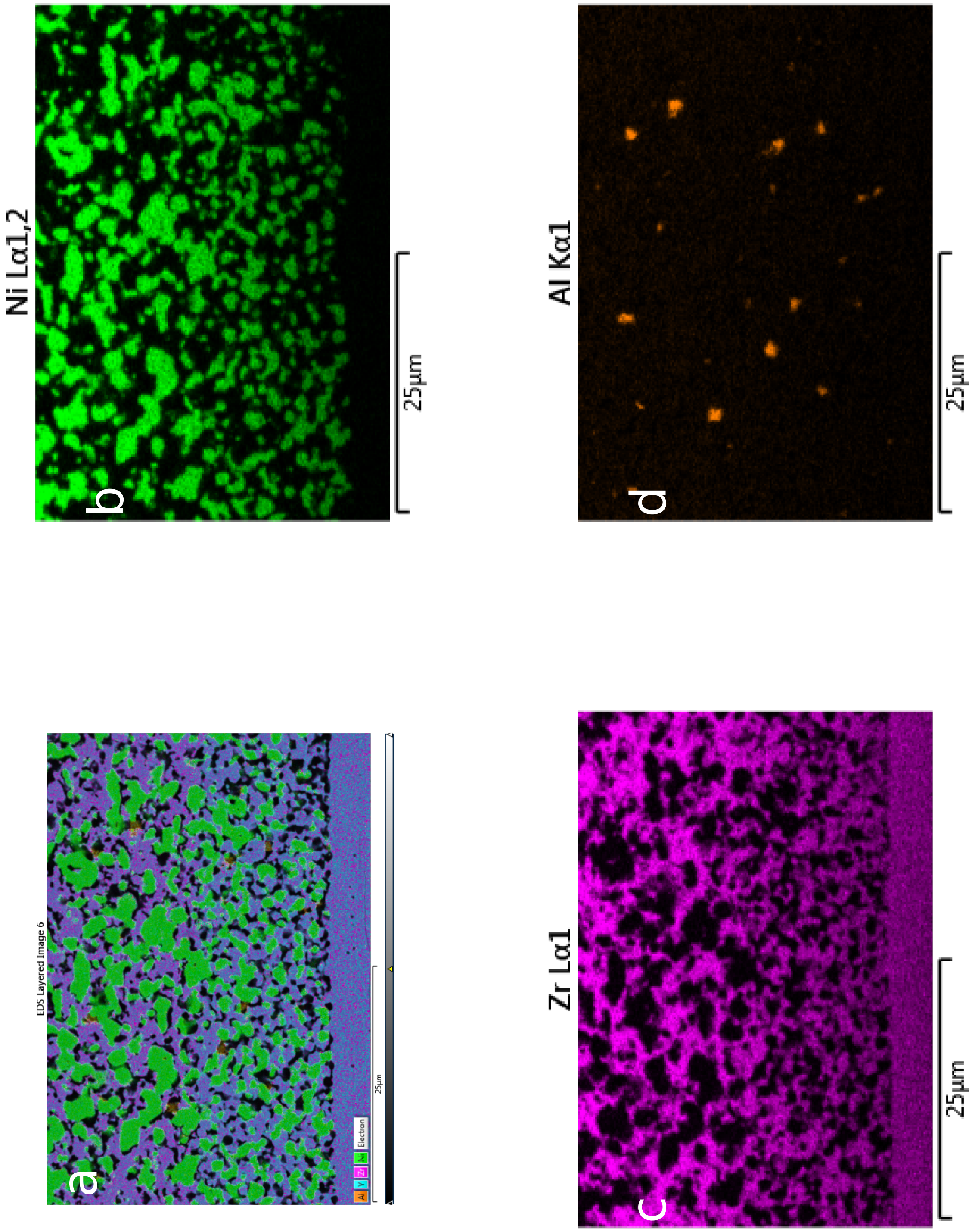

Figure D.19: 04HU in

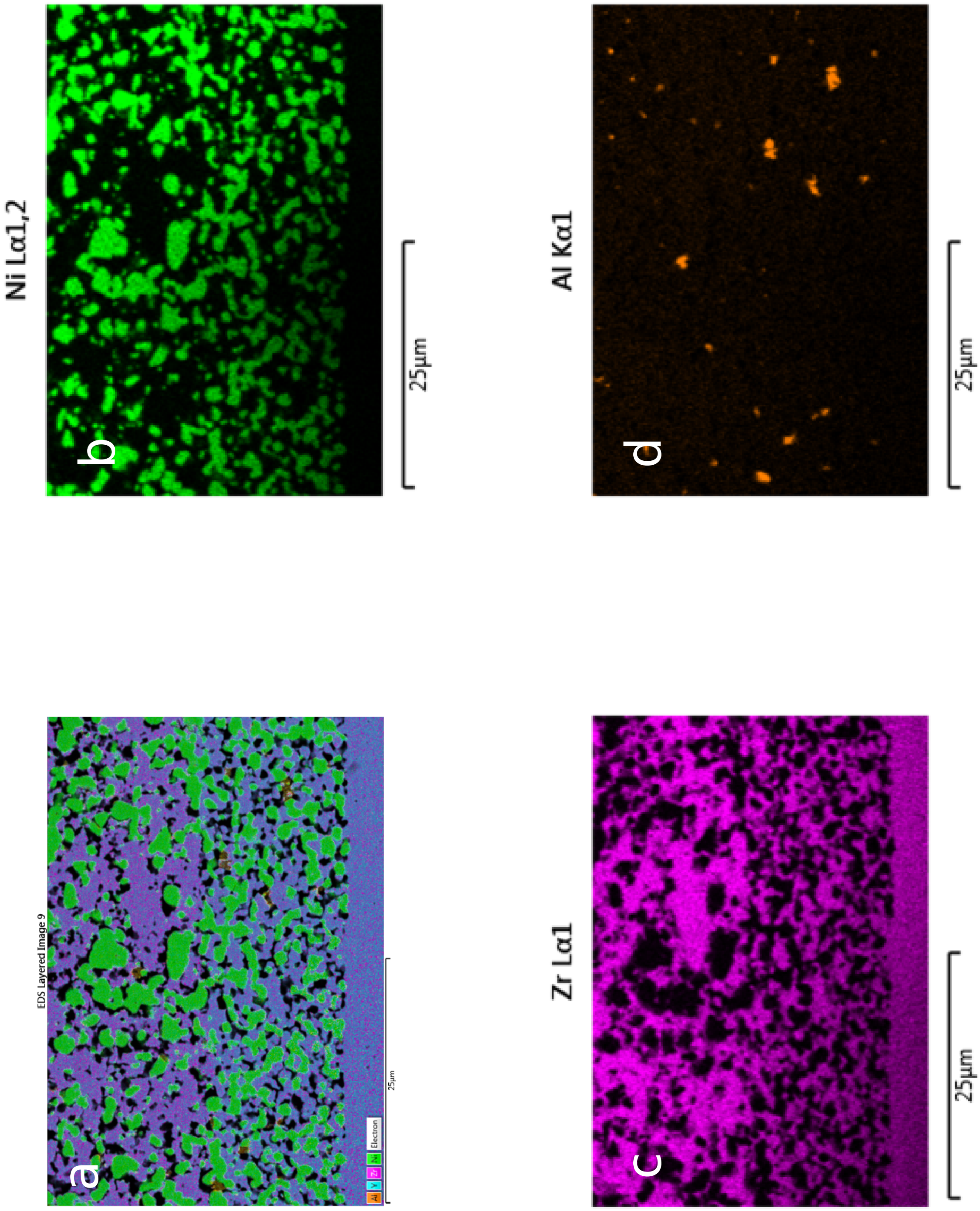

Figure D.20: 04HU out

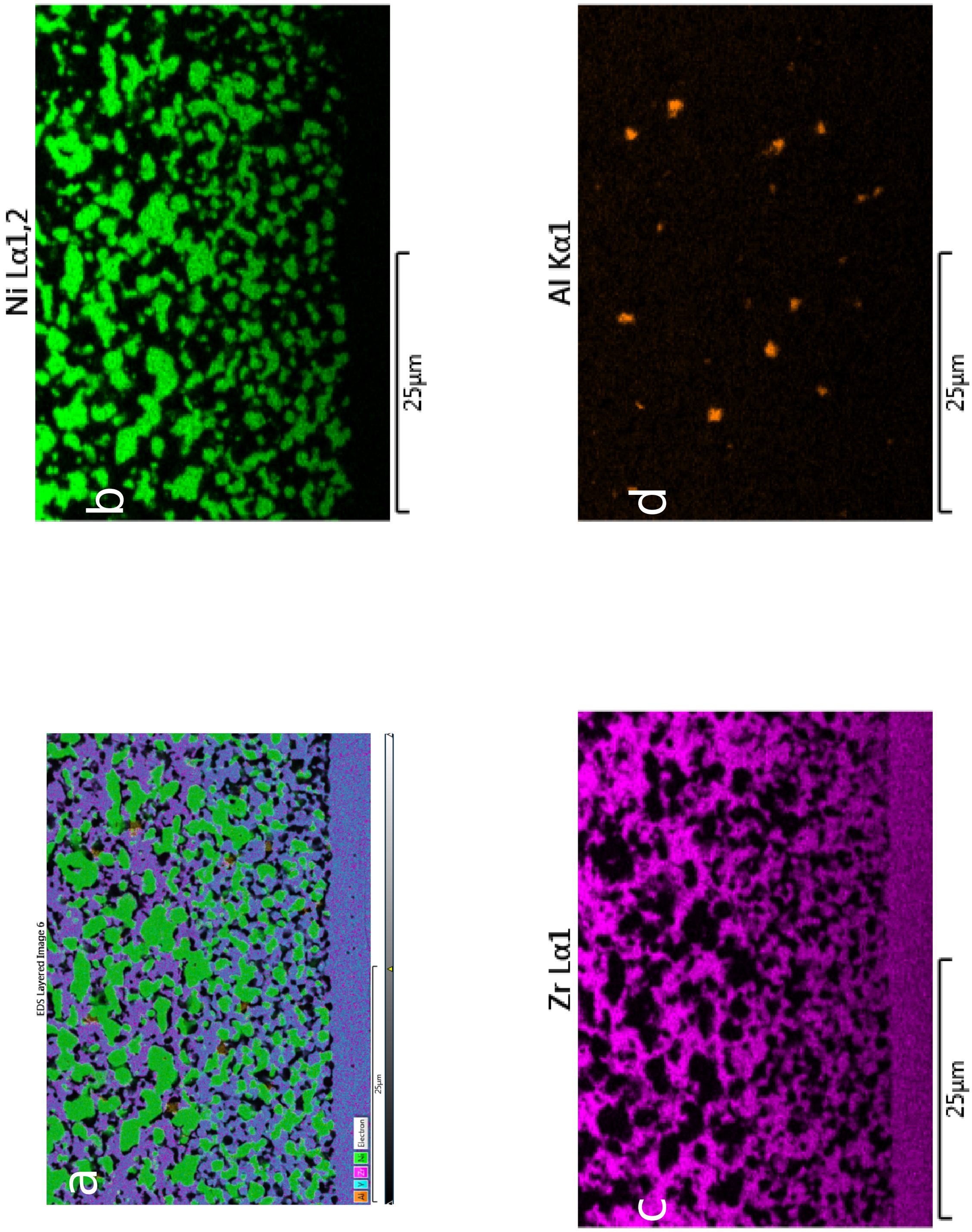

Figure D.21: 04HU in

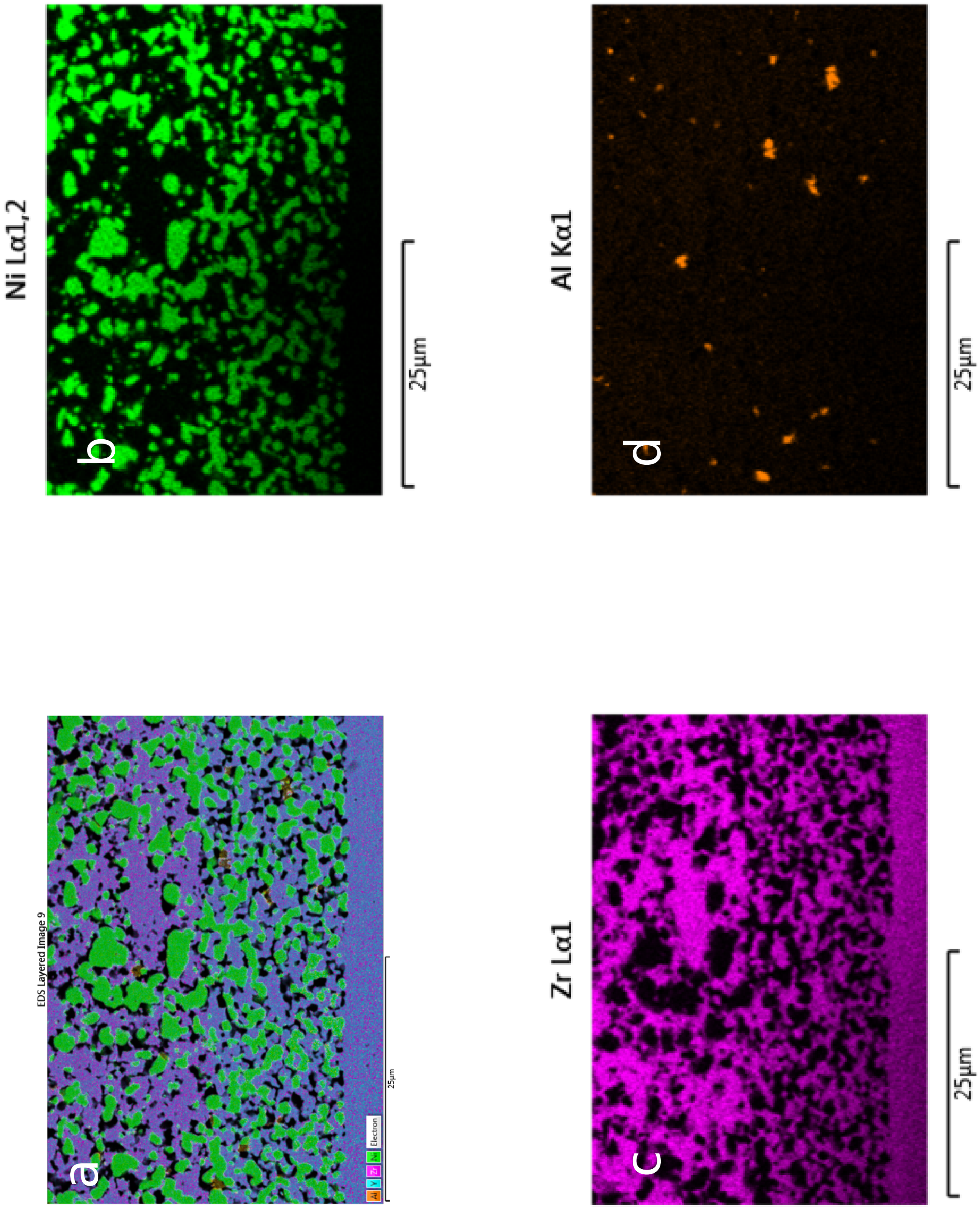

Figure D.22: 04HU out

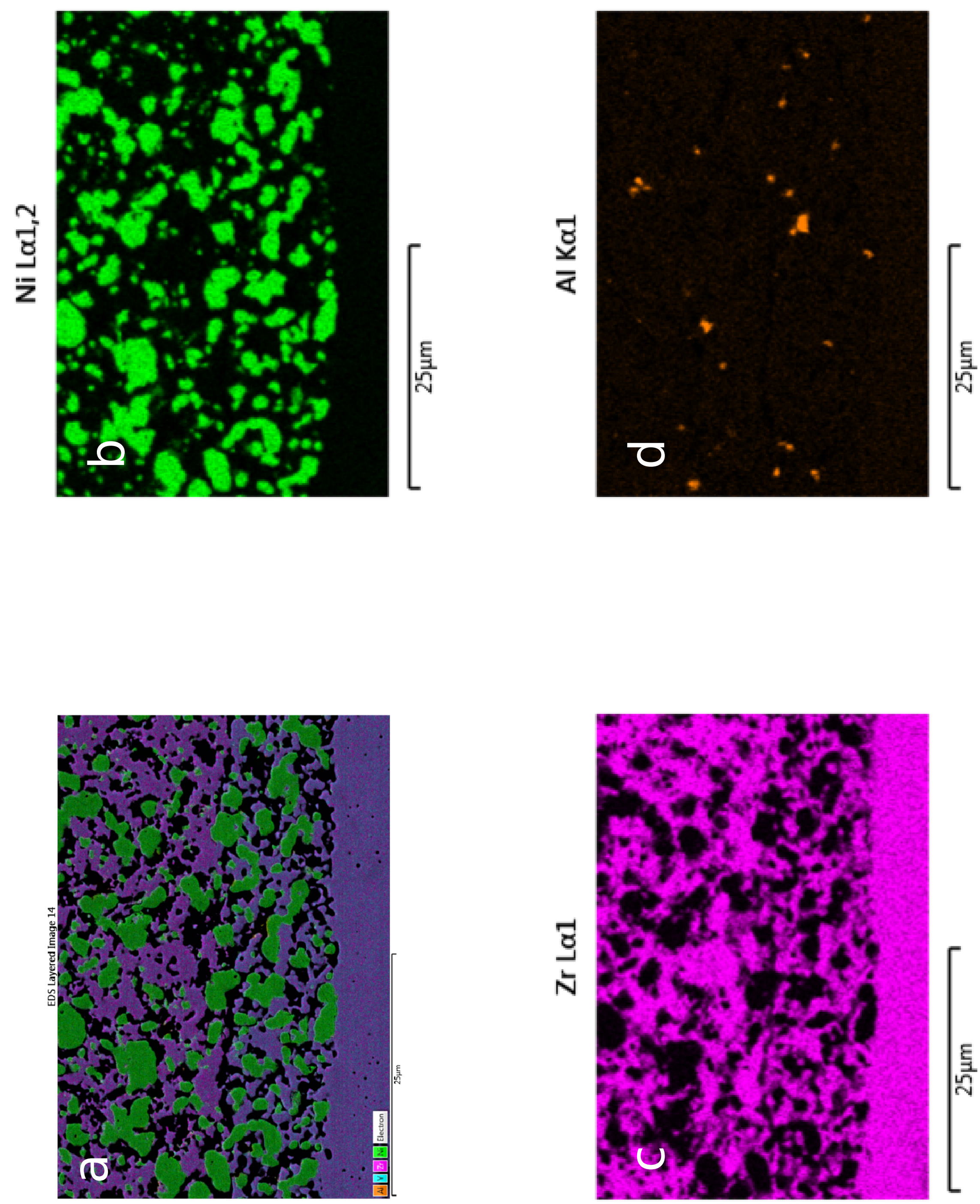

Figure D.23: 06HU-1 in

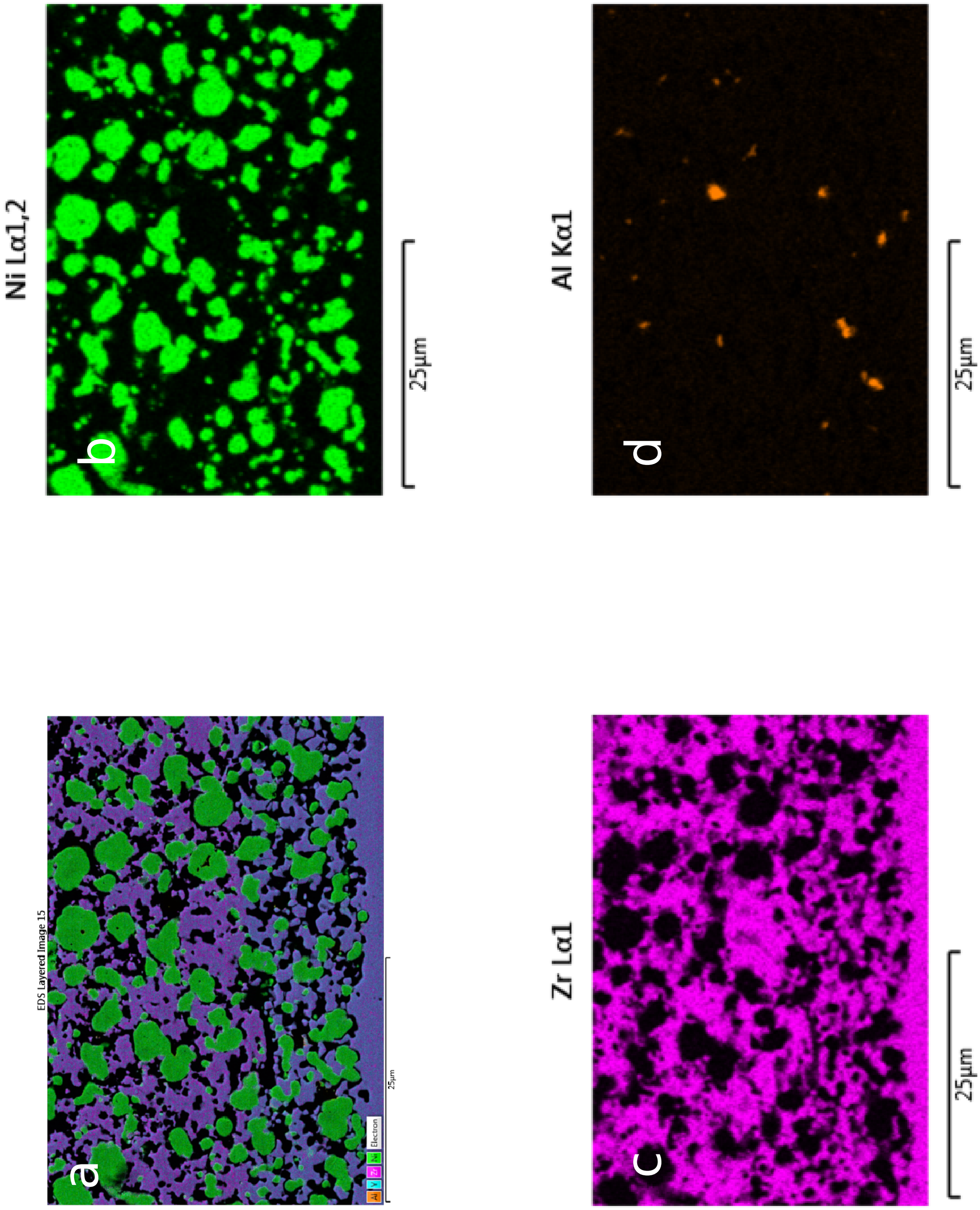

Figure D.24: 06HU-1 out

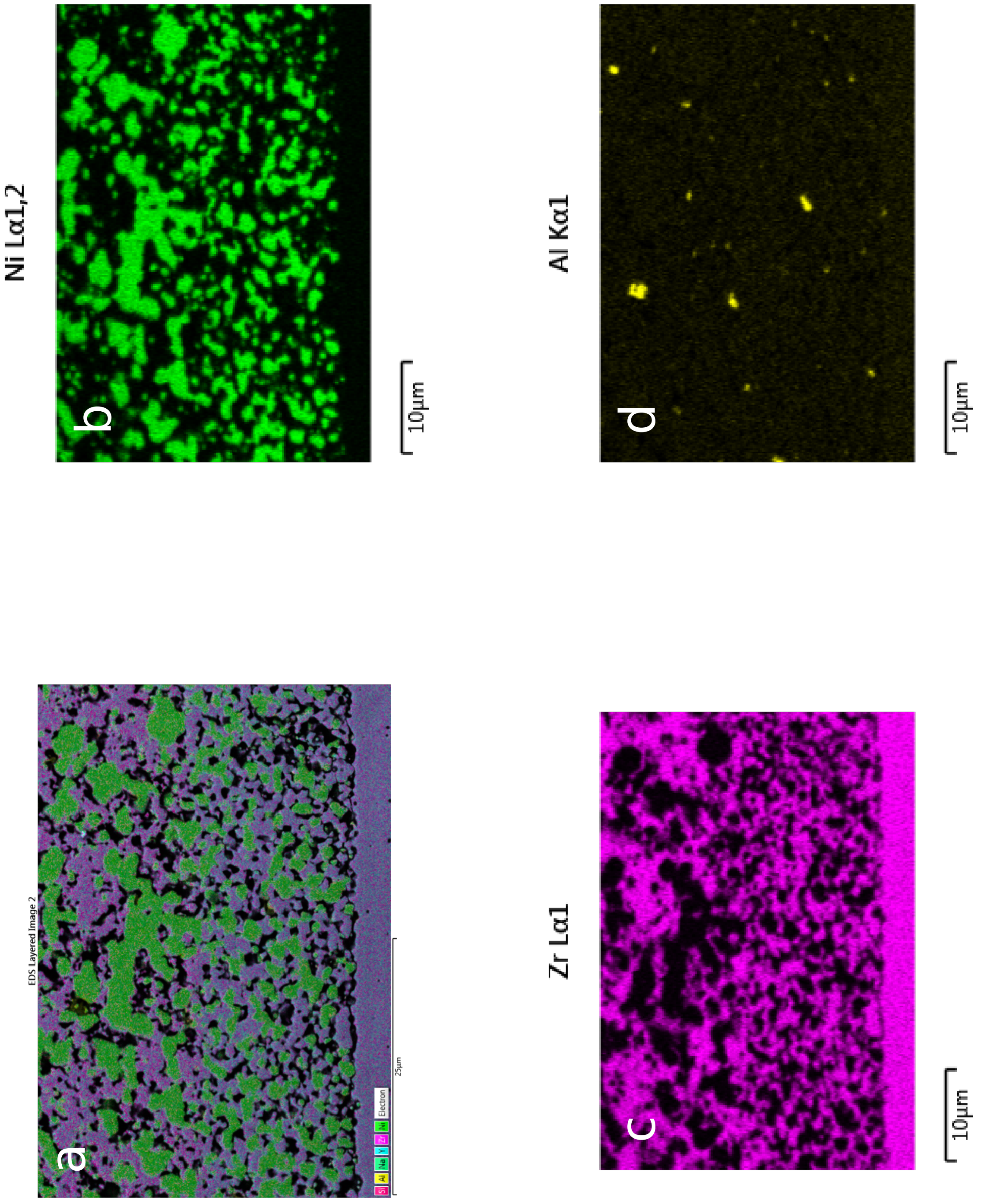

Figure D.25: 06LU-1 in

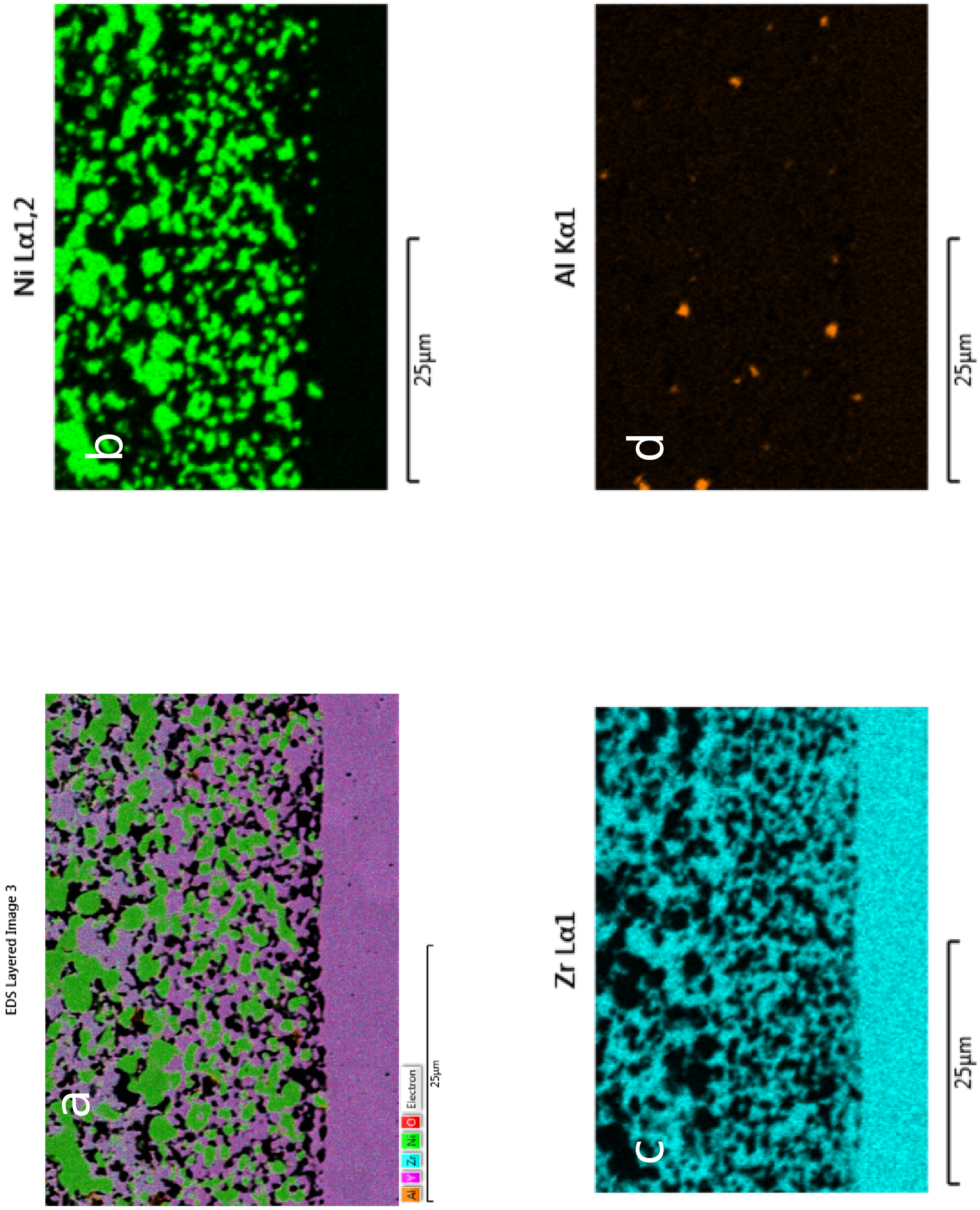

Figure D.26: 06LU-1 out

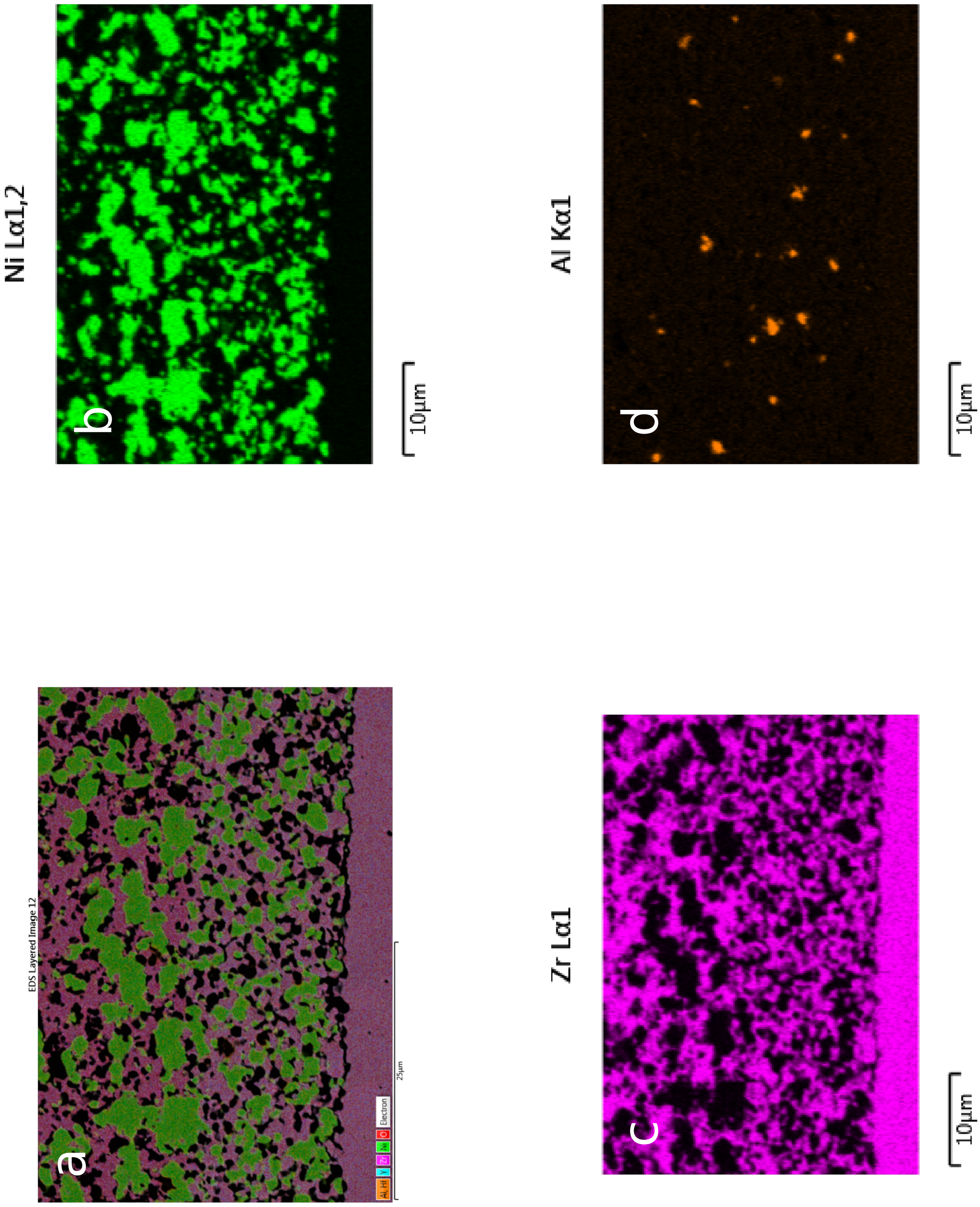

Figure D.27: 08LU in

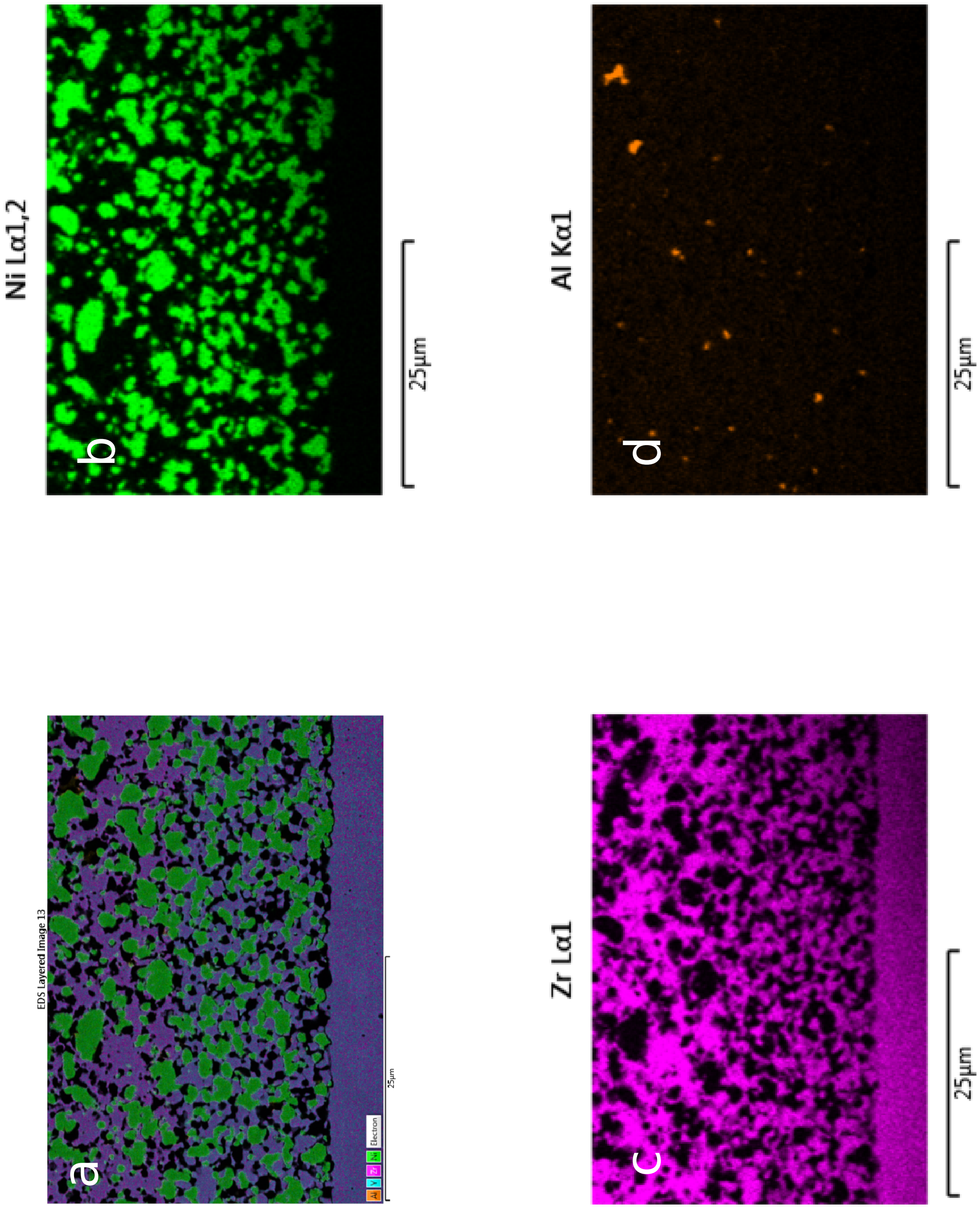

Figure D.28: 08LU out

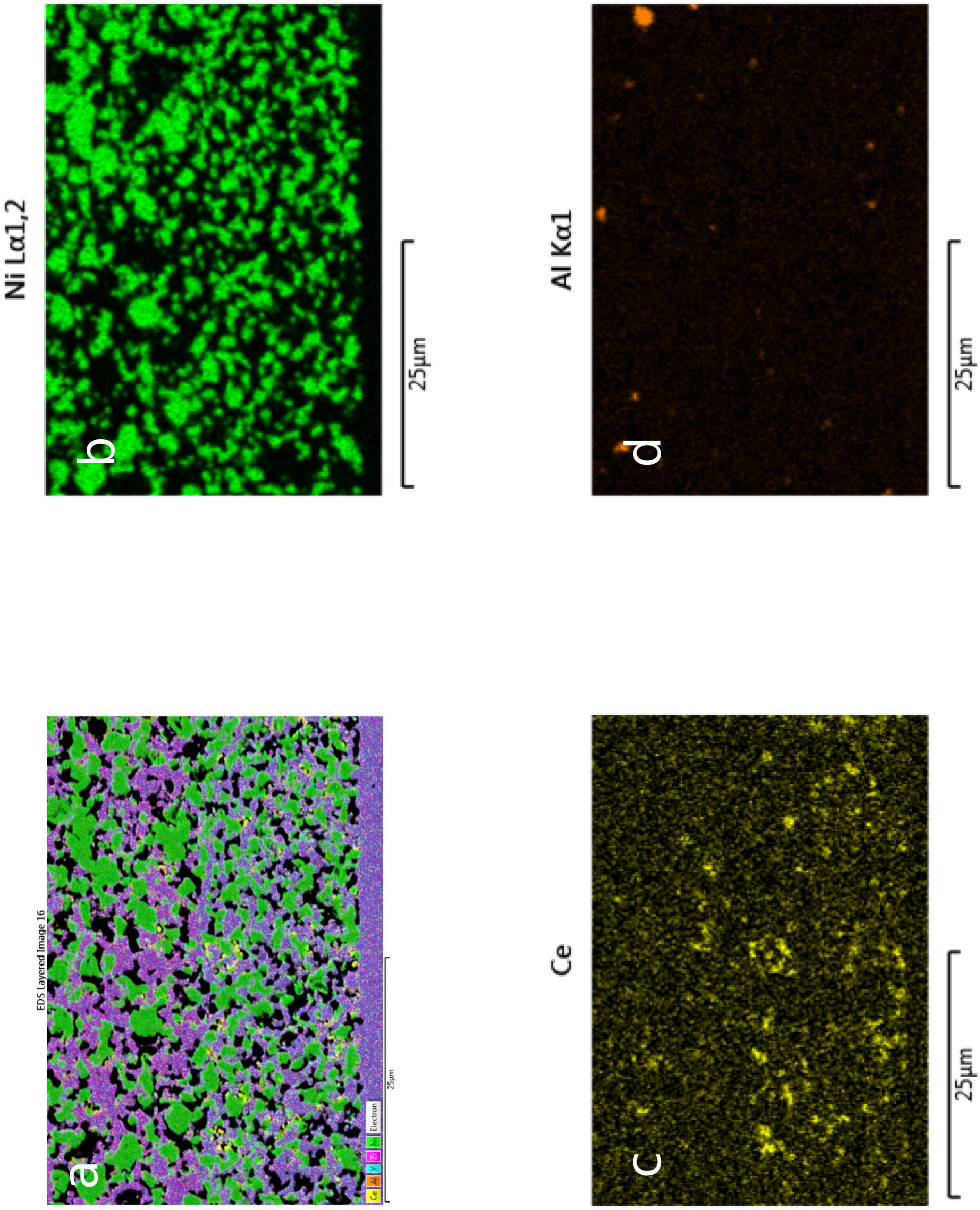

Figure D.29: CGO-2 in

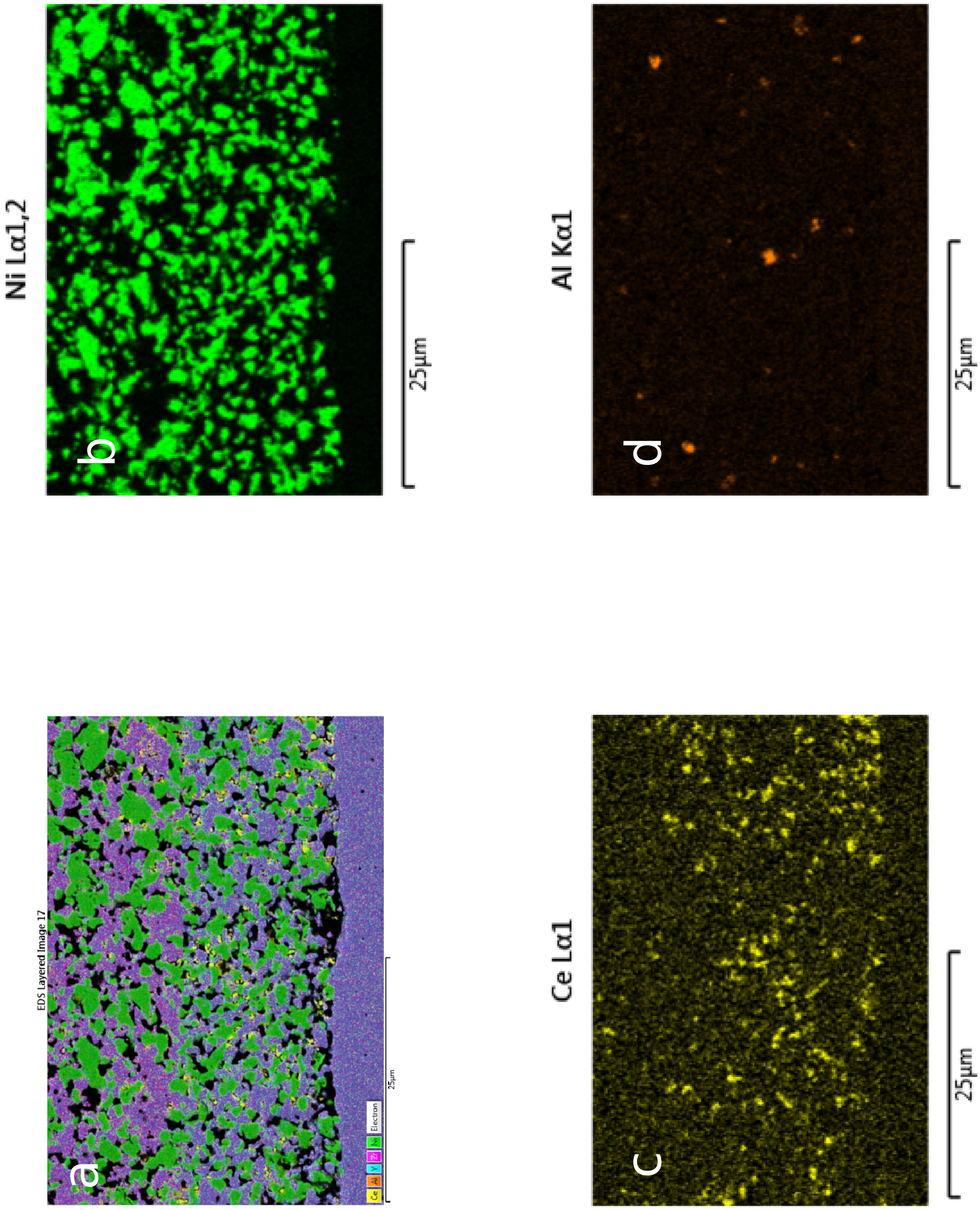

Figure D.30: CGO-2 out

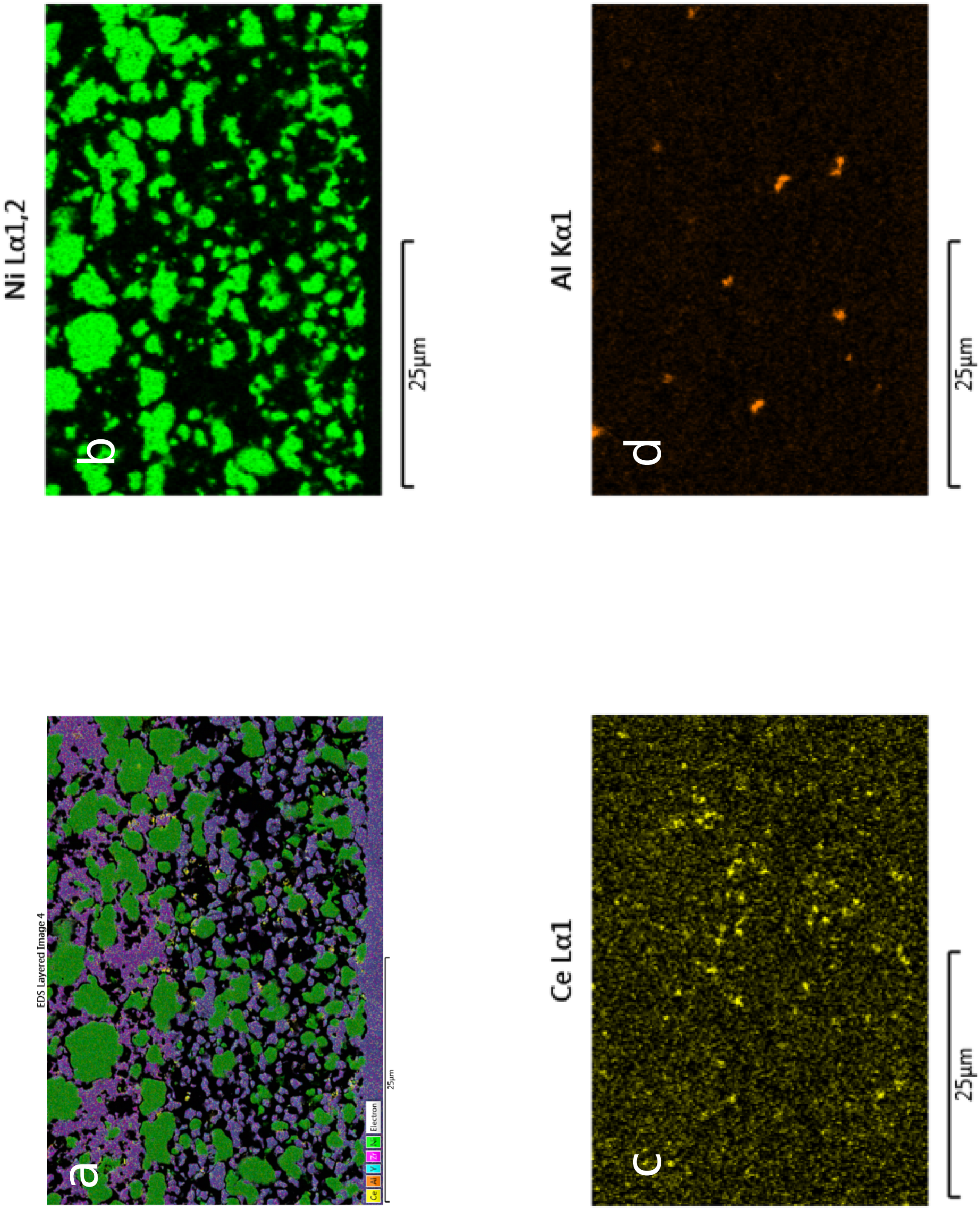

Figure D.31: CGO-4 in

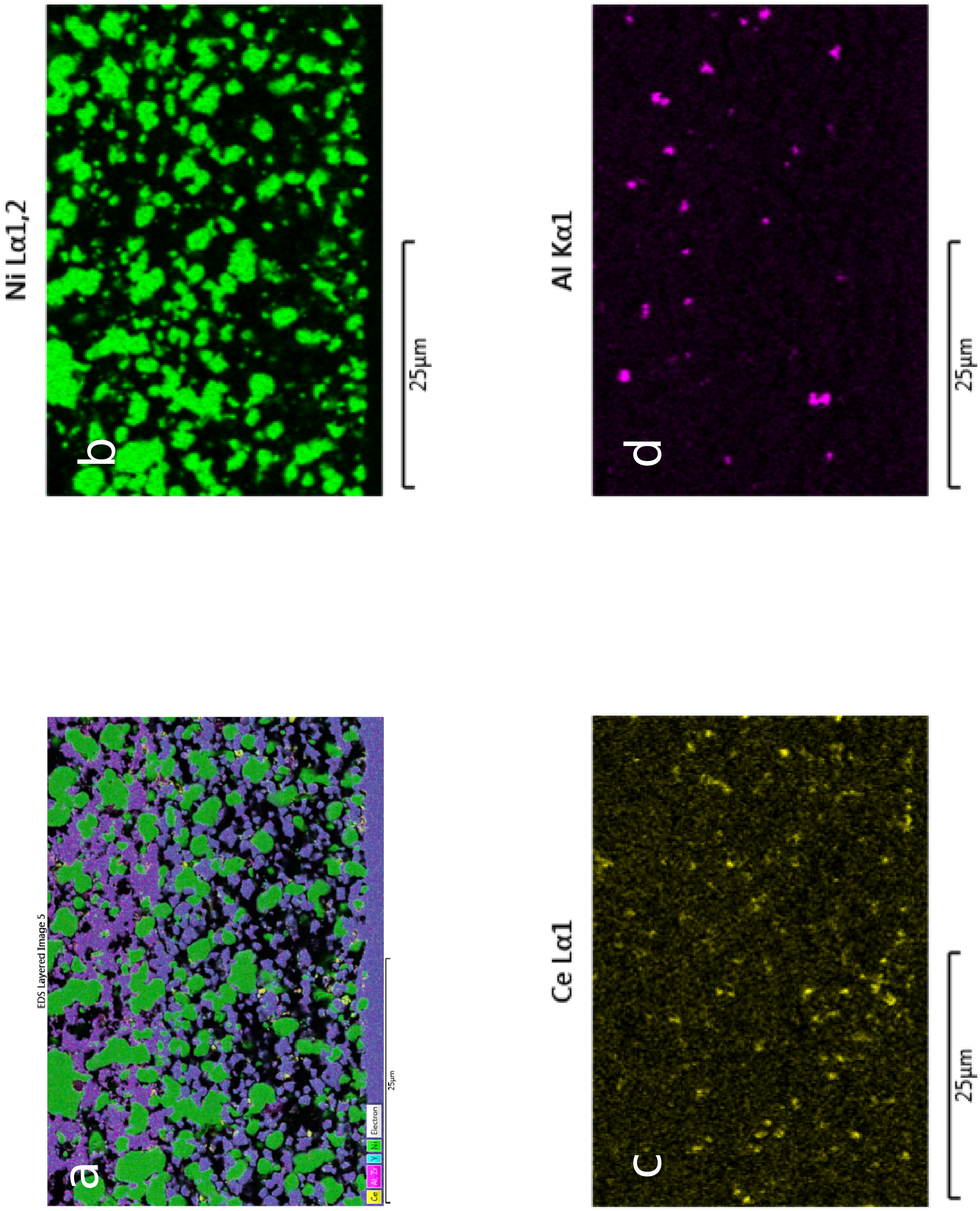

Figure D.32: CGO-4 out

Appendix E

Method for Pore Fraction Correction

The pore-size distribution and fraction was investigated as described in chapter 2 using the secondary electron detector with an acceleration voltage of 15 kV.
Figure E.1 a) shows a micrograph recorded at previously stated settings. A yellow circle in the figure highlights an issue, the structure beneath the surface of the cross section is visible, due to the epoxy filled pores being transparent.

This depth of view can be recognised by the human eye since it it is based on texture and context. This is however not the case for the image analysis software imageJ [119], which was used for discerning the pores based on a contrast thresholding method. Using the recorded pictures for determining the fraction of pores and the pore size distribution would hence lead to an underestimation of both. This issue was unfortunately discovered too late in the project to redo the microscopy for all samples.
This means that the results for the individual pore sizes are wrong, and hence also the size distribution thereof. An attempt has been made to correct the phase fraction of the pores.
The correction of the pore fraction assumes the error is systematic. To correct the data two more assumptions are stated:

1 - Isotropic Microstructure Perpendicular to the Fuel gas Flow The sections above (fig. 5.2) have shown that the structure of the fuel electrode is anisotropic along the fuel gas flow, which is caused by a varying gas composition and current/overpotential distribution. The current/overpotential distribution is also anisotropic moving away from the electrolyte into the support layer, which causes the Ni to migrate and the structure to become anisotropic. This anisotropy has lately been shown by Brus et. al. [240]. These factors are however expected to affect the microstructure isotropically at the same gas composition, why the microstructure is expected to be isotropic for two points at the same distance along the gas flow. This is also the implicit basis for other microstructural studies [20, 195], where the structure is assumed to be characteristic for a given point along the flow of the fuel gas.

2 - Consistent Penetration Depth The penetration depth is dependent on the energy of the incident electron and the density of the material [241]. The first is mainly based on the acceleration voltage and current used during SEM operation. This means that by using the same acceleration voltage and current during analysis of a given material, the penetration depth into said material is expected to be constant.

The purpose of the correction is to determine the depth of view/penetration depth. Since the epoxy/pores are transparent they act as windows into the underlying layers. Figure E.1 b) shows an SOEC as seen from above, the black and green parts symbolising the area with or without an active oxygen electrode respectively. Coloured lines drawn at the fuel gas inlet symbolises cross-sections. Imagine recording a SEM micrograph of the cross-section at the yellow line, if the pores are not transparent the actual pore fraction will be observed. This can be stated mathematically

$$F_{obs} = F_{act} \tag{E.1}$$

where F_{obs} is the observed pore fraction and F_{act} is the actual pore fraction. This means that if the actual pore fraction is 25%, a 25% pore fraction will be observed. If the pores are transparent they will act as windows, such that parts of the cross-section at the red line can be seen. In this example the depth of the red line lies at a point where the pore fraction within the ”windows” is the same at the actual pore fraction.

Assuming a pore fraction of 25%, meaning through layer 0(yellow) 25% of layer 1 can be seen. The observed pore fraction can be calculated as the product of the layers, yielding 6.25%. This pore fraction is the expected average of all the ”windows”. This can be expressed mathematically

$$F_{obs} = F_{act} \cdot F_{act} = F_{act}^2 \tag{E.2}$$

This example can be continued in the case of the pores overlapping/coinciding between layer 0 (yellow) and 1 (red), meaning that the layer 2 (2) will be visible. Layer 2, is similarly assumed to have a pore fraction of 25%. Due to the assumption of isotropy the distance between layer 1 and 2 will be identical with that between 0 and 1. This will lead to the pore fraction observed at layer 2 to be:

$$F_{obs} = F_{act} \cdot F_{act} \cdot F_{act} = F_{act}^{3} \tag{E.3}$$

While the actual distance between layers remains unknown, the assumption of isotropy means that the distance between layers for which the pore fraction (i.e. layer 1) observed through the pores of the upper layer (i.e. layer 0) is constant. This means that the observed pore fraction can be expressed as the number of layers, rather than actual penetration depth, as

$$F_{obs} = F_{act}^{n+1} \tag{E.4}$$

Where n is the number of layers (cross-sections) in the depth of view. While similar logic might have been done, it has not been possible to find in the literature.
F_{obs} was in this project determined to be 16.3% for the pores of SEM-ref. A 3D-reconstruction of a SOEC of similar fuel electrode specifications found a pore fraction of 24.3% in an non-tested SOEC [195]. Using $F_{act} = 24.3\%$ as boundary condition for SEM-ref, and isolating for n, gives $n = 0.282$. This means that the penetration depth is much less than one ”layer”.

Figure E.1 c) shows the relationship between F_{act} and F_{obs} as the full line. The dotted line in the figure represents the deviation between the two. The two subfigures highlights the F_{obs} (blue) and deviation (yellow) at the coloured areas in the figure. The ranges have been chosen to reflect the ranges wherein the observed/calculated fraction lies. From this it can be seen that the correction can be approximated to linear within the applied range. The red and green lines shows that linearity persist in case of a ±33% deviation in the penetration.
Figure E.1 d) shows the relationship between the total charge experienced during the test and the pore fraction, for both the fractions as observed (blue dots), and the corrected fractions (black ’x’s). The purpose of this figure is to show that the correction does not create any artificial correlations between the points. Any correlation between charge and pore fraction is discussed in chapter 5

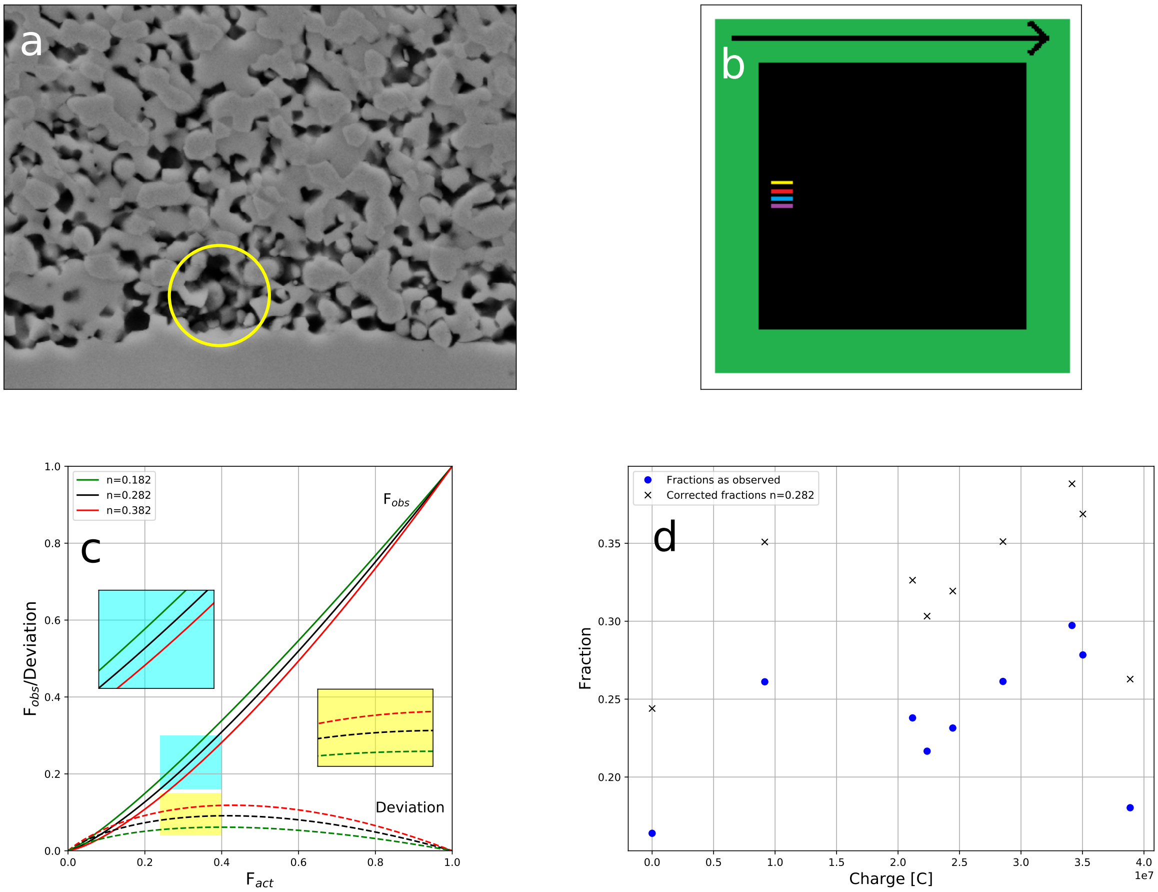

Figure E.1: a) SEM micrograph of SEM-Ref. b) Graphic representation of SOEC as seen from above, the arrow represents the direction of the gas-flow to the fuel electrode, yellow line represents similar lengths. c) Comparison between observed and actual pore-fraction at different values of n when corrected using the formula $F_{obs} = F_{act}^{n}$(full lines), and the arising deviation thereof (dotted lines). Subfigures within c) corresponds to data from similarly coloured areas. d) Pore fractions as observed (blue dots) and corrected (black 'x') as function of the experienced charge during long-term testing.

Bibliography

[1] G.S. Callendar. “Artificial production”. In: *Q. J. R. Meteorol. Soc.* 1909 (1938), pp. 223–240.

[2] World Commission on Environment and Development. “Report of the World Commission on Environment and Development: Our Common Future (The Brundtland Report)”. In: *Med. Confl. Surviv.* (1987). ISSN: 0748-8009. DOI: `10.1080/07488008808408783`.

[3] David Herring. *What can we do to slow or stop global warming?* 2020. URL: `https://www.climate.gov/news-features/climate-qa/what-can-we-do-slow-or-stop-global-warming` (visited on 25/01/2023).

[4] NASA. *Responding to Climate Change*. 2023. URL: `https://climate.nasa.gov/solutions/adaptation-mitigation/` (visited on 25/01/2023).

[5] United Nations. *Transforming Our World: The 2030 Agenda for Sustainable Development*. Tech. rep. 2015. DOI: `10.1201/b20466-7`. URL: `sustainabledevelopment.un.org`.

[6] Matthew C. Nisbet and Teresa Myers. “The polls-trends twenty years of public opinion about global warming”. In: *Public Opin. Q.* 71.3 (2007), pp. 444–470. ISSN: 0033362X. DOI: `10.1093/poq/nfm031`.

[7] Valerie Hase et al. “Climate change in news media across the globe: An automated analysis of issue attention and themes in climate change coverage in 10 countries (2006–2018)”. In: *Glob. Environ. Chang.* 70.September (2021). ISSN: 09593780. DOI: `10.1016/j.gloenvcha.2021.102353`.

[8] Sandra Venghaus, Meike Henseleit and Maria Belka. “The impact of climate change awareness on behavioral changes in Germany: changing minds or changing behavior?” In: *Energy. Sustain. Soc.* 12.1 (2022), pp. 1–11. ISSN: 21920567. DOI: `10.1186/s13705-022-00334-8`. URL: `https://doi.org/10.1186/s13705-022-00334-8`.

[9] Priyardarshi R. Shukla et al. *Climate Change 2022 Mitigation of Climate Change*. 2022.

[10] Thomas F. Stocker et al. *WG1AR5_ALL_FINAL.pdf*. Tech. rep. Cambridge, 2013, pp. 1–1500.

[11] Pierre Friedlingstein et al. "Global Carbon Budget 2022". In: *Earth Syst. Sci. Data* 14.11 (Nov. 2022), pp. 4811–4900. ISSN: 1866-3516. DOI: `10.5194/essd-14-4811-2022`. URL: `https://essd.copernicus.org/articles/14/4811/2022/`.

[12] Vaclav Smil. *Energy Transitions: Global and National Perspectives*. Second edi. Santa Barbara, California: Praeger, 2016, p. 296. ISBN: 978-1-4408-5324-0.

[13] Charles Moore et al. "European Electricity Review 2022". In: *Ember* February (2022), p. 34. URL: `https://ember-climate.org/insights/research/european-electricity-review-2022/`.

[14] Eadaoin Doddy Clarke and Conor Sweeney. "Solar energy and weather". In: *Weather* 77.3 (2022), pp. 90–91. ISSN: 14778696. DOI: `10.1002/wea.4124`.

[15] Giovani Manuel Pitra and K. S.Sastry Musti. "Duck Curve with Renewable Energies and Storage Technologies". In: *Proc. - 2021 IEEE 13th Int. Conf. Comput. Intell. Commun. Networks, CICN 2021* (2021), pp. 66–71. DOI: `10.1109/CICN51697.2021.9574671`.

[16] Mogens Bjerg Mogensen et al. *High-temperature electrolysis*. Ed. by Werner Sitte and Rotraut Merkle. Bristol, 2023, p. 500. ISBN: 9781420006070. DOI: `10.1201/9781420006070.ch3`.

[17] S. C. Singhal and Xiao Dong Zhou. "Fuel Cells - Solid Oxide Fuel Cells | Systems". In: *Encycl. Electrochem. Power Sources* (2009), pp. 99–119. DOI: `10.1016/B978-044452745-5.00262-8`.

[18] Per Hjalmarsson et al. "Durability of high performance Ni-yttria stabilized zirconia supported solid oxide electrolysis cells at high current density". In: *J. Power Sources* 262 (2014), pp. 316–322. ISSN: 03787753. DOI: `10.1016/j.jpowsour.2014.03.133`. URL: `http://dx.doi.org/10.1016/j.jpowsour.2014.03.133`.

[19] Jingbo Yan et al. "High-efficiency intermediate temperature solid oxide electrolyzer cells for the conversion of carbon dioxide to fuels". In: *J. Power Sources* 252 (2014), pp. 79–84. ISSN: 03787753. DOI: `10.1016/j.jpowsour.2013.11.047`. URL: `http://dx.doi.org/10.1016/j.jpowsour.2013.11.047`.

[20] Anne Hauch et al. "Ni/YSZ electrodes structures optimized for increased electrolysis performance and durability". In: *Solid State Ionics* 293 (2016), pp. 27–36. ISSN: 01672738. DOI: `10.1016/j.ssi.2016.06.003`. URL: `http://dx.doi.org/10.1016/j.ssi.2016.06.003`.

[21] Yuefeng Song et al. “High-Temperature CO2 Electrolysis in Solid Oxide Electrolysis Cells: Developments, Challenges, and Prospects”. In: *Adv. Mater.* 31.50 (2019), pp. 1–18. ISSN: 15214095. DOI: `10.1002/adma.201902033`.

[22] Ming Chen, Xiaofeng Tong and Simov Ovtar. “ Lessons Learned from Operating a Solid Oxide Electrolysis Cell at 1.25 a/cm 2 for One Year ”. In: *ECS Meet. Abstr.* MA2021-03.1 (2021), pp. 213–213. DOI: `10.1149/ma2021-031213mtgabs`.

[23] Aiswarya Krishnakumar Padinjarethil et al. “Electrochemical Characterization and Modelling of Anode and Electrolyte Supported Solid Oxide Fuel Cells”. In: *Front. Energy Res.* 9.September (2021), pp. 1–19. ISSN: 2296598X. DOI: `10.3389/fenrg.2021.668964`.

[24] K. Tamm et al. “Solid oxide fuel cell anodes prepared by infiltration of strontium doped lanthanum vanadate into doped ceria electrolyte”. In: *Electrochim. Acta* 106 (2013), pp. 398–405. ISSN: 00134686. DOI: `10.1016/j.electacta.2013.05.127`. URL: `http://dx.doi.org/10.1016/j.electacta.2013.05.127`.

[25] Tal Z. Sholklapper et al. “LSM-infiltrated solid oxide fuel cell cathodes”. In: *Electrochem. Solid-State Lett.* 9.8 (2006), pp. 376–379. ISSN: 10990062. DOI: `10.1149/1.2206011`.

[26] Hernán Monzón and Miguel A. Laguna-Bercero. “CO2 and steam electrolysis using a microtubular solid oxide cell”. In: *JPhys Energy* 2.1 (2020). ISSN: 25157655. DOI: `10.1088/2515-7655/ab4250`.

[27] Z. Ma et al. “Developments in CO2 Electrolysis of Solid Oxide Electrolysis Cell with Different Cathodes□”. In: *Fuel Cells* 20.6 (2020), pp. 650–660. ISSN: 16156854. DOI: `10.1002/fuce.201900240`.

[28] Matthias Riegraf, Alexander Surrey and Rémi Costa. “Ni/CGO-Based Electrolyte-Supported Cells During Co-Electrolysis: The Role of Feed Gas Impurities”. In: *ECS Meet. Abstr.* MA2021-03.1 (2021), pp. 75–75. DOI: `10.1149/ma2021-03175mtgabs`.

[29] Publisher Taylor et al. “Fuel Cells”. In: *Encycl. Environ. Manag. Fuel Cells* January 2015 (2014), pp. 37–41. DOI: `10.1081/E-EEM-120050576`.

[30] H. Hassanzadeh and S. H. Mansouri. “Efficiency of ideal fuel cell and Carnot cycle from a fundamental perspective”. In: *Proc. Inst. Mech. Eng. Part A J. Power Energy* 219.4 (2005), pp. 245–254. ISSN: 09576509. DOI: `10.1243/095765005X28571`.

[31] Publisher Taylor et al. “Electrolysis”. In: *Encycl. Environ. Manag. Electrolysis* January 2015 (2014), pp. 37–41. DOI: `10.1081/E-EEM-120050577`.

[32] Minghai Shen et al. “Progress and prospects of reversible solid oxide fuel cell materials”. In: *iScience* 24.12 (2021), p. 103464. ISSN: 25890042. DOI: `10.1016/j.isci.2021.103464`. URL: `https://doi.org/10.1016/j.isci.2021.103464`.

[33] Konrad Motylinski et al. “Dynamic modelling of reversible solid oxide cells for grid stabilization applications”. In: *Energy Convers. Manag.* 228.September 2020 (2021), p. 113674. ISSN: 01968904. DOI: `10.1016/j.enconman.2020.113674`. URL: `https://doi.org/10.1016/j.enconman.2020.113674`.

[34] Masashi Mori et al. “Evaluation of Ni and Ti-doped Y2O3 stabilized ZrO2 cermet as an anode in high-temperature solid oxide fuel cells”. In: *Solid State Ionics* 160.1-2 (2003), pp. 1–14. ISSN: 01672738. DOI: `10.1016/S0167-2738(03)00144-9`.

[35] Monika Backhaus-Ricoult. “SOFC - A playground for solid state chemistry”. In: *Solid State Sci.* 10.6 (2008), pp. 670–688. ISSN: 12932558. DOI: `10.1016/j.solidstatesciences.2007.11.021`.

[36] Johan Hjelm et al. “Electrochemical Characterization of Planar Anode Supported SOFC with Sr-Doped Lanthanum Cobalt Oxide Cathodes”. In: *ECS Meet. Abstr.* MA2008-01.10 (2008), pp. 384–384. DOI: `10.1149/ma2008-01/10/384`.

[37] Søren Højgaard Jensen et al. “SOFC Ni-electrode Resistance Distribution Investigated by Gas Concentration Impedance in a Plug-Flow Setup”. In: *ECS Trans.* 13.26 (2008), pp. 307–315. ISSN: 1938-5862. DOI: `10.1149/1.3050402`.

[38] A. Kromp et al. “Electrochemical analysis of reformate-fuelled anode supported SOFC”. In: *J. Electrochem. Soc.* 158.8 (2011). ISSN: 00134651. DOI: `10.1149/1.3597177`.

[39] K. Kendall. *Portable Early Market SOFCs*. 2nd ed. Elsevier Ltd., 2016, pp. 329–356. ISBN: 9780124104532. DOI: `10.1016/B978-0-12-410453-2.00010-5`. URL: `http://dx.doi.org/10.1016/B978-0-12-410453-2.00010-5`.

[40] Bo Yu et al. “Advance in highly efficient hydrogen production by high temperature steam electrolysis”. In: *Sci. China, Ser. B Chem.* 51.4 (2008), pp. 289–304. ISSN: 10069291. DOI: `10.1007/s11426-008-0054-z`.

[41] M. A. Laguna-Bercero et al. “Steam Electrolysis Using a Microtubular Solid Oxide Fuel Cell”. In: *J. Electrochem. Soc.* 157.6 (2010), B852. ISSN: 00134651. DOI: `10.1149/1.3332832`.

[42] Xiufu Sun et al. “Durability of Solid Oxide Electrolysis Cell and Interconnects for Steam Electrolysis”. In: *ECS Trans.* 57.1 (2013), pp. 3229–3238.

[43] Lawrence Berkeley. “Sunfire SOEC steam electrolysis module for Salzgitter Flachstahl”. In: *Fuel Cells Bull.* 2017.7 (2017), p. 12. ISSN: 14642859. DOI: `10.1016/s1464-2859(17)30269-9`.

[44] Anne Hauch et al. “A Decade of Solid Oxide Electrolysis Improvements at DTU Energy”. In: *ECS Trans.* 75.42 (2017), pp. 3–14. ISSN: 1938-6737. DOI: `10.1149/07542.0003ecst`.

[45] Basma Mewafy et al. “Influence of Surface State on the Electrochemical Performance of Nickel-Based Cermet Electrodes during Steam Electrolysis”. In: *ACS Appl. Energy Mater.* 2.10 (2019), pp. 7045–7055. ISSN: 25740962. DOI: `10.1021/acsaem.9b00779`.

[46] Velia Fabiola Valdés-López et al. “Carbon monoxide poisoning and mitigation strategies for polymer electrolyte membrane fuel cells – A review”. In: *Prog. Energy Combust. Sci.* 79.0 (2020). ISSN: 03601285. DOI: `10.1016/j.pecs.2020.100842`.

[47] Yang Li et al. “Carbon monoxide powered fuel cell towards H2-onboard purification”. In: *Sci. Bull.* 66.13 (2021), pp. 1305–1311. ISSN: 20959281. DOI: `10.1016/j.scib.2021.02.006`. URL: `https://doi.org/10.1016/j.scib.2021.02.006`.

[48] Georgina Jeerh, Mengfei Zhang and Shanwen Tao. “Recent progress in ammonia fuel cells and their potential applications”. In: *J. Mater. Chem. A* 9.2 (2021), pp. 727–752. ISSN: 20507496. DOI: `10.1039/d0ta08810b`.

[49] Ken Takeuchi et al. “Direct-DME SOFC for Intermediate Operation Temperature Using Proton Conductor as the Electrolyte”. In: *ECS Meet. Abstr.* MA2011-01.12 (2011), pp. 875–875. DOI: `10.1149/ma2011-01/12/875`.

[50] Chao Su et al. “Further performance enhancement of a DME-fueled solid oxide fuel cell by applying anode functional catalyst”. In: *Int. J. Hydrogen Energy* 37.8 (2012), pp. 6844–6852. ISSN: 03603199. DOI: `10.1016/j.ijhydene.2012.01.057`. URL: `http://dx.doi.org/10.1016/j.ijhydene.2012.01.057`.

[51] Soichiro Sameshima et al. “Cell performance of SOFC using CH4-CO2 mixed gases”. In: *Ceram. Int.* 40.4 (2014), pp. 6279–6284. ISSN: 02728842. DOI: `10.1016/j.ceramint.2013.11.086`. URL: `http://dx.doi.org/10.1016/j.ceramint.2013.11.086`.

[52] Bryan Jackson. “Engineering the Solid Oxide Fuel Cell Through Infiltrating the Porous Electrodes”. PhD thesis. 2018.

[53] Arthur L. Kohl and Richard B. Nielsen. “Thermal and Catalytic Conversion of Gas Impurities”. In: *Gas Purif.* 1997, pp. 1136–1186. DOI: `10.1016/b978-088415220-0/50013-6`.

[54] S. Nady et al. “Power to X Systems: STATE-OF-THE-ART (PTX)”. In: *IFAC-PapersOnLine* 55.12 (2022), pp. 300–305. ISSN: 24058963. DOI: `10.1016/j.ifacol.2022.07.328`. URL: `https://doi.org/10.1016/j.ifacol.2022.07.328`.

[55] Junwei Wu et al. “Editorial: High Temperature Solid Oxide Cells”. In: *Front. Chem.* 9.September (2021), pp. 1–3. ISSN: 22962646. DOI: `10.3389/fchem.2021.719826`.

[56] Shan Wang, Aolin Lu and Chuan Jian Zhong. “Hydrogen production from water electrolysis: role of catalysts”. In: *Nano Converg.* 8.1 (2021). ISSN: 21965404. DOI: `10.1186/s40580-021-00254-x`. URL: `https://doi.org/10.1186/s40580-021-00254-x`.

[57] B. Yildiz, J. Smith and T. Sofu. “Thermal-fluid and Electrochemical Modeling and Performance Study of a Planar Solid Oxide Electrolysis Cell : Analysis on SOEC Resistances , Size , and Inlet Flow Conditions”. In: *Argonne Natl. Lab. Nucl. Eng. Div.* II (2006), pp. 06–52.

[58] Mogens Bjerg Mogensen et al. “Relation Between Ni Particle Shape Change and Ni Migration in Ni–YSZ Electrodes – a Hypothesis”. In: *Fuel Cells - Spec. Issue 12th Eur. SOFC SOE Forum* 17.4 (2017), pp. 434–441.

[59] Martina Trini et al. “Comparison of microstructural evolution of fuel electrodes in solid oxide fuel cells and electrolysis cells”. In: *J. Power Sources* 450.November 2019 (2020), p. 227599. ISSN: 0378-7753. DOI: `10.1016/j.jpowsour.2019.227599`. URL: `https://doi.org/10.1016/j.jpowsour.2019.227599`.

[60] R. Vaßen, D. Simwonis and D. Stöver. “Modelling of the agglomeration of Ni-particles in anodes of solid oxide fuel cells”. In: *J. Mater. Sci.* 36.1 (2001), pp. 147–151. ISSN: 00222461. DOI: `10.1023/A:1004849322160`.

[61] Anke Hagen et al. “Degradation of anode supported SOFCs as a function of temperature and current load”. In: *J. Electrochem. Soc.* 153.6 (2006), pp. 1165–1171. ISSN: 00134651. DOI: `10.1149/1.2193400`.

[62] San Ping Jiang. “Sintering behavior of Ni/Y2O3-ZrO2 cermet electrodes of solid oxide fuel cells”. In: *J. Mater. Sci.* 38.18 (2003), pp. 3775–3782. ISSN: 00222461. DOI: `10.1023/A:1025936317472`.

[63] M. V. Ananyev et al. “Characterization of Ni-cermet degradation phenomena I. Long term resistivity monitoring, image processing and X-ray fluorescence analysis”. In: *J. Power Sources* 286 (2015), pp. 414–426. ISSN: 03787753. DOI: `10.1016/j.jpowsour.2015.03.168`. URL: `http://dx.doi.org/10.1016/j.jpowsour.2015.03.168`.

[64] Mogens Bjerg Mogensen et al. “Review of Ni migration in SOC electrodes”. In: *Eur. SOFC SOE Forum* Lucerne.Switzerland (2020).

[65] Anne Hauch et al. “CO2 electrolysis – Gas impurities and electrode overpotential causing detrimental carbon deposition”. In: *J. Power Sources* 506.May (2021). ISSN: 03787753. DOI: `10.1016/j.jpowsour.2021.230108`.

[66] V. Duboviks et al. “A Raman spectroscopic study of the carbon deposition mechanism on Ni/CGO electrodes during CO/CO2 electrolysis”. In: *Phys. Chem. Chem. Phys.* 16.26 (2014), pp. 13063–13068. ISSN: 14639076. DOI: `10.1039/c4cp01503g`.

[67] Maria Navasa et al. “Localized carbon deposition in solid oxide electrolysis cells studied by multiphysics modeling”. In: *J. Power Sources* 394.May (2018), pp. 102–113. ISSN: 03787753. DOI: `10.1016/j.jpowsour.2018.05.039`. URL: `https://doi.org/10.1016/j.jpowsour.2018.05.039`.

[68] Youkun Tao, Sune Dalgaard Ebbesen and Mogens Bjerg Mogensen. “ Carbon Deposition in Solid Oxide Cells during Co-Electrolysis of H 2 O and CO 2 ”. In: *J. Electrochem. Soc.* 161.3 (2014), F337–F343. ISSN: 0013-4651. DOI: `10.1149/2.079403jes`.

[69] Youkun Tao et al. “Carbon nanotube growth on nanozirconia under strong cathodic polarization in steam and carbon dioxide”. In: *ChemCatChem* 6.5 (2014), pp. 1220–1224. ISSN: 18673899. DOI: `10.1002/cctc.201300941`.

[70] V. Duboviks et al. “Carbon deposition behaviour in metal-infiltrated gadolinia doped ceria electrodes for simulated biogas upgrading in solid oxide electrolysis cells”. In: *J. Power Sources* 293 (2015), pp. 912–921. ISSN: 03787753. DOI: `10.1016/j.jpowsour.2015.06.003`. URL: `http://dx.doi.org/10.1016/j.jpowsour.2015.06.003`.

[71] Theis Løye Skafte et al. “Carbon Deposition during CO 2 Electrolysis in Ni-Based Solid-Oxide-Cell Electrodes”. In: *ECS Trans.* MA2015-03.1 (2015), pp. 395–395. DOI: `10.1149/ma2015-03/1/395`.

[72] Theis Løye Skafte et al. “Carbon deposition and sulfur poisoning during CO2 electrolysis in nickel-based solid oxide cell electrodes”. In: *J. Power Sources* 373.October 2017 (2018), pp. 54–60. ISSN: 03787753. DOI: `10.1016/j.jpowsour.2017.10.097`. URL: `https://doi.org/10.1016/j.jpowsour.2017.10.097`.

[73] Rupert Way et al. “Empirically grounded technology forecasts and the...” In: *INET Oxford Work. Pap. No. 2021-01* (2021). URL: `https://www.inet.ox.ac.uk/publications/no-2021-01-empirically-grounded-technology-forecasts-and-the-energy-transition/`.

[74] Yoshio Matsuzaki and Isamu Yasuda. “Poisoning effect of sulfur-containing impurity gas on a SOFC anode: Part I. Dependence on temperature, time, and impurity concentration”. In: *Solid State Ionics* 132.3 (2000), pp. 261–269. ISSN: 01672738. DOI: `10.1016/s0167-2738(00)00653-6`.

[75] Anke Hagen, Jens F.B. Rasmussen and Karl Thydén. “Durability of solid oxide fuel cells using sulfur containing fuels”. In: *J. Power Sources* 196.17 (2011), pp. 7271–7276. ISSN: 03787753. DOI: `10.1016/j.jpowsour.2011.02.053`. URL: `http://dx.doi.org/10.1016/j.jpowsour.2011.02.053`.

[76] Anne Hauch et al. “Sulfur Poisoning of SOFC Anodes: Effect of Overpotential on Long-Term Degradation”. In: *J. Electrochem. Soc.* 161.6 (2014), F734–F743. ISSN: 0013-4651. DOI: `10.1149/2.080406jes`.

[77] Anke Hagen, Gregory B. Johnson and Per Hjalmarsson. “Electrochemical evaluation of sulfur poisoning in a methane-fuelled solid oxide fuel cell: Effect of current density and sulfur concentration”. In: *J. Power Sources* 272 (2014), pp. 776–785. ISSN: 03787753. DOI: `10.1016/j.jpowsour.2014.08.125`. URL: `http://dx.doi.org/10.1016/j.jpowsour.2014.08.125`.

[78] A. Kromp et al. “Electrochemical Analysis of Sulfur-Poisoning in Anode Supported SOFCs Fuelled with a Model Reformate”. In: *J. Electrochem. Soc.* 159.5 (2012), B597–B601. ISSN: 0013-4651. DOI: `10.1149/2.015206jes`.

[79] Matthias Riegraf et al. “The Influence of Sulfur Formation on Performance and Reforming Chemistry of SOFC Anodes Operating on Methane Containing Fuel”. In: *J. Electrochem. Soc.* 162.12 (2015), F1324–F1332. ISSN: 0013-4651. DOI: `10.1149/2.0291512jes`.

[80] Sune D. Ebbesen et al. “Poisoning of solid oxide electrolysis cells by impurities”. In: *J. Electrochem. Soc.* 157.10 (2010). ISSN: 00134651. DOI: `10.1149/1.3464804`.

[81] Takuto Kushi. “Effects of sulfur poisoning on degradation phenomena in oxygen electrodes of solid oxide electrolysis cells and solid oxide fuel cells”. In: *Int. J. Hydrogen Energy* 42.15 (2017), pp. 9396–9405. ISSN: 03603199. DOI: `10.1016/j.ijhydene.2017.01.151`. URL: `http://dx.doi.org/10.1016/j.ijhydene.2017.01.151`.

[82] Muhammad Shirjeel Khan et al. “Fundamental mechanisms involved in the degradation of nickel–yttria stabilized zirconia (Ni–YSZ) anode during solid oxide fuel cells operation: A review”. In: *Ceram. Int.* 42.1 (2016), pp. 35–48. ISSN: 02728842. DOI: `10.1016/j.ceramint.2015.09.006`. URL: `http://dx.doi.org/10.1016/j.ceramint.2015.09.006`.

[83] Paul Boldrin et al. "Strategies for Carbon and Sulfur Tolerant Solid Oxide Fuel Cell Materials, Incorporating Lessons from Heterogeneous Catalysis". In: *Chem. Rev.* 116.22 (2016), pp. 13633–13684. ISSN: 15206890. DOI: `10.1021/acs.chemrev.6b00284`.

[84] John Bøgild Hansen. "Correlating sulfur poisoning of SOFC nickel anodes by a temkin isotherm". In: *Electrochem. Solid-State Lett.* 11.10 (2008), pp. 178–181. ISSN: 10990062. DOI: `10.1149/1.2960521`.

[85] Jens R. Rostrup-Nielsen and Ib Alstrup. "Innovation and science in the process industry Steam reforming and hydrogenolysis". In: *Catal. Today* 53.3 (1999), pp. 311–316. ISSN: 09205861. DOI: `10.1016/S0920-5861(99)00125-X`.

[86] Sune Dalgaard Ebbesen, John Bøgild Hansen and Mogens Mogensen. "Biogas Upgrading Using SOEC with a Ni-ScYSZ Electrode". In: *ECS Trans.* 57.1 (2013), pp. 3217–3227. ISSN: 1938-5862. DOI: `10.1149/05701.3217ecst`.

[87] Rainer Küngas. " Review—Electrochemical CO 2 Reduction for CO Production: Comparison of Low- and High-Temperature Electrolysis Technologies ". In: *J. Electrochem. Soc.* 167.4 (2020), p. 044508. ISSN: 0013-4651. DOI: `10.1149/1945-7111/ab7099`.

[88] Yuanxin Li et al. "Efficient carbon dioxide electrolysis based on perovskite cathode enhanced with nickel nanocatalyst". In: *Electrochim. Acta* 153 (2015), pp. 325–333. ISSN: 00134686. DOI: `10.1016/j.electacta.2014.11.151`. URL: `http://dx.doi.org/10.1016/j.electacta.2014.11.151`.

[89] Lingting Ye et al. "Enhanced CO 2 electrolysis with a SrTiO 3 cathode through a dual doping strategy". In: *J. Mater. Chem. A* 7.6 (2019), pp. 2764–2772. ISSN: 20507496. DOI: `10.1039/c8ta10188d`.

[90] Changli Zhu et al. "Perovskite SrFeO3−Δ decorated with Ni nanoparticles for high temperature carbon dioxide electrolysis". In: *Int. J. Hydrogen Energy* 43.36 (2018), pp. 17040–17047. ISSN: 03603199. DOI: `10.1016/j.ijhydene.2018.07.148`. URL: `https://doi.org/10.1016/j.ijhydene.2018.07.148`.

[91] Subiao Liu, Qingxia Liu and Jing Li Luo. "The excellence of La(Sr)Fe(Ni)O3 as an active and efficient cathode for direct CO2 electrochemical reduction at elevated temperatures". In: *J. Mater. Chem. A* 5.6 (2017), pp. 2673–2680. ISSN: 20507496. DOI: `10.1039/c6ta09151b`.

[92] Yihang Li et al. "Mixed-Conductor Sr2Fe1.5Mo0.5O6-δ as Robust Fuel Electrode for Pure CO2 Reduction in Solid Oxide Electrolysis Cell". In: *ACS Sustain. Chem. Eng.* 5.12 (2017), pp. 11403–11412. ISSN: 21680485. DOI: `10.1021/acssuschemeng.7b02511`.

[93] Yunan Jiang et al. "Sr2Fe1.4Mn0.1Mo0.5O6-: δ perovskite cathode for highly efficient CO2 electrolysis". In: *J. Mater. Chem. A* 7.40 (2019), pp. 22939–22949. ISSN: 20507496. DOI: `10.1039/c9ta07689a`.

[94] Wenying Li et al. "Carbon deposition on patterned nickel/yttria stabilized zirconia electrodes for solid oxide fuel cell/solid oxide electrolysis cell modes". In: *J. Power Sources* 276 (2015), pp. 26–31. ISSN: 03787753. DOI: `10.1016/j.jpowsour.2014.11.106`. URL: `http://dx.doi.org/10.1016/j.jpowsour.2014.11.106`.

[95] Elcogen. *Elcogen - SOEC*. 2023. URL: `https://elcogen.com/products/solid-oxide-electrolysis-cells/` (visited on 25/01/2023).

[96] Dehua Dong et al. "Hierarchically ordered porous Ni-based cathode-supported solid oxide electrolysis cells for stable CO2 electrolysis without safe gas". In: *J. Mater. Chem. A* 5.46 (2017), pp. 24098–24102. ISSN: 20507496. DOI: `10.1039/c7ta06839e`.

[97] Yuefeng Song et al. "Pure CO2 electrolysis over an Ni/YSZ cathode in a solid oxide electrolysis cell". In: *J. Mater. Chem. A* 6.28 (2018), pp. 13661–13667. ISSN: 20507496. DOI: `10.1039/c8ta02858c`.

[98] Jiayue Wang et al. "Threshold catalytic onset of carbon formation on CeO2 during CO2 electrolysis: mechanism and inhibition". In: *J. Mater. Chem. A* 7 (2019), pp. 15233–15243. DOI: `10.1039/c9ta03265g`.

[99] Daniel Bøgh Drasbæk. "Novel anodes for solid oxide fuel cells". PhD thesis. Technical University of Denmar, 2019.

[100] Martha M. Welander et al. "What does carbon tolerant really mean?: Operando vibrational studies of carbon accumulation on novel solid oxide fuel cell anodes prepared by infiltration". In: *Phys. Chem. Chem. Phys.* 22.17 (2020), pp. 9815–9823. ISSN: 14639076. DOI: `10.1039/d0cp00195c`.

[101] Subiao Liu, Qingxia Liu and Jing Li Luo. "Highly Stable and Efficient Catalyst with in Situ Exsolved Fe-Ni Alloy Nanospheres Socketed on an Oxygen Deficient Perovskite for Direct CO2 Electrolysis". In: *ACS Catal.* 6.9 (2016), pp. 6219–6228. ISSN: 21555435. DOI: `10.1021/acscatal.6b01555`.

[102] Jinhai Lu et al. "Highly efficient electrochemical reforming of CH4/CO2 in a solid oxide electrolyser". In: *Sci. Adv.* 4.3 (2018), pp. 1–8. ISSN: 23752548. DOI: `10.1126/sciadv.aar5100`.

[103] A. Nechache, M. Cassir and A. Ringuedé. "Solid oxide electrolysis cell analysis by means of electrochemical impedance spectroscopy: A review". In: *J. Power Sources* 258 (2014), pp. 164–181. ISSN: 03787753. DOI: `10.1016/j.jpowsour.2014.01.110`. URL: `http://dx.doi.org/10.1016/j.jpowsour.2014.01.110`.

[104] Raghbir Singh Khandpur. *Impedance Spectroscopy*. 2020, pp. 1021–1024. ISBN: 9780470041406. DOI: `10.1002/9781119288190.ch188`.

[105] Bernard A. Boukamp and Henny J.M. Bouwmeester. "Interpretation of the Gerischer impedance in solid state ionics". In: *Solid State Ionics* 157.1-4 (2003), pp. 29–33. ISSN: 01672738. DOI: `10.1016/S0167-2738(02)00185-6`.

[106] Yunxiang Lu, Cortney Kreller and Stuart B. Adler. "Measurement and Modeling of the Impedance Characteristics of Porous La1−xSxCoO3−δ Electrodes". In: *J. Electrochem. Soc.* 156.4 (2009), B513. ISSN: 00134651. DOI: `10.1149/1.3079337`.

[107] Anne Hauch et al. "Re-activation of degraded nickel cermet anodes - Nanoparticle formation via reverse current pulses". In: *J. Power Sources* 377.November 2017 (2018), pp. 110–120. ISSN: 03787753. DOI: `10.1016/j.jpowsour.2017.11.088`. URL: `https://doi.org/10.1016/j.jpowsour.2017.11.088`.

[108] Christopher Graves. *RAVDAV data analysis software, version 0.9.7*. 2012.

[109] Peter Atkins and Julio de Paula. *Physical Chemistry Thermodynamics, Structure, And Change*. 10th. Oxford University Press, 2014. ISBN: 9780199697403.

[110] Ronald Mirman. *Point Groups, Space Groups, Crystals, Molecules*. World Scientific Publishing Company, 1999, p. 744. ISBN: 9810237324.

[111] George Socrates. *Infrared and Raman characteristic group frequencies : tables and charts : Tables and Charts*. 3rd. Wiley, 2001, p. 347. ISBN: 0470093072.

[112] Barbara Lafuente et al. "Highlights in Mineralogical Crystallography". In: *Highlights Mineral. Crystallogr.* Ed. by Thomas Armbruster and Rosa Micaela Danisi. Berlin, München, Boston: De Gruyter, 2015. Chap. 1. The pow, pp. 1–30. DOI: `https://doi.org/10.1515/9783110417104-003`.

[113] Kazuo Nakamoto and Chris W Brown. *Introductory Raman Spectroscopy*. 1994, pp. 406–421. ISBN: 9780122541056. DOI: `10.1016/c2009-0-21238-4`.

[114] Anthony R. West. *Solid State Chemistry and its Applications*. 2nd. Chichester: John Wiley & Sons, Tid, 2014. ISBN: 9781119942948.

[115] Jeol. *Field emission gun*. 2022. URL: `https://www.jeol.co.jp/en/words/emterms/search%7B%5C_%7Dresult.html?keyword=field-emission%20electron%20gun` (visited on 25/08/2022).

[116] Peter J. Goodhew, John Humphreys and John Humphreys. “Electron Microscopy and Analysis”. In: *Electron Microsc. Anal.* (2000). DOI: `10.1201/9781482289343`.

[117] Case School of Engineering. *Electron Microscopy*. 2022. URL: `https://engineering.case.edu/research/centers/swagelok-surface-analysis-materials/image-analysis/electron-microscopy` (visited on 24/08/2022).

[118] K. Thydén, Y. L. Liu and J. B. Bilde-Sørensen. “Microstructural characterization of SOFC Ni-YSZ anode composites by low-voltage scanning electron microscopy”. In: *Solid State Ionics* 178.39-40 (2008), pp. 1984–1989. ISSN: 01672738. DOI: `10.1016/j.ssi.2007.12.075`.

[119] Caroline A. Schneider, Wayne S. Rasband and Kevin W. Eliceiri. “NIH Image to ImageJ: 25 years of image analysis”. In: *Nat. Methods* 9.7 (2012), pp. 671–675. ISSN: 15487091. DOI: `10.1038/nmeth.2089`.

[120] L.M. Das. *Hydrogen-fueled internal combustion engines*. x. Elsevier Ltd., 2016, pp. 177–217. ISBN: 9781782423638. DOI: `10.1016/b978-1-78242-363-8.00007-4`. URL: `http://dx.doi.org/10.1016/B978-1-78242-363-8.00007-4`.

[121] John Emsley. *Nature’s Building Blocks - An A-Z Guide to the Elements - New Edition*. First as n. Oxford: Oxford University Press, 2011, p. 699. ISBN: 978-0-19-960563-7.

[122] Mogens Bjerg Mogensen and Peter Vang Hendriksen. *Testing of Electrodes, Cells and Short Stacks*. Elsevier Ltd, 2003, pp. 261–289. ISBN: 9781856173872. DOI: `10.1016/B978-185617387-2/50027-1`. URL: `http://dx.doi.org/10.1016/B978-185617387-2/50027-1`.

[123] Anne Hauch. “Performance and Durability of Solid Oxide Electrolysis Cells”. PhD thesis. Technical University of Denmark, 2007. DOI: `10.1149/ma2006-01/24/842`.

[124] Søren Højgaard Jensen. *Solid oxide electrolyser cell*. -. 2006, pp. 1–134. ISBN: ISBN 1399-2236.

[125] Ming Chen et al. “Microstructural Degradation of Ni/YSZ Electrodes in Solid Oxide Electrolysis Cells under High Current”. In: *J. Electrochem. Soc.* 160.8 (2013), F883–F891. ISSN: 0013-4651. DOI: `10.1149/2.098308jes`.

[126] Michael Reisert, Ashish Aphale and Prabhakar Singh. “Solid oxide electrochemical systems: Material degradation processes and novel mitigation approaches”. In: *Materials (Basel).* 11.11 (2018). ISSN: 19961944. DOI: `10.3390/ma11112169`.

[127] Xiufu Sun et al. “Effect of Anode Side Purge Gas on the Degradation of Solid Oxide Electrolysis Cells”. In: *ECS Meet. Abstr.* MA2021-03.1 (2021), pp. 68–68. DOI: `10.1149/ma2021-03168mtgabs`.

[128] Haldor Topsøe A/S et al. *Electrical upgrading of biogas*. Tech. rep. 2018, p. 47. URL: `https://energiforskning.dk/sites/energiteknologi.dk/files/slutrapporter/slutrapport%7B%5C_%7Deudp%7B%5C_%7Delupgraded%7B%5C_%7Dbiogas.pdf`.

[129] Joshua Mermelstein and Oliver Posdziech. “Development and Demonstration of a Novel Reversible SOFC System for Utility and Micro Grid Energy Storage”. In: *Fuel Cells* 17.4 (2017), pp. 562–570.

[130] Haldor Topsoe. *DeLille Oxygen Co. leases two eCOs™ units for cost-competitive onsite CO production*. 2019. URL: `https://blog.topsoe.com/delille-oxygen-co.-leases-two-ecos-units-for-cost-competitive-onsite-co-production` (visited on 17/11/2022).

[131] A. Leonide. “SOFC Modelling and Parameter Identification by means of Impedance Spectroscopy”. PhD thesis. 2010. ISBN: 9783866445383.

[132] Anders Kring Clausen et al. “CGO-Infiltrated Ni / YSZ SOEC Fuel Electrodes for Increased Carbon Tolerance During CO2 Electrolysis”. In: *ECS Trans.* 103.1 (2021), pp. 1945–1954. DOI: `https://doi.org/10.1149/10301.1971ecst`.

[133] Stephen J. McPhail et al. “Adressing planar solid oxide cell degradation mechanisms: Acritical review of selected components”. In: *Electrochem. Sci. Adv.* 2.5 (2022). DOI: `https://doi.org/10.1002/elsa.202100024`. URL: `https://chemistry-europe.onlinelibrary.wiley.com/doi/full/10.1002/elsa.202100024`.

[134] Shiqing Hu et al. “Rational design of CO2 electroreduction cathode via in situ electrochemical phase transition”. In: *J. Energy Chem.* 66 (2022), pp. 603–611. ISSN: 20954956. DOI: `10.1016/j.jechem.2021.08.069`. URL: `https://doi.org/10.1016/j.jechem.2021.08.069`.

[135] A. Leonide et al. “Evaluation and modeling of the cell resistance in anode-supported solid oxide fuel cells”. In: *J. Electrochem. Soc.* 155.1 (2008), pp. 36–41. ISSN: 00134651. DOI: `10.1149/1.2801372`.

[136] Xiufu Sun et al. “Degradation in Solid Oxide Electrolysis Cells During Long Term Testing”. In: *Fuel Cells* 19.6 (2019), pp. 740–747. DOI: `10.1002/fuce.201900081`.

[137] Simona Ovtar et al. “Boosting the performance and durability of Ni/YSZ cathode for hydrogen production at high current densities: Via decoration with nano-sized electrocatalysts”. In: *Nanoscale* 11.10 (2019), pp. 4394–4406. ISSN: 20403372. DOI: `10.1039/c8nr07678b`.

[138] Sune Dalgaard Ebbesen, Ruth Knibbe and Mogens Mogensen. “Co-Electrolysis of Steam and Carbon Dioxide in Solid Oxide Cells”. In: *J. Electrochem. Soc.* 159.8 (2012), F482–F489. ISSN: 0013-4651. DOI: `10.1149/2.076208jes`.

[139] Jean-Claude Njodzefon et al. “Electrode Kinetics and Gas Conversion in Solid Oxide Cells”. PhD thesis. 2015. URL: `http://orbit.dtu.dk/en/publications/electrode-kinetics-and-gas-conversion-in-solid-oxide-cells(2a0261a3-c5c8-407f-b3c8-529ca3ece8af).html`.

[140] S. Primdahl and M. Mogensen. “Gas Conversion Impedance: A Test Geometry Effect in Characterization of Solid Oxide Fuel Cell Anodes”. In: *J. Electrochem. Soc.* 145.7 (1998), pp. 2431–2438. ISSN: 0013-4651. DOI: `10.1149/1.1838654`.

[141] A. Feinberg and C. H. Perry. “Structural disorder and phase transitions in ZrO2-Y2O3 system”. In: *J. Phys. Chem. Solids* 42.6 (1981), pp. 513–518. ISSN: 00223697. DOI: `10.1016/0022-3697(81)90032-9`.

[142] G S Duesberg et al. “Polarized Raman Spectroscopy on Isolated Single-Wall Carbon Nanotubes”. In: *Phys. Rev. Lett.* 85.25 (2000), pp. 5436–5439. URL: `papers2://publication/uuid/BD01C9C3-9617-4BFE-A85C-C7B84276B614`.

[143] M. S. Dresselhaus et al. “Raman spectroscopy on isolated single wall carbon nanotubes”. In: *Carbon N. Y.* 40.12 (2002), pp. 2043–2061. ISSN: 00086223. DOI: `10.1016/S0008-6223(02)00066-0`.

[144] Ming Chen et al. “Thermoneutral Operation of Solid Oxide Electrolysis Cells in Potentiostatic Mode”. In: *ECS Trans.* 78.1 (2017), pp. 3077–3088. ISSN: 1938-6737. DOI: `10.1149/07801.3077ecst`.

[145] Xiufu Sun et al. “An operation strategy for mitigating the degradation of solid oxide electrolysis cells for syngas production”. In: *J. Power Sources* 506.June (2021), p. 230136. ISSN: 03787753. DOI: `10.1016/j.jpowsour.2021.230136`. URL: `https://doi.org/10.1016/j.jpowsour.2021.230136`.

[146] Malcolm W. Chase. *NIST-JANAF Thermochemical Tables*. 4th. Vol. 9. New York: American Chemical Society, 1998. ISBN: 1-56396-831-2.

[147] Krijn P. De Jong and John W. Geus. “Carbon Nanofibers: Catalytic Synthesis and Applications”. In: *Catal. Rev. - Sci. Eng.* 42.4 (2000), pp. 481–510. ISSN: 01614940. DOI: `10.1081/CR-100101954`.

[148] Sune Dalgaard Ebbesen and Mogens Mogensen. “Electrolysis of carbon dioxide in Solid Oxide Electrolysis Cells”. In: *J. Power Sources* 193.1 (2009), pp. 349–358. ISSN: 03787753. DOI: `10.1016/j.jpowsour.2009.02.093`.

[149] Morris D. Argyle and Calvin H. Bartholomew. “Heterogeneous catalyst deactivation and regeneration: A review”. In: *Catalysts* 5.1 (2015), pp. 145–269. ISSN: 20734344. DOI: `10.3390/catal5010145`.

[150] José Luís Figueiredo et al. *Progress in Catalyst Deactivation*. 54. 1982, pp. 93–102. ISBN: 9024726905. DOI: `10.1007/978-94-009-7597-2_7`.

[151] David Peterson and Eric Miller. “Hydrogen and Fuel Cells Program Record - Hydrogen Production Cost from Solid Oxide Electrolysis”. In: *Hydrog. Fuel Cells Progr. Rec. - Hydrog. Prod. Cost from Solid Oxide Electrolysis* (2016), pp. 1–11.

[152] A. Mohammed Hussain et al. “Effective improvement of interface modified strontium titanate based solid oxide fuel cell anodes by infiltration with nano-sized palladium and gadolinium-doped cerium oxide”. In: *Electrochim. Acta* 113 (2013), pp. 635–643. ISSN: 00134686. DOI: `10.1016/j.electacta.2013.09.066`. URL: `http://dx.doi.org/10.1016/j.electacta.2013.09.066`.

[153] Jimmi Nielsen et al. “Infiltrated La0.4Sr0.4Fe0.03Ni0.03Ti0.94O3 based anodes for all ceramic and metal supported solid oxide fuel cells”. In: *J. Power Sources* 372.September (2017), pp. 99–106. ISSN: 03787753. DOI: `10.1016/j.jpowsour.2017.10.066`. URL: `https://doi.org/10.1016/j.jpowsour.2017.10.066`.

[154] T. B. Mitchell-Williams et al. “Infiltration of commercially available, anode supported SOFC’s via inkjet printing”. In: *Mater. Renew. Sustain. Energy* 6.2 (2017), pp. 1–9. ISSN: 21941467. DOI: `10.1007/s40243-017-0096-2`.

[155] Chengsheng Ni et al. “Microstructure dependence of performance degradation for intermediate temperature solid oxide fuel cells based on the metallic catalyst infiltrated La-and Ca-doped SrTiO3 anode support”. In: *J. Mater. Chem. A* 6.13 (2018), pp. 5398–5406. ISSN: 20507496. DOI: `10.1039/c7ta09534a`.

[156] R. C. Maher et al. “The Reduction Properties of M–Doped (M=Zr, Gd) CeO2/YSZ Scaffolds Co–Infiltrated with Nickel”. In: *Energy Technol.* 6.10 (2018), pp. 2045–2052. DOI: `10.1002/ente.201800146`.

[157] San Ping Jiang and Siew Hwa Chan. “A review of anode materials development in solid oxide fuel cells”. In: *J. Mater. Sci.* 39.14 (2004), pp. 4405–4439. ISSN: 0022-2461. DOI: `10.1023/b:jmsc.0000034135.52164.6b`.

[158] Elena Marzia Sala et al. "Current understanding of ceria surfaces for CO2 reduction in SOECs and future prospects – A review". In: *Solid State Ionics* 375.July 2021 (2022), p. 115833. ISSN: 01672738. DOI: `10.1016/j.ssi.2021.115833`. URL: `https://doi.org/10.1016/j.ssi.2021.115833`.

[159] William C. Chueh et al. "High electrochemical activity of the oxide phase in model ceria-Pt and ceria-Ni composite anodes". In: *Nat. Mater.* 11.2 (2012), pp. 155–161. ISSN: 14764660. DOI: `10.1038/nmat3184`.

[160] J. Vohs and R. J. Gorte. "High-Performance SOFC Cathodes Prepared by Infiltration". In: *Adv. Mater.* 21.9 (2009), pp. 943–956. DOI: `https://doi.org/10.1002/adma.200802428`.

[161] Nazan Muzaffar et al. "Fabrication and electrochemical performance of zn-doped La0.2Sr0.25Ca0.45TiO3 infiltrated with nickel-CGO, iron, and cobalt as an alternative anode material for solid oxide fuel cells". In: *Catalysts* 9.3 (2019). ISSN: 20734344. DOI: `10.3390/catal9030269`.

[162] Mohamad Khoshkalam et al. " Enhanced Activity of Pr 6 O 11 and CuO Infiltrated Ce 0.9 Gd 0.1 O 2 Based Composite Oxygen Electrodes ". In: *J. Electrochem. Soc.* 167.2 (2020), p. 024505. ISSN: 19457111. DOI: `10.1149/1945-7111/ab6821`.

[163] Theis Løye Skafte et al. "Reactivating the Ni-YSZ electrode in solid oxide cells and stacks by infiltration". In: *J. Power Sources* 378.August 2017 (2018), pp. 685–690. ISSN: 03787753. DOI: `10.1016/j.jpowsour.2018.01.021`. URL: `https://doi.org/10.1016/j.jpowsour.2018.01.021`.

[164] Alfred Junio Samson, Martin Sgaard and Nikolaos Bonanos. "Electrodes for solid oxide fuel cells based on infiltration of Co-based materials". In: *Electrochem. Solid-State Lett.* 15.4 (2012), pp. 54–57. ISSN: 10990062. DOI: `10.1149/2.020204esl`.

[165] Ragnar Kiebach et al. "On the Properties and Long-Term Stability of Infiltrated Lanthanum Cobalt Nickelates (LCN) in Solid Oxide Fuel Cell Cathodes". In: *J. Electrochem. Soc.* 164.7 (2017), F748–F758. ISSN: 0013-4651. DOI: `10.1149/2.0361707jes`.

[166] Jingyi Chen et al. "Fabrication and Characterisation of Nanoscale Ni-CGO Electrode from Nano-Composite Powders". In: *ECS Trans.* 91.1 (2019), pp. 1799–1805. ISSN: 1938-6737. DOI: `10.1149/09101.1799ecst`.

[167] Xiaofeng Tong et al. "An Up-scalable, Infiltration-Based Approach for Improving the Durability of Ni/YSZ Electrodes for Solid Oxide Cells". In: *J. Electrochem. Soc.* 167.2 (2020), p. 024519. ISSN: 0013-4651. DOI: `10.1149/1945-7111/ab6f5c`.

[168] Zhuoluo A. Feng, Michael L. Machala and William C. Chueh. “Surface electrochemistry of CO2 reduction and CO oxidation on Sm-doped CeO2-x: Coupling between Ce3+ and carbonate adsorbates”. In: *Phys. Chem. Chem. Phys.* 17.18 (2015), pp. 12273–12281. ISSN: 14639076. DOI: `10.1039/c5cp00114e`.

[169] Zhenlong Zhao et al. “Enhanced intermediateerature CO2 splitting using nonstoichiometric ceria and ceria-zirconia”. In: *Phys. Chem. Chem. Phys.* 19.37 (2017), pp. 25774–25785. ISSN: 14639076. DOI: `10.1039/c7cp04789d`.

[170] Jin Goo et al. “Electrochimica Acta Durable and High-Performance Direct-Methane Fuel Cells with Coke-Tolerant Ceria-Coated Ni Catalysts at Reduced Temperatures”. In: *Electrochim. Acta* 191 (2016), pp. 677–686. ISSN: 0013-4686. DOI: `10.1016/j.electacta.2016.01.091`. URL: `http://dx.doi.org/10.1016/j.electacta.2016.01.091`.

[171] Hideto Kurokawa, Tal Z Sholklapper and Craig P Jacobson. “Ceria Nanocoating for Sulfur Tolerant Ni-Based Anodes of Solid Oxide Fuel Cells Ceria Nanocoating for Sulfur Tolerant Ni-Based Anodes of Solid Oxide Fuel Cells”. In: *Electrochem. Solid-State Lett.* 10.9 (2007). DOI: `10.1149/1.2748630`.

[172] Jeong Woo Yun et al. “Analysis of the regenerative H 2 S poisoning mechanism in temperature solid oxide fuel cells”. In: *Int. J. Hydrogen Energy* 36.1 (2010), pp. 787–796. ISSN: 0360-3199. DOI: `10.1016/j.ijhydene.2010.10.060`. URL: `http://dx.doi.org/10.1016/j.ijhydene.2010.10.060`.

[173] Vladislav Duboviks et al. “ In-Operando Raman Spectroscopy Study of Passivation Effects on Ni-CGO Electrodes in CO 2 Electrolysis Conditions ”. In: *ECS Trans.* 57.1 (2013), pp. 3111–3117. ISSN: 1938-5862. DOI: `10.1149/05701.3111ecst`.

[174] Peyman Khajavi et al. “Strength and hydrothermal stability of NiO–stabilized zirconia solid oxide cells fuel electrode supports”. In: *J. Eur. Ceram. Soc.* 41.7 (2021), pp. 4206–4216. ISSN: 1873619X. DOI: `10.1016/j.jeurceramsoc.2021.01.052`.

[175] Xiaofeng Tong et al. “A 4 × 4 cm2 Nanoengineered Solid Oxide Electrolysis Cell for Efficient and Durable Hydrogen Production”. In: *ACS Appl. Mater. Interfaces* 11.29 (2019), pp. 25996–26004. ISSN: 19448252. DOI: `10.1021/acsami.9b07749`.

[176] Tania Ramos et al. “Performance-Microstructure Relations in Ni/CGO Infiltrated Nb-doped SrTiO3 SOFC Anodes”. In: *ECS Trans.* 45.1 (2012), pp. 389–402.

[177] A Tsoga et al. “Gadolinia-Doped Ceria and Yttria Stabilized Zirconia Interfaces: Regarding their Application for SOFC Technology”. In: *Acta Mater.* 48 (2000), pp. 4709–4714. ISSN: 1359-6454.

[178] Huixia Xu et al. “Interdiffusion between gadolinia doped ceria and yttria stabilized zirconia in solid oxide fuel cells: Experimental investigation and kinetic modeling”. In: *J. Power Sources* 441.September (2019), p. 227152. ISSN: 03787753. DOI: `10.1016/j.jpowsour.2019.227152`. URL: `https://doi.org/10.1016/j.jpowsour.2019.227152`.

[179] Simon Lawson. “Environmental degradation of zirconia ceramics”. In: *J. Eur. Ceram. Soc.* 15.6 (1995), pp. 485–502. ISSN: 09552219. DOI: `10.1016/0955-2219(95)00035-S`.

[180] Isabel Montero et al. “Ceramics Sintered in Reducing Conditions”. In: *J. Am. Ceram. Soc.* 87.12 (2004), pp. 2282–2285.

[181] M. Faisal Riyad, Mohammadreza Mahmoudi and Majid Minary-Jolandan. “Manufacturing and Thermal Shock Characterization of Porous Yttria Stabilized Zirconia for Hydrogen Energy Systems”. In: *Ceramics* 5.3 (2022), pp. 472–483. ISSN: 25716131. DOI: `10.3390/ceramics5030036`.

[182] S. Lübke and H. D. Wiemhöfer. “Electronic conductivity of Gd-doped ceria with additional Pr-doping”. In: *Solid State Ionics* 117.3-4 (1999), pp. 229–243. ISSN: 01672738. DOI: `10.1016/s0167-2738(98)00408-1`.

[183] Søren Højgaard Jensen et al. “Advanced Test Method of Solid Oxide Cells in a Plug-Flow Setup”. In: *J. Electrochem. Soc.* 156.6 (2009), B757. ISSN: 00134651. DOI: `10.1149/1.3116247`.

[184] A. Leonide et al. “Performance simulation of current/voltage-characteristics for SOFC single cell by means of detailed impedance analysis”. In: *J. Power Sources* 196.17 (2011), pp. 7343–7346. ISSN: 03787753. DOI: `10.1016/j.jpowsour.2010.10.052`. URL: `http://dx.doi.org/10.1016/j.jpowsour.2010.10.052`.

[185] X. Yue and J.T.S. Irvine. “Understanding of CO2 Electrochemical Reduction Reaction Process via High Temperature Solid Oxide Electrolysers”. In: *ECS Trans.* 68.1 (2015), pp. 3535–3551.

[186] Stephen J. McPhail, Viviana Cigolotti and Angelo Moreno. *Fuel Cells in the Waste-to-Energy Chain*. 2012, p. 228. ISBN: 9781447123682. DOI: `10.2174/97816080528511060101`.

[187] Jun Zhang et al. “Comparison of solid oxide fuel cell (SOFC) electrolyte materials for operation at 500 °C”. In: *Solid State Ionics* 344.October 2019 (2020), p. 115138. ISSN: 01672738. DOI: 10.1016/j.ssi.2019.115138. URL: https://doi.org/10.1016/j.ssi.2019.115138.

[188] Maarten Verbraeken. “Advanced supporting anodes for Solid Oxide Fuel Cells”. PhD thesis. 2005, pp. 6–70.

[189] M Brown, S Primdahl and M Mogensen. “Structure / Performance Relations for Ni / Yttria □ Stabilized Zirconia Anodes for Solid Oxide Fuel Cells Structure / Performance Relations for Ni / Yttria-Stabilized Zirconia Anodes for Solid Oxide Fuel Cells”. In: *J. Electrochem. Soc.* 147.2 (2000), pp. 475–485.

[190] Ting Shuai Li et al. “Effect of reduction temperature on the electrochemical properties of a Ni/YSZ anode-supported solid oxide fuel cell”. In: *J. Alloys Compd.* 495.1 (2010), pp. 138–143. ISSN: 09258388. DOI: 10.1016/j.jallcom.2010.01.103. URL: http://dx.doi.org/10.1016/j.jallcom.2010.01.103.

[191] Anne Hauch et al. “Nanoscale chemical analysis and imaging of solid oxide cells”. In: *Electrochem. Solid-State Lett.* 11.3 (2008). ISSN: 10990062. DOI: 10.1149/1.2828845.

[192] M. Scheffler et al. “Nickel-catalyzed in situ formation of carbon nanotubes and turbostratic carbon in polymer-derived ceramics”. In: *Mater. Chem. Phys.* 84.1 (2004), pp. 131–139. ISSN: 02540584. DOI: 10.1016/j.matchemphys.2003.11.003.

[193] Christopher Graves et al. “Sustainable hydrocarbon fuels by recycling CO2 and H 2O with renewable or nuclear energy”. In: *Renew. Sustain. Energy Rev.* 15.1 (2011), pp. 1–23. ISSN: 13640321. DOI: 10.1016/j.rser.2010.07.014.

[194] Sune Dalgaard Ebbesen et al. “High temperature electrolysis in alkaline cells, solid proton conducting cells, and solid oxide cells”. In: *Chem. Rev.* 114.21 (2014), pp. 10697–10734. ISSN: 15206890. DOI: 10.1021/cr5000865.

[195] Yijing Shang et al. “3D microstructural characterization of Ni/YSZ electrodes in long-term CO2 electrolysis”. In: *15th Eur. SOFC SOE Forum* (2022).

[196] Federico Monaco. “Analysis of the degradation in solid oxide cells operated in fuel cell and electrolysis modes”. PhD thesis. UNIVERSITE GRENOBLE ALPES, 2020. URL: https://tel.archives-ouvertes.fr/tel-02971294.

[197] A. Faes et al. “Nickel-zirconia anode degradation and triple phase boundary quantification from microstructural analysis”. In: *Fuel Cells* 9.6 (2009), pp. 841–851. ISSN: 16156854. DOI: 10.1002/fuce.200800147.

[198] Zhenjun Jiao and Naoki Shikazono. “Study on the effects of polarization on local morphological change of nickel at active three-phase-boundary using patterned nickel-film electrode in solid oxide fuel cell anode”. In: *Acta Mater.* 135 (2017), pp. 124–131. ISSN: 13596454. DOI: `10.1016/j.actamat.2017.05.051`. URL: `http://dx.doi.org/10.1016/j.actamat.2017.05.051`.

[199] F. Tietz. “Thermal expansion of SOFC materials”. In: *Ionics (Kiel).* 5.1-2 (1999), pp. 129–139. ISSN: 18620760. DOI: `10.1007/BF02375916`.

[200] Jérôme Chevalier et al. “The tetragonal-monoclinic transformation in zirconia: Lessons learned and future trends”. In: *J. Am. Ceram. Soc.* 92.9 (2009), pp. 1901–1920. ISSN: 00027820. DOI: `10.1111/j.1551-2916.2009.03278.x`.

[201] Jyung Dong Lin and Jenq Gong Duh. “Crystallite Size and Microstrain of Thermally Aged Low-Ceria- and Low-Yttria-Doped Zirconia”. In: *J. Am. Ceram. Soc.* 81.4 (1998), pp. 853–860.

[202] Jyung Dong Lin and Jenq Gong Duh. “The use of X-ray line profile analysis in the tetragonal to monoclinic phase transformation of ball milled, as-sintered and thermally aged zirconia powders”. In: *J. Mater. Sci.* 32.18 (1997), pp. 4901–4908. ISSN: 00222461. DOI: `10.1023/A:1018668006162`.

[203] Ruth Knibbe et al. “Durability of solid oxide cells”. In: *Green* 1.2 (2011), pp. 141–169. ISSN: 18698778. DOI: `10.1515/GREEN.2011.015`.

[204] J.H.E. Jeffes. “Ellingham Diagrams”. In: *Encycl. Mater. Sci. Technol.* (2001), pp. 2751–2753. DOI: `10.1016/b0-08-043152-6/00490-3`.

[205] Anne Hauch et al. “Silica Segregation in the Ni/YSZ Electrode”. In: *J. Electrochem. Soc.* 154.7 (2007), A619. ISSN: 00134651. DOI: `10.1149/1.2733861`.

[206] Anne Hauch et al. “Solid Oxide Electrolysis Cells: Microstructure and Degradation of the Ni/Yttria-Stabilized Zirconia Electrode”. In: *J. Electrochem. Soc.* 155.11 (2008), B1184. ISSN: 00134651. DOI: `10.1149/1.2967331`.

[207] Sergey V. Ushakov et al. “Structure and Thermal Expansion of Yttria Stabilized Zirconia and La 2 Zr 2 O 7 above 1500 °C from Neutron Diffraction on Levitated Samples”. In: *J. Am. Ceram. Soc.* 98.10 (2015), pp. 3381–3388.

[208] Shiyang Cheng et al. “ Ionic/Electronic Conductivity, Thermal/Chemical Expansion and Oxygen Permeation in Pr and Gd Co-Doped Ceria Pr x Gd 0.1 Ce 0.9-x O 1.95-δ ”. In: *J. Electrochem. Soc.* 164.13 (2017), F1354–F1367. ISSN: 0013-4651. DOI: `10.1149/2.0531713jes`.

[209] Rebecca J. O’Toole et al. “Particle atomic layer deposition of alumina for sintering yttria-stabilized cubic zirconia”. In: *J. Am. Ceram. Soc.* 102.5 (2019), pp. 2283–2293. ISSN: 15512916. DOI: `10.1111/jace.16091`.

[210] L. Holzer et al. “Microstructure degradation of cermet anodes for solid oxide fuel cells: Quantification of nickel grain growth in dry and in humid atmospheres”. In: *J. Power Sources* 196.3 (2011), pp. 1279–1294. ISSN: 03787753. DOI: `10.1016/j.jpowsour.2010.08.017`. URL: `http://dx.doi.org/10.1016/j.jpowsour.2010.08.017`.

[211] Mario Burbano et al. “A dipole polarizable potential for reduced and doped CeO2 obtained from first principles”. In: *J. Phys. Condens. Matter* 23.25 (2011). ISSN: 09538984. DOI: `10.1088/0953-8984/23/25/255402`.

[212] S. R. Bishop et al. “Reducing the chemical expansion coefficient in ceria by addition of zirconia”. In: *Energy Environ. Sci.* 6.4 (2013), pp. 1142–1146. ISSN: 17545706. DOI: `10.1039/c3ee23917a`.

[213] Shaorong Wang et al. “Expansion Behavior of Ce 1−yGd yO2.0−0.5y−δ under Various Oxygen Partial Pressures Evaluated by HTXRD”. In: *J. Electrochem. Soc.* 150.7 (2003), A952. ISSN: 00134651. DOI: `10.1149/1.1580133`.

[214] Erich C. Fein et al. *Statistics for Research Students*. Toowoomba: University of Southern Queensland, 2021, p. 177. URL: `https://usq.pressbooks.pub/statisticsforresearchstudents/`.

[215] D. The et al. “Microstructural comparison of solid oxide electrolyser cells operated for 6100 h and 9000 h”. In: *J. Power Sources* 275 (2015), pp. 901–911. ISSN: 03787753. DOI: `10.1016/j.jpowsour.2014.10.188`.

[216] Byung Kook Kim, Jin Woo Hahn and Kyoung R. Han. “Quantitative phase analysis in tetragonal-rich tetragonal/monoclinic two phase zirconia by Raman spectroscopy”. In: *J. Mater. Sci. Lett.* 16.8 (1997), pp. 669–671. ISSN: 02618028. DOI: `10.1023/A:1018587821260`.

[217] Hans F. M. Boelens et al. “New background correction method for liquid chromatography with diode array detection, infrared spectroscopic detection and Raman spectroscopic detection”. In: *J. Chromatogr. A* 1057 (2004), pp. 21–30.

[218] G. Kartopu and M. Es-Souni. “Microstructural properties of solution-deposited La0.7Sr 0.3MnO3 and LaMnO3 thin films”. In: *J. Appl. Phys.* 99.3 (2006). ISSN: 00218979. DOI: `10.1063/1.2164534`.

[219] S. A. Muhammed Ali et al. “Optical, mechanical and electrical properties of LSCF–SDC composite cathode prepared by sol–gel assisted rotary evaporation technique”. In: *J. Sol-Gel Sci. Technol.* 86.2 (2018), pp. 493–504. ISSN: 15734846. DOI: `10.1007/s10971-018-4636-8`. URL: `http://dx.doi.org/10.1007/s10971-018-4636-8`.

[220] John D. Kirtley et al. “In Operando Optical Studies of SOFCs Operating with Butanol”. In: *ECS Meet. Abstr.* MA2015-03.1 (2015), pp. 233–233. DOI: `10.1149/ma2015-03/1/233`.

[221] M. A. Pimenta et al. “Studying disorder in graphite-based systems by Raman spectroscopy”. In: *Phys. Chem. Chem. Phys.* 9.11 (2007), pp. 1276–1291. ISSN: 14639076. DOI: `10.1039/b613962k`.

[222] Aiswarya Padinjarethil and Anke Hagen. “Identification of Degradation Parameters in SOC Using In-Situ and Ex-Situ Approaches”. In: *ECS Meet. Abstr.* MA2021-03.1 (2021), pp. 67–67. DOI: `10.1149/ma2021-03167mtgabs`.

[223] Vanja Subotić and Christoph Hochenauer. “Analysis of solid oxide fuel and electrolysis cells operated in a real-system environment: State-of-the-health diagnostic, failure modes, degradation mitigation and performance regeneration”. In: *Prog. Energy Combust. Sci.* 93.March (2022). ISSN: 03601285. DOI: `10.1016/j.pecs.2022.101011`.

[224] Sune Dalgaard Ebbesen and Mogens Mogensen. “Exceptional durability of solid oxide cells”. In: *Electrochem. Solid-State Lett.* 13.9 (2010). ISSN: 10990062. DOI: `10.1149/1.3455882`.

[225] Matthias Riegraf et al. “The influence of sulfur impurities in industrial COx gases on solid oxide electrolysis cell (SOEC) degradation”. In: *J. Power Sources* 559.January (2023). ISSN: 03787753. DOI: `10.1016/j.jpowsour.2023.232669`.

[226] Rainer Küngas et al. “Lifetime Capacity – An Important Performance Metric for SOEC Stacks”. In: *ECS Trans.* 91.1 (2019), pp. 2601–2611. ISSN: 1938-6737. DOI: `10.1149/09101.2601ecst`.

[227] Mogens B. Mogensen et al. “Ni migration in solid oxide cell electrodes: Review and revised hypothesis”. In: *Fuel Cells* 21.5 (2021), pp. 415–429. ISSN: 16156854. DOI: `10.1002/fuce.202100072`.

[228] H. Kim et al. “Cu-Ni Cermet Anodes for Direct Oxidation of Methane in Solid-Oxide Fuel Cells”. In: *J. Electrochem. Soc.* 149.3 (2002), A247. ISSN: 00134651. DOI: `10.1149/1.1445170`.

[229] Joshua Mermelstein, Marcos Millan and Nigel Brandon. “The impact of steam and current density on carbon formation from biomass gasification tar on Ni/YSZ, and Ni/CGO solid oxide fuel cell anodes”. In: *J. Power Sources* 195.6 (2010), pp. 1657–1666. ISSN: 03787753. DOI: `10.1016/j.jpowsour.2009.09.046`.

[230] Benjamin Königshofer et al. “Towards strategies to mitigate degradation and regenerate performance of a solid oxide electrolyzer during co-electrolysis operation”. In: *J. Power Sources* 556.November 2022 (2023). ISSN: 03787753. DOI: `10.1016/j.jpowsour.2022.232404`.

[231] William A Maza et al. “ Operando Studies of Carbon Removal and Partial Oxidation in Solid Oxide Fuel Cells ”. In: *ECS Trans.* 91.1 (2019), pp. 629–640. ISSN: 1938-6737. DOI: `10.1149/09101.0629ecst`.

[232] Theis Løye Skafte et al. “Selective high-temperature CO2 electrolysis enabled by oxidized carbon intermediates”. In: *Nat. Energy* 4.10 (2019), pp. 846–855. ISSN: 20587546. DOI: `10.1038/s41560-019-0457-4`. URL: `http://dx.doi.org/10.1038/s41560-019-0457-4`.

[233] Aiswarya Krishnakumar Padinjarethil. “Identification of acceleration parameters for SOC degradation: Data-Driven and Experimental Approaches.” PhD thesis. Danish Technical University, 2022, p. 326.

[234] A. Tsoga, P. Nikolopoulos and A. Naoumidis. “Modified YSZ/Ni structures with improved stability”. In: *Ionics (Kiel).* 2.5-6 (1996), pp. 427–434. ISSN: 18620760. DOI: `10.1007/BF02375822`.

[235] A. Tsoga, A. Naoumidis and P. Nikolopoulos. “Wettability and interfacial reactions in the systems Ni/YSZ and Ni/Ti-TiO2/YSZ”. In: *Acta Mater.* 44.9 (1996), pp. 3679–3692. ISSN: 13596454. DOI: `10.1016/1359-6454(96)00019-5`.

[236] D. Skarmoutsos, P. Nikolopoulos and A. Tsoga. “Titania doped YSZ for SOFC anode Ni-cermet”. In: *Ionics (Kiel).* 5.5-6 (1999), pp. 455–459. ISSN: 18620760. DOI: `10.1007/BF02376013`.

[237] Ryan Davis et al. “Phase wettability and microstructural evolution in solid oxide fuel cell anode materials”. In: *Acta Mater.* 78 (2014), pp. 271–281. ISSN: 13596454. DOI: `10.1016/j.actamat.2014.06.037`. URL: `http://dx.doi.org/10.1016/j.actamat.2014.06.037`.

[238] A. Kaiser et al. “Electrical characterization of highly titania doped YSZ”. In: *Ionics (Kiel).* 4.3-4 (1998), pp. 215–219. ISSN: 18620760. DOI: `10.1007/BF02375948`.

[239] M. T. Colomer et al. “Effect of titania doping and sintering temperature on titanium local environment and electrical conductivity of YSZ”. In: *J. Alloys Compd.* 689 (2016), pp. 512–524. ISSN: 09258388. DOI: `10.1016/j.jallcom.2016.07.164`. URL: `http://dx.doi.org/10.1016/j.jallcom.2016.07.164`.

[240] Grzegorz Brus, Hiroshi Iwai and Janusz S. Szmyd. "An Anisotropic Microstructure Evolution in a Solid Oxide Fuel Cell Anode". In: *Nanoscale Res. Lett.* 15.1 (2020), pp. 1–9. ISSN: 1556276X. DOI: `10.1186/s11671-019-3226-1`.

[241] Jeol. *Penetration Depth*. URL: `https://www.jeol.com/words/semterms/20121024.045259.php` (visited on 17/01/2023).